Kaon Identification Upgrade and Search for the Dark Photon Production in the $\pi^0 \to \gamma A'$ Decay, at NA62

by

Jack Dylan Sanders

A thesis submitted to the University of Birmingham for the degree of

DOCTOR OF PHILOSOPHY

UNIVERSITY OF BIRMINGHAM

Supervisors:

Prof. Evgueni Goudzovski

Prof. Cristina Lazzeroni

Dr. Angela Romano

Particle Physics Research Group

School of Physics and Astronomy

University of Birmingham

May 2025

Abstract

The 2022–2024 data from the NA62 experiment at CERN has been used to search for dark photon (A') production in the $\pi^0 \to A'\gamma$ decay, and subsequent prompt decay $A' \to e^+e^-$. Within the mass range $6 \leq m_{A'} \leq 121.6\,\mathrm{MeV}/c^2$ no signal is observed and an exclusion limit on the mixing parameter ϵ^2 across the mass range is obtained.

The NA62 beam consists of 6 % kaons, therefore requiring beam particle identification conducted by the KTAG. The KTAG comprises a differential Cherenkov counter with achromatic ring focus (CEDAR) and a purpose-built photon-detection system. Since 2016, NA62 has employed a CEDAR with a nitrogen radiator gas. To reduce the amount of material in the beam's path, a new CEDAR utilising hydrogen gas (H_2) as a radiator has been used since 2023. The CEDAR-Hydrogen (CEDAR-H) detector design, testing and commissioning at NA62 are presented. The CEDAR with H_2 achieved a kaon identification efficiency of 99.7 % and a kaon time resolution of 66 ps.

Finally, software developments towards the design of the High Intensity Kaon Experiments (HIKE) facility are presented.

Acknowledgements

I am tremendously grateful for the teaching and collaboration of my colleagues, for which I could not have completed this work. I want to mention a few in particular.

I would like to thank my supervisors, Evgueni Goudzovski, Cristina Lazzeroni, and Angela Romano, for their guidance throughout my time at the University of Birmingham and during the writing process for this thesis.

I also extend my gratitude to my fellow NA62 collaborators who have been a part of my work and for the successful operation of the NA62 experiment. I would like to thank John Fry and Chris Parkinson for their passage of knowledge relating to the CEDAR and their hard work to get the new CEDAR detector designed, tested and working at NA62. I would also like to thank the many students in the office who helped me throughout this journey and whom I now call my friends.

Finally, I would like to thank my family, especially Emily, who has endured my long nights of work and periods away at CERN. I am immensely grateful for her support and I couldn't have done it without her.

Declaration of author's contributions

Chapter 1 sets out the theoretical framework for the thesis. The Standard Model and the role of kaon physics within it are briefly reviewed to provide context for the NA62 experiment and future kaon experiments. The chapter also include theoretical foundations for the Dark Photon. The NA62 experiment is presented in Chapter 2 with descriptions of the sub-detectors and the latest result for the $K^+ \to \pi^+ \nu\bar{\nu}$ decay. During the period 2021–2024 I completed data taking shifts as well as expert shifts for the kaon identification detector (KTAG) and the experiments trigger system to assist with the collection of data.

Chapter 3 describes the development and commissioning of the CEDAR-H detector at CERN. Section 3.1 describes the principle of operation of the CEDAR as well as the construction of the vessel. The design of the CEDAR-H is described in Section 3.1 and was completed prior to my involvement. The characterisation of the optical elements was completed by CERN engineers but was consolidated and documented by myself. The simulation required for the alignment of the spherical mirror was completed by myself. I was involved in the test-beam in Section 3.3 by completing a number of shifts. I conducted the analysis of the data from the test-beam presented in Section 3.3. I was involved in the installation of CEDAR-H in NA62 described in Section 3.4 which was conducted at the start of my long term attachment in 2023. I was involved in the commissioning in 2023 described in Section 3.5 and produced the analysis. The commissioning in 2024 was also completed by myself and other members of the Birmingham group. I was involved in the monitoring of the KTAG performance in the period 2021–2024 by conducting shifts as the detector expert as briefly described in Section 3.5.

The search for the Dark Photon described in Chapter 4 is entirely my work with the exception of the results referenced from other experiments.

Chapter 5 set outs the possibility for future kaon experiments. Section 5.1 describes the High Intensity Kaon Experiments (HIKE) and the planned detector setups for three separate phases. Section 5.2 describes my contributions to the NA62 software where I developed and tested new features to allow the introduction of new detectors. Section 5.3 presents the development of an upgraded KTAG by the University Birmingham group. I have collected information from reports and presentations to describe the development of the upgrade. I completed the implementation and testing of the upgrades in the new software framework, producing performance results. In Section 5.4 the upgraded Ring Imaging Cherenkov counter (RICH) photon-detection system is described which I completed from design to implementation in the software framework. Section 5.5 provides the detector rates for HIKE Phase 2 which I evaluated.

No other qualifications were obtained from the work completed within this thesis.

Contents

List of Acronyms

$K_{2\pi D}$ $K \to \pi^+ \pi^0_D$. 85–93, 95–98, 101

$K_{\mu 3D}$ $K \to \pi^0_D \mu^+ \nu_\mu$. 89–92, 95–97

ALD Atomic Layer Deposition. 124

ANTI-0 veto hodoscope. 38, 39

ASIC Application-Specific Integrated Circuits. 27

BSM Beyond the Standard Model. 1, 8

CE Collection Efficiency. 127

CEDAR differential Cherenkov counter with achromatic ring focus. i, 21–26, 43–50, 52–54, 56, 57, 59, 60, 67, 69–72, 79, 147

CEDAR-H CEDAR-Hydrogen. i, 25, 26, 49–83, 147

CEDAR-N CEDAR-North. 23, 43, 45, 51, 52

CEDAR-W CEDAR-West. 23–25, 43, 45, 47, 49–52, 54, 61, 66, 68, 79–83, 147

CHANTI Charged particle Anti-coincidence detector. 28

CKM Cabibbo-Kobayashi-Maskawa. 4–8, 11

CL Confidence Level. 13, 15, 94, 95, 101–103, 107–109, 111

CP Charge-Parity. 4, 9, 13–15

DP Dark Photon. 1, 16, 17, 84, 85, 91–95, 100–102, 104–111

DSS Detector Safety System. 69

FCNC Flavour Changing Neutral Current. 11, 13

FV Fiducial Volume. 19, 20, 22, 28, 38, 39, 44, 90, 91, 103, 108, 116, 139, 141

GTK GigaTracker. 22, 26–28

H_2 hydrogen gas. i, 44, 50–57, 68, 69, 71, 72, 74, 75, 77–79, 147

HASC Hadronic Sampling Calorimeter. 37

HIKE High-intensity Kaon Experiments. 2, 10, 112, 142, 143, 147, 148

IAC Integrated Anode Charge. 123–125

IRC Intermediate-Ring Calorimeter. 32

K_{e3} $K^+ \to \pi^0 e^+ \nu$. 132–134, 136

LAV Large Angle Veto. 22, 33

LEE Look-Elseware Effect. 94, 100, 105

LKr Liquid Krypton Calorimeter. 22, 31, 32, 34, 85, 89

LS3 CERN Long Shutdown 3. 112

MC Monte Carlo. 41, 67, 84, 86–106, 108, 111, 117, 127, 133–137, 140–143

MCP-PMT Micro-Channel Plate Photomultiplier. 123, 127

MUV Muon Veto System. 35

N_2 nitrogen gas. 43, 44, 50, 51, 54, 57, 68, 71–73, 79, 147

PDG Particle Data Group. 99

PET Polyethylene Terephthalate. 29

PID Particle Identification. 23, 87, 89

PMT Photomultiplier Tube. 24, 47, 49, 51–54, 56, 58–63, 67, 70, 75, 80, 114

$K_{\pi\nu\bar{\nu}}$ $K^+ \to \pi\nu\bar{\nu}$. 30, 31, 41, 42

QCD Quantum Chromodynamics. 3, 8, 12

QE Quantum Efficiency. 25, 53, 123, 125, 131, 132

QFT Quantum Field Theory. 3

RICH Ring Imaging Cherenkov counter. 22, 23, 30, 32, 34, 89

SAC Small Angle Calorimeter. 23, 32

SiPM Silicon Photomultiplier. 28, 35, 38, 130–133, 135–139

SM Standard Model. 1, 3, 6–8, 13, 15, 16, 19, 84, 112

spill SPS beam pulse. 56

SPS Super Proton Synchrotron. 1, 18, 23, 43

TDAQ Trigger and Data Acquisition system. 19

TFF Transition Form Factor. 98–100

UL Upper Limit. 94, 95, 101–103, 106–108, 110, 147

VC Veto-Counter. 38

List of Figures

List of Tables

Introduction

The understanding of the fundamental components and interactions of the universe at the smallest of scales has culminated in the formation of the Standard Model (SM) of particle physics. The SM stands out as one of the most successful theories produced by science. However, it does not cover all the observations such as neutrino masses, the existence of dark matter, matter-antimatter asymmetry and the fourth fundamental force of gravity.

Most modern particle physics experiments aim to test the SM as precisely as possible and to search for new physics Beyond the Standard Model (BSM). Two experimental methods are employed to reach these aims. One is to reach ever-increasing energies to directly produce and observe new heavier particles. Examples of this method are the experiments at the Large Hadron Collider at CERN, such as ATLAS and CMS, that discovered the Higgs boson in 2012. The second method involves collecting large data sets to search for rare processes where any deviations from the SM can provide evidence of BSM physics. An example of this method is the observation of the $K^+ \to \pi^+\nu\bar{\nu}$ decay by NA62 at the CERN Super Proton Synchrotron (SPS). The aim of the experiment is to measure the branching ratio of the decay that is precisely predicted by the SM. A more detailed description of the SM and the role of kaon physics can be found in Chapter 1.

The work completed within this thesis was undertaken within the NA62 and HIKE collaborations. The thesis includes the theoretical foundations for the work completed throughout, in Chapter 1. Chapter 2 describes the NA62 experimental setup and the latest results published by the collaboration of the observation of $K^+ \to \pi^+\nu\bar{\nu}$ decay. Chapter 3 describes the development of a new CEDAR detector with a hydrogen radiator gas used for the NA62 kaon identification system. An analysis to search for the Dark Photon (DP) at NA62 is presented in Chapter 4.

Finally, the work completed for the High-intensity Kaon Experiments (HIKE) proposal is presented in Chapter 5. The HIKE experiment involves the continued data collection of the $K^+ \to \pi^+\nu\bar{\nu}$ decay in Phase 1 and to observe the $K_L \to \pi^0 l^+ l^-$. This includes the upgrades to the NA62 offline software to facilitate simulations of new experimental setups and calculations of the detector rates for Phase 2.

Chapter 1

Theoretical Foundations

1.1 The Standard Model of Particle Physics

The Standard Model (SM) of particle physics is a Quantum Field Theory (QFT) that describes the fundamental matter and three of the four forces in the universe. The matter content of the SM comprises 12 elementary fermions (and their anti-particles), five vector bosons that mediate the three fundamental forces, and a scalar boson responsible for particle masses (Figure 1.1). There are six quark flavours: up, down, charm, strange, top and bottom. Depending on their charge, they are separated into three generations or two types. There are also three lepton flavours, each with a corresponding neutrino. It is important to note that the SM is not a complete theory. An example of this is the gravitational force, which is not included in the SM. However, at the small scales of particle physics, this force is neglected due to its weaker coupling compared to the other three forces (strong, electromagnetic and weak).

The SM has a total non-Abelian gauge symmetry group of SU(3)×SU(2)×U(1). The SU(3) group governs the strong interactions between quarks in the form of Quantum Chromodynamics (QCD). The strong force is mediated by the gluon. The SU(2)×U(1) groups describe the electroweak interactions [1], which are mediated by the photon and $W^{\pm}$, Z^0 bosons. The SU(3) is an exact gauge symmetry while the electroweak symmetry is spontaneously broken by the Higgs field [2], resulting in the massive electroweak bosons ($W^{\pm}$ and Z^0).

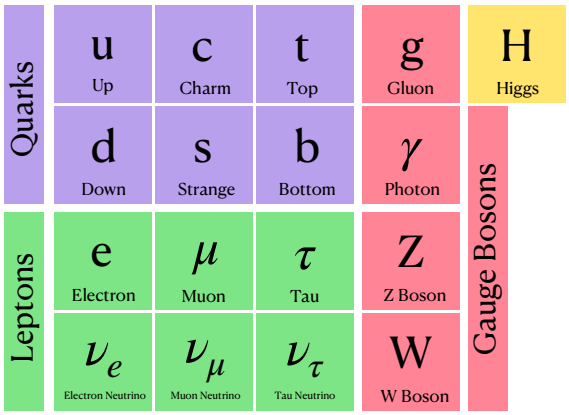

Figure 1.1: The particle content of the Standard Model of particle physics with the 12 fermions shown in purple and green, the five vector bosons shown in red and the Higgs scalar boson shown in yellow.

1.2 Quark Mixing and the CKM Matrix

Electroweak symmetry breaking gives rise to massive quarks, with the strong and weak eigenstates diverging. The weak eigenstates (d', s', b') of down, strange and bottom quarks, which are associated with the weak interaction, are related to the mass eigenstates (d, s, b) through the Cabibbo-Kobayashi-Maskawa (CKM) matrix V_{CKM} [3, 4], with the following relation:

$$\begin{bmatrix} d' \\ s' \\ b' \end{bmatrix} = V_{\text{CKM}} \begin{bmatrix} d \\ s \\ b \end{bmatrix} = \begin{bmatrix} V_{ud} & V_{us} & V_{ub} \\ V_{cd} & V_{cs} & V_{cb} \\ V_{td} & V_{ts} & V_{tb} \end{bmatrix} \begin{bmatrix} d \\ s \\ b \end{bmatrix}. \tag{1.1}$$

The elements of the CKM matrix determine the strength of the interaction between quark flavours. Interaction vertices involving the transition from a quark type i to j introduce a coupling factor of V_{ij} and a corresponding transition probability given by $|V_{ij}|^2$.

As a unitary 3×3 matrix, the CKM matrix can be described by four parameters: three mixing angles (θ_{12}, θ_{13}, θ_{23}) which dictate the couplings between each generation of quarks and one phase (δ) which introduces Charge-Parity (CP) violation [4]. A number of different parametrisations of the matrix are possible, but the

three-angle and one-phase formalism is the standard choice [5],

$$V_{\text{CKM}} = \begin{bmatrix} c_{12}c_{13} & s_{12}c_{13} & s_{13}e^{-i\delta} \\ -s_{12}c_{23} - c_{12}s_{23}s_{13}e^{i\delta} & c_{12}c_{23} - s_{12}s_{23}s_{13}e^{i\delta} & s_{23}c_{13} \\ s_{12}s_{23} - c_{12}c_{23}s_{13}e^{i\delta} & -c_{12}s_{23} - s_{12}c_{23}s_{13}e^{i\delta} & c_{23}c_{13} \end{bmatrix} \tag{1.2}$$

where $c_{ij} = \cos\theta_{ij}$ and $s_{ij} = \sin\theta_{ij}$. The mixing angles θ_{ij} can be selected to satisfy $0 \leq \theta_{ij} \leq \frac{\pi}{2}$ such that $c_{ij}, s_{ij} \geq 0$.

Experimental data shows that there is a hierarchical structure to the components of the CKM matrix,

$$s_{12} \ll s_{23} \ll s_{13}. \tag{1.3}$$

Based on this hierarchy, the Wolfenstein parametrisation [6] describes the CKM using the parameters:

$$\begin{aligned} s_{12} &= \lambda, \\ s_{23} &= A\lambda^2, \\ s_{13} &= A\lambda^3(\rho + i\eta), \end{aligned} \tag{1.4}$$

resulting in

$$V_{\text{CKM}} = \begin{bmatrix} 1 - \frac{\lambda^2}{2} & \lambda & A\lambda^3(\rho - i\eta) \\ -\lambda & 1 - \frac{\lambda^2}{2} & A\lambda^2 \\ A\lambda^3(1 - \rho - i\eta) & -A\lambda^2 & 1 \end{bmatrix} + O(\lambda^4). \tag{1.5}$$

The CKM matrix is expanded in terms of λ and provides a hierarchical structure which reflects the pattern where transitions between quarks of the same/adjacent generations are stronger compared to distant ones. Expanding the CKM matrix in powers up to $O(\lambda^3)$ results in the loss of unitary. However, unitary can be restored by including $O(\lambda^5)$ [7] correction to the bottom left component of Equation 1.5,

$$V_{td} = A\lambda^3(1 - \bar{\rho} - i\bar{\eta}), \tag{1.6}$$

where

$$\begin{aligned} \bar{\rho} &= \rho\left(1 - \frac{\lambda^2}{2}\right), \\ \bar{\eta} &= \eta\left(1 - \frac{\lambda^2}{2}\right). \end{aligned} \tag{1.7}$$

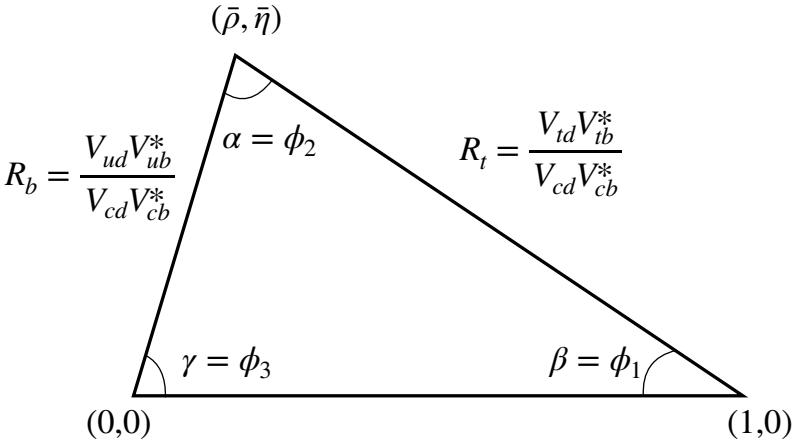

Figure 1.2: Sketch of the most common unitary triangle $V_{ud}V_{ub}^* + V_{cd}V_{cb}^* + V_{td}V_{tb}^* = 0$.

The unitary nature of the CKM matrix imposes conditions on the rows and columns:

$$\sum_i V_{ij}V_{kj}^* = \delta_{ik} \tag{1.8}$$

where δ_{ik} denotes the Kronecker symbol, which equals 1 when elements $j = k$ and 0 otherwise. This results in six vanishing combinations of the CKM matrix, which can be represented as triangles in the complex plane. The most commonly used, with elements at leading order contributions of $A\lambda^3$ are,

$$V_{ud}V_{ub}^* + V_{cd}V_{cb}^* + V_{td}V_{tb}^* = 0. \tag{1.9}$$

In the Wolfenstein parameterization (Equation 1.5), the equation takes the form,

$$1 + \frac{V_{td}V_{tb}^*}{V_{cd}V_{cb}^*} = -\frac{V_{ud}V_{ub}^*}{V_{cd}V_{cb}^*} = \bar{\rho} + i\bar{\eta} \tag{1.10}$$

leading to the triangle in Figure 1.2.

The CKM matrix components are fundamental parameters of the SM. A large number of experiments have contributed to the measurements of the CKM, with a global fit yielding [8]:

$$\begin{bmatrix} |V_{ud}| & |V_{us}| & |V_{ub}| \\ |V_{cd}| & |V_{cs}| & |V_{cb}| \\ |V_{td}| & |V_{ts}| & |V_{tb}| \end{bmatrix} = \begin{bmatrix} 0.97436^{+0.00014}_{-0.00019} & 0.22498^{+0.00081}_{-0.00062} & 0.00373^{+0.00019}_{-0.00015} \\ 0.22484^{+0.00081}_{-0.00061} & 0.97351^{+0.00016}_{-0.00019} & 0.04160^{+0.00066}_{-0.00121} \\ 0.00857^{+0.00018}_{-0.00037} & 0.04088^{+0.00066}_{-0.00119} & 0.999125^{+0.000052}_{-0.000027} \end{bmatrix}. \tag{1.11}$$

Through measurement of the CKM matrix components, it is possible to constrain the unitary triangle of Figure 1.2, as depicted in Figure 1.3,

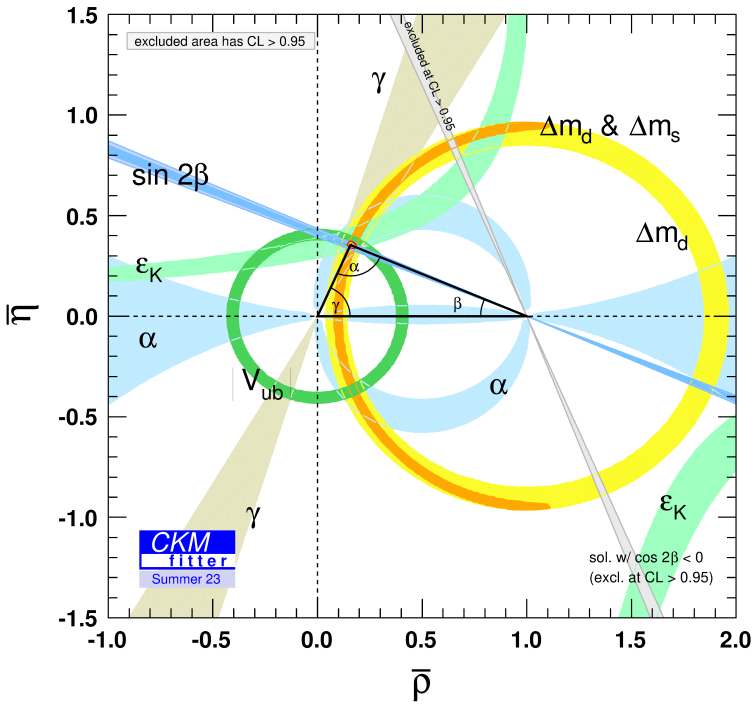

Figure 1.3: Constraints for the most common unitary triangle in the $(\bar{\rho},\bar{\eta})$ plane [8].

Including the four CKM components discussed above, there are nineteen free parameters of the SM:

- Four CKM matrix parameters: three mixing angles and one CP-violating phase.
- Six quark masses: up, down, charm, strange, top, and bottom: M_u, M_d, M_c, M_s, M_t and M_b.
- Three charged lepton masses: M_e, M_μ, and M_τ.
- Three gauge couplings associated with the Standard Model gauge group $\mathrm{SU}(3)_C \times \mathrm{SU}(2)_L \times \mathrm{U}(1)_Y$, which correspond to the strong, weak, and hypercharge interaction and are denoted by, g_s, g, and g'.
- Two Higgs sector parameters: the vacuum expectation value (v) and the Higgs boson mass (M_H).
- One QCD vacuum angle (θ_{QCD}), related to CP violation in the strong interaction.

Each of these parameters must be determined through experiment to the highest possible precision, as the SM does not predict their values. However, relations between the parameters, such as the unitary CKM matrix, allows for internal consistency tests within the SM. Any statistically significant deviations between experimental results and theoretical understanding or inconsistencies between different determinations of the parameters could be a hint of Beyond the Standard Model (BSM) physics.

As mentioned previously, a feature of the CKM matrix is that the diagonal components which describe the transitions within the quark generations dominate. The off-diagonal elements describing flavour-changing charged current transitions are suppressed between one generation and doubly suppressed for transitions between two generations. This suppression between two generations leads to rare processes, such as the decay $K^+ \to \pi^+ \nu\bar{\nu}$, discussed in Section 1.3.1.

1.3 Kaon Physics

The first possible observation of a meson, a particle composed of a quark-antiquark pair, was made in 1943 by Leprince-Ringuet and L'heritier [9, 10] and predated the discovery of the pion in 1947 [11]. Utilising a cloud chamber to measure cosmic rays, they found the first evidence of a particle with a mass of 990 times the mass of the electron [12]. However, given the uncertainty of the observation it was possible that the upper limit on the measured mass could reach the proton mass, therefore it was not credited for the discovery. In 1947, while similarly studying cosmic rays with cloud chambers, G. D. Rochester and C. C. Butler published a result which included two pictures showing forked tracks [13]. One of the tracks showed the decay of a neutral particle into two charged daughter particles, which turned out to be a decay of the neutral kaon to two charged pions. The other track showed the decay of a charged particle into charged and neutral daughter particles. This result was later confirmed in 1950 by a group in Cal-tech who observed multiple instances of these decays [14]. Between these publications, a group in Bristol used emulsion chambers to observe the decay of a charged particle into three charged particles [15], known then as the tau decay. This resulted in what was known as the

tau-theta problem, where seemingly the same particle was decaying into final states with different parities: Theta to two pions (+1) and Tau to three pions (-1). This eventually led to the discovery that parity is not conserved in weak interactions [16].

In the early 1950s, these particles would be described as K-mesons, for which there are four interaction (weak) eigenstates (K^+, K^-, K^0 and $\bar{K^0}$). These particles are produced via the strong interaction but decay via the weak interaction. Experiments continued to measure the characteristics of the K mesons and found features such as unusually long lifetimes (10^{-10} seconds) despite their rapid production [17]. These features arise from the fact the production of K mesons occurs through the strong interaction, whereas their decays proceed through the weak interaction. These deviations from the other previously discovered mesons, such as the pion, suggested the existence of a new quantum number named strangeness [18, 19]. The strangeness quantum number applies to all strongly interacting particles and is conserved in strong interactions but violated in weak ones.

Into the late 1950s and early 1960s, the neutral kaon became the centre of a number of studies because their relative ease of production and long lifetimes made them easy to study. Despite the fact that parity is violated in weak interactions, it was still believed that the combination of CP would be conserved. Through experiment, the two mass (strong) eigenstates of the neutral kaon showed to have different lifetimes, which resulted in their names K_L for long and K_S for short [20]. Each of these eigenstates had different CP values with the K_S having $CP = +1$ decaying to two pions and the K_L having $CP = -1$ decaying to three pions. However, in 1964, it was observed that the K_L also decayed to two pions [21] proving that the CP symmetry is indeed violated in weak decays. This decay is an example of indirect CP violation as it occurs through neutral kaon mixing. The first evidence of direct CP violation, where the violation occurs within the decay, was provided by the NA31 experiment in 1993 [22]. The process was conclusively observed by the KTeV and NA48 collaborations in the late 1990s [23, 24].

Kaon physics has continued to be investigated into the 21st century, with the NA62 collaboration at CERN conducting the study of K^+ decays. The main NA62 physics goal is to measure the branching fraction of the ultra-rare $K^+ \to \pi^+\nu\bar{\nu}$, described in more detail in Section 1.3.1. The K^+ consists of an up quark and an

Kaon Type	Quark Content	Mass (MeV/c^2)	Lifetime (s)
K^+	$u\bar{s}$	493.677 ± 0.015	$(1.238 \pm 0.002) \times 10^{-8}$
K^-	$\bar{u}s$	493.677 ± 0.015	$(1.238 \pm 0.002) \times 10^{-8}$
K^0	$d\bar{s}$	497.611 ± 0.013	-
$\bar{K}^0$	$\bar{d}s$	497.611 ± 0.013	-
K^0_L	Mixed state of K^0 and $\bar{K}^0$	-	$(5.116 \pm 0.021) \times 10^{-8}$
K^0_S	Mixed state of K^0 and $\bar{K}^0$	-	$(0.8954 \pm 0.0004) \times 10^{-10}$

Table 1.1: Properties of charged and neutral kaons [12].

Decay Mode	Shorthand Notation	Branching Ratio [%]
$K^+ \to \mu^+\nu_\mu$	$K_{\mu 2}$	63.56 ± 0.11
$K^+ \to \pi^+\pi^0$	$K_{2\pi}$	20.67 ± 0.08
$K^+ \to \pi^+\pi^+\pi^-$	$K_{3\pi}$	5.583 ± 0.024
$K^+ \to \pi^0 e^+\nu_e$	K_{e3}	5.07 ± 0.04
$K^+ \to \pi^0\mu^+\nu_\mu$	$K_{\mu 3}$	3.352 ± 0.034
$K^+ \to \pi^+\pi^0\pi^0$	$K_{3\pi 0}$	1.760 ± 0.023

Table 1.2: Main decay modes of the positively charged kaon (K^+) with their shorthand notation and branching ratios [12].

anti-strange quark, with the other kaon types described in Table 1.1. The six most common decay modes of the positively charged kaon, along with their shorthand notation, are shown in Table 1.2.

Future experimental efforts in kaon physics aim to investigate the neutral kaon modes. This is addressed by the High-intensity Kaon Experiments (HIKE) proposal which is detailed in Section 5. HIKE planned to have multiple phases. HIKE plans to continue measuring the branching fraction of $K^+ \to \pi^+\nu\bar{\nu}$, then to observe $K^0_L \to \pi^0 l^+ l^-$ (described in Section 1.3.2) and eventually $K^0_L \to \pi^0\nu\bar{\nu}$ (described in Section 1.3.1).

1.3.1 The $K \to \pi\nu\bar{\nu}$ decay

The $K^+ \to \pi^+\nu\bar{\nu}$ decay proceeds through a Flavour Changing Neutral Current (FCNC) interaction which is extremely suppressed in the SM due to CKM and

GIM suppression [25]. The decay amplitude is dominated by the contributions from the box and penguin Feynman diagrams shown in Figure 1.4. The decay is the transformation of an anti-strange quark into an anti-down quark and a neutrino pair, leaving the up quark unchanged. The branching ratio is dominated by the Z^0 penguin diagrams and, after summing over the three neutrino flavours, can be formulated as [26]

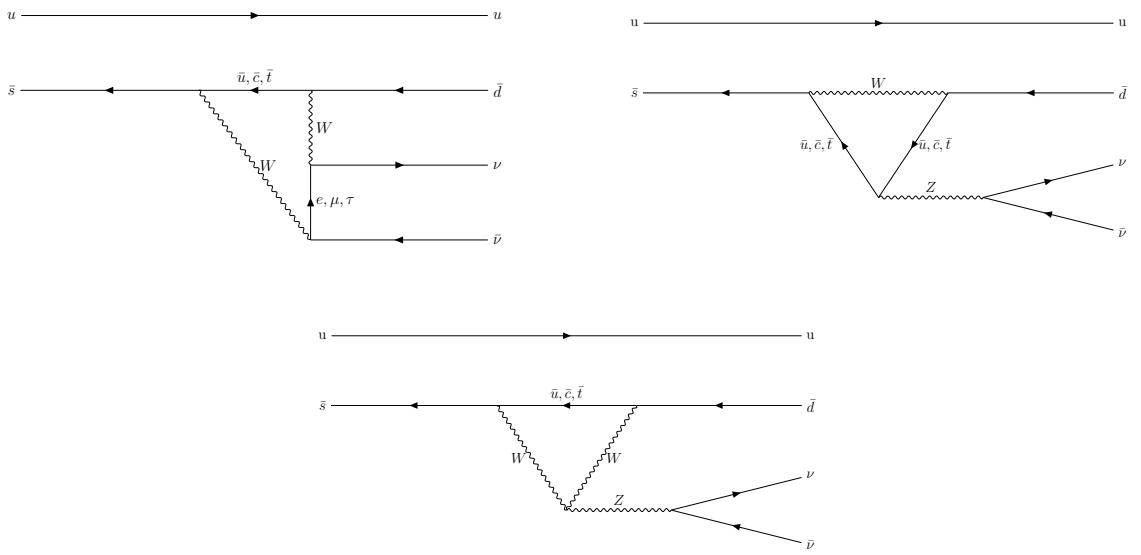

Figure 1.4: Feynman diagrams for the $K^+ \to \pi^+ \nu\bar{\nu}$ decay.

$$\mathcal{B}(K^+ \to \pi^+ \nu\bar{\nu}) = \kappa_+ (1 + \Delta_{EM}) \left[\left(\frac{\mathfrak{Im}(\lambda_t)}{\lambda^5} X(x_t) \right)^2 + \left(\frac{\mathfrak{Re}(\lambda_c)}{\lambda} P_c(X) + \frac{\mathfrak{Re}(\lambda_t)}{\lambda^5} X(x_t) \right)^2 \right] \tag{1.12}$$

with

$$\kappa_+ = (5.173 \pm 0.025) \times 10^{-11} \left(\frac{\lambda}{0.225} \right)^8, \qquad \Delta_{EM} = -0.003, \tag{1.13}$$

where $x_t = M_t^2 / M_W^2$ is the ratio of the mass of the top quark and the mass of the $W^\pm$ boson, λ originates from the Wolfenstein parametrisation of the CKM matrix and $\lambda_i = V_{is}^* V_{id}$ where V_{ij} are CKM matrix elements. The Δ_{EM} takes into account the correction from radiative photon exchanges, and κ_+ condenses the relevant hadronic matrix elements. The terms $X(x_t)$ and $P_c(X)$ are the loop functions which describe contributions from the top and charm quark. The $X(x_t)$ can be described by the

equation [27, 26],

$$X(x_t) = X^{(0)} + \frac{\alpha_s}{4\pi}X_t^{(1)} + \frac{\alpha}{4\pi}X_t^{(EW)} = 1.481 \pm 0.005 \pm 0.008 \tag{1.14}$$

where $X^{(0)}$ is the leading order contribution, $X_t^{(1)}$ is the next-to-leading order (NLO) QCD correction and $X_t^{(EW)}$ is the electroweak correction. The $P_c(X)$ term describes the contribution from the charm quark which is defined as [28],

$$P_c(X) = P_c^{SD}(X) + \delta P_{c,u} = 0.404 \pm 0.024 \tag{1.15}$$

where $\delta P_{c,u}$ is the long distance contribution arising from non-local effects involving intermediate hadronic states and $P_c^{SD}(X)$ is the short distance contribution arising from loop diagrams with internal charm quarks [28],

$$P_c^{SD}(X) = \frac{1}{\lambda^4}\left(\frac{2}{3}X_{NNL}^e + \frac{1}{3}X_{NNL}^\tau\right) \tag{1.16}$$

where X_{NNL}^l are loop functions from the charm quark interacting with electron and tau neutrinos, produced from NLO QCD and NNLO calculations. It is possible to represent λ_t and λ_c from Equation 1.12 as [29],

$$\mathfrak{Re}(\lambda_t) = -\left(1 - \frac{\lambda^2}{2}\right)A^2\lambda^5(1-\bar{\rho}), \tag{1.17}$$

$$\mathfrak{Im}(\lambda_t) = A^2\lambda^5\eta, \tag{1.18}$$

$$\mathfrak{Re}(\lambda_c) = -\lambda\left(1 - \frac{\lambda^2}{2}\right), \tag{1.19}$$

yielding the following prediction for the $K^+ \to \pi^+\nu\bar{\nu}$ branching fraction (1.12) in terms of the Wolfenstein parameters

$$\mathcal{B}(K^+ \to \pi^+\nu\bar{\nu}) = \kappa_+ A^4 X(x_t)^2 \frac{1}{\sigma}((\sigma\bar{\eta})^2 + (\rho_0 - \bar{\rho})^2), \tag{1.20}$$

where $\sigma = (1/(1-\frac{\lambda^2}{2}))^2$ and $\rho_0 = 1 + \frac{P_0(X)}{A^2X(x_t)}$. Equation 1.20 represents an ellipse in the unitary triangle plane $(\bar{\rho}, \bar{\eta})$ shown in Figure 1.5, with centre at $(\rho_0, 0)$, a semi-major axis equal to $\sqrt{\frac{\mathcal{B}}{\kappa_+ A^4 X(x_t)^2}}$ and a semi-minor axis of $\sqrt{\frac{\mathcal{B}}{\sigma\kappa_+ A^4 X(x_t)^2}}$. The ellipse constrains the parameters $(\bar{\rho}, \bar{\eta})$ and is depicted in Figure 1.6.

The $K_L \to \pi^0\nu\bar{\nu}$ decay is dominated by contributions from Feynman diagrams similar to Figure 1.4, but with a down quark spectating the decay compared to an up quark for the charged mode. The decay is theoretically clean and almost entirely CP violating, dominated by top-quark loop contributions [30]. This gives a branching

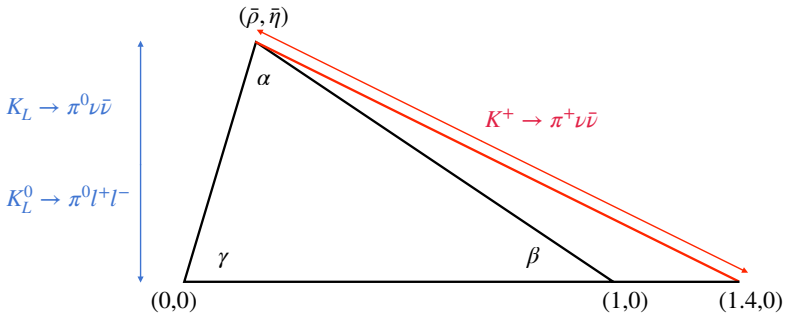

Figure 1.5: Diagram of the unitary triangle and its relationship with rare kaon decays.

fraction depending only on the imaginary part of the top loop from Equation 1.12, which is CP violating,

$$\mathcal{B}(K_L \to \pi^0\nu\bar{\nu}) = \kappa_L \left(\frac{\mathfrak{Im}(\lambda_t)}{\lambda^5} X(x_t) \right)^2 \tag{1.21}$$

with

$$\kappa_L = (2.231 \pm 0.013) \times 10^{-10} \left(\frac{\lambda}{0.225} \right)^8. \tag{1.22}$$

In the Wolfenstein parametrisation, the equation takes the form,

$$\mathcal{B}(K_L \to \pi^0\nu\bar{\nu}) = \kappa_L \eta^2 A^4 X(x_t)^2. \tag{1.23}$$

The decay can be used to further constrain the parameter $\bar{\eta}$ and is shown in Figure 1.5 and 1.6.

Inputting experimental values into the equations for the branching fractions produces the SM predictions [31],

$$\mathcal{B}(K^+ \to \pi^+\nu\bar{\nu}) = (8.60 \pm 0.42) \times 10^{-11} \tag{1.24}$$

and

$$\mathcal{B}(K_L \to \pi^0\nu\bar{\nu}) = (2.94 \pm 0.15) \times 10^{-11}. \tag{1.25}$$

The first observation and measurement of the branching fraction for the $K^+ \to \pi^+\nu\bar{\nu}$ decay was obtained by NA62 in 2024 and is described in Section 2. The leading experimental result for the branching fraction of the $K_L \to \pi^0\nu\bar{\nu}$ decay is an upper limit obtained at a 90 % Confidence Level (CL) by the KOTO experiment [32],

$$\mathcal{B}(K_L \to \pi^0\nu\bar{\nu}) < 220 \times 10^{-11}. \tag{1.26}$$

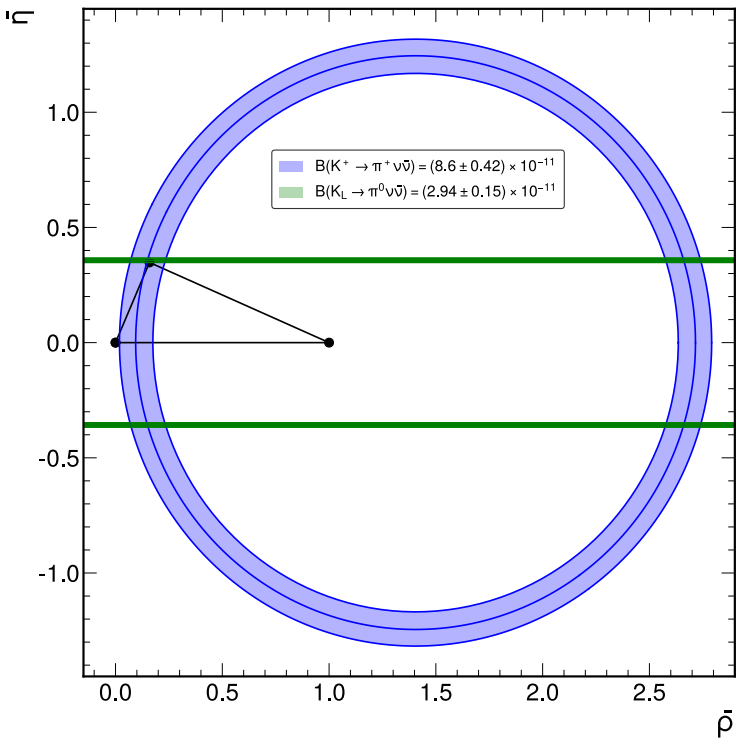

Figure 1.6: Constraints on the unitary triangle from the SM predictions for the branching fractions of $K^+ \to \pi^+\nu\bar{\nu}$ and $K_L \to \pi^0\nu\bar{\nu}$ decays [12]. The width of the bands are the extent of the errors on the branching fractions.

1.3.2 The $K_L^0 \to \pi^0 l^+ l^-$ decay

The decay $K_L^0 \to \pi^0 l^+ l^-$ is a FCNC transition of a strange quark into a down quark and a lepton-lepton pair. The prediction of the branching fraction is less theoretically clean compared to $K \to \pi\nu\bar{\nu}$ with contributions through three processes: direct CP violating, indirect CP violating and CP conserving components. The SM branching fraction for the $K_L^0 \to \pi^0 l^+ l^-$ decay can be described as [33, 34]

$$\mathcal{B}(K_L^0 \to \pi^0 l^+ l^-) = \left(C_{mix}^l \pm C_{int}^l \left(\frac{\mathfrak{Im}(\lambda_t)}{10^{-4}} \right) + C_{dir}^l \left(\frac{\mathfrak{Im}(\lambda_t)}{10^{-4}} \right) + C_{CPC}^l \right) \times 10^{-12}, \tag{1.27}$$

where C_{mix}^l represents the contributions due to $K_S - K_L$ mixing, C_{int}^l the interference of the indirect and direct CP violating decays. The $\pm$ represents the constructive and destructive interference. The C_{dir}^l is the contribution of direct CP violating and C_{CPC}^l is the long distance CP conserving contribution. This results in the branching

fractions for the $K_L^0 \to \pi^0 e^+ e^-$ and $K_L^0 \to \pi^0 \mu^+ \mu^-$ decays,

$$\mathcal{B}(K_L^0 \to \pi^0 e^+ e^-) = \left(15.7|a_S|^2 \pm 6.2|a_S| \left(\frac{\mathfrak{Im}(\lambda_t)}{10^{-4}}\right) + 2.4 \left(\frac{\mathfrak{Im}(\lambda_t)}{10^{-4}}\right)\right) \times 10^{-12} \tag{1.28}$$

and

$$\mathcal{B}(K_L^0 \to \pi^0 \mu^+ \mu^-) = \left(3.7|a_S|^2 \pm 1.6|a_S| \left(\frac{\mathfrak{Im}(\lambda_t)}{10^{-4}}\right) + 1.0 \left(\frac{\mathfrak{Im}(\lambda_t)}{10^{-4}}\right) + 5.2\right) \times 10^{-12}. \tag{1.29}$$

The $|a_S|$ term depicts the decay form factor calculated from the measurement of the branching fraction of $K_S \to \pi^0 l^+ l^-$ at NA48/1 experiment as $|a_S| = 1.2 \pm 0.2$ [35, 36]. Equations 1.28 and 1.29 show the main difference between the two decay modes. The CP conserving contribution due to the two-photon intermediate state only occurs in the muon decay as it is negligible in the helicity-suppressed electron mode.

Utilising the above equations, the expected SM branching fractions can be described as [37],

$$\mathcal{B}(K_L^0 \to \pi^0 e^+ e^-) = 3.54^{+0.98}_{-0.85}(1.56^{+0.62}_{-0.49}) \times 10^{-11} \tag{1.30}$$

and

$$\mathcal{B}(K_L^0 \to \pi^0 \mu^+ \mu^-) = 1.41^{+0.28}_{-0.26}(0.95^{+0.22}_{-0.21}) \times 10^{-11}. \tag{1.31}$$

The separate values for the branching ratios represent the constructive vs destructive interference introduced in Equations 1.28 and 1.29. The state-of-the-art experimental constraints on the branching fraction of $K_L^0 \to \pi^0 l^+ l^-$ decays at a 90 % CL are the upper limits obtained by the KTeV experiment [38, 39]

$$\mathcal{B}(K_L^0 \to \pi^0 e^+ e^-) < 28 \times 10^{-11} \tag{1.32}$$

and

$$\mathcal{B}(K_L^0 \to \pi^0 \mu^+ \mu^-) < 38 \times 10^{-11}. \tag{1.33}$$

1.4 Dark Photon

As mentioned above, the SM is not a complete theory. A significant component of the universe remains unexplained. For instance, the observed rise in the cosmic-ray positron fraction with energy, along with the anomaly in the muon's magnetic

moment $(g-2)$ [40], suggest the possible existence of hidden sectors. The hidden sectors is a collection of theories that propose the existence of new particles and forces that are not part of the SM. A possible extension of the SM foresees a new $U(1)$ gauge symmetry with an associated boson, the Dark Photon (DP), which kinematically mixes with the SM hypercharge $U(1)_Y$ [41]. There are two separate benchmark cases of the DP specified by the Physics Beyond Colliders group for future study [42]:

- BC1 - The massive DP decays into only SM particles.
- BC2 - The DP is massive and decays mostly into dark-sector particles.

For the BC1 case, the hypothetical DP (denoted A') with a GeV scale mass could resolve some of the discrepancies arising from the observations of the $(g-2)$ muon gyromagnetic ratio measurement and the rise of cosmic-ray positron fraction with energy. The addition of the DP introduces two unknown parameters: the mass $M_{A'}$ and a kinetic mixing parameter ϵ denoting the strength of the DP interaction with SM particles. A DP with a mass that is less than a neutral pion can be produced in the $\pi^0 \to \gamma A'$ decay. The branching fraction for the π^0 decay is [43]

$$\mathcal{B}(\pi^0 \to \gamma A') = 2\epsilon^2 \left(1 - \frac{M_{A'}^2}{M_{\pi^0}^2}\right)^3 \mathcal{B}(\pi^0 \to \gamma\gamma). \tag{1.34}$$

Within the mass range considered for the DP, the only decay into SM particles that is both kinematically allowed and occurs at leading order in the coupling constant is $A' \to e^+e^-$. The A' would decay via $A' \to \gamma\gamma\gamma$ and $A' \to \nu\bar{\nu}$ proceeding through higher-order processes, which are highly suppressed for low ϵ values. Hence, it is safe to assume that $\mathcal{B}(A' \to e^+e^- = 1)$. This assumption allows the expected decay width to be described as [43]

$$\Gamma_{A'} \approx \Gamma(A' \to e^+e^-) = \frac{1}{3}\alpha\epsilon^2 M_{A'} \sqrt{1 - \frac{4M_e^2}{M_{A'}^2}} \left(1 + \frac{4M_e^2}{M_{A'}^2}\right), \tag{1.35}$$

where α is the fine structure constant. For the DP mass range $2M_e < M_{A'} < M_{\pi^0}$, the life time of the DP is calculated,

$$c\tau_{A'} = \frac{\hbar c}{\Gamma_{A'}} \approx 0.8\,\mu\text{m} \times \left(\frac{10^{-6}}{\epsilon^2}\right)\left(\frac{100\,\text{MeV}/c}{M_{A'}}\right) \tag{1.36}$$

Through experiment it is possible to set limits on the branching ratio of the DP production, with the final goal of setting limits on the mixing parameter. Within

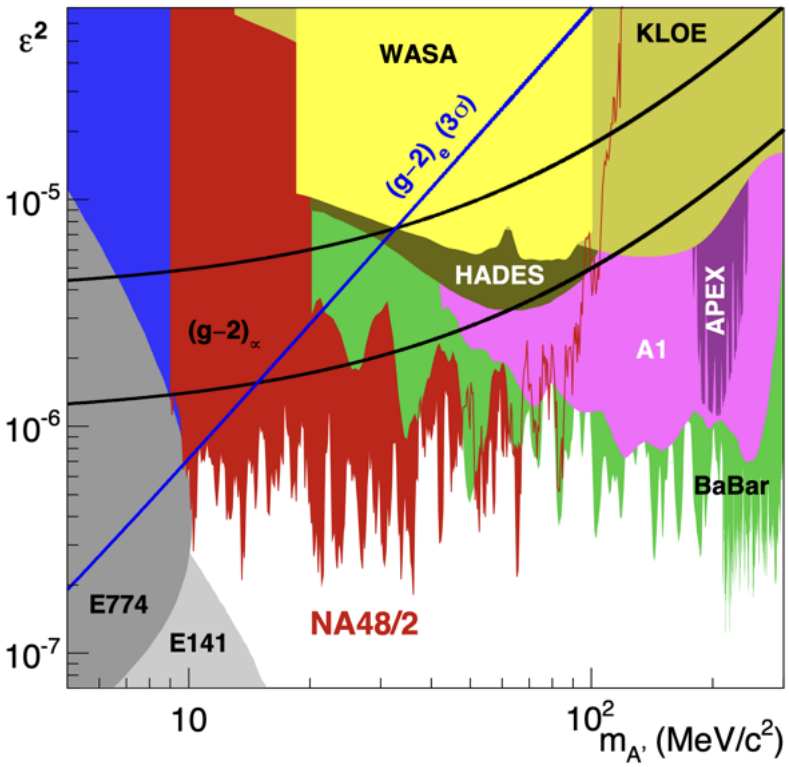

Figure 1.7: Experimental constraints on the BC1 dark photon in the ϵ (mixing parameter) and $M_{A'}$ (dark photon mass) phase-space [44].

the DP mass range $2M_e < M_{A'} < M_{\pi^0}$, the leading result for the upper limit of ϵ^2 is from the NA48/2 experiment [44], shown in Figure 1.7. The study described in Section 4 sets out to improve the limits on the DP mixing parameter set by NA48/2 with data collected from the NA62 experiment.

Chapter 2

The NA62 Experiment

2.1 Overview

The NA62 experiment is a fixed target experiment located in the ECN3 experimental hall in the North Area of CERN where a 400 GeV/c particle beam is provided by the Super Proton Synchrotron (SPS). The main goal of the experiment is to measure the branching fraction of the ultra-rare charged kaon decay $K^+ \to \pi^+\nu\bar{\nu}$. Alongside, there is an extensive physics program of precision and rare decay measurements, as well as searches for forbidden processes and exotic particles.

The experiment employs a decay-in-flight technique to obtain a large number of charged kaon decays, in the order of 10^{13} within the time frame of a few years. The experimental setup was designed to fulfil the requirements for the challenging measurement of $K^+ \to \pi^+\nu\bar{\nu}$, which involves the detection of the K^+ upstream and the detection of the product π^+, with a missing energy-momentum carried away by the undetected neutrino-antineutrino pair. The reconstructed 4-momenta of the kaon P_{K^+} and the pion P_{π^+} are used to calculate the squared missing mass:

$$m^2_{miss} = (P_{K^+} - P_{\pi^+})^2. \tag{2.1}$$

This requires precise spacial measurement of the K^+ and π^+ candidates, provided by the beam (section 2.3.2) and secondary (section 2.3.4) particle spectrometers. The measurement of the missing mass is used for kinematic rejection of the main background K^+ decays; $K^+ \to \pi^+\pi^0$, $K^+ \to \pi^+\pi^+\pi^-$ and $K^+ \to \mu^+\nu_\mu$ by selecting two regions shown in Figure 2.1.

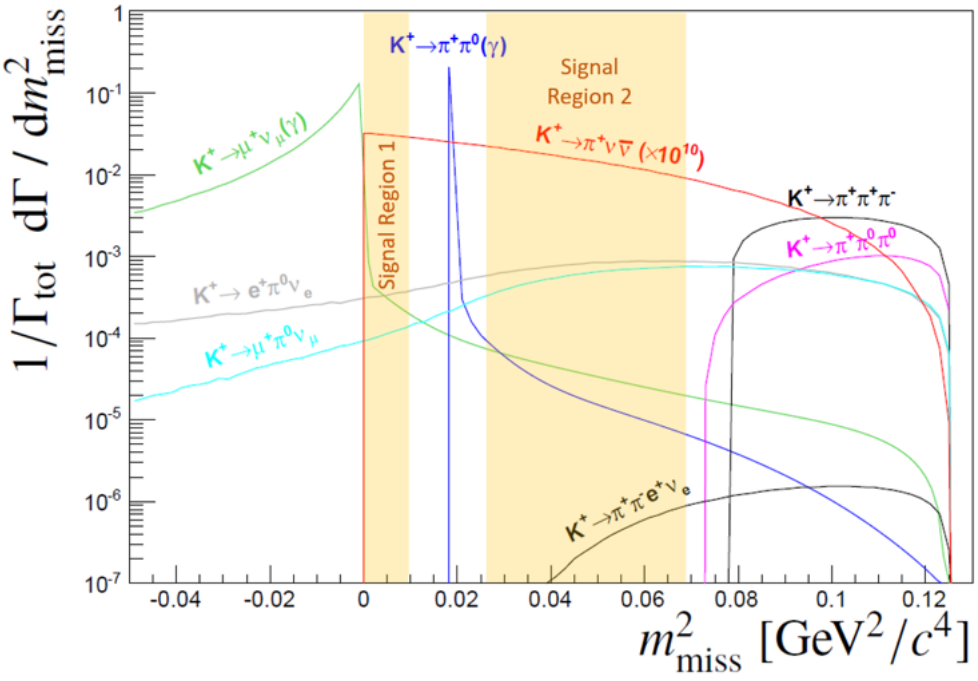

Figure 2.1: Expected squared missing mass distributions of main kaon decays and $K^+ \to \pi^+\nu\bar{\nu}$ (scaled by 10^{10} for for visibility). The solid coloured areas show the signal regions used to reject the dominant kaon decays kinematically [46].

The NA62 collaboration has observed the $K^+ \to \pi^+\nu\bar{\nu}$ [45], measuring the branching ratio,

$$\mathcal{B}(K^+ \to \pi^+\nu\bar{\nu}) = (13^{+3.3}_{-3.0}) \times 10^{-11}. \tag{2.2}$$

This represents the rarest particle decay measured to date, agreeing with the Standard Model (SM) predictions (Equation 1.24) within $1.7\,\sigma$. With more data to be analysed NA62 plans to obtain a precision of better than 20 %.

The rest of this chapter covers how NA62 fulfils the requirements to collect kaon decays within the Fiducial Volume (FV). Section 2.2 describes the NA62 beam-line from the target through the detector. The detector comprises a number of sub-detectors, described in Section 2.3, with the Trigger and Data Acquisition system (TDAQ) following in Section 2.4. A description of the offline software can be found in Section 2.5.

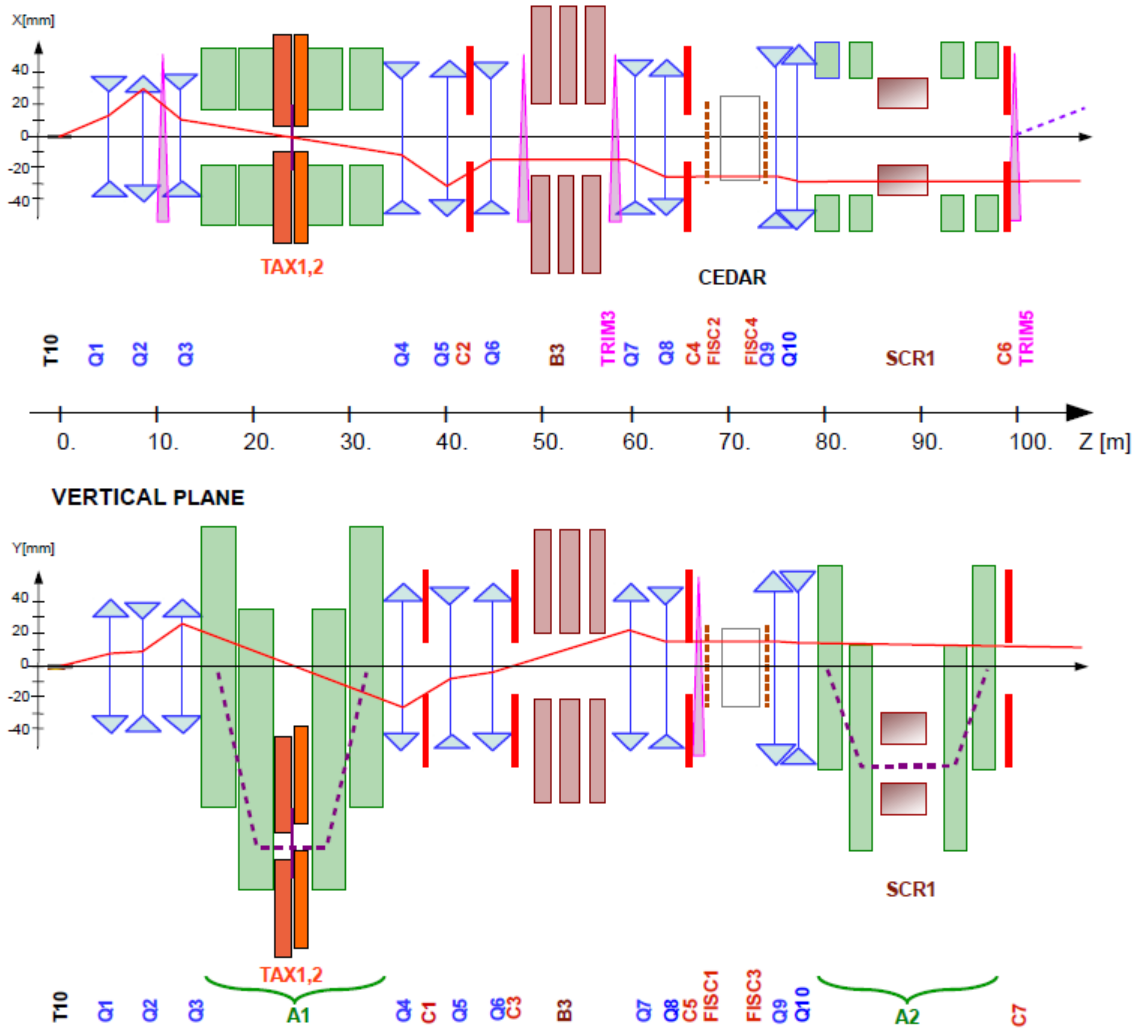

Figure 2.2: Schematic of K12 beamline from T10 target at 0 m to the entrance of the NA62 decay region at 102.4m [46].

2.2 The NA62 Beam-Line

The NA62 experiment at CERN uses a hadron beam extracted from the SPS with a nominal momentum of 400 GeV/c, directed onto a 400 mm long, 2 mm diameter beryllium rod that forms the fixed target (T10) located at 0 m in Figure 2.2. The beam derived from the T10 target, referred to as K12, is a high-intensity unseparated hadron beam with a nominal momentum of 75 GeV/c. The beam momentum was chosen to maximise the fraction of kaons decaying within the FV with respect to the other beam components.

The elements of the K12 beam-line are shown in Figure 2.2 and comprise a number of components. First are three quadrupole magnets (Q1, Q2 and Q3), used to

focus the beam with a large solid angle acceptance of ±2.7 mrad horizontally and ±1.5 mrad vertically at a 75 GeV/c central momentum. Next follows an achromat (A1), which selects a beam of a 75 GeV/c momentum with a 1 % rms momentum. The A1 achromat comprises four dipole magnets that vertically deflect the beam, the first two deflect the beam 110 mm downwards, while the final two deflect the beam upwards towards the original axis. Between these pairs of magnets, there are a pair of water-cooled beam-dump units (TAX1 and TAX2) with a set of holes to select the required 75 GeV/c momentum beam while absorbing unwanted secondary beam particles and any remaining primary protons. TAX1&2 can be closed to act as a secondary target for use in dump mode or for safety when access is required downstream. Between the TAX1&2, a radiator consisting of tungsten plates with a thickness of up to 5 mm is introduced into the path of the beam. The radiator is optimised to reduce positron energy while minimising the loss of energy to hadrons. A triplet of quadrupoles (Q4, Q5, Q6) follows, which refocuses the beam in the vertical direction and produces a parallel beam in the horizontal direction. The space between the quadrupoles is occupied by a pair of collimators (C1, C2), which redefines the horizontal and vertical acceptance of the beam. The collimator after the Q6 quadrupole (C3) is employed to absorb positrons that have their momenta degraded by the radiator and again redefines the acceptance in the vertical direction.

The beam next passes through a 40 mm field-free hole in a set of iron plates, placed between three 2 m dipole magnets (B3). The vertical magnetic field in the iron plates is used to deflect muons. Any deviation in the beam due to stray fields in the beam hole is cancelled out by a pair of steering dipoles (TRIM2 and TRIM3). Two quadrupoles (Q7, Q8) follow and ensure that the beam is parallel before the KTAG, which comprises of a differential Cherenkov counter with achromatic ring focus (CEDAR) and a purpose-built photon detection system, described in Section 2.3.1. Before the KTAG, a pair of collimators (C4 and C5) are used to absorb particles in the tails of the spacial distribution of the beam.

For beam monitoring, two pairs of filament scintillator counters (FISC 1, 3 and FISC 2, 4) are installed at either end of the KTAG. Used in coincidence the FISCs can measure the beam divergence which is tuned to ensure the condition of paral-

lelism is satisfied through the CEDAR vessel.

Following the KTAG are two quadrupoles (Q9 and Q10), used to focus the beam before the beam tracking system, the GigaTracker (GTK). The GTK comprises four stations made up of silicon pixel detectors described in Section 2.3.2 and are installed in the beam vacuum. The GTK stations are installed so that the space between GTK1 and GTK3 is occupied by a second achromat (A2), which comprises four dipole magnets that deflect the beam 60 mm vertically, allowing for the beam particle momenta to be measured. The return yokes of the third and fourth magnets and a magnetised iron collimator (SCR1) defocus beam muons, which are ejected from the beam between the second and third magnets. A pair of cleaning collimators (C6 and C7) used to absorb beam particles outside of the acceptance are located before the final GTK station (GTK3), which is at the entrance to the decay region ($Z = 102.4\,\mathrm{m}$). A steering magnet (TRIM5) is then used to deflect the beam in the horizontal direction by an angle of $+1.2\,\mathrm{mrad}$.

At $Z = 102.4\,\mathrm{m}$ a large 117 m vacuum pipe (Bluetube) begins, evacuated to a pressure of $10^{-6}\,\mathrm{mbar}$ by several cryo-pumps along its length. The Bluetube, shown in Figure 2.3, is made up of 19 cylindrical sections ranging in diameter, from 1.92 m in the first section after GTK3 to 2.4 m in the middle section and then 2.8 m in the region containing the STRAW spectrometer. The first section is defined as the decay region or FV between $Z = 105\,\mathrm{m}$ and $Z = 180\,\mathrm{m}$. Further downstream, the Bluetube hosts a number of detectors: eleven Large Angle Veto (LAV) stations and four STRAW spectrometer chambers. The LAV stations are used in the photon detection system described in Section 2.3.6. The STRAW spectrometer chambers along with a large aperture dipole magnet (MNP33) provide kinematic measurements of the charged products of kaons decaying within the decay region, described in Section 2.3.4. The MNP33 magnet provides a $270\,\mathrm{MeV}/c$ momentum kick in the horizontal direction, deflecting the $75\,\mathrm{GeV}/c$ beam by $-3.6\,\mathrm{mrad}$, so that combined with the TRIM5 deflection, the beam passes through the central aperture of the Liquid Krypton Calorimeter (LKr). The path of the beam is shown in Figure 2.4, showing the deflection in the horizontal direction. After the final STRAW spectrometer chamber (STRAW4), the Bluetube is closed off with a thin aluminium window (except for the beam hole), separating the vacuum from the 17 m long, neon-filled Ring Imaging

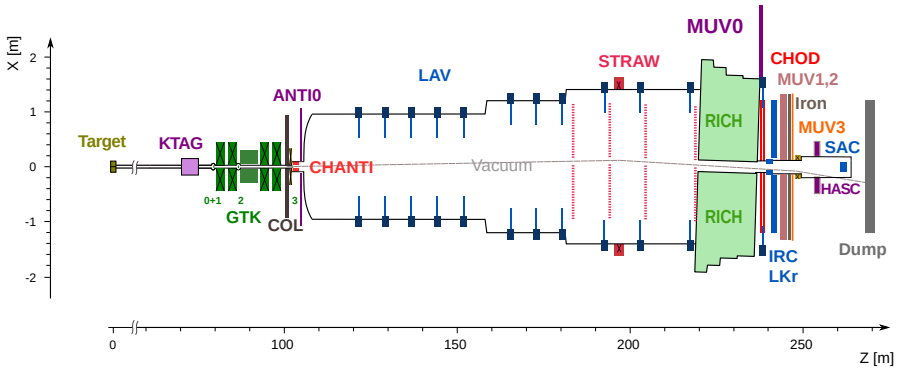

Figure 2.3: X-Z diagram of NA62 detector setup.

Cherenkov counter (RICH). The RICH is designed to distinguish between secondary pions and muons produced in kaon decays and is part of the Particle Identification (PID) system as described in Section 2.3.5. The beam is transported through the remaining downstream detectors in a vacuum and is deflected $-13.2\,\text{mrad}$ in the negative direction by a dipole magnet (BEND) to sweep the beam away from the Small Angle Calorimeter (SAC) acceptance, located within the vacuum beam pipe. Finally, the beam is absorbed in a beam dump.

2.3 NA62 Detectors

The setup of the sub-detectors are shown in Figure 2.3 and are described below.

2.3.1 KTAG

As the NA62 beam is unseparated and kaons only account for 6 % of the beam composition, the kaons must be identified. Kaon identification is provided by the KTAG located at $Z = 69.4\,\text{m}$. It comprises a CEDAR vessel and a purpose-built photon detection system. CEDARs were developed at CERN in the 1970s [47] for secondary beam particle detection at the SPS and come in two types: CEDAR-West (CEDAR-W) and CEDAR-North (CEDAR-N). Until the NA62 2023 run, the CEDAR vessel was a CEDAR-W filled with a nitrogen radiator. The CEDAR exploits the properties of the produced Cherenkov light which is dependent on the

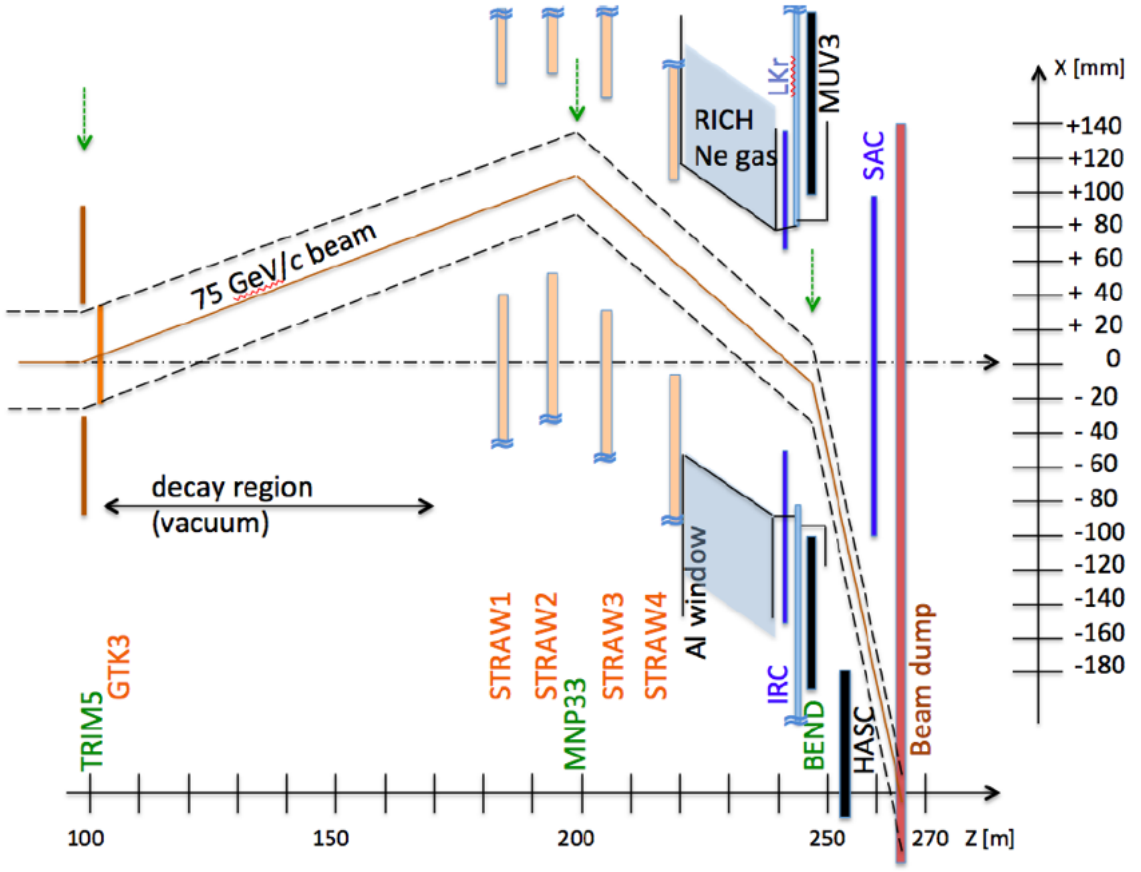

Figure 2.4: Schematic of K12 beamline after GTK3 [46].

beam particle speed β,

$$cos(\theta) = \frac{1}{\beta n}, \tag{2.3}$$

where θ is the angle of the Cherenkov light produced, $\beta = \frac{p}{\gamma m}$ where p is the particle momentum, γ is the Lorentz factor and m is the mass of the particle. The CEDAR is designed so that when a beam of charged particles with fixed momenta enters the radiator gas with a constant refractive index, the angle of Cherenkov light is only affected by the mass of the beam particles. The pressure is set at 1.7 bar of nitrogen in the CEDAR-W so that the light from the kaon is focused by a set of lenses through exit windows which are then detected by photo detectors. The light from the other beam components does not reach the PMT arrays but other particles can be selected by altering the pressure within the vessel.

In the original CERN design, the Cherenkov light exiting each CEDAR exit window was detected by a single ET-9820QB Photomultiplier Tube (PMT) placed directly on the exit window. A particle was identified if there was a coincidence of

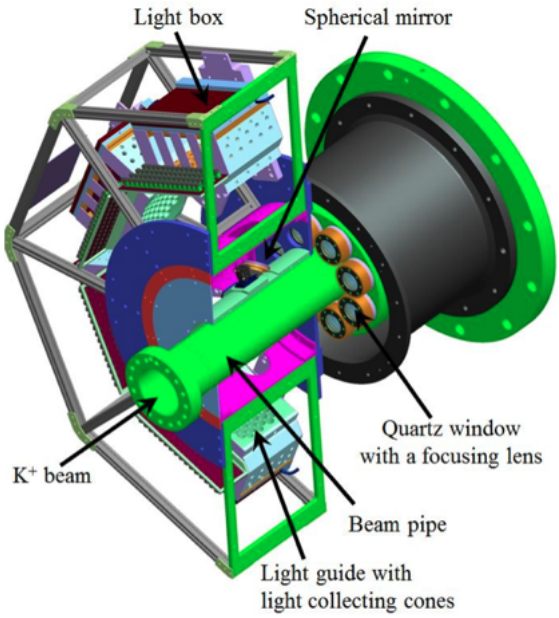

Figure 2.5: Model of the upstream part of the CEDAR and the KTAG photon-detection system [46].

at least six PMTs out of eight. However, these PMTs would not fulfil the timing (≤ 100 ps) and rate requirements (45 MHz of kaons) at NA62.

For NA62, a photon-detection system shown in Figure 2.5 was designed, constructed and mounted to the upstream end of the CEDAR vessel. The photon light from the CEDAR exit windows is reflected radially 90 degrees by eight spherical mirrors onto eight PMT matrices, referred to as sectors. Each PMT matrix is equipped with an array of 48 single-anode Hamamatsu PMTs of two types: 32 of type R9880-110 and 16 of type R7400. The Quantum Efficiency (QE) is the probability of a PMTs photocathode to convert a photon of a specific wavelength and emit a photo-electron into the vacuum of the PMT. The QE for both Hamamatsu PMTs are shown in Figure 2.6. The signals from the PMT arrays are clustered by the reconstruction algorithm into kaon candidates within a nominal 2 ns time window. A kaon is identified when there are at least five sectors in coincidence (5-fold coincidence). The clustering provides, on average, 18 photo-electrons per kaon candidate. The PMTs can achieve a single hit time resolution of 300 ps, resulting in a reconstructed kaon time resolution of 70 ps. A kaon identification efficiency above 99 % is achieved with the KTAG and CEDAR-W [48].

In 2023, a new CEDAR with a hydrogen radiator CEDAR-Hydrogen (CEDAR-H) was installed in the NA62 beam-line after design at the University of Birmingham

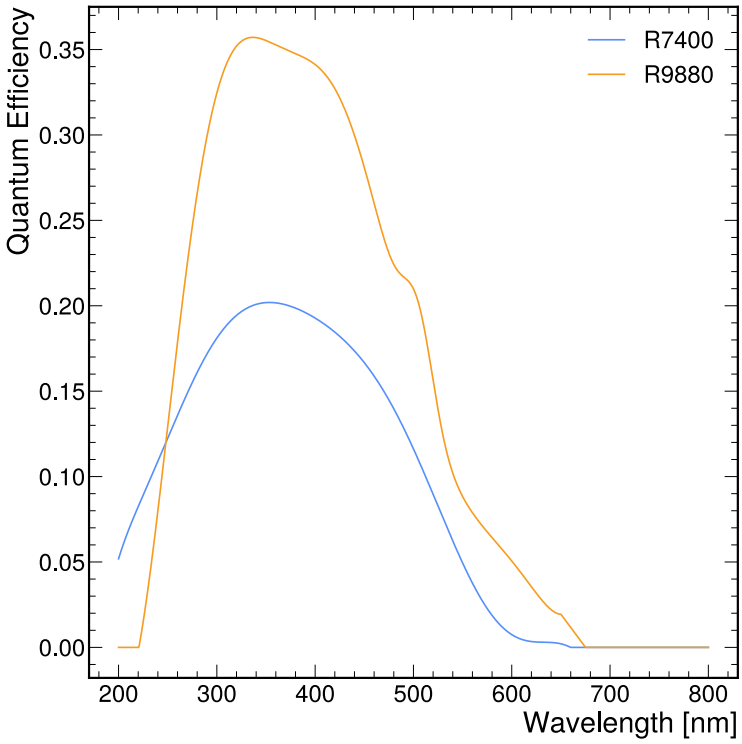

Figure 2.6: Quantum Efficiency of both types of PMT used in the KTAG photon-detection system (Hamamatsu R9880-110 and R7400).

and construction and testing at CERN. The new CEDAR uses the basic principles as previous CEDARs but uses hydrogen as a radiator gas to reduce the material within the path of the beam. This required the design of new optical elements in the CEDAR and the photon detection system. A detailed description of the CEDAR and its optical elements, along with the design, testing and installation of the new CEDAR-H, can be found in Section 3.

2.3.2 GigaTracker (GTK)

The precise measurement of each beam particle's momentum, time, and position is provided by the four GTK stations. The GTK is a beam spectrometer comprising hybrid silicon trackers placed within the vacuum pipe and an achromat upstream of the decay volume. As particles of differing momenta are deflected by different amounts in a magnetic field, the momentum of a particle can be measured by comparing the positions of the particles in each station. The detector was designed to measure a particle momentum at a resolution of 0.2 % and its direction at the exit of

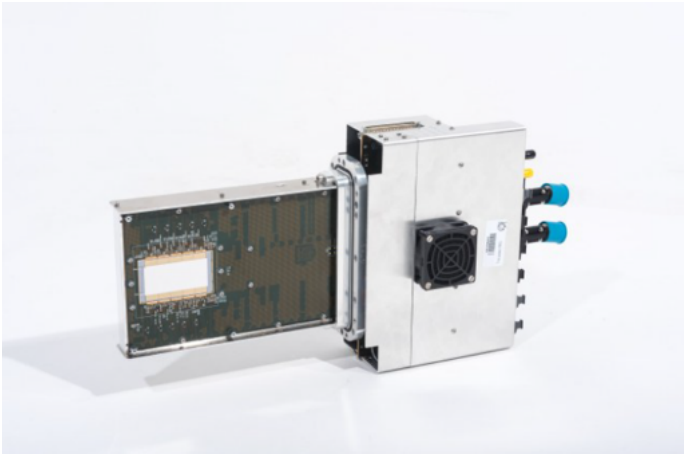

Figure 2.7: Image of GTK station [46].

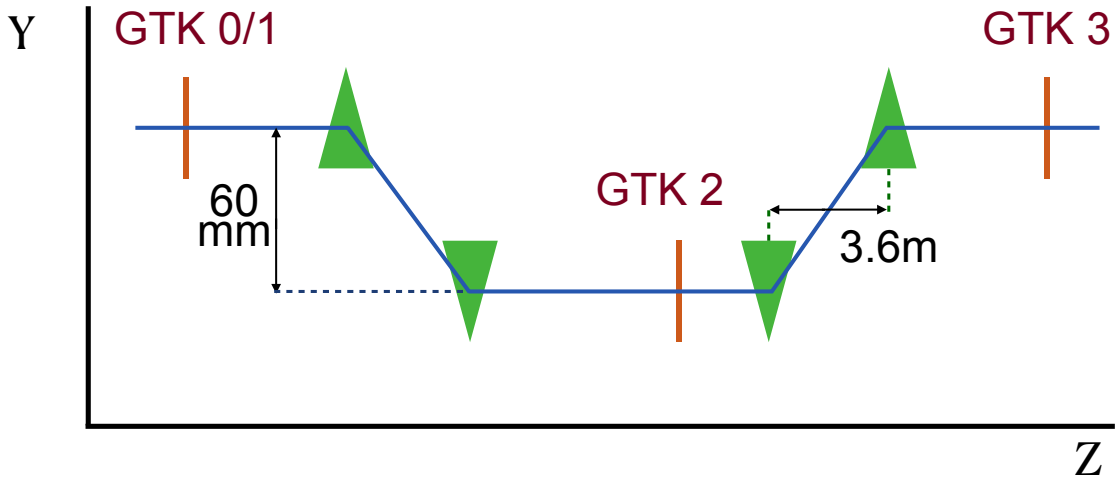

Figure 2.8: Schematic of GTK stations within the achromat, edited from [46] (not to scale).

the achromat to 16 µrad. Each GTK station has a time resolution of 200 ps, which results in an overall track time resolution of 100 ps [49]. The layout of the GTK is shown in Figure 2.8.

Each station consists of 18,000 pixels of size $300 \times 300\,\mu m^2$ in a matrix of 200×90, covering a total area of $62.8 \times 27\,mm^2$ and is read out by Application-Specific Integrated Circuits (ASIC). As the tracker is placed directly within the beam, the number of interactions with the beam must be minimised by utilising the smallest material possible. The material budget for each station was set at $0.5\,\%X_0$, corresponding to 500 µm of Silicon.

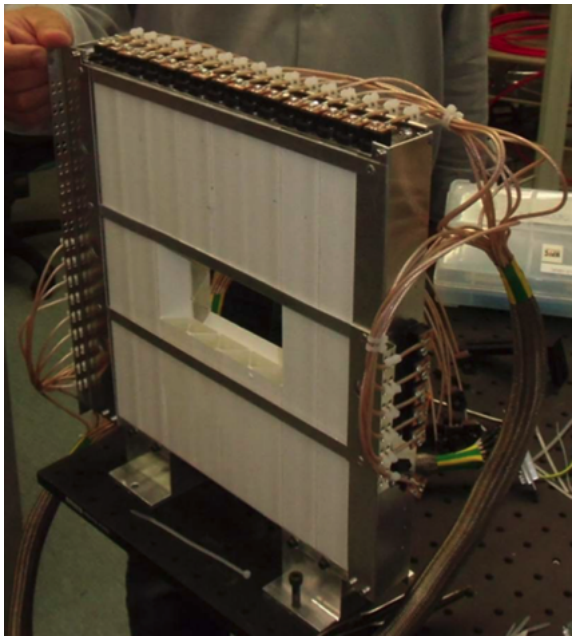

Figure 2.9: Image of a single CHANTI station [46].

2.3.3 Charged Particle Anti-coincidence detector (CHANTI)

The Charged particle Anti-coincidence detector (CHANTI) is located downstream of the GTK, and its primary goal is to provide the rejection of charged particles produced from inelastic collisions of beam particles with the final GTK station. Vetoing these particles is imperative as they enter the decay volume and result in background for $K^+ \to \pi^+\nu\bar{\nu}$. The detector is also used to identify the muon halo close to the beam. The CHANTI detector is a set of six square hodoscope stations comprising two planes, one placed vertically and the other horizontally, with a fully constructed station shown in Figure 2.9. The planes are comprised of polystyrene-based scintillator bars equipped with fast wavelength-shifting (WLS) fibres. The fibres are then readout by Silicon Photomultipliers (SiPMs).

2.3.4 Straw Spectrometer (STRAW)

The STRAW spectrometer provides measurements of the momenta of charged particles produced in K^+ decays within the FV. It comprises four chambers and a large aperture dipole magnet (MNP33), providing measurement of secondary particle momentum with a resolution of

$$\frac{\sigma(p)}{p} = 0.30\,\% \oplus 0.005\,\% \cdot p, \tag{2.4}$$

Chamber	Beam Hole Size (cm)	Beam Hole Offset (X, Y, Z)
1	6	101.2 mm, 0 mm, 183 m
2	6	114.4 mm, 0 mm, 193 m
3	6	92.4 mm, 0 mm, 204 m
4	6	52.8 mm, 0 mm, 218 m

Table 2.1: Straw spectrometer chamber beam-hole positions.

where p is the track momentum in GeV/c. The first term represents the contribution due to multiple scattering, while the second is from the intrinsic detector resolution. The chambers are downstream from the decay region, with the first chamber located at $Z = 183\,\text{m}$ and the second 10 m further downstream. The MNP33 magnet is situated downstream of chamber two at $Z = 197.6\,\text{m}$ and provides an integrated field of 0.9 Tm. Chambers 3 and 4 are located downstream of the MNP33, $Z = 204\,\text{m}$ and 219 m respectively.

Each chamber comprises four views (X, Y, V, and U) rotated at 0°, 90°, +45°, and −45°, each with four layers of straws as shown in Figures 2.10 and 2.11. The views have a gap near the centre of around 12 cm with no straws, such that when they are combined to form a chamber, an octagonal hole with an apothem of 6 cm is produced for the beam to pass through. As shown in Figure 2.4, the beam hole for each chamber is not centred and instead follows the deflection of the beam before and after the MNP33 magnet, with the beam hole parameters defined in Table 2.1.

The straws are 2.1 m long drift tubes that are 9.82 mm in diameter, made from 36 µm thick Polyethylene Terephthalate (PET), coated on the inside with 50 nm of copper and 20 nm of gold. The straws are filled with a mixture of 70 % argon and 30 % CO_2 at atmospheric pressure and have a central gold-plated tungsten anode wire. The straws act like proportional counters: when a charged particle passes through the gas, it is ionised, creating electron-ion pairs that drift to the opposite electrodes, inducing a charge on the anode wire. When the electron approaches the anode wire, the electric field strength increases dramatically, producing Townsend avalanches. This provides a large multiplication of the signal, producing a charge pulse, which is read out by the detector electronics.

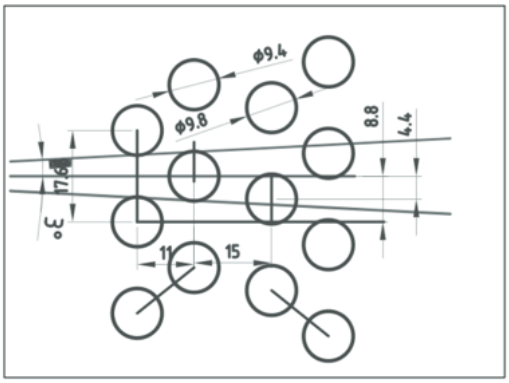

Figure 2.10: Top down diagram of the straw placement in each view [50].

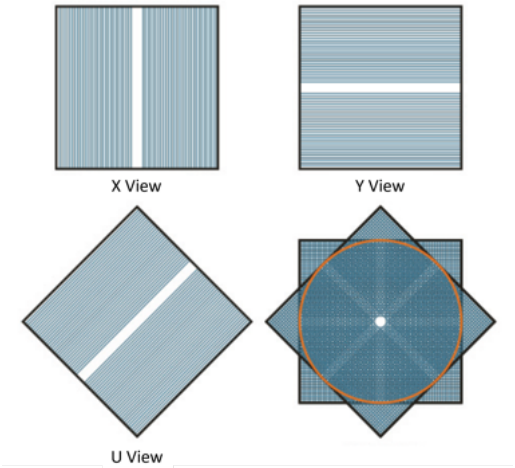

Figure 2.11: Diagram showing placement of views in a straw chamber. Edited from [50].

2.3.5 Ring Imaging Cherenkov counter (RICH)

The RICH is designed to separate secondary pion and muons within a momentum range of 15–35 GeV/c as required by the necessity to suppress the $K^+ \to \mu^+\nu_\mu$ background in the $K^+ \to \pi\nu\bar{\nu}$ ($K_{\pi\nu\bar{\nu}}$) analysis. The majority of the muon suppression comes from kinematic selections and the response difference between pions and muons in the calorimeters. However, another factor of 100 is required in the momentum range 15-35 GeV/c which is provide by the RICH.

The RICH is a 17.5 m long cylindrical vessel comprising four steel sections with diameters decreasing from 4.2 m at the upstream section to accommodate the PMT flanges to 3.2 m in the downstream end. The radiator vessel is separated from the vacuum decay tube by an aluminium window of 2 mm thickness and radius of 1.1 m at the upstream end, allowing minimal material in the path of particles entering the detector. A lightweight aluminium beam pipe connected to the vacuum tube passes through the vessel, ending with a 4 mm thick, 1.4 m radius aluminum exit window. The vessel contains neon gas at atmospheric pressure with a refractive index of $n = 1 + 62.8 \times 10^{-6}$ at a wavelength of 300 nm, corresponding to a Cherenkov threshold for charged pion of 12.5 GeV/c.

A mosaic of 20 spherical mirrors (18 hexagonal and two semi-hexagonal) with a focal length of 17 m is located at the downstream end of the vessel as shown in

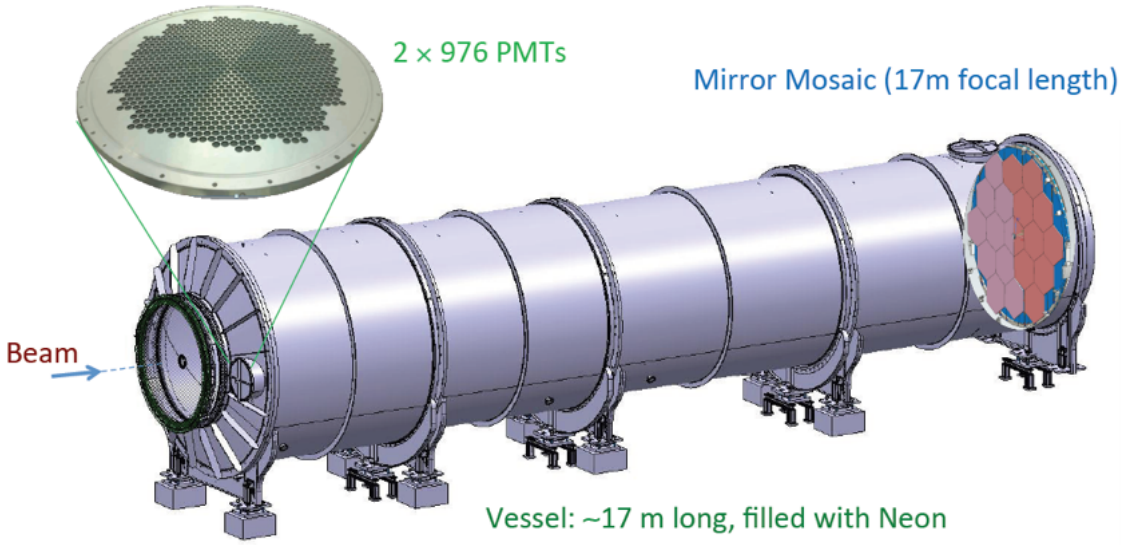

Figure 2.12: Schematic of RICH detector, showing the beam entering the upstream end on the left. A zoomed-in image of one of the two PMT flanges shows the layout of the PMT arrays. The mirrors are also shown at the downstream end of the vessel [51].

Figure 2.12. This mirror system reflects and focuses the Cherenkov light toward two PMT arrays located at the upstream end of the vessel. The two PMT arrays are located on either side of the entrance window (see Figure 2.12), each consisting of 976 Hamamatsu R7400-U03 PMTs. The PMTs have an 8 mm^2 active area and are packed into a hexagonal lattice, with individual Winston cones directing light onto the active areas.

The particles are identified using a cut on the particle mass, calculated from the particle velocity using the reconstructed Cherenkov ring radius shown in Figure 2.13 and momentum measured by the spectrometer. It is clear that separating pions and muons within the desired momentum range is possible.

2.3.6 Photon Detection System

The photon detection system provides a rejection power of 10^8 for the main decay background $K_{2\pi}$ for $K_{\pi\nu\bar{\nu}}$. It is made up of four calorimeters used to detect and reject kaon decays with photons in the final state, with coverage from 0 to 50 mrad.

Photons with production angles between 1 and 8.5 mrad are covered by the NA48 LKr. The LKr is a quasi-homogeneous calorimeter consisting of a large cryostat

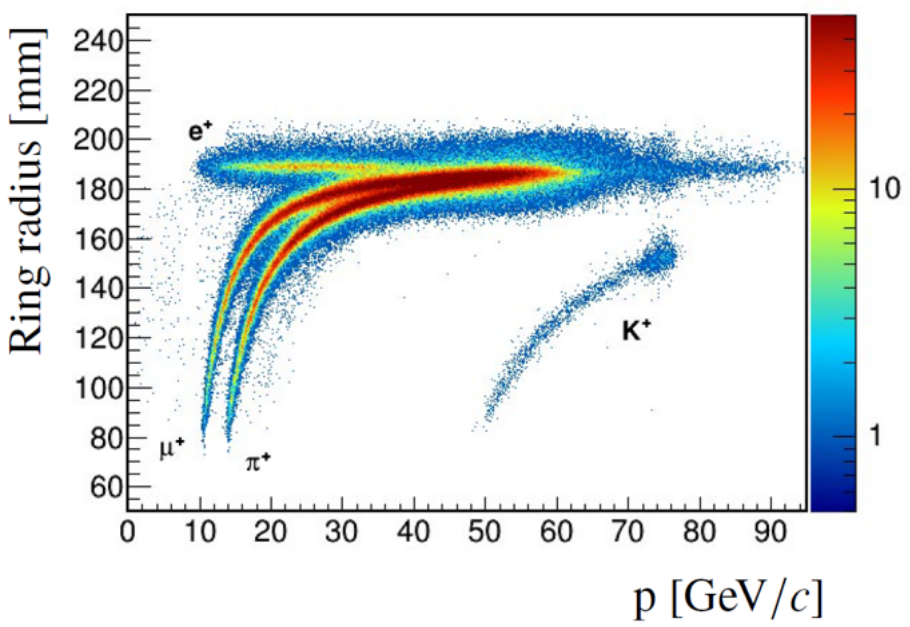

Figure 2.13: RICH Cherenkov ring radius as a function of the particle momentum [51].

containing 9000 litres of liquid krypton, which extends from the beam-pipe to a radius of 128 cm and has a depth of 127 cm. This corresponds to 27 radiation lengths, allowing for the full capture of electromagnetic showers produced. Thin beryllium-copper ribbons make up the 13,248 longitudinal cells, depicted in Figure 2.14, each consisting of a central anode and cathodes on either side. Each anode ribbon is connected at the downstream end to preamplifiers and to a high voltage of 3 kV to provide the drift field required for the ionisation. The LKr energy resolution can be parametrised as,

$$\frac{\sigma_E}{E} = \frac{4.8\,\%}{\sqrt{E}} \oplus \frac{11\,\%}{E} \oplus 0.9\,\% \tag{2.5}$$

where E is the energy in GeV.

Photons with small production angles between 0 and 1 mrad are detected by the Intermediate-Ring Calorimeter (IRC) and SAC. The IRC wraps around the beam pipe and consists of layers of lead and scintillating material. The light is collected by WLS fibres bundled into four groups which is readout by a Hamamatsu PM. The SAC, which is located just upstream of the beam dump within the beam vacuum, comprises of 70 lead plates with 70 plastic scintillators in between readout by WLS fibres resulting in a total material of 19 X_0. The fibres are bundled into four groups which are then read out by Hamamatsu PMs, resulting in four channels.

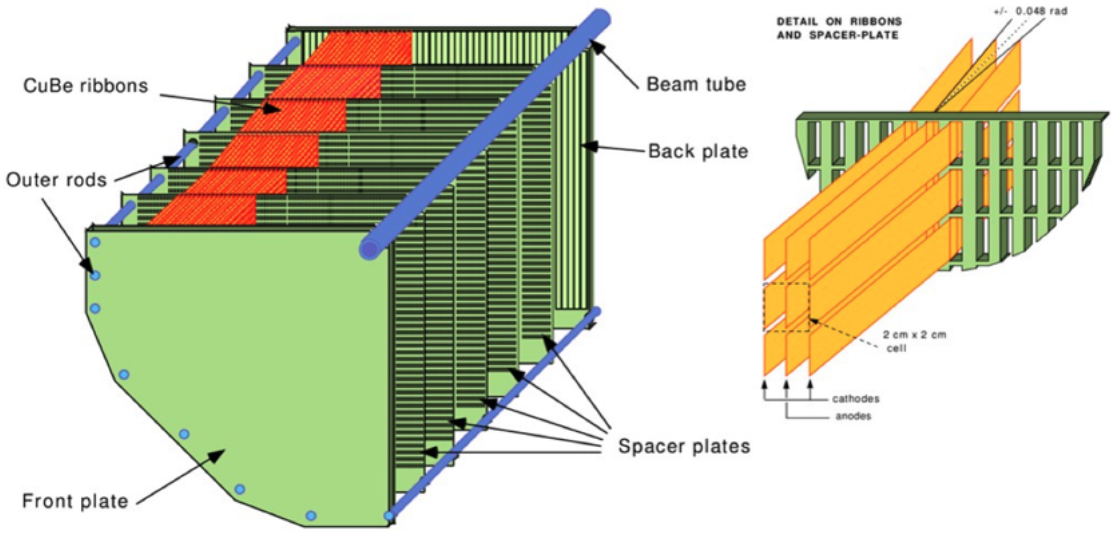

Figure 2.14: Left, a schematic of the structure of a single quadrant of the LKr. Right, the layout of cells within the quadrant [51].

Figure 2.15: Photo of the installation of LAV1 at NA62 in 2008.

The LAV provides coverage from 8.5 to 50 mrad, with 12 stations positioned along and beyond the decay volume. Eleven of the LAV stations are along the vacuum volume with the final station placed upstream of the LKr. A LAV station consists of a barrel of lead glass blocks surrounding the boundary of the vacuum volume [52], see LAV1 picture in Figure 2.15. The electromagnetic showers produced in each of the glass blocks result in the emission of Cherenkov light, which is then detected by a Hamamatsu R2238 76 mm diameter photomultiplier attached to the back side. The single photon detection efficiencies for the photon veto detectors at NA62 are shown in Figure 2.16. The efficiencies are calculated using a tag-and-probe method. In this approach $K^+ \to \pi^+\pi^0$ decays are collected where $\pi^0 \to \gamma\gamma$ follows. One

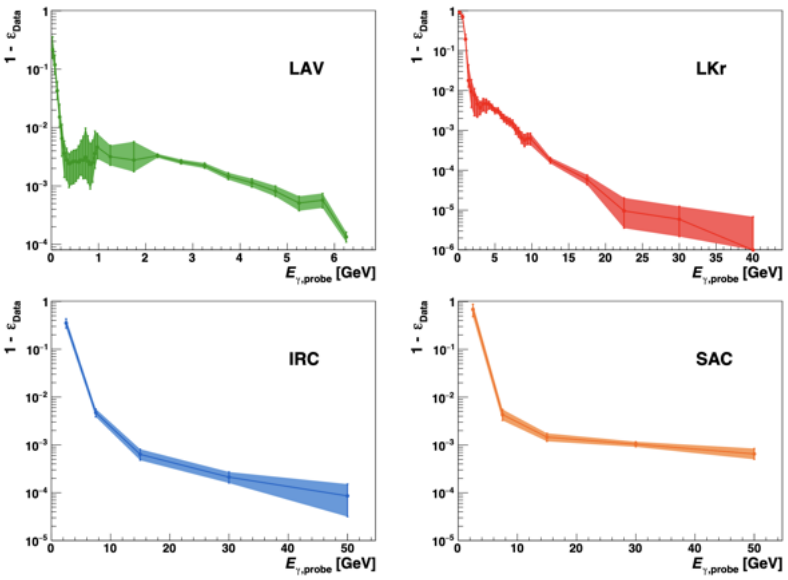

Figure 2.16: Detection efficiency of a photon as a function of the photon energy for the photon veto detectors: LAV (top left), LKr (top right), IRC (bottom left) and SAC (bottom right) [53].

or two photons are then reconstructed by the LKr which are used to measure the efficiency of the photon detectors. One photon is designated as a tagged photon where its energy, position and other kinematic information from the decay is used to determine which photon detector should detect the other photon (probed).

2.3.7 Charged Particle Hodoscopes

The charged particle hodoscopes comprise a pair of scintillator detectors which cover the acceptance downstream of the RICH and upstream of the LKr. The main function of the charged particle hodoscopes is to provide input to the first level of the NA62 trigger system.

The NA48-CHOD, used in NA62's predecessor experiment NA48 [54], is located upstream of LAV12, just after the RICH. The NA48-CHOD consists of two planes of 20 mm thick plastic scintillator slabs, 64 vertical and 64 horizontal as shown in Figure 2.17. Each scintillator slab is individually connected to photomultipliers via a light guide. A signal in both planes is required to produce a track time with a resolution of 200 ps. The charged particle rate at the NA48-CHOD is 13 MHz, with the overall rate at 35 MHz mainly resulting from particles produced from interactions with upstream detectors. The CHOD is located after the twelfth LAV station, before

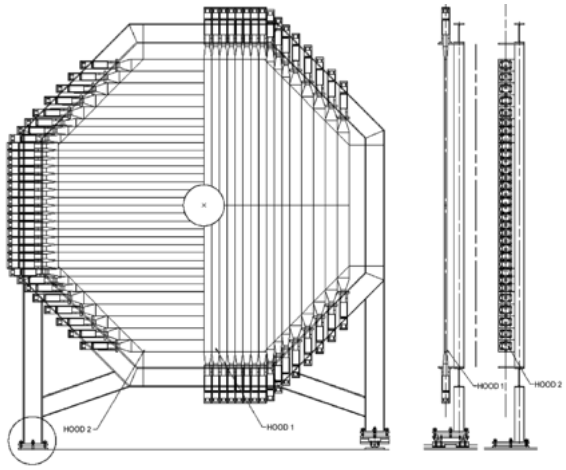

Figure 2.17: Schematic of the NA48-CHOD [54].

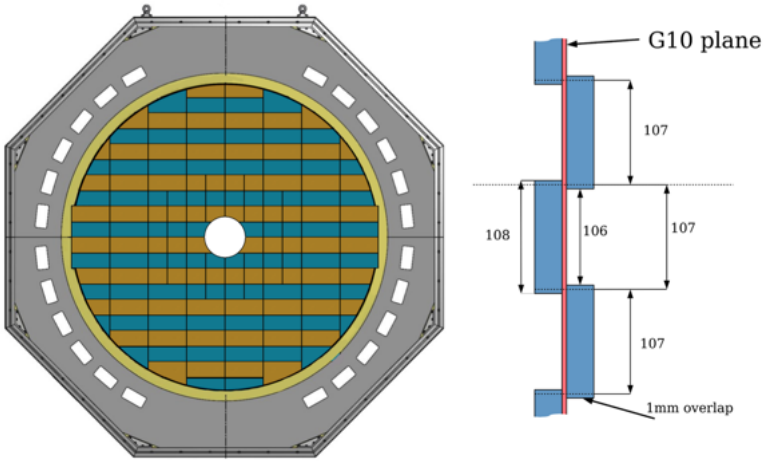

Figure 2.18: Layout of the NA62 CHOD. Left, the front cross-section of scintillating tiles with the support structure. Right, side cross-section of the scintillating tiles [55].

the LKr and consists of an array of 152 plastic scintillator tiles of 30 mm thickness that cover an acceptance radius of between 140 and 1070 mm, and is shown in Figure 2.18. The rows of tiles overlap by 1 mm and are supported by a glass fibre foil (G10). The light produced from each tile is collected with a WLS fibre and is bundled into groups of four, read out by SiPMs. The overall time resolution of the detector is 1.1 ns. The CHOD sustains a particle rate of 13 MHz at a nominal beam intensity with the individual channel rates shown in Figure 2.19.

2.3.8 Muon Veto System

The Muon Veto System (MUV) is used to discriminate between pions and muons in conjunction with the RICH and LKr. The system comprises a hadronic sam-

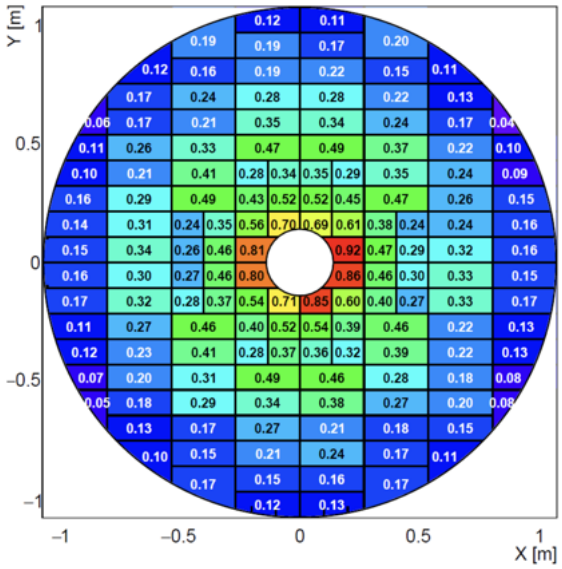

Figure 2.19: Channel rates of the CHOD in MHz at a nominal beam intensity of 750 MHz [46].

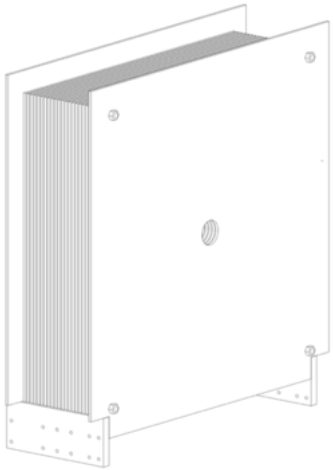

Figure 2.20: Schematic of the MUV1 module used in the Muon Veto System at NA62.

pling calorimeter made from two modules, MUV1 and MUV2, utilising steel as an absorber material. MUV1 is a newly designed module for NA62, and MUV2 was repurposed from the front of the NA48 hadronic calorimeter [54]. MUV1 consists of 24 iron plates with a thickness of 26.8 mm and 23 layers of scintillator strips placed in between that are 9 mm thick with a width of 60 mm, as shown in Figure 2.20. The scintillator strips alternate between horizontal and vertical, resulting with 12 horizontal and 13 vertical. The material of MUV1 produces a total material of 4.1 X_0. The light produced within the strips is collected by WLS fibres and read out by PMTs. MUV2 is similar in construction with 2×22 strips per plane versus

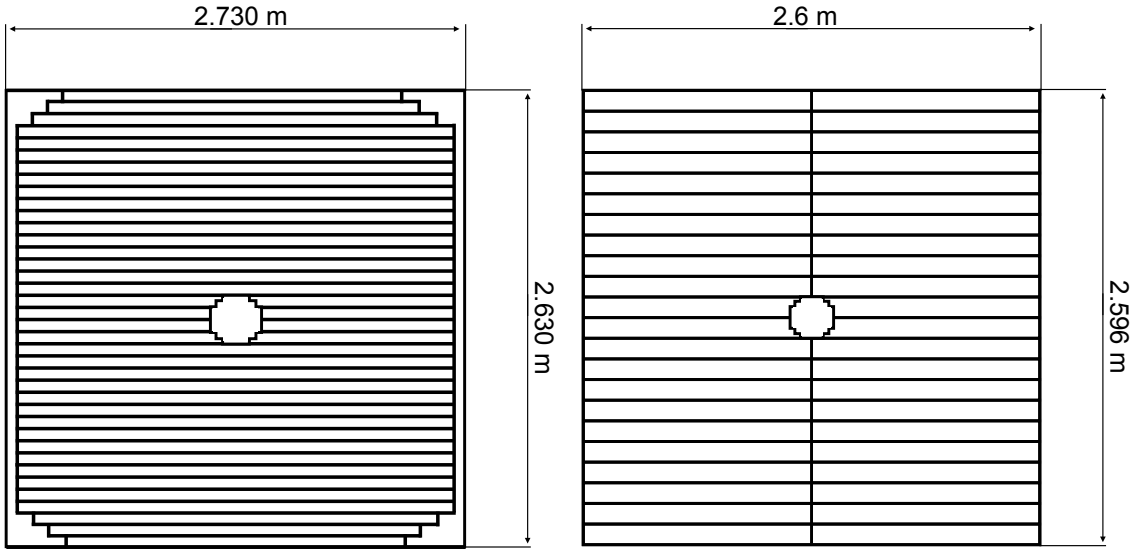

Figure 2.21: Layout of scintillating tiles for a horizontal layer for: Left, MUV1 and Right, MUV2.

48 for MUV1, as shown in Figure 2.21. MUV2 has thinner steel plates, at 25 mm thick, resulting in a reduced total thickness of 3.7 X_0. Downstream of the hadronic calorimeter, the MUV3 detector located behind an 80 cm thick iron wall is used for muon identification. The MUV3 comprises of 148 scintillator tiles with a thickness of 59 mm. Eight of the tiles around the beam pipe are smaller to account for the high particle rate. Each tile is read out directly by two PMTs, with a time resolution of 0.6 ns. The overall muon rate within the detector is 13 MHz for a nominal beam intensity, with the individual channel rates shown in Figure 2.22. The MUV3 is primarily used within the L0 trigger as a muon veto. Additionally, there is a peripheral muon veto detector (MUV0), which is a scintillator hodoscope designed to detect low momentum π^- from the kaon decay $K^+ \to \pi^+\pi^+\pi^-$, which are deflected into the positive X direction and miss the acceptance of the RICH.

2.3.9 Other detectors

The Hadronic Sampling Calorimeter (HASC) is located downstream of the MUV3 and BEND magnet which deflects positively charged particles in the negative X direction. The HASC is designed to detect π^+ from the kaon decay $K^+ \to \pi^+\pi^+\pi^-$ and comprises of nine modules of 60 lead plates and 60 scintillator layers covering an acceptance of -0.48 m to -0.18 m in X and -0.15 m to 0.15 m in Y from the beam

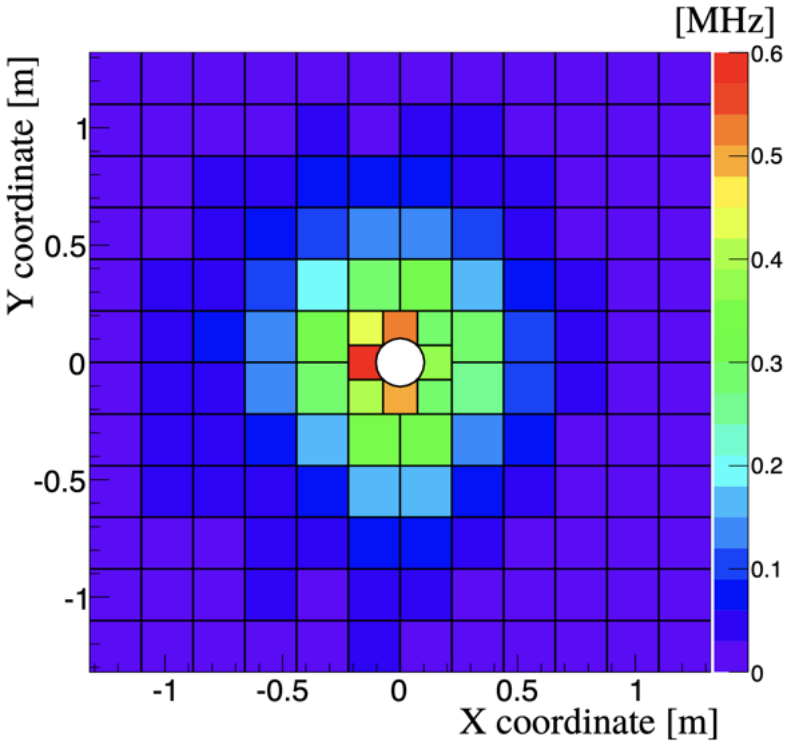

Figure 2.22: MUV3 geometry and channel rates for nominal beam intensity [46].

axis. Each layer has 10 longitudinal sections which are optically coupled to WLS fibres and read out by SiPMs. A second HASC station was added to the opposite side of the beam to cover the positive X direction and to make the overall station symmetric.

The Veto-Counter (VC) was designed and built to suppress the backgrounds produced by decays of kaons upstream of the FV. The VC comprises three scintillator stations, with two placed before the final collimator, separated by a lead plate and one after the final collimator. Each station comprises nine tiles of size 40 mm × 120 mm and two 20 mm × 120 mm , with the smaller tiles located on either side of the beam pipe. The tiles are read out by PMTs.

A veto hodoscope (ANTI-0) was placed just before the entrance to the FV. The ANTI-0 is designed to veto the beam halo particles when they enter the FV. This is to reject halo particles from being identified as secondary decay products. The detector comprises 280 scintillator tiles, read out by four SiPM [56]. The expected channel rate for the ANTI-0 is shown in Figure 2.23.

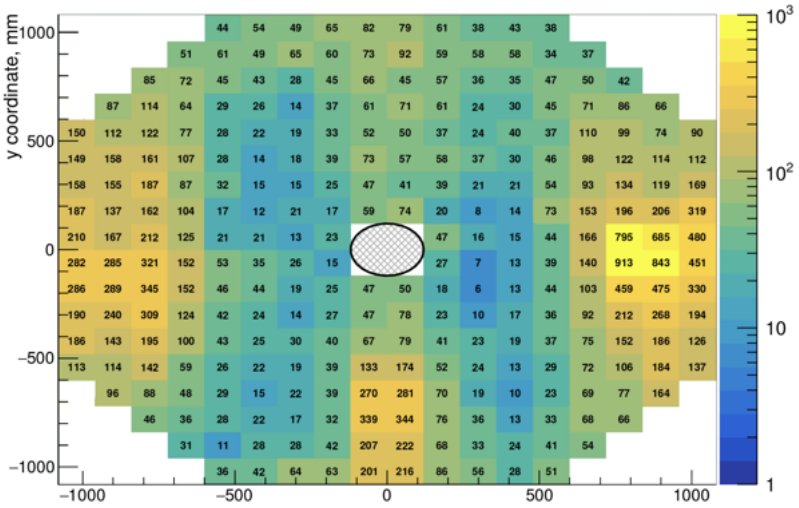

Figure 2.23: Channel rate in kHz for the ANTI-0 for a nominal beam intensity [56].

2.4 Trigger and Data Acquisition System (TDAQ)

The high intensity of the beam necessitates a triggering system capable of reducing the stored data while retaining essential information to meet the experiment's physics objectives. The NA62 trigger system is comprised of two stages: a hardware trigger (L0) and a software trigger (L1), known as the High-Level Trigger (HLT). Each stage of the trigger system is designed to reduce the incoming rate by a factor of 10. With a rate of $\mathcal{O}(10\,\text{MHz})$ kaon decays within the FV, the L0 was designed to reduce this to $\mathcal{O}(1\,\text{MHz})$ and the L1 to reduce the rate written to storage to $\mathcal{O}(100\,\text{kHz})$.

To fit with NA62 broad physics goals, the trigger system is designed to be flexible. At the L0 trigger, packets of data are sent from fast sub-detectors, containing the results of the conditions found in Table 2.2 and is processed by the L0 Trigger Processor (L0TP). These L0 trigger conditions can be combined, producing a trigger line, such as those used in the 2024 run shown in Table 2.3. The coincidence of the L0 conditions from Table 2.2 have to be within 6.25 ns of the trigger reference time which is provided by the RICH detector. Once an event passes the L0 trigger other detectors then send information packets to the NA62 PC farm for use in the L1 trigger.

The L1 trigger then uses a number of algorithms for three more detectors, which are described in Table 2.4. The L1 trigger conditions can be combined to produce a L1 trigger stream shown in Table 2.3. L0 and L1 trigger streams are combined to

Detector	Condition	Description
RICH	RICH	At least two signals in the detector
	RICH3	At least three signals in the detector
	RICH8	At least eight signals in the detector
CHOD	Q1	At least one signal in the detector
	H3	At least three signals in the detector
	Q2	At least one signal in each of two different quadrants
	QX	At least one signal in each of two diagonally-opposite quadrants
	UTMC	Fewer than five signals in the detector
NA48-CHOD	NA48-CHOD	At least one signal in the detector
MUV3	M1	At least one signal in the detector
	MO1	At least one signal in the outer tiles
	MO2	At least two signals in the outer tiles
	MOQX	At least one signal in each of two diagonally-opposite quadrants
LKr	E5	At least 5 GeV deposited in the LKr
	E10	At least 10 GeV deposited in the LKr
	E20	At least 20 GeV deposited in the LKr
	E30	At least 40 GeV deposited in the LKr
	E40	At least 40 GeV deposited in the LKr
	C2E5	At least 5 GeV deposited in the LKr by at least two clusters
	LKr40	Logical OR between E40 and C2E5

Table 2.2: List of L0 trigger conditions for each detector at NA62.

form a trigger mask defined in Table 2.3 to fulfil the experiments numerous physics goals. For an event to be saved to permanent storage, the event has to satisfy at least one mask. Each mask can have a corresponding downscaling, which reduces the rate of events passing that trigger to minimise the amount saved to permanent storage. However, this results in the loss of interesting physics data so the downscaling is minimised as much as possible.

A more detailed explanation of the full NA62 trigger system and the resultant performance can be found here [57].

Trigger	L0 Conditions	L1 Conditions	Downscaling
Normalisation	RICH×RICH3×!M1×Q1	KTAG×STRAW-1TRK	400
$K_{\pi\nu\bar{\nu}}$	RICH×RICH3×!M1×!QX×UTMC×!E40	KTAG×!LAV2-11×STRAW-MUV3	1
Min-Bias	RICH×Q1		400
RK_{norm}	RICH×RICH3×!QX×UTMC×!E40	KTAG×!LAV2-11×STRAW	500
Electron Multi-Track	RICH×RICH8×QX×H3×E20×C2E5	STRAW-MM	1
Multi-Track	RICH×RICH8×QX×H3	KTAG×STRAW-ExoTight	100
Muon Multi-Track	RICH×RICH8×MO2×QX×H3	KTAG×STRAW-ExoTight	1
Multi Cluster	RICH×Q1×E30	KTAG×STRAW	10
Pion Charge Exchange	RICH×RICH8×Q2×E30×C2D5	STRAW-ExoTight	4
Neutrino	!RICH16×MOQX×!Q2×UTMC×E5	KTAG×STRAW-1TRK	1

Table 2.3: List of triggers used for the NA62 2024 run, along with the L0 and L1 conditions and the relevant downscaling factors.

2.5 NA62 Software

The NA62 collaboration maintains an offline software framework (na62fw) which is used for the physics analysis of data collected from the experiment. The software framework comprises of three packages:

- NA62MC: A GEANT4 [58] based Monte Carlo simulation of the experiment, used to compare against the data collected.
- NA62Reconstruction: Reconstruction software used to create hits and candidates for all sub-detectors from data collected by the experiment and data from Monte Carlo (MC) simulations.
- NA62Analysis: A software toolkit to conduct physics analysis on the reconstructed data.

Each module of na62fw utilises the tools found within the ROOT analysis framework [59]. A description of the software framework can be found in Section 5.2.

Detector	**Condition**	**Description**
KTAG	KTAG5	Signals in at least five sectors within a 5 ns time window
LAV	LAV2-11	At least three signals in LAV stations 2-11 within a 4 ns time window
STRAW	STRAW	Designed for collection of $K_{\pi\nu\bar{\nu}}$ decays, requiring a single positive track originating from the Fiducial Volume, momentum below 50 GeV/c, closest distance of approach (CDA) to the nominal beam axis below 200 mm with a Z position upstream of the first STRAW station
	STRAW-Exo	At least one negatively charged track
	STRAW-ExoTight	Extension of STRAW-Exo requiring the negative track to have momentum below 65 GeV/c, a CDA below 500 mm from the nominal beam axis and a Z position of the CDA of at least 80 m
	STRAW-MMiss	Extension of STRAW-ExoTight, which includes a requirement on the missing mass squared from the track and the nominal beam four-momenta to suppress $K^+ \to \pi^+\pi^+\pi^-$ decays
	STRAW-MT	At least three tracks originating from the FV
	STRAW-DV5	Pairs of tracks originating from a displaced vertex with a CDA at least 50 mm from the nominal beam axis
	STRAW-1TRK	One positively charged track originating in the FV with a momentum less than 65 GeV/c
	STRAW-MUV3	Extension of STRAW to include extrapolation of the track to the acceptance of MUV3 and requiring it to be within $\|x\|\&\|y\| < 1320$ and a radius of 103 mm

Table 2.4: List of L1 trigger conditions used at NA62.

Chapter 3

The CEDAR-H Detector

As described in Section 2, until 2022 NA62, has utilised a CEDAR-West (CEDAR-W) filled with nitrogen gas (N_2) at a nominal gas pressure of 1.71 bar (absolute pressure) to identify kaons from the unseparated hadron beam. For the searches for ultra-rare decays it is essential to reduce backgrounds from dominant kaon decays and from upstream sources produced by scattered beam particles. Minimising the amount of material in the path of the beam is required to reduce the upstream backgrounds. It is possible to design a new differential Cherenkov counter with achromatic ring focus (CEDAR) with hydrogen as the radiator gas to reduce the amount of multiple scattering of beam particles within the vessel. The design, testing and commissioning of this new detector is detailed in this chapter.

CEDARs were designed and built at CERN to identify secondary beam particles at the Super Proton Synchrotron (SPS) [47]. Two types of CEDAR were developed at CERN: CEDAR-W and CEDAR-North (CEDAR-N), corresponding to the areas of use. The two designs differ in terms of the momentum range in which they can identify beam particles, CEDAR-N are able to separate kaons and pions up to 300 GeV/c and detect protons down to 60 GeV/c. CEDAR-W can detect protons down to 12 GeV/c and separate kaons and pions up to 150 GeV/c.

The CEDAR-W with N_2, contributes the most significant amount of material in the path of the beam, corresponding to $39 \times 10^{-3}\,X_0$, where X_0 is one radiation length. The CEDAR vessel contributes $3.9 \times 10^{-3}\,X_0$ and the N_2 gas $35 \times 10^{-3}\,X_0$. The material from the CEDAR-W with N_2 results in the multiple scattering of beam particles, introducing an angular divergence in the beam of 32 µrad. It is

Parameter	**N_2**	**H_2**
Gas pressure (absolute)	1.71 bar	3.8 bar
Total material (X_0)	39×10^{-3}	7.3×10^{-3}
– Vessel contribution (X_0)	3.9×10^{-3}	3.9×10^{-3}
– Gas contribution (X_0)	35×10^{-3}	3.4×10^{-3}
Beam angular divergence	32 µrad	13 µrad

Table 3.1: Comparison of material budget and beam divergence for CEDAR filled with N_2 and hydrogen gas (H_2).

proposed that a CEDAR filled with H_2 would reduce the material due to the radiator gas's lower density. Using H_2 as a radiator gas would require a pressure of 3.8 bar to produce a similar Cherenkov angle as N_2 gas at 1.71 bar. H_2 at this pressure introduces $3.4 \times 10^{-3}\, X_0$ of material, which would result in a factor of five reduction in material compared to N_2, resulting in a total material of $7.3 \times 10^{-3}\, X_0$. The expected angular beam divergence is 13 µrad in both the horizontal and vertical dimensions. A summary of the material budget of each detector is shown in Table 3.1.

Taking into account that the four GTK stations contribute $20 \times 10^{-3}\, X_0$, the total beam material along the beamline reduces from $59 \times 10^{-3}\, X_0$ to $27 \times 10^{-3}\, X_0$. Using the full NA62 simulation based on GEANT4 [58], the fraction of particles interacting inelastically upstream of the decay volume would reduce from 2.1 % to 0.9 %. The reduction in interactions would result in higher kaon transmission (number of kaons reaching the decay volume) and reduced signal rates in the downstream detectors. This results in improved performance of the hardware trigger designed to collect $K^+ \to \pi^+ \nu\bar{\nu}$. Simulations show that the introduction of H_2 instead of N_2 as a radiator gas in the CEDAR reduces the number of elastically scattered particles originating upstream of GTK3 which interact with detectors downstream of the Fiducial Volume (FV) by 40 %. The reduction in particle flux reduces the trigger rate by 15 %, which will improve the stability of data acquisition [60].

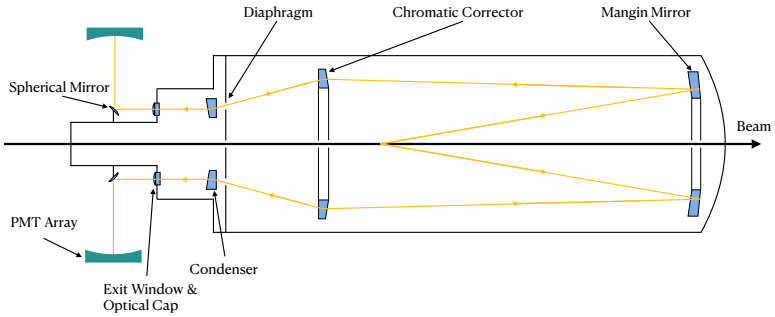

Figure 3.1: Diagram describing the optics of the CEDAR+KTAG photon-detection system and the expected Cherenkov light ring path in orange.

3.1 CEDAR Design

A CEDAR comprises a thermally insulated gas vessel separated into two sections: a 4.3 m long cylinder with an inner diameter of 53 cm and a vessel cap which differs in length, depending on the CEDAR variant. The CEDAR-W has a vessel cap length of 34 cm compared to 28 cm for the CEDAR-N variant. The vessel cap is attached to the main cylinder at the upstream end. The gas vessel is separated from the vacuum of the beam pipe by two aluminium windows at the upstream and downstream ends. A description of the CEDAR vessel, along with the optics enclosed, is shown in Figure 3.1.

The beam is designed to pass through the CEDAR vessel along the longitudinal axis through the radiator gas and aluminium windows. When the beam particles pass through the vessel at a velocity v between

$$\frac{c}{n} < v < c \tag{3.1}$$

where c is the speed of light in a vacuum, and n is the refractive index of the radiator gas, Cherenkov light is produced. The Cherenkov light from the beam particles is emitted as cones with a semi-aperture angle dependent on the speed of the beam particle,

$$\cos\theta_c = \frac{1}{\beta n} \tag{3.2}$$

with n being the refractive index of the radiator gas, θ_c is the semi-aperture angle and β the beam particle velocity defined as $\beta = \frac{p}{\sqrt{p^2+M^2}}$ where M is the particles mass and p is the momentum. A differential counter is designed to focus the Cherenkov light to a ring image in order to distinguish particles of different masses. Particles of different masses produce ring images of different radii.

The number of photons produced by a particle (N) per unit distance traversed within the radiator (x), per unit wavelength (λ) is defined by the Frank-Tamm formula [61]

$$\frac{d^2N}{dxd\lambda} = \frac{2\pi\alpha}{\lambda^2}\sin^2\theta_c = \frac{2\pi\alpha}{\lambda^2}\left(1 - \frac{1}{\beta^2 n^2(\lambda)}\right), \tag{3.3}$$

where $n(\lambda)$ is the wavelength dependent refractive index and α is the fine structure constant.

The CEDAR contains optical elements inside the vessel to allow the reflection and focusing of the produced Cherenkov light to reach the diaphragm at a radius of 100 mm, as displayed in Figure 3.1 as the orange lines. Photons are produced throughout the length of the vessel towards the downstream end and the light is reflected back upstream by a Mangin mirror [62]. The Mangin mirror comprises two spherical surfaces, with the downstream surface cemented onto a concave mirror having an identical radius of curvature. The radius at which the light is focused at the focal point is defined as,

$$R_{focal} = f\theta_c \tag{3.4}$$

where f_m is the focal length for the entire system. The focal length of a Mangin mirror with two spherical surfaces is defined as,

$$\frac{1}{f_m} = \frac{2n_m}{r_2} - \frac{2(n_m - 1)}{r_1} \tag{3.5}$$

where n_m is the refractive index of the Mangin mirror, r_1 and r_2 are the radii of curvature of the refracting and reflecting surfaces. The mirror is designed to reduce spherical aberrations, an effect intrinsic to lenses and curved mirrors. This is where light that strikes the spherical surface off-centre is refracted/reflected to different points compared to the light that would strike the centre of the mirror. After the mirror, the light goes through a plano-convex lens named the Chromatic Corrector, which is designed in such a way that it corrects for the chromatic dispersion of the radiator gas and directs the light towards the diaphragm. Chromatic dispersion occurs due to different wavelengths of light refracting differently in a medium, causing the Cherenkov ring to disperse, which would result in some of the light being lost when it reaches the small diaphragm opening. For a plano-convex lens the focal distance is defined as

$$\frac{1}{f_{cc}} = \frac{(n_{cc} - 1)}{r_{cc}} \tag{3.6}$$

where n_{cc} is the refractive index of the Chromatic Corrector and r_{cc} is the radius of curvature of the convex side. Combined with the Mangin mirror the final focal distance for the system is calculated as

$$\frac{1}{f} = \frac{1}{f_m} + \frac{1}{f_{cc}} - \frac{d}{f_m f_{cc}} \tag{3.7}$$

where d is the distance between the Mangin mirror and the corrector lens. Both the Mangin mirror and the Chromatic corrector have a hole in the centre to allow for the beam to pass through without impacting the optics. The optical parameters for the CEDAR-W are found in Table 3.2.

The diaphragm is shown in Figure 3.2, as a disk with eight separate apertures and is located at the focal distance of the Mangin mirror. Each aperture has an inner and outer element which allows the aperture to open to 20 mm and close to 0 mm symmetrically about a radius of 100 mm. These elements can be seen in Figure 3.2 (right), where the aperture is set at a small value, used only to select a single Cherenkov ring of radius 100 mm. The mechanism is operated by a stepper motor connected to the shaft shown in Figure 3.2 (left). Turning the shaft clockwise opens the diaphragm, and counter-clockwise closes it. The shaft is connected to a potentiometer that measures the rotation, which is used to convert to an aperture in millimetres after calibration. A pair of end switches are in place at the extreme ends of the rotation to alert the user if the aperture is fully open or fully closed, which is essential to avoid any damage to the mechanical system.

The light that passes through the aperture of the diaphragm then traverses a condenser lens (one element for each of the 8 apertures), designed to direct the light out of the exit windows parallel to the longitudinal axis. The design of the condenser lenses is shown in Figure 3.3 and is shown after the diaphragm in Figure 3.2 (right). The light exits the CEDAR through eight quartz exit windows placed around the beam pipe at the upstream end of the CEDAR, shown in Figure 3.4. Attached to the exit windows are quartz filters designed to attenuate light below 240 nm. In the original CEDAR design [47], light exiting the CEDAR through the exit windows is detected by eight ET-9820QB Photomultiplier Tubes (PMTs), with one attached to each window. A particle is identified when there is a coincidence of signals in at least six PMTs. However, as original CEDARs are designed for beam fluxes of kHz, they would not be applicable for NA62 which operates with beam fluxes of 10s of

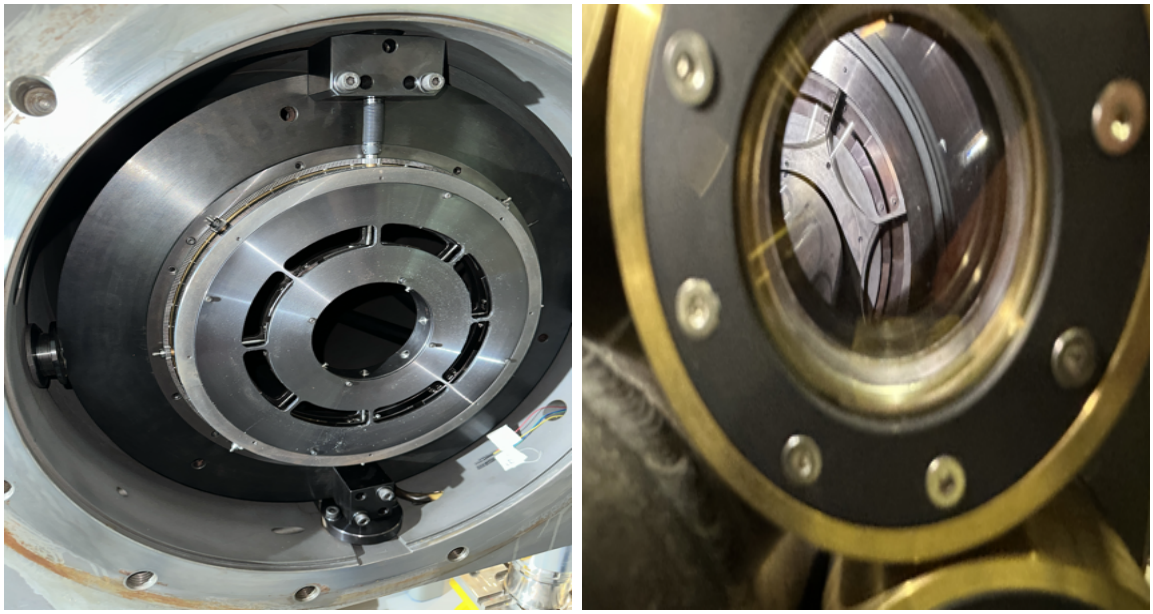

Figure 3.2: Photos showing the CEDAR diaphragm. On the left, a fully open diaphragm is shown in the CERN clean room with the front of the CEDAR fully removed. On the right, a slightly open diaphragm is shown through one of the quartz exit windows, allowing light to exit the CEDAR vessel.

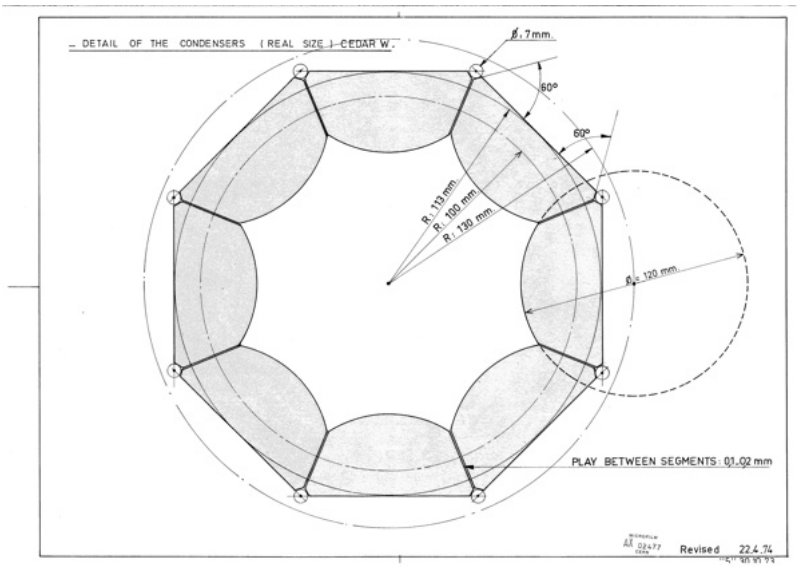

Figure 3.3: Engineering drawing showing the placement of the CEDAR condenser lenses which are shaded in grey. The lenses are arranged symmetrically around the beam axis and are used to focus the Cherenkov light at the CEDAR exit windows.

MHz. This implies strict timing requirements on the selection of kaons of less than 100 ps. To achieve these strict requirements, a photon detection system called the KTAG was purpose-built [48] and attached to the upstream end of the CEDAR. The light exiting the quartz windows traverses through optical caps attached to the exit windows, which focuses the light onto spherical mirrors. The eight spherical

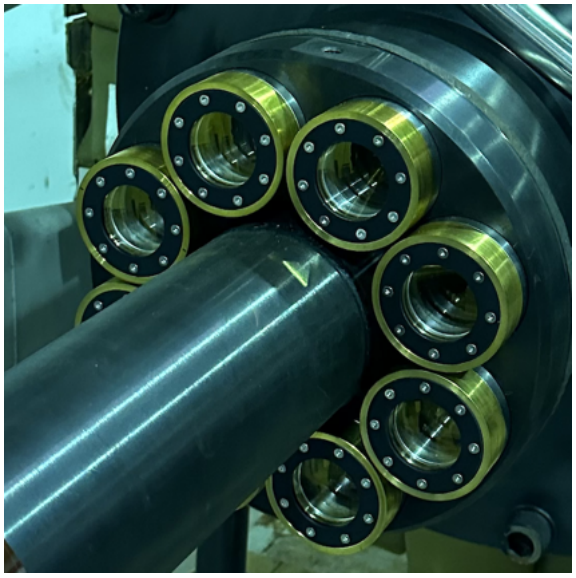

Figure 3.4: Image showing the exit windows and nose at the upstream end of the CEDAR-W.

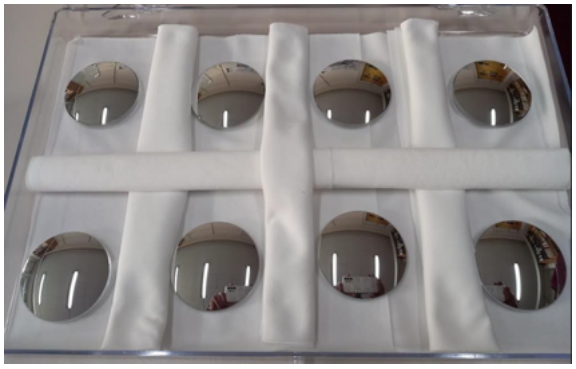

Figure 3.5: Image showing each of the CEDAR-Hydrogen (CEDAR-H) spherical mirrors before installation into the KTAG photon-detection system.

mirrors, one for each exit window, reflect the light 90 degrees onto eight PMT arrays and broaden the light to increase the resultant light spot. The spherical mirrors are manufactured from off-the-shelf optical lenses, then coated in aluminium and are shown in Figure 3.5. Each light spot is defined as a sector. Each sector contains a light guide before a PMT array equipped with 48 Hamamatsu PMTs (32 of type R9880U-110 and 16 of type R7400U-03). The light guide consists of a matrix of cones coated by aluminised mylar to maximise their reflectivity and are used to direct light onto the active area of each PMT. The CEDAR is designed to allow the light emitted at a specific angle to pass through a diaphragm aperture by selecting the pressure of the radiator gas. When the pressure of the gas is raised the density increases which results in the refractive index increasing. The increase in refractive index results in

an increase in the Cherenkov production angle, as defined in Equation 3.2 and the final Cherenkov ring image radius. For an ideal gas this is defined as

$$(n-1) \propto P/T, \tag{3.8}$$

where n is the refractive index, P is the pressure and T is the temperature of the gas. This allows a pressure to be selected where a kaon at 75 GeV/c produces a Cherenkov ring radius of 100 mm at the diaphragm, matching the centre of the CEDAR aperture. Selecting an aperture of less than 2.5 mm allows only the light from the kaon to pass through the diaphragm, with the central radius of the pion ring being 2 mm larger and the central radius of the proton ring being 6 mm smaller, shown in Figure 3.6. The selection of a single particle Cherenkov ring depends on the beam divergence being less than 100 µm and the axis of the CEDAR vessel being aligned parallel to the beam. This is to ensure that the divergence of the Cherenkov light is minimised. The CEDAR alignment to the beam is performed using a pair of motors at the downstream end of the detector. The motors displace the downstream end by ±5 mm in both the X and Y direction, pivoting the CEDAR vessel around the fixed upstream end.

At a temperature of 293 K, the nominal gas pressure to select kaons at 75 GeV/c is defined at 1.71 bar for N_2 in CEDAR-W and 3.85 bar for H_2 in CEDAR-H, with the values changing by 0.34 % for every 1 K of temperature difference. The CEDAR vessel is sealed and insulated in order to operate as a closed volume with a fixed amount of gas. It is also expected to be insensitive to fluctuations in the environmental temperature due to the extensive insulation around the pressure vessel.

3.2 Development of CEDAR-H

In Figure 3.7, simulations of the CEDAR-W with H_2 radiator gas show that the correction of the chromatic dispersion is inefficient, and photons of different wavelengths still display different radii at the diaphragm after the correction. In this configuration, it is not feasible to only select the light from kaons using the CEDAR diaphragm aperture without sacrificing light yield and operating at a lower detection efficiency. It is decided that a new vessel has to be developed with updated

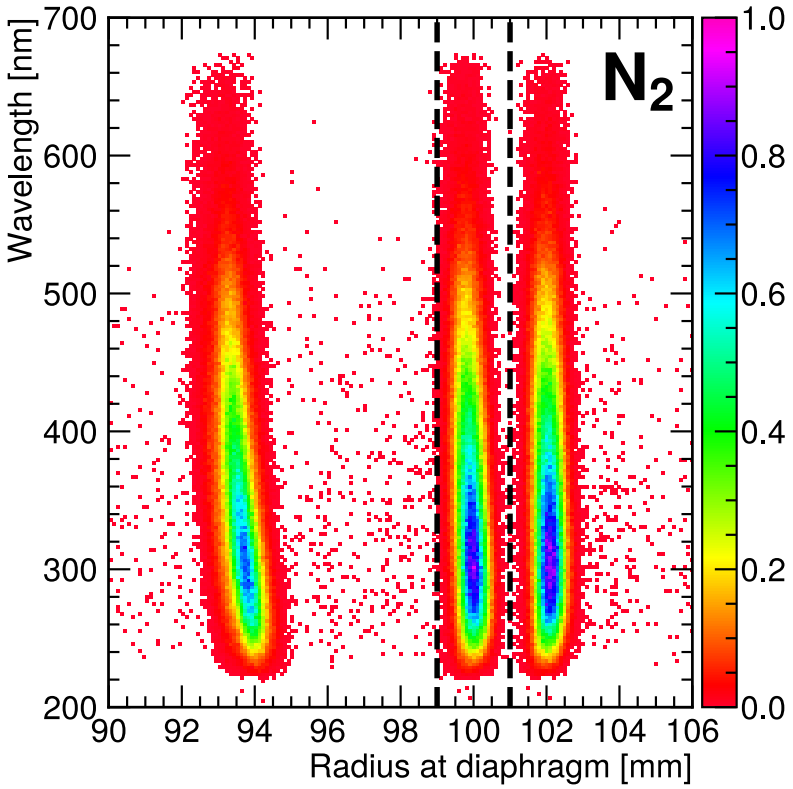

Figure 3.6: Simulated Cherenkov ring radius vs wavelength at the diaphragm for CEDAR-W with N_2 at a nominal pressure of 1.71 bar with the KTAG PMT effective quantum efficiency applied. The black dashed lines represent the edges of a 2 mm diaphragm aperture.

optics optimised for use with H_2. The vessel is called CEDAR-H. An available CEDAR-N vessel is chosen as the CEDAR-H structure, which reduces the costs as most of the mechanical components, such as the diaphragm and mirror supports, are not modified due to their complexity. This reduces the degrees of freedom for optimisation to three: the radii of curvature of the chromatic corrector lens and the two surfaces of the Mangin mirror. Initial parameters of the optical components are found using an analytical ray-tracing procedure [63, 64]. The parameters are iterated to achieve a ring radius of 100 mm and to minimise the width of the ring at the focal distance of the Mangin mirror. Due to the pressure-dependent effects of the chromatic dispersion and spherical aberration, each computation for the optical elements is completed at pressures between 3.8 to 4.1 bar in steps of 0.1 bar.

Once the initial parameters have been found, a full GEANT4 [58] simulation is employed to validate and optimise the results from the analytical computation. The GEANT4 simulation further traced the light coming out of the CEDAR vessel

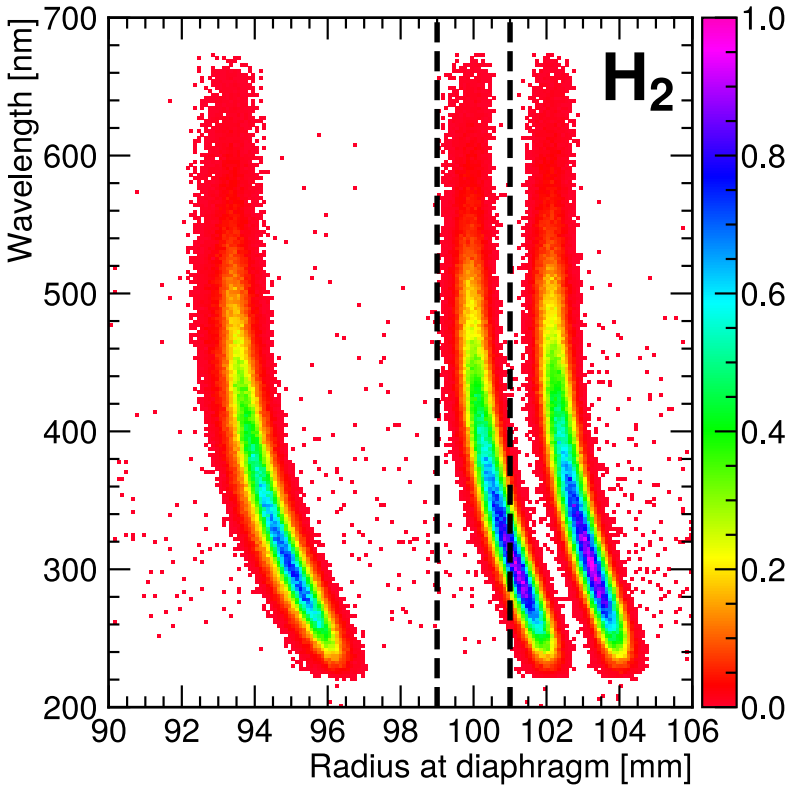

Figure 3.7: Simulated Cherenkov ring radius vs wavelength at the diaphragm for CEDAR-W with H_2 at a pressure of 3.67 bar with the KTAG PMT effective quantum efficiency applied. The black dashed lines represent the edges of a 2 mm diaphragm aperture.

through the diaphragm aperture, and then reflected by the spherical mirrors onto the PMT arrays, as shown in Figure 3.1. The simulation is then used to modify the optical parameters to maximise the number of photons reaching the KTAG PMTs. The radius of the beam hole of the Mangin mirror is reduced with respect to the original CEDAR design, resulting in a larger reflective surface and increasing number of photons reaching the PMTs. The spherical mirrors outside the vessel are upgraded to improve the light distribution on the PMT arrays. It is found that using the condenser lenses from the CEDAR-W as opposed to the CEDAR-N resulted in more significant photon yield.

The optimisation studies produce results with negligible differences in the number of photons reaching the PMT array between 3.8 and 4.1 bar as the increase of Cherenkov photons at high pressure is counteracted by the improved light distribution on the array at low pressures. Due to H_2 safety considerations, the lower pressure of 3.8 bar is selected. The optics sufficiently correct the chromatic disper-

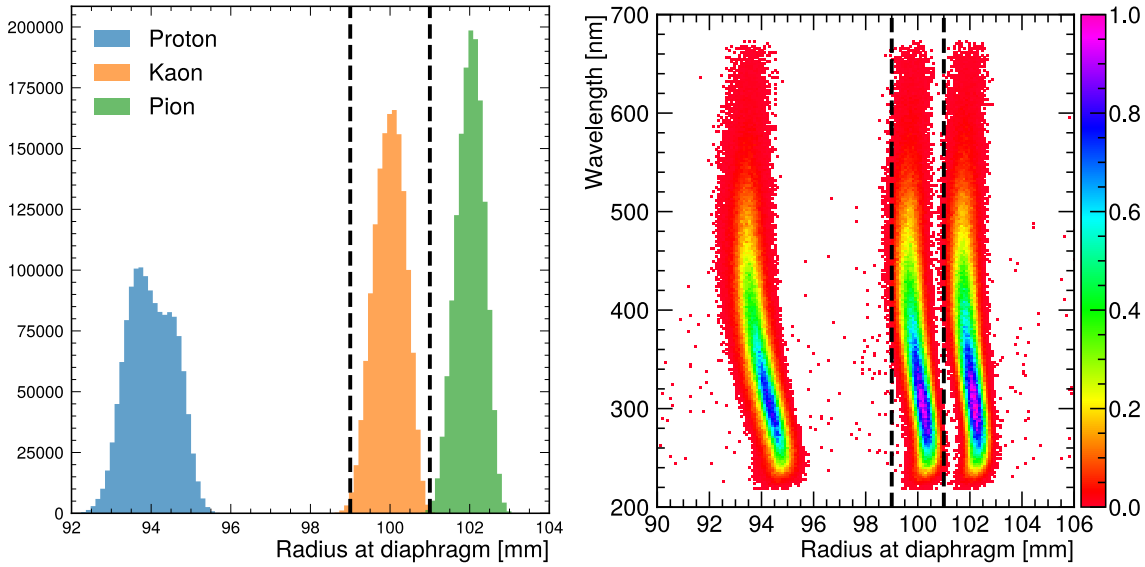

Figure 3.8: Simulated Cherenkov ring radius at the diaphragm of CEDAR-H with H_2 at 3.8 bar for proton, kaon, and pion beam particles and against wavelength. Both plots have the effective KTAG PMT Quantum Efficiency (QE) applied.

sion at this pressure setting, producing a Gaussian width of 0.4 mm for the kaon and pion rings at the diaphragm (Figure 3.8). This configuration allows for the selection of kaons with a 2 mm CEDAR diaphragm with minimal light from the pion passing through.

The full GEANT4 simulation at a pressure of 3.8 bar and a diaphragm aperture of 2 mm with the optimised optical parameters results in an expected kaon identification probability (at least five sectors) of 99.5 % and a pion misidentification probability of less than 10^{-4}, which satisfy, and exceed the requirements set for operation at NA62.

The CEDAR-H was constructed at CERN in 2022 using the mechanical and optical parameters found in Table 3.2. The Mangin mirror and chromatic corrector are constructed using high-quality quartz blanks and tested by an external company (Winlight [65]) to sub-micron tolerances. The measured reflectivity of the Mangin mirror is shown in Figure 3.9, peaking at just under 90 % for a wavelength of 350 nm.

Each optical component is tested and measured to ensure that their performance does not diverge from the specifications determined by simulations. The transmittance for each of the condenser lenses is shown in Figure 3.10, with each lens having over 90 % transmittance above 240 nm. Light at wavelengths below 240 nm does not

CEDAR Type		**CEDAR-W**	**CEDAR-H**
Nominal gas type		N_2	H_2
Nominal pressure [bar]		1.71	3.80
Gas vessel cylinder	Length	4500	4500
	Inner radius	267	267
Gas vessel cap	Length	339	280
	Inner radius	139	139
Chromatic corrector	Position along the beam axis	1855	1902
	Radius of curvature	1385	1307
	Central thickness	20	20
	Inner radius	75	75
	Outer radius	160	160
Mangin mirror	Position along the beam axis	5353	5362
	Radius of curvature:		
	- refracting surface	6615	8994
	- reflecting surface	8610	9770
	Central thickness	40	40
	Inner radius	50	40
	Outer radius	150	150
Diaphragm	Position along the beam axis	872	911
	Aperture central radius	100	100
Condensers	Position along the beam axis	832	871
	Maximum thickness	10	10
	Radius of curvature	300	300
Quartz windows	Position along the beam axis	472	531
	Thickness	10	10
	Radius	22.5	22.5
	Radial distance to window centre	103	103
Optical caps	Position along the beam axis	450	450
	Maximum thickness	4.24	4.24
	Radius of curvature	114.62	114.62
Spherical mirrors	Position along the beam axis	322	322
	Radius of curvature	51.68	77.52
	Diameter	50	50
	Radial distance to mirror centre	106	106

Table 3.2: Optical and mechanical parameters of CEDAR-W and CEDAR-H. All values are in millimetres unless otherwise stated. Positions along the beam axis are quoted with respect to the upstream end of the CEDAR. Double horizontal lines separate optical elements inside and outside the CEDAR vessel [60].

impact the light yield due to the UV quartz filters described in Section 3.1 which are attached to the exit windows. The measured transmittance of each of the quartz exit windows is shown in Figure 3.11.

The spherical mirrors used in the KTAG to reflect the light onto PMT arrays are produced at CERN from commercially available spherical lenses coated with

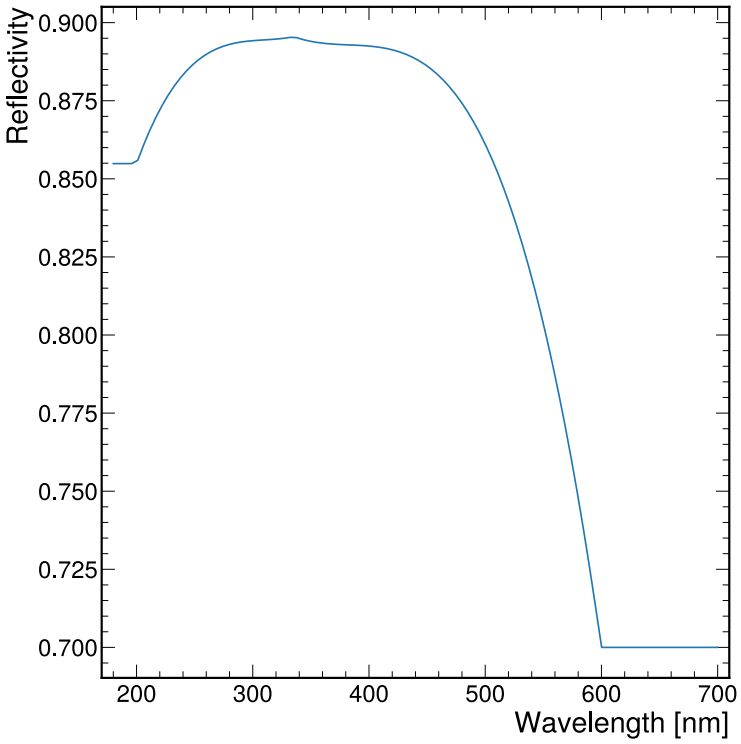

Figure 3.9: Measured reflectivity of CEDAR-H Mangin mirror conducted by Winlight System.

a reflective aluminium surface. The measured reflectivity is shown in Figure 3.12, with the mirrors grouped in groups of four which have similar characteristics.

3.3 CEDAR-H Test-beam

After construction of the CEDAR-H detector, it was tested and characterised in 2022 during a test at the H6 beamline at CERN, shown in Figure 3.13. The test-beam has three main aims:

1. Understand the safety procedures related to H_2 gas operations.
2. To ensure that the optics have been installed and aligned correctly;
3. To measure the kaon identification efficiency and pion misidentification probability at several different diaphragm apertures.

The H6 beamline is located at the CERN north area and is produced from 400 GeV/c primary protons from the SPS interacting with a target consisting of

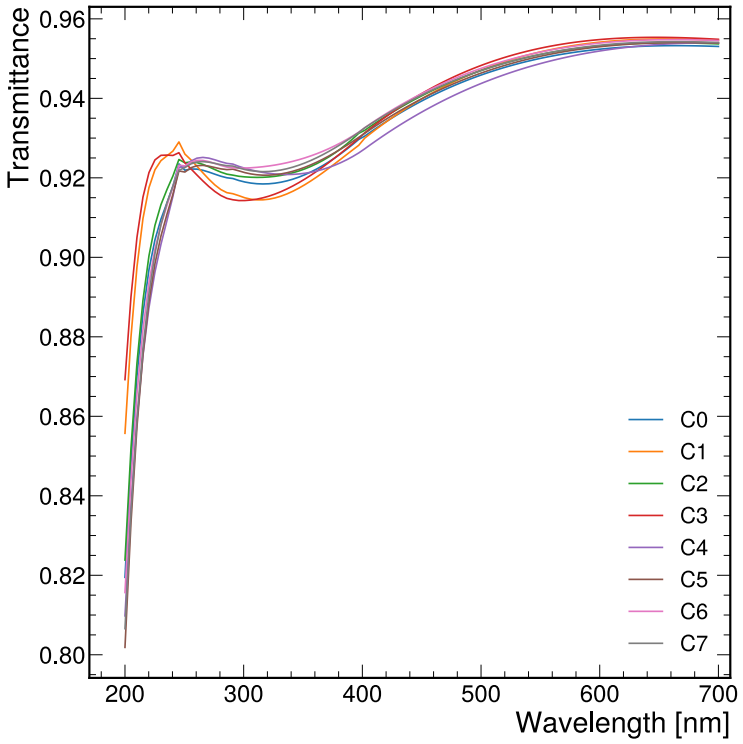

Figure 3.10: Measured transmittance of CEDAR-H condenser lenses conducted by engineers at CERN [66].

a beryllium rod, producing an unseparated 75 GeV/c hadron beam similar to the NA62 beam. CEDAR-H is installed 440 m downstream of the target, compared to 70 m when installed in NA62, resulting in a similar beam composition when compared to NA62, with 4 % kaons, 25 % protons, and 71 % pions. The beam divergence at the entrance of the CEDAR is 80 µm in the H6 beamline compared to 70 µm in NA62, well within the operating divergence of 100 µm for the CEDAR.

For the test-beam, an ET 9820QB PMT is installed directly onto each exit window without the optical caps and is operated at a voltage of 2 kV with a 30 mV discriminator threshold voltage to achieve single photo-electron sensitivity. The test setup is illustrated in Figure 3.14 where a pair of scintillating counters are installed at each end of the detector to provide a trigger when each beam particle passed through the vessel. For a typical SPS beam pulse (spill), there are 2.8×10^5 particles. For each triggered particle within the spill, the six, seven and eight-fold coincidences are recorded for later analysis. The N-fold coincidences are defined where N PMTs are in coincidence within a given time window.

Due to the flammable nature of H_2 gas, some safety considerations have to be

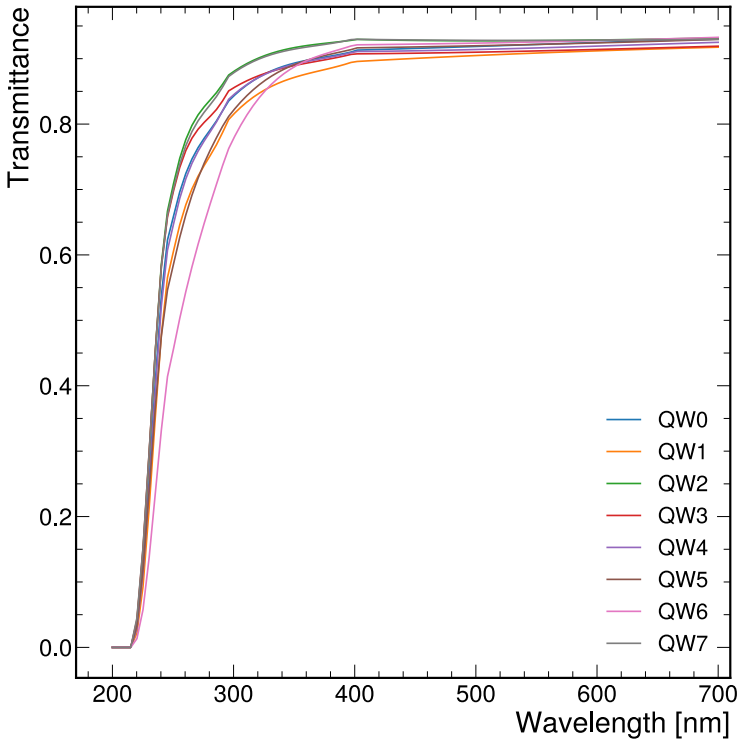

Figure 3.11: Measured transmittance of CEDAR-H quartz exit windows conducted by engineers at CERN [66].

made compared to running with N_2. An area of 1 m radius around the ends of the CEDAR-H is designated as an explosive atmosphere (ATEX) zone where extra care has to be taken to avoid the chance of a spark forming. The setup is certified by CERN before the start of the test-beam. A number of changes are implemented by CERN on the gas systems in H6 to accommodate the safety systems for operation with H_2. The pressure is monitored by the gas control software and alarms are implemented if drops in pressure are observed. Also, some operational changes compared to N_2 are modified for the pressure scans, where a maximum pressure is set at 4.4 bar to reduce the chance of a vessel rupture.

3.3.1 Alignment of CEDAR-H

After the installation, the first step of the test is to conduct an alignment of the CEDAR-H vessel with the beamline. As described in Section 3.1, the CEDAR is attached to XY motors, which are used to align the vessel to the beam. The diagram in Figure 3.15 depicts how moving the CEDAR vessel would impact the position

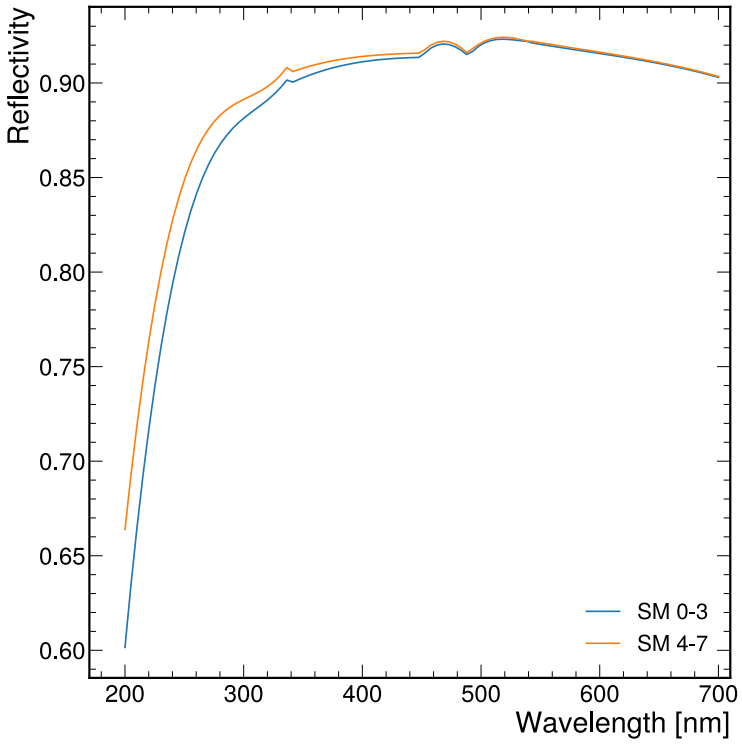

Figure 3.12: Measured reflectivity of KTAG spherical mirrors conducted by engineers at CERN [66].

Figure 3.13: Image of CEDAR-H being installed on the H6 beamline at CERN in 2022.

of the Cherenkov ring at the diaphragm. The alignment aims to centre the ring directly within the diaphragm aperture to maximise the light yield. It is possible to quantify the alignment in two ways: to maximise the number of detected photons per beam particle and to balance the number of detected photons per trigger on each PMT.

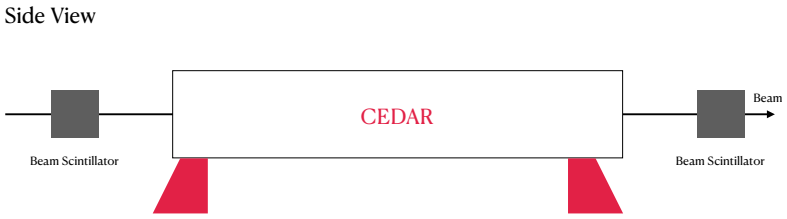

Figure 3.14: Diagram showing the CEDAR test-beam setup in H6 from the side view.

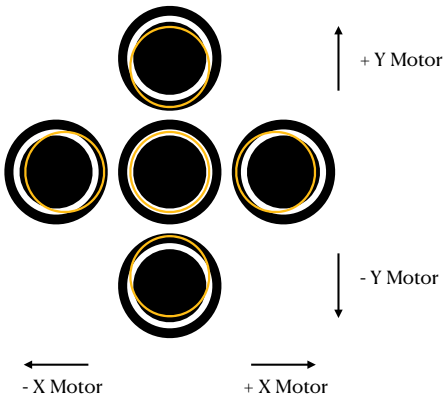

Figure 3.15: Diagram depicting the movements of the Cherenkov ring at the diaphragm during an alignment.

A coarse alignment is completed first, where the gas pressure is set at 4.2 bar and the diaphragm set at the widest aperture of 19 mm to allow the light from all beam particles to pass through the diaphragm, with the results shown in Figure 3.16. The motor positions are moved until the counts on the PMT per trigger are around 100 % and are balanced (shown on the right of Figure 3.16). A large aperture allows for the rough calculation of the PMT efficiency, as a fully efficient detector would expect the number of photo-electrons on each PMT to equal the number of triggers. In Figure 3.16 the percentage efficiency for the eight PMTs is shown on the right. It shows that the PMTs are at least 95 % efficiency with the average being 98.3 %.

A fine alignment with a smaller diaphragm aperture is essential to ensure the detector's alignment with the beam. The second alignment is conducted at a pressure of 4.29 bar, where the proton ring have a radius of 100 mm at the diaphragm with a diaphragm aperture of 1.3 mm. The alignment results are shown in Figure 3.17 and are checked at three different aperture settings. The three aperture settings are chosen to ensure that the Cherenkov ring is aligned within the aperture. As the aperture is closed, it is expected that the number of photo-electrons per PMT would

```
*************************************************************************
--2 PM/MEAN--  --ALIGNMENT--    PRESS =    4.291 Bar   8     97  100     1
    100        X  =   1.35 mm   MASS  =      NaN GeV   7 100         98  2
 99       99   Y  =   3.59 mm   NPE/PM=    2.159       6  95         98  3
    100        Dia=  19.01 mm   TRIG  = 2.800e+05      5    100   98     4
*************************************************************************
```

Figure 3.16: Output of data collection for CEDAR-H at the end of the first alignment. From left, the mean number of detected photons per group of two PMTs normalised to the trigger, the positions of the XY motors, the diaphragm aperture (DIA), the gas pressure (PRESS), the average number of detected photons (NPE) per PM, the number of triggers (TRIG). The spacial alignment of the PMTs is shown on the right, showing the position pon each CEDAR exit window.

```
*************************************************************************
--2 PM/MEAN--  --ALIGNMENT--    PRESS =    4.291 Bar   8     20   18     1
     99        X  =   1.35 mm   MASS  =      NaN GeV   7  19         19  2
 101       97  Y  =   3.59 mm   NPE/PM=    1.354       6  20         19  3
    101        Dia=   1.00 mm   TRIG  = 2.745e+05      5     19   20     4
*************************************************************************
--2 PM/MEAN--  --ALIGNMENT--    PRESS =    4.291 Bar   8     18   16     1
     99        X  =   1.35 mm   MASS  =      NaN GeV   7  17         15  2
 104       93  Y  =   3.59 mm   NPE/PM=    1.043       6  18         16  3
    102        Dia=   0.79 mm   TRIG  = 2.835e+05      5     16   18     4
*************************************************************************
--2 PM/MEAN--  --ALIGNMENT--    PRESS =    4.292 Bar   8     23   25     1
    100        X  =   1.35 mm   MASS  =      NaN GeV   7  23         23  2
 100       97  Y  =   3.59 mm   NPE/PM=    2.086       6  25         23  3
    102        Dia=   2.02 mm   TRIG  = 2.785e+05      5     24   25     4
*************************************************************************
```

Figure 3.17: Output of data collection on CEDAR at the end of the second alignment showing the positions of the XY motors, the diaphragm aperture, pressure of the CEDAR, the average number of photo-electrons per PM and then the spacial alignment of the PMTs. Each entry is recorded at a different diaphragm aperture of 0.79, 1 and 2.02 mm.

decrease but if aligned, the balance across the PMTs would not change. Figure 3.17 shows that the vessel is aligned successfully, with the counts on the PMTs being uniform within a couple percent. It is also expected that the counts per trigger would represent the beam composition at a 2 mm aperture, where the proton fraction is within a few percent of the expected value. The CEDAR is successfully aligned at the proton pressure with motor positions of: $X = 1.35\,\text{mm}$ and $Y = 3.59\,\text{mm}$ with an average PMT efficiency of 98.3 %.

3.3.2 Pressure and Diaphragm Scans

The remaining goals of the test-beam are to determine the parameters for operation at NA62. This includes the determination of the kaon pressure to maximise kaon yield, the optimal diaphragm aperture to maximise light from the kaon and minimising the impact of light from the pion. This is completed through a number of pressure and diaphragm scans described below.

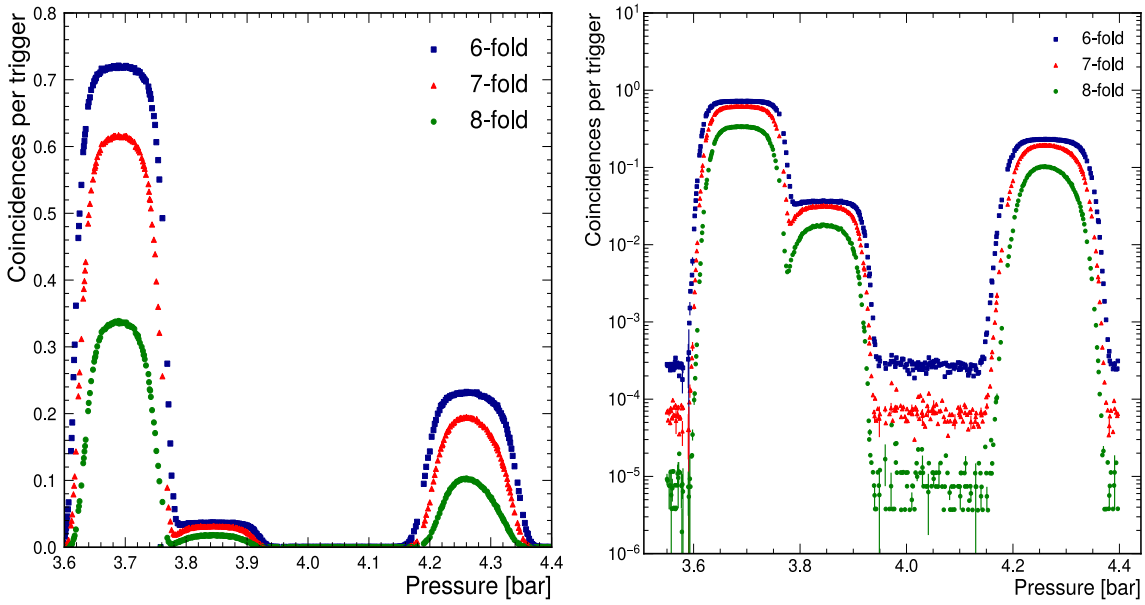

Figure 3.18: Results of the first pressure scan at the H6 test-beam at a diaphragm aperture of 2.3 mm showing coincidences per trigger against pressure.

To determine the kaon operating pressure, a pressure scan is performed. Before the scan, the pressure of the CEDAR-H is set at the highest pressure (4.4 bar), where there are no selected beam particles. A selected beam particle is defined when there is signal in at least 6 PMTs in coincidence. The scan consists of reducing the pressure in small steps and collecting data at each step. This is completed at a diaphragm width of 2.3 mm, larger than the standard operating setting used with the CEDAR-W at NA62. The aperture is chosen to maximise the light yield of the detector. This is to compare the computed beam composition to the expected for the H6 beamline. The results of the pressure scan are found in Figure 3.18, with each beam component visible in the plots. The protons produce a maximum light yield at 4.26 bar with 0.232 coincidences per trigger, with the build-up in coincidences caused by the gradual entrance of the Cherenkov ring into the aperture of the diaphragm. The kaon has a maximum light yield at 3.844, with 0.037 coincidences per trigger, and the pion has a maximum light yield at 3.69 bar, with 0.721 coincidences per trigger. The fraction of triggers is within 1–2 % of the expected beam composition, resulting in the selection of a particle in 99.1 % of the triggers. It is expected that not all light from the proton ring would pass through the 2.3 mm diaphragm aperture due to its large Gaussian width and distorted shape, shown in Figure 3.8.

The resultant light yield of CEDAR-H is computed from the 6, 7, and 8 coinci-

dences per trigger shown in Figure 3.18 using either of the two equations,

$$\lambda = \ln\left[1 + \frac{8}{\eta_7/\eta_8 - 1}\right] \tag{3.9}$$

and

$$\lambda = \ln\left[1 + \frac{14}{\sqrt{4 - 7(1 - \eta_6/\eta_8)} - 2}\right], \tag{3.10}$$

where η_N is defined as the probability of an N-fold coincidence and λ is the number of photo-electrons per PMT. The ratios η_8/η_7 and η_8/η_6 are shown in Figure 3.19 together with the resultant photons per PMT. The two equations 3.9 and 3.10 are used to cross-check the result and then averaged. At the pion pressure (3.68 bar), $\eta_8/\eta_6 = 0.435$ and $\eta_8/\eta_7 = 0.500$, which produces an average light yield of $\lambda = 2.37$ photons per PMT. The proton yields slightly less light with $\eta_8/\eta_6 = 0.420$ and $\eta_8/\eta_7 = 0.525$ producing an average of $\lambda = 2.30$. At the kaon pressure (3.844 bar), the ratios of $\eta_8/\eta_6 = 0.500$ and $\eta_8/\eta_7 = 0.535$ produce an average yield of $\lambda = 2.45$, which results in a total of 19.63 photo-electrons per kaon. This suggests that the optics have been correctly manufactured and installed. However, the diaphragm is wider with respect to the normal NA62 setting. It is clear that the 2.3 mm diaphragm can not be used in NA62 due to the unsatisfactory kaon-pion separation seen in Figure 3.18. This would result in a non-zero probability for misidentification of a pion at the kaon pressure.

Several pressure scans are completed at different diaphragm apertures to select a working point with a maximised light yield and low pion misidentification (pion-kaon separation), and the results are shown in Figure 3.20. The corresponding coincidence ratios and average number of photo-electrons per beam particle are detailed in Table 3.3. The pressure scan at 2 mm is shown in the top left plot of Figure 3.20; this provides a light yield similar to the 2.3 mm pressure scan but with greater separation between the pion and kaon peaks, however, there is no clear separation in the six-fold coincidences. NA62 uses at least five sector coincidences for particle identification, so it is important to achieve a clear separation with six coincidences, which is the closest criteria available for the test-beam. The top right of Figure 3.20 is at a similar diaphragm aperture used at NA62 of 1.7 mm. Compared to the 2 mm pressure scan, the light yield decreased by 1.7 %, but the separation of the kaon-pion peak increased dramatically, with the estimated six sector coincidences of

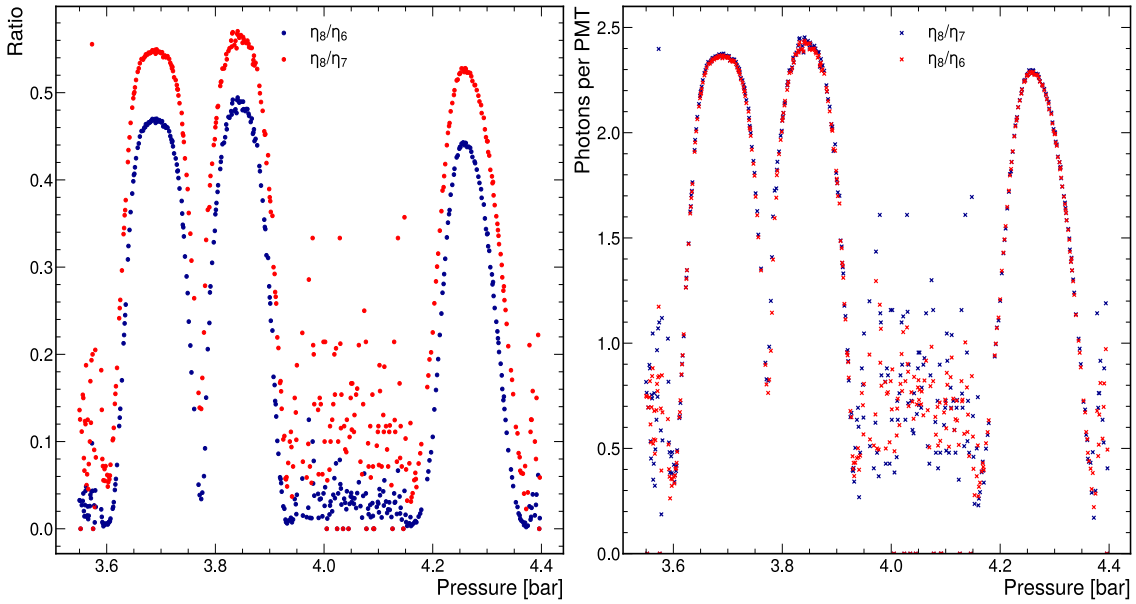

Figure 3.19: Left, Ratios of η_8/η_7 and η_8/η_6 and right, photons per PMT calculated with Equations 3.9 & 3.10 with respect to pressure at a diaphragm aperture of 2.3 mm.

the pion peak falling well below 10^{-6} at the kaon pressure. The final pressure scans at 1.2 mm and 1 mm, in Figure 3.20 show complete separation between the kaon-pion peaks. However, the maximum light yield at the individual particle pressures is reduced, as the peaks no longer have a flat peak. This suggests that at 1.3 mm the diaphragm aperture is narrower than the width of the Cherenkov ring, which results in the loss of light at the diaphragm. This is shown in Table 3.3, where at a diaphragm width of 1 mm, the average number of photo-electrons per kaon is 16.03. This corresponds to an identification efficiency of less than 95 % when using five sectors, which is below the acceptable threshold for operation in NA62.

Diaphragm Aperture [mm]	**Proton**			**Kaon**			**Pion**		
	η_6/η_8	η_7/η_8	**Avg PE**	η_6/η_8	η_7/η_8	**Avg PE**	η_6/η_8	η_7/η_8	**Avg PE**
2.0	0.825	0.510	17.84	0.869	0.568	19.46	0.853	0.544	18.83
1.7	0.790	0.471	16.70	0.859	0.558	19.13	0.843	0.534	18.52
1.2	0.695	0.388	14.37	0.827	0.517	18.00	0.813	0.500	17.54
1.0	0.581	0.385	13.12	0.759	0.448	16.03	0.757	0.446	16.00

Table 3.3: Table containing the ratios of η_6/η_8 and η_7/η_8, as well as the average number photo-electrons per beam particle at the peak values from the pressure scans at different diaphragm apertures.

A secondary test of the particle identification efficiency is conducted by scanning the diaphragm aperture at a pressure of 3.85 bar. The results are shown in Figure 3.21, where the number of photo-electrons per trigger is visualised against

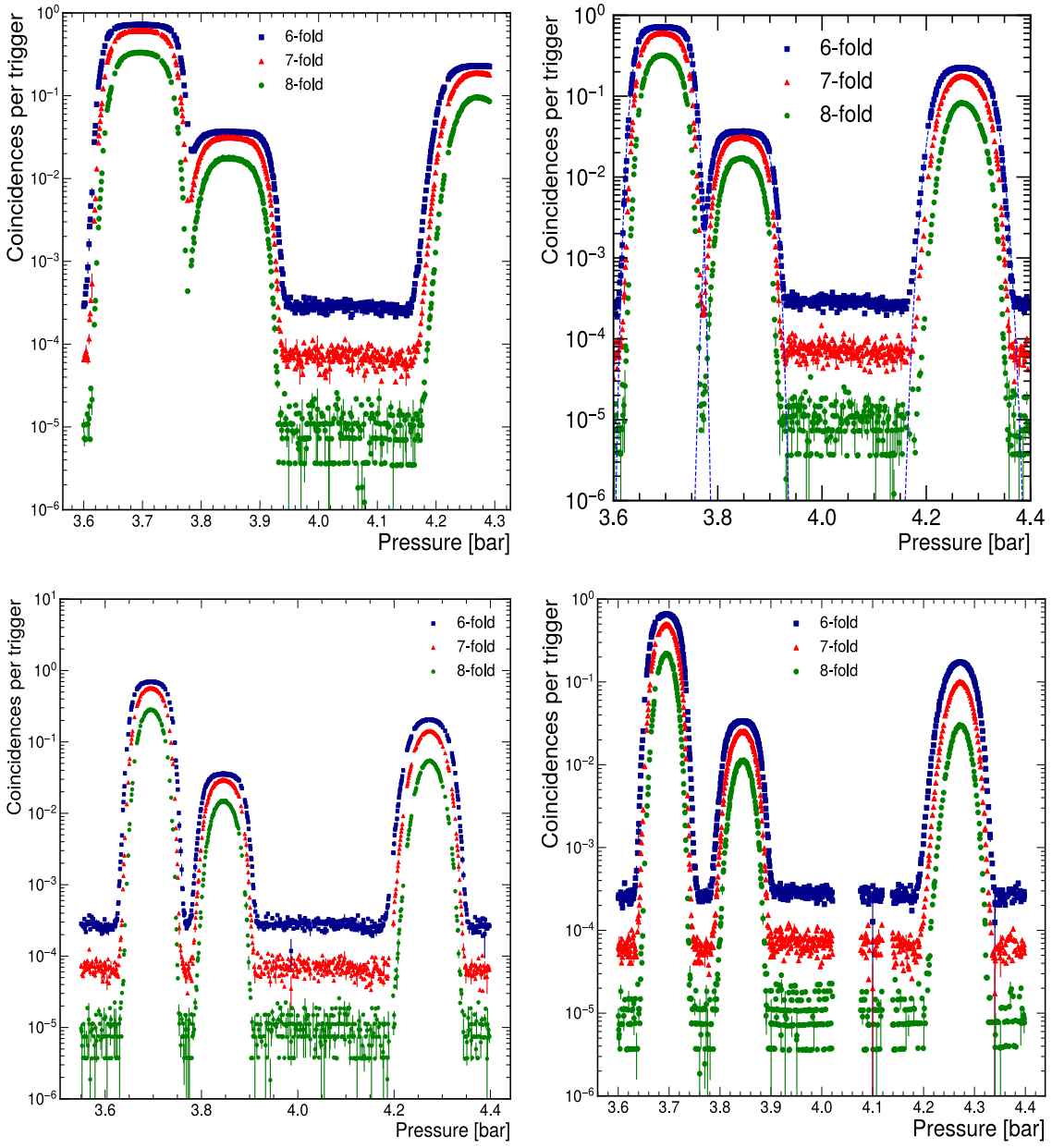

Figure 3.20: Results of the CEDAR-H pressure scans taken during the 2022 test-beam. Top left is conducted with a diaphragm aperture of 2 mm, top right with a diaphragm aperture of 1.7 mm, bottom left with a diaphragm aperture of 1.2 mm and bottom right with a diaphragm aperture of 1 mm.

the diaphragm aperture. The scan is completed by shutting the diaphragm as much as possible and then increasing the diaphragm aperture while recording the 6, 7, and 8-fold coincidences. From Figure 3.21, it is clear that diaphragm apertures of less than 2 mm result in progressively lower light yield. This reiterates the results where the pressure scans in Figure 3.20 with apertures smaller than 2 mm result in lower light yield. When the diaphragm is opened greater than 3 mm, the Cherenkov

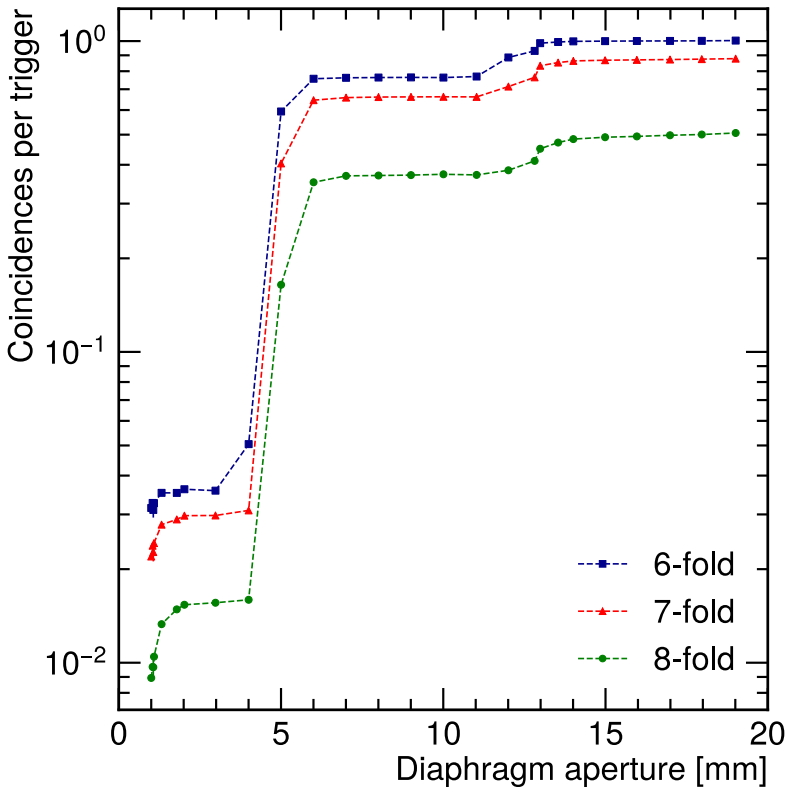

Figure 3.21: Plot showing the results of the diaphragm scan during the H6 test-beam at a pressure of 3.85 bar (kaon pressure).

light from the pion contributes to the 6-fold coincidences. At apertures greater than 4 mm the 7 and 8-fold coincidences are then affected. At 11 mm, the light from the protons enter the aperture. Cherenkov light from all the particles pass through the apertures wider than 13 mm. The diaphragm scan continues up to 19 mm, which is the maximum aperture of the diaphragm limited by the end switch, where the total six-fold coincidences per trigger reaches about 0.99, accounting for a particle identification efficiency of 99 %. Considering all of the pressure scans completed during the test-beam, the optimal working point for CEDAR-H is found to be at a pressure of 3.85 bar with a diaphragm aperture of 1.7 mm. This diaphragm aperture is chosen as it provides a light yield of 19.13 photo-electrons per kaon, along with an acceptable pion misidentification probability.

Figure 3.22: CEDAR-H being installed on the NA62 beamline 2023.

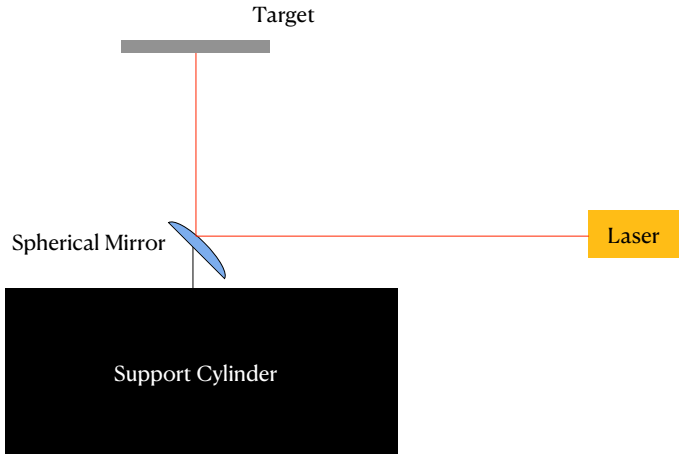

Figure 3.23: Diagram of the setup used to align the KTAG spherical mirrors and the lasers path.

3.4 Installation at NA62

3.4.1 Mechanical and Optical Setup

CEDAR-H was installed on the NA62 beamline in 2023, involving several steps. First, the KTAG photon-detection system was disassembled from the CEDAR-W, with the CEDAR-W vessel then removed from the beamline. The CEDAR-H was brought to the NA62 underground cavern and installed on the beamline, shown in Figure 3.22.

The upgraded spherical mirrors for CEDAR-H are aligned with a laser beam and

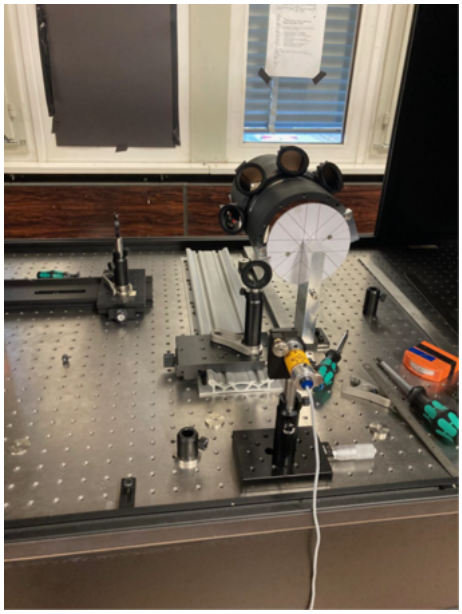

Figure 3.24: Image of the four spherical mirrors being aligned whilst attached to the CEDAR support cylinder [67].

secured to a support cylinder, depicted in Figure 3.23 and 3.24. The alignment of the mirrors begins with the positioning of the laser. Data from the NA62 Monte Carlo (MC) simulation provides information about the direction of light exiting the CEDAR-H vessel. A photon that hits the centre of the spherical mirror is selected, and the positions at the exit window and the spherical mirror are recorded. The vector is then calculated from the mirror centre to the exit window and used to set up the laser for the mirror alignment. A target representing the PMT array, shown in Figure 3.25, is placed at the correct distance from the spherical mirror. The laser is placed to simulate the direction of light exiting the CEDAR-H and the spherical mirror is adjusted so that the laser light hits the centre of the target, ensuring that the light would hit the centre of the PMT array. The spherical mirror is adjusted using a screw located at the back of the support, shown in Figure 3.25 (left). The process is then repeated for all eight spherical mirrors.

The mirror support cylinder is then attached to the nose of the CEDAR-H. The KTAG photon-detection system is reassembled at the upstream end of the vessel, and all connections are reconnected and tested.

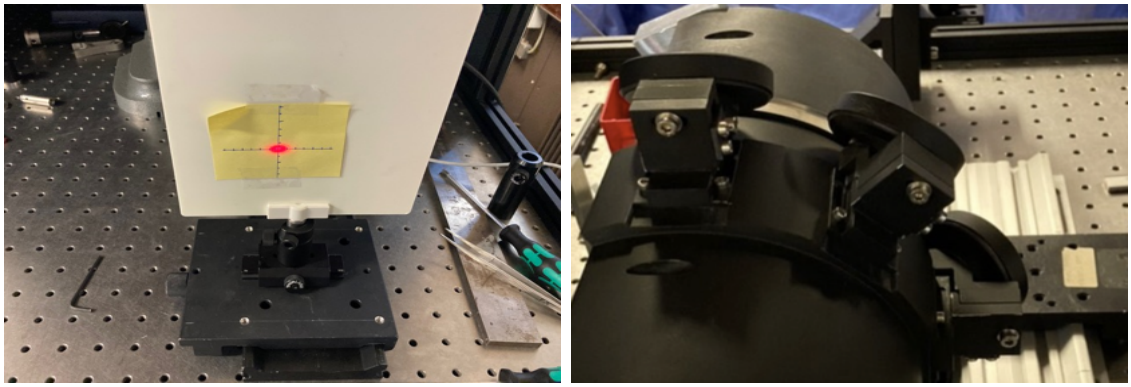

Figure 3.25: Left, image of the target used for the alignment of the spherical mirrors and right, image showing the back of the spherical mirror and the screw used to modify its position [67].

3.4.2 Hydrogen Safety

Compared to the setup of the CEDAR-W, several modifications are made due to the requirements for the use of H_2 within the ECN3 experimental hall. It is expected that some amount of gas would leak from the CEDAR-H, so all precautions have to be taken in order to prevent the concentration of gas from reaching dangerous levels between the Lower Explosive Limit (LEL) of 4 % and Upper Explosive Limit of 75 % volume in air for H_2. Any area where there is a potential for a H_2 leak is designated as an ATEX zone 2. In the ATEX zones, there are no electrical connectors, and metal parts of the CEDAR-H are grounded to prevent any ignition sources. During H_2 operation, the diaphragm end switches are manually isolated through a key located by the KTAG electronics rack, as these are not ATEX rated and have the potential to create a spark. The ATEX zones extend 80 cm from the CEDAR-H vessel and require experts to have ATEX training in order to access. Any confined space where the H_2 can accumulate, such as the KTAG enclosure and the box containing the diaphragm potentiometer and motor is flushed with a constant supply of N_2 to prevent the build-up of H_2. A safety interlock is installed to turn off the KTAG electronics in the event the supply of N_2 is interrupted. Another interlock is in place to turn off the KTAG electronics if there is a sizeable pressure drop in the CEDAR-H vessel. The pressure sensor precision limits the defined pressure drop for the interlock. A small leak is defined to be a measured drop in pressure of 0.02 mbar per minute measured by a rolling average across an hour. A major leak interlock,

Figure 3.26: CEDAR-H installed in the NA62 beamline (left) and the KTAG photon-detection system reassembled at the upstream end of the vessel (right).

which would represent a rupture of the aluminium windows, would be triggered if the pressure drops by 0.1 mbar per second. This major leak interlock would cut power to the CEDAR and neighbouring areas, turning off vacuum pumps and the GTK. To avoid the possibility of the window rupture, the CEDAR-H has a safety valve attached to the exhaust on top of a CEDAR vessel, which limits the pressure in the vessel to a maximum value of 5 bar. The aluminium windows have been tested to withstand a pressure of 7.5 bar before installation so that the safety valve would prevent any damage to the windows.

Dedicated flammable gas detectors are installed on the top of the metal pavilions at both upstream and downstream ends of the CEDAR-H vessel, shown in Figure 3.26. The detectors monitor the concentration of H_2 levels outside the vessel and result in a warning if the concentration exceeds 10 % of the LEL. The gas detectors are connected to the CEDAR-H Detector Safety System (DSS). A concentration of 20 % of the LEL generates a level 3 alarm, which would cut the power in the area if the alarm is triggered, and the CERN fire brigade would be informed. The main metal pavilion covers the upstream end of the CEDAR-H vessel, the KTAG photon-detection system, and the gas distribution panel, and it is designed to guide any leaking gas to the H_2 sensor. Another smaller metal pavilion is installed at the

downstream end of the vessel.

During the installation, the CEDAR-H is leak tested at 3.85 bar for 10 days, where the leak rate is measured to be 0.2 litres per day at standard pressure and temperature. This satisfies the safety requirements for use in ECN3, given the measured airflow from the ventilation of the experimental hall.

3.5 Commissioning at CERN

The commissioning of the CEDAR-H in the NA62 beamline was completed at the start of the 2023 run. The goals of the commissioning are to ascertain the operational working point for kaon detection at NA62 and to ensure that the detector is operational after its transport and installation.

After the CERN beam experts completed the start-of-run activities and the beam is steered through the CEDAR-H vessel, the beam intensity is set at 10 % of the NA62 nominal value, corresponding to a particle rate of 60 MHz. Periodic triggers are used during the CEDAR-H commissioning in order to select all beam particles and measure the beam composition. This trigger is where a period is selected between the start of burst (SoB) and end of burst (EoB) at which data are collected. At the beam intensity selected, the period is set so that 2×10^5 triggers per spill are collected. For each triggered event, the KTAG data acquisition system records the time and the channel ID of each PMT signal within a 100 ns time window defined by the trigger. Individual PMT signals are clustered into candidates by an algorithm that selects the hits within a 4 ns time window. As each individual PMT signal is recorded, the light yield is defined using a different method when compared to the test-beam. In the test-beam, the ratios of the coincidences are used to calculate the light yield using Equations 3.9 & 3.10. However, at NA62, the exact light yield is measured precisely due to the high granularity of the KTAG photon-detection system and is defined as the number of photo-electrons per beam particle candidate. The identification of the beam particle utilised a 5-fold coincidence, compared to the 6-fold used in the test-beam, due to the reduced noise level with the KTAG photon-detection system.

As the CEDAR has been removed from H6, then moved to ECN3 and installed

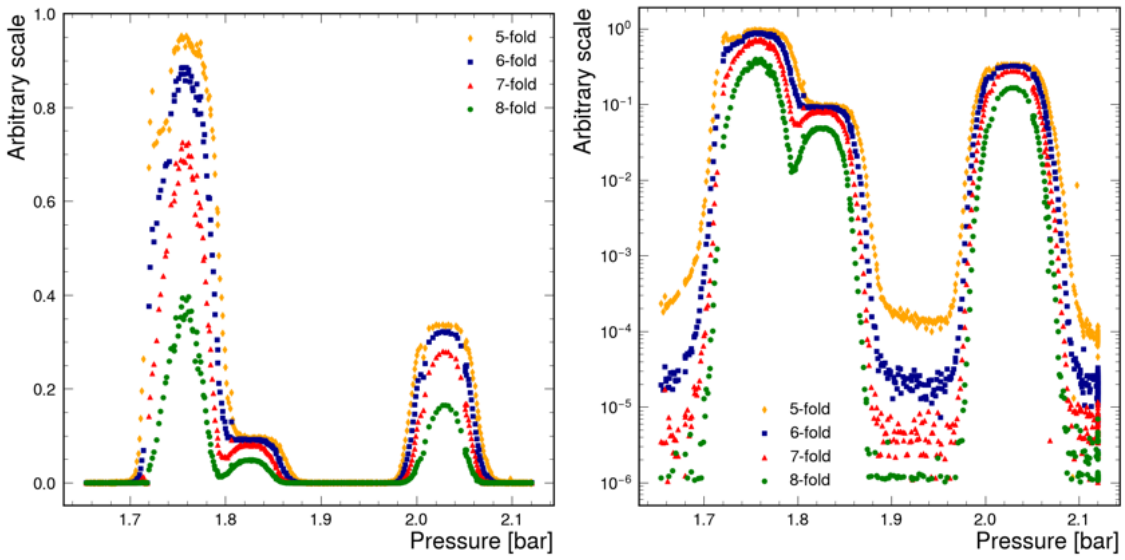

Figure 3.27: Pressure scan with CEDAR-H with N_2 going from a 1.5 bar to 2.12 bar at a diaphragm aperture of 1.45 mm.

into the beamline, the first step of the commissioning is to validate that the detector is functional using N_2 before filling the vessel with H_2. This allows for the confirmation of the basic functionality of the detector without the complications added by H_2, in case a hardware intervention is needed. The basic functionality includes the ability for the new CEDAR to collect Cherenkov light from the beam components, confirming that the optics are still operational and that the KTAG was reassembled successfully. It is important to note that any results from this phase are preliminary due to the distorted nature of the Cherenkov light in the CEDAR-H with a N_2 radiator gas.

The CEDAR-H vessel is filled with N_2 to 1.5 bar. A pressure scan is then completed going up in pressure to 2.12 bar, at a diaphragm aperture of 1.45 mm with the results shown in Figure 3.27. This pressure scan is used to determine the pressure at which each beam element can be selected. The pressure scan in Figure 3.27 showed that the pressures for the proton is at 2.03 bar, the kaon is at 1.82 bar and the pion at 1.76 bar. The narrow peaks for each beam component with no flat tops suggests that the vessel is not correctly aligned and/or that the diaphragm aperture is too small. The pion-kaon peaks are not separated, which is not expected with a small diaphragm, so it is assumed that the detector alignment with the beam is not correct.

A coarse alignment is conducted at a diaphragm aperture of 1.45 mm and at the proton pressure of 2.03 bar. It is done at the proton pressure as it is an isolated peak and is more efficient for alignment, with the results shown in Figure 3.28. The procedure is the same as the one done in the test-beam where the motors on the upstream end of the vessel moved in both X and Y dimensions, pivoting the vessel about the downstream end. The detector is positioned at $Y = -1.943$ mm and $X = -2.219$ mm, resulting in an average of 20.6 photo-electrons per candidate. The alignment results are shown in Figure 3.28, where the Y motor position is first moved in the positive direction, which causes a decrease in the number of photo-electrons per candidate. The Y motor position is then moved in the negative direction until the maximum is found at $Y = -2.051$ mm. The gaps in the results show the instability of the motors, as it is not possible to return to the same point after moving due to the inaccuracy in the control system. The X motor position is modified until a maximum is found at $X = -2.155$ mm. The final position of the CEDAR-H with N_2 is $X = -2.155$ mm and $Y = -2.051$ mm, with an average of 20.9 photo-electrons per candidate. However, the maximum is found at the edge of the usable range in the Y direction, it is possible that the maximum light yield is not found and is further in negative Y. As this would be much harder to conduct with H_2 in the CEDAR, the vessel is manually lowered 2 mm by reducing the height of the upstream foot. The maximum photo-electrons per candidate is now located at $Y = -0.05$ mm, while the X is unchanged. The Y motor values from now on are not comparable to these alignment results.

The tests with N_2 confirm that the optics are still functional after being moved from H6 and installed in NA62, so it is decided to proceed with the next phase, filling the CEDAR vessel with H_2 and performing a full alignment. The final alignment must be completed with H_2 as it is possible that results would differ due to the misshapen rings caused by using N_2 in CEDAR-H.

The CEDAR-H is filled with H_2 to 4.3 bar where a small pressure scan is conducted to find the best value to collect Cherenkov light from the proton. The pressure is adjusted by ± 0.2 bar and the light yield is recorded. The maximum light yield is found at a pressure of 4.3 bar.

An alignment is conducted at a diaphragm aperture of 6 mm to allow the light

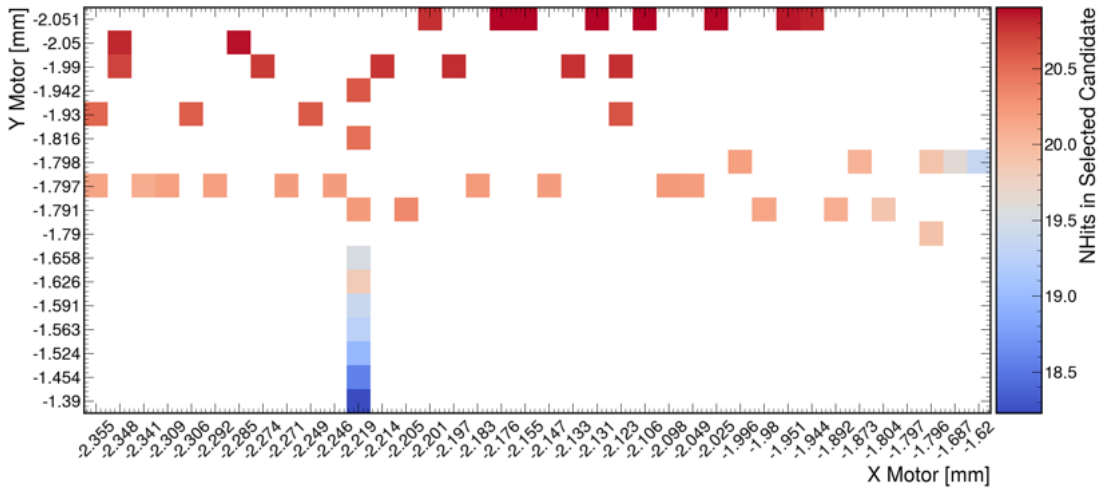

Figure 3.28: Results of the alignment of CEDAR-H with N_2 at the start of NA62 2022 run, at a diaphragm aperture of 1.45 mm and a pressure of 2.031 bar.

produced from protons only. This allows for a course alignment, where the motors are moved until the number of photo-electrons on each sector are balanced. The results of the alignment are shown in Figure 3.29. At the start of the alignment the CEDAR-H is in the position of $X = -2.144$ mm and $Y = -2.025$ mm, where a proton candidate has, on average, 15.58 photo-electrons. The Y motor position is modified, increasing by around 0.1 mm and then stopping to take a number of measurements to increase the number of events collected. This is repeated, which results in the number of photo-electrons per proton candidate increasing. The maximum photo-electrons of 21.07 is achieved at $Y = -0.725$ mm. To ensure that this is the maximum point, the Y motor is moved until the number of photo-electrons decreases. When this occurs, the detector is moved back to the previous maximum. The X motor position is moved in both the positive and negative direction to find the maximum number of photo-electrons. It is found that the detector is aligned in the X dimension in its original state, so the X motor is returned to its original position. The final position of the CEDAR-H is $X = -2.144$ mm and $Y = -0.725$ mm, resulting with the average number of photo-electrons per proton candidate of 21.07.

The first pressure scan is completed with a diaphragm aperture of 1.8 mm. The pressure is set above the proton pressure at 4.4 bar and the pressure is slowly decreased as data is recorded. The data is reconstructed using a 4 ns time window,

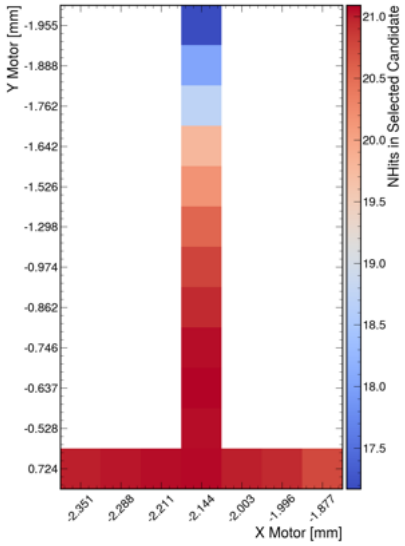

Figure 3.29: Results of the first alignment of CEDAR-H with H_2 at the proton pressure of 4.3 bar with a diaphragm aperture of 6 mm.

with the results shown in Figure 3.30. Compared to the test-beam, the y-axis of Figure 3.30 is arbitrary as the total number of triggers is not recorded. Instead, the number of coincidences is normalised to the beam intensity, which in NA62 is measured through counts in an argonion chamber detector located at the end of the experiment. This made the direct beam composition difficult to calculate, but the ratios of the three peaks are used to check if the composition is what was expected. Figure 3.30 shows the proton pressure at 4.3 bar and the kaon pressure at 3.88 bar. At the kaon pressure the maximum light yield corresponds to 21.71 ± 0.02 photo-electrons per kaon candidate. The kaon pressure in NA62 is higher than what was found at the test-beam, 3.88 bar compared to 3.85 bar due to a 2 K temperature difference of the radiator gas in ECN3. The pion pressure can not be precisely determined due to the large flux of pions in the beam which overwhelms the NA62 readout system, producing inconsistent results between 3.68 and 3.76 bar. However, the falling edge of the pion peak is not effected, allowing for the estimation of the pion misidentification probability. At the kaon pressure of 3.88 bar the measured normalised 5-fold coincidence value is 0.0956 (see Figure 3.30). The estimated pion contribution to the normalised 5-fold coincidence is 5.36×10^{-6}. The pion misidentification probability is estimated from the ratio of the kaon and pion contribution,

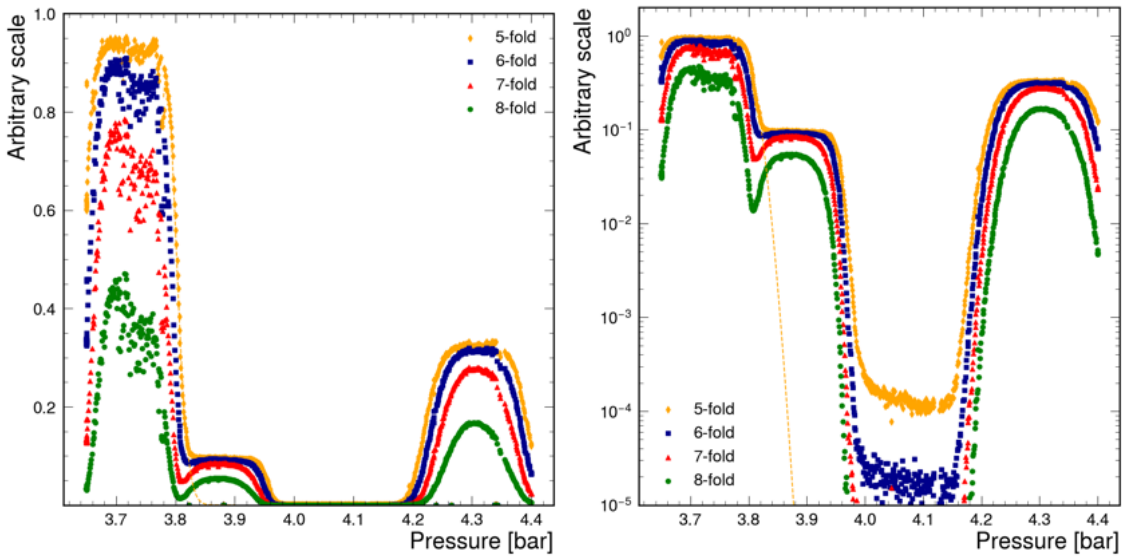

Figure 3.30: Pressure scan of CEDAR-H with H_2 at a diaphragm aperture of 1.8 mm.

and is found to be 0.6×10^{-5} at the kaon pressure.

The light yield obtained with a 1.8 mm diaphragm aperture compared with the results from the test-beam at a 2 mm aperture (Figure 3.20), produces an increase of over 10 %. This increase is due to the addition of the KTAG photon-detection system compared to the single PMTs used in the test-beam.

The photo-electrons per candidate and pion misidentification probability suggests that a diaphragm aperture of 1.8 mm is the best candidate for operation as it fulfils all the requirements for operation at NA62. A final alignment is conducted at the selected operational aperture. The diaphragm is kept at 1.8 mm and the alignment procedure is repeated. The smaller diaphragm allowed for a fine alignment, with the diaphragm aperture being only just wide enough for the single ring from the kaon to pass through. The results of the alignment are shown in Figure 3.31, where the vessel is moved in both X and Y directions to produce a 2D map of motor positions and the corresponding average number of photo-electrons per candidate. The motor position where the maximum light yield is found to be at $X = -2.258$ mm and $Y = -0.591$ mm with an average of 21.68 ± 0.01 photo-electrons per kaon candidate. A pressure scan is completed across the pion and kaon peak with a diaphragm aperture of 1.5 mm with the results shown in Figure 3.32. The separation compared to the previous pressure scan in Figure 3.30 is greater, with the pion contribution to the 5-fold coincidence estimated to be consistent with a zero misidentification prob-

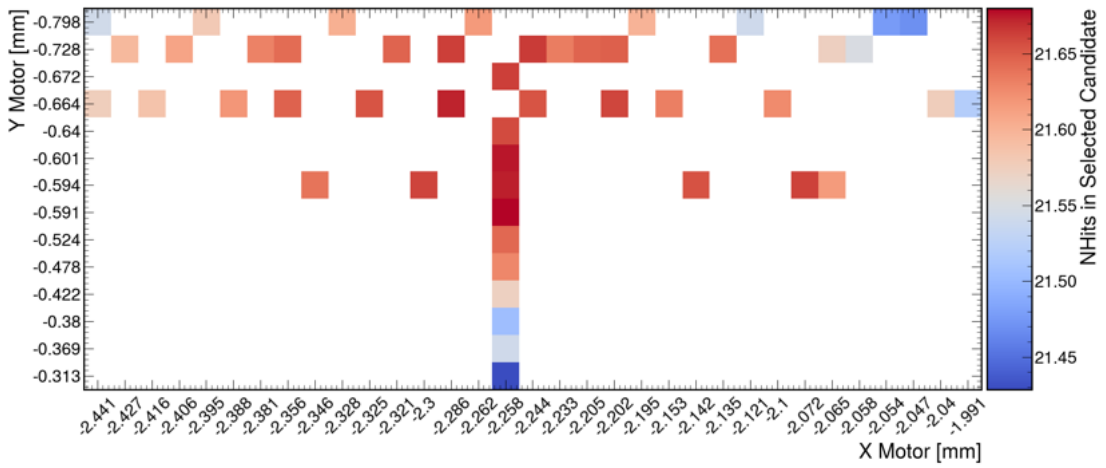

Figure 3.31: Results of alignment of CEDAR-H at the kaon pressure of 3.88 bar with a diaphragm aperture of 1.5 mm.

ability. However, the number of photo-electrons per kaon candidate is 21.47 ± 0.04, a lower light yield compared to the previous pressure scan completed with a 1.8 mm diaphragm aperture.

The results show that the CEDAR-H is operational in NA62 and is able to separate the kaon and pion peaks with a high level of confidence. It is decided that the pressure scan from the 1.8 mm diaphragm aperture produces the best results for use at NA62 due to the superior light yield, resulting in a better kaon identification efficiency. The pion misidentification probability is estimated to be less than 10^{-4}, which is acceptable for use at NA62.

A diaphragm scan is completed to quantify the light yield with respect to the aperture, where the diaphragm is varied between 0 and 6.5 mm. The results are shown in Figure 3.33. As the diaphragm is opened, the number of coincidences increases as the Cherenkov light from the kaon pass through the aperture, maximising at 1.75 mm, smaller than the selected diaphragm for operation set above. The number of coincidences are stable up to 2.75 mm where the 5-fold coincidences become sensitive to the light from the pion.

After the successful commissioning of CEDAR-H in NA62, the operational parameters for the 2023 run are as follows:

- alignment: $X = -2.258$ mm and $Y = -0.591$ mm;

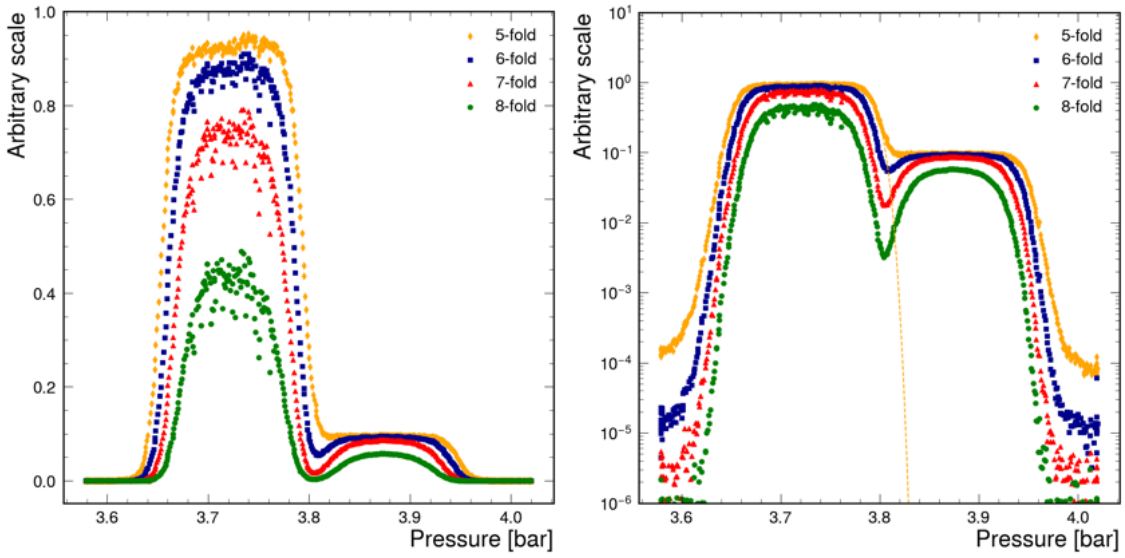

Figure 3.32: Pressure scan of CEDAR-H with H_2 at a diaphragm aperture of 1.5 mm.

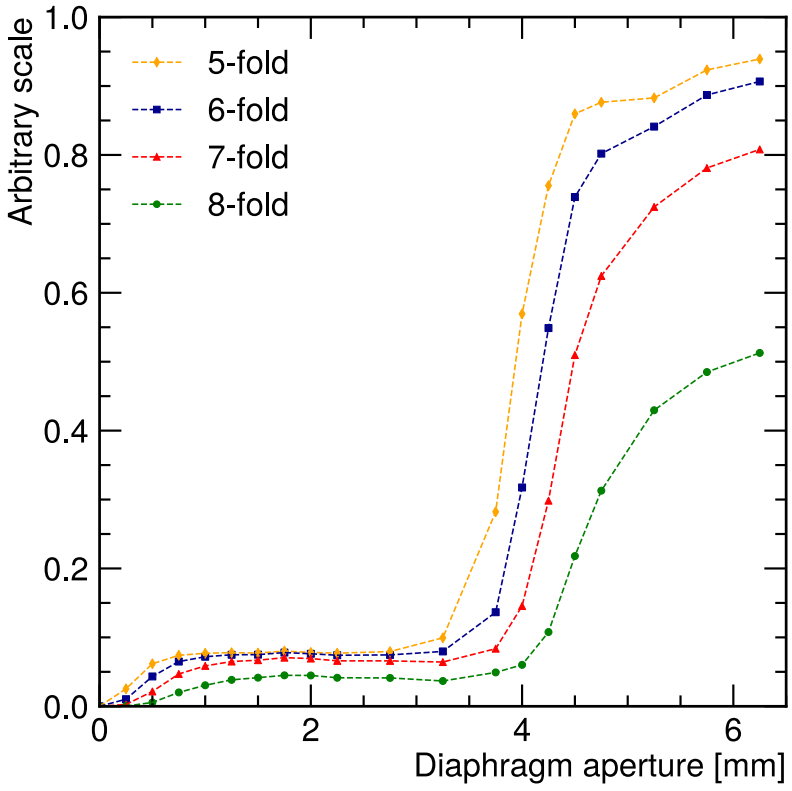

Figure 3.33: Results of diaphragm scan taken at 3.88 bar.

- kaon pressure: 3.88 bar;
- diaphragm aperture: 1.8 mm.

The commissioning procedure described above is extensive but is required due to the new detector installation in 2023. At the start of each data taking run, the

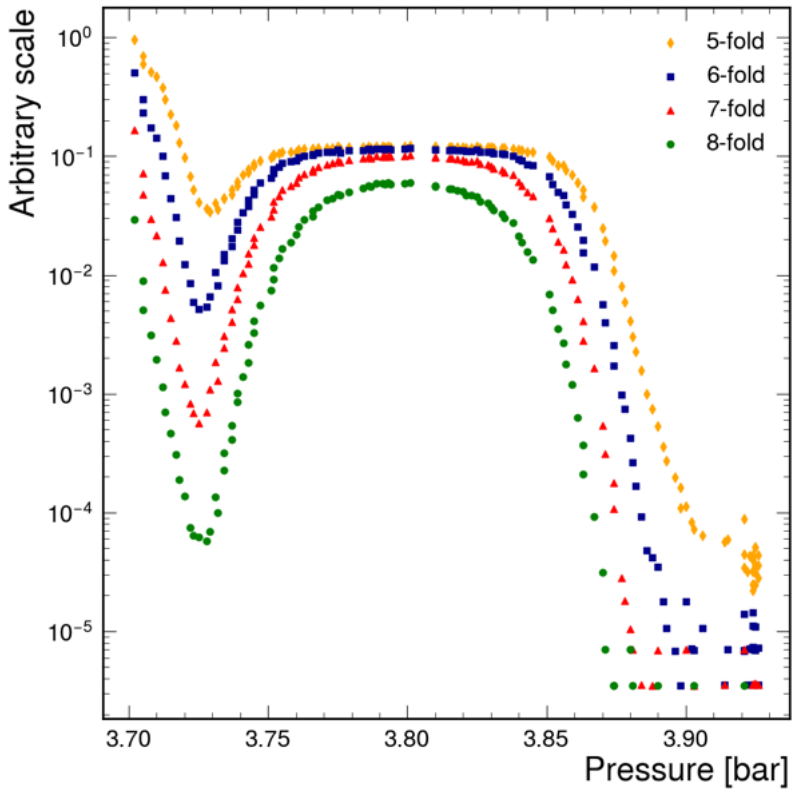

Figure 3.34: Results of CEDAR-H pressure scan at the start of NA62's 2024 run with a diaphragm aperture of 1.5 mm.

commissioning has to be repeated with alignment and pressure scans to ensure the detector is still operational and to find the working point for the run. Though the detector does not move between years, the beam position can move compared to previous years. Slight movements of the vessel can be possible at each H_2 filling due to possible deformation of the beam-pipe when the detector is brought in and out of vacuum. Also, it is possible that the pressure set points for the beam particles could differ due to the environmental changes in ECN3.

For example, the commissioning of the CEDAR-H in 2024, with the pressure scan of the kaon peak shown in Figure 3.34, shows that the environmental changes in ECN3 impact the set pressure points for the beam particles. The kaon pressure is found to be 3.81 bar, which is 0.07 bar lower than the previous year. This change is acceptable at the start of the run when the detector working point is set during the commissioning time, but whilst taking data, the conditions are monitored to ensure that the light yield for the kaons is at its maximum. Due to the changes to the working point pressure between the test-beam and between the 2023 and 2024 runs,

a new method is developed to monitor the CEDAR-H and to take into account the environmental variables to ensure the refractive index of the radiator gas does not change by large amounts which would result in lower kaon detection efficiency. The pressure of the vessel and temperature at both the front and back of the CEDAR are recorded and shown in Figure 3.35 for the 2023 run and Figure 3.36 for the 2024 run. The pressure is divided by temperature (p/T), as the ratio should be consistent for a sealed vessel like the CEDAR, and the ratio is multiplied by a room temperature of 293.15 K, resulting in the pressure at normalised room temperature. Even though the CEDAR is extensively insulated, it is designed to mitigate sharp temperature changes. However, the insulation does not stop the CEDAR vessel from slowly changing temperature with the environment due to seasonal variations. To mitigate this, the CEDAR is sealed with a fixed amount of gas and the pressure is allowed to vary. While operating with the CEDAR-W with N_2 it is possible to operate without monitoring due to minimal gas leakage from the vessel. However, for CEDAR-H it is now essential to monitor the p/T due to the increased leakage of the H_2 gas from the vessel.

An example of how the p/T method is utilised is in the final days of the 2023 run in Figure 3.35 where the actual pressure increased by nearly 10 mbar, whereas the normalised pressures stay constant, suggesting that the temperature in ECN3 increased, reinforcing that the pressure should not be automatically maintained at a fixed pressure. However, as CEDAR-H is not perfectly sealed, especially for H_2, a small leak is expected, so there is a gradual decrease in the normalised pressure. The normalised pressure and the resultant number of photo-electrons per candidate are used to decide if the CEDAR requires extra filling during the run due to the small loss of gas, which can be seen in Figures 3.35 and 3.36 as the large spikes in pressure at various points.

3.6 CEDAR-H Performance at NA62

The performance of the CEDAR-H in standard NA62 run conditions is assessed using data collected in 2023 and compared to CEDAR-W with data collected in 2022. A sample of kaons is collected using a selection of $K^+ \to \pi^+\pi^+\pi^-$ decays

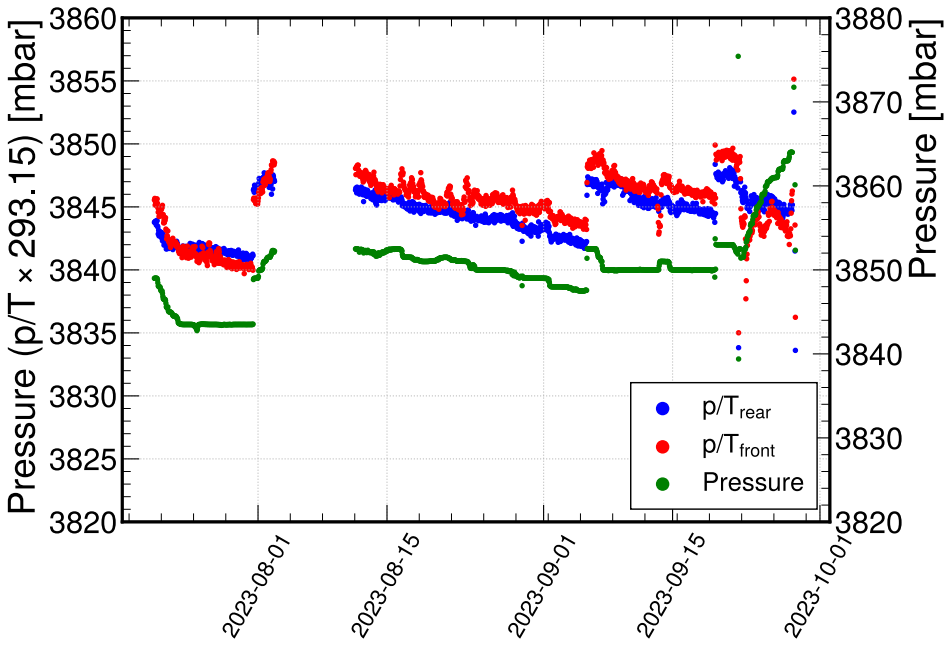

Figure 3.35: The recorded pressure and pressure over temperature times room temperature for CEDAR-H during the 2023 NA62 run.

fully reconstructed using the STRAW spectrometer, described in Section 2.3.4. The KTAG is used to reconstruct the kaon candidates using a nominal 2 ns clustering time window. The number of photo-electrons per kaon is measured from events that have at least a five-sector coincidence, and the results are shown in Figure 3.37. The light yield is calculated by fitting a Poissonian distribution between 4 and 24 photo-electrons. The fitting range is selected to remove the contributions from the large number of photo-electrons, produced from secondary kaons in coincidence, reconstructed as a single kaon. The average light yield for the CEDAR-H is 20.6 photo-electrons per kaon compared to 18.1 for CEDAR-W. The estimated time resolution of the KTAG + CEDAR-H is calculated to be 66 ps using the equation,

$$\sigma_t = \frac{\sigma_{PMT}}{\sqrt{N_{PE}}} \tag{3.11}$$

where σ_{PMT} is the single photo-electron time resolution of the PMTs of 300 ps, and N_{PE} is the number of photo-electrons per candidate, compared to 71 ps for CEDAR-W.

The kaon tagging efficiency is calculated by comparing the number of N-Fold coincidences against the total number of expected kaons. The results of the com-

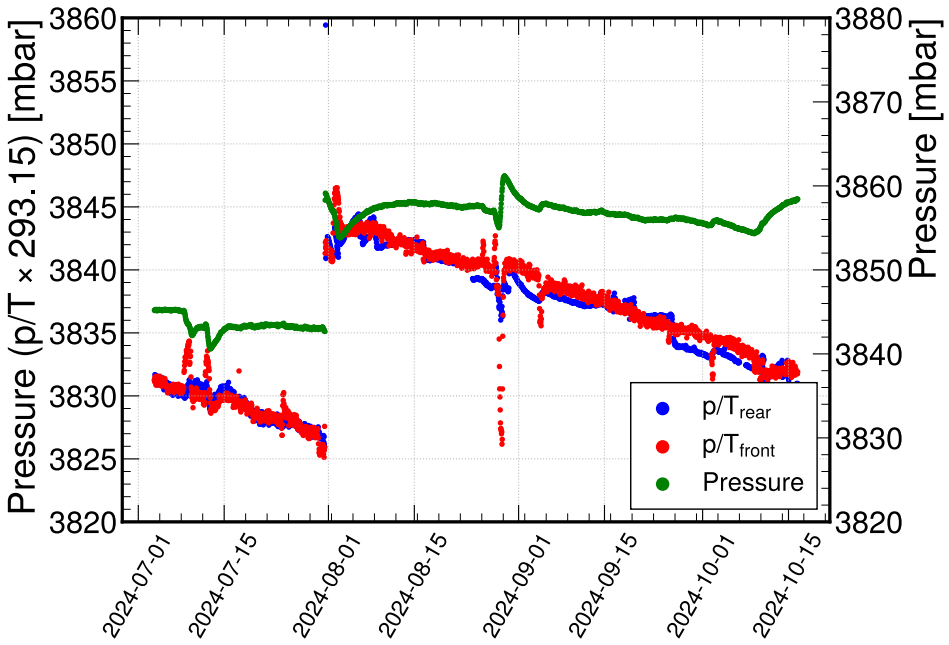

Figure 3.36: The recorded pressure and pressure over temperature times room temperature for CEDAR-H during the 2024 NA62 run.

putation are shown in Figure 3.38, with CEDAR-H having a kaon identification efficiency of 99.7 % compared to 99.5 % for CEDAR-W. The identification efficiency is compared to the analytical expectation with the photo-electron yield produced from Figure 3.37, calculated assuming an ideal detector and uniform photo-electrons across all eight sectors. The results for both detectors show that the eight sector efficiencies are higher than the expectation due to the contribution from secondary kaons in coincidence.

3.7 Conclusions

The CEDAR-H detector was successfully tested at a test-beam at CERN in 2022 and was approved for use at NA62. The detector was installed at NA62 in 2023 where it was commissioned and an operational working point for kaon detection was set with the following parameters,

- Kaon pressure: 3.88 bar,
- Diaphragm aperture: 1.8 mm.

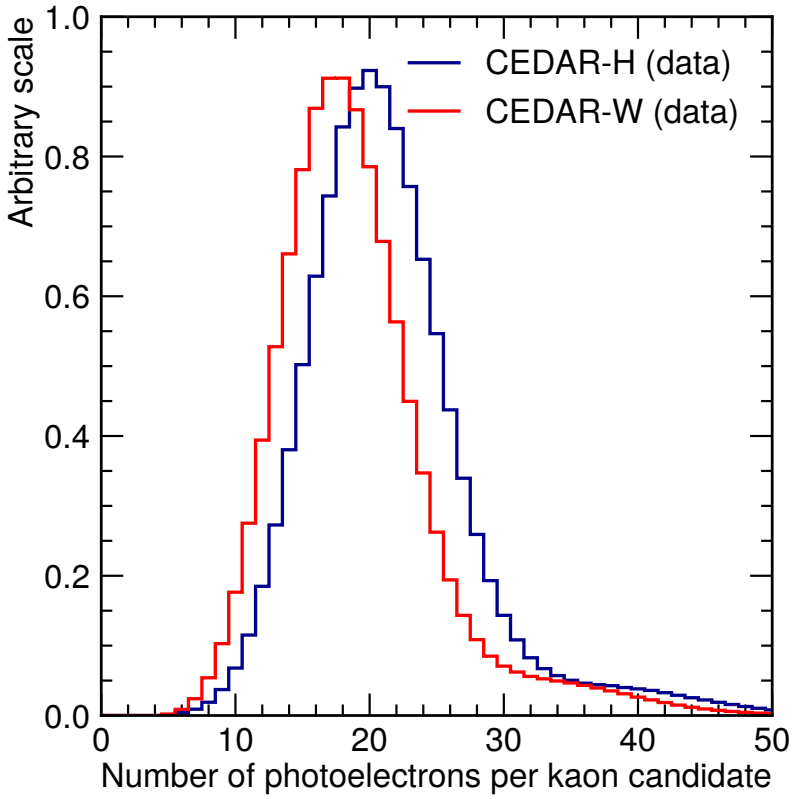

Figure 3.37: Comparison of the number of photo-electrons per kaon candidate of CEDAR-H in 2023 and CEDAR-W in 2022.

At this working point the CEDAR-H obtained an average number of 20.6 photo-electrons per kaon candidate at NA62, a 14 % increase with respect to CEDAR-W with an estimated pion misidentification probability of at least 10^{-4}. The light yield represented a kaon identification efficiency of 99.7 % and a kaon time resolution of 66 ps. The improvement of CEDAR-H compared to CEDAR-W represented a successful design, testing and commissioning of the detector for use at NA62.

The CEDAR-H has been in operation since 2023 and has performed reliably and has exceeded the requirements for NA62.

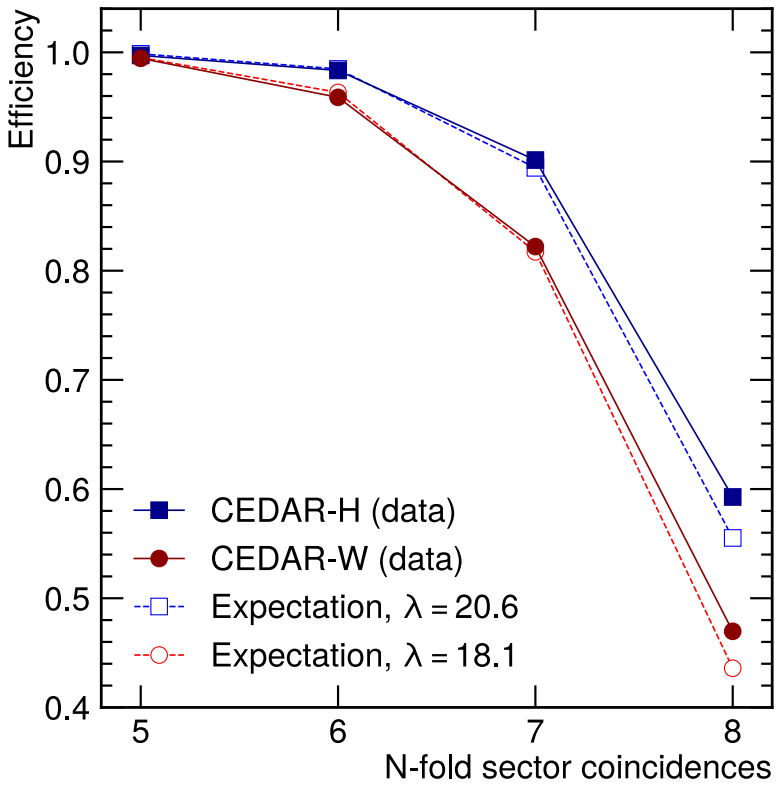

Figure 3.38: Comparison of the number of kaon identification efficiency for CEDAR-H in 2023 and CEDAR-W in 2022 with the expectation values for a given photo-electron yield as a function of at least N coincidences in sectors.

Chapter 4

Search for the Dark Photon in π^0 decays at NA62

This chapter describes the search for the Dark Photon (DP), also denoted A', at NA62 with the data collected in 2022–2024. It outlines the selection criteria for the analysis and provides the acceptances at NA62. The search strategy for the DP is then presented, followed by two different methods used to estimate the background. The first method relies on Monte Carlo (MC) simulations to model the background. However, due to large statistical uncertainties associated with the MC, a second method is introduced, which uses the side bands of the observed data to model the background. Both background methods are used as inputs in the DP method to produce two separate results for the analysis.

The analysis aims to set limits on the mixing parameter of the DP, utilising production through the decay of $\pi^0 \to \gamma A'$ and subsequent prompt decay into Standard Model (SM) particles $A' \to e^+e^-$. The theoretical background for this hypothetical DP is described in Section 1.4. The NA62 experiment, described in Section 2, provides a clean sample of π^0 particles through the decay $K^+ \to \pi^+\pi^0$ with a branching ratio of 20.67 %. With the assumption that the DP decays promptly, the decay signature is identical to the π^0 Dalitz decay $\pi^0_D \to \gamma e^+e^-$. The Dalitz decay represents the background for the DP search and determines the sensitivity.

By definition, the dark photon is the mediator of the vector portal [42] and therefore shares the quantum numbers of the SM photon, $J^{PC} = 1^{--}$. As a result the Dalitz decay is used to model the signal. The spin of the A' directly affects the

kinematics and angular distribution of the final-state particles.

4.1 $\boldsymbol{\pi^0_D}$ Event Selection

The selection for the DP search originates from the search at NA48/2 [44]. The $K \to \pi^+\pi^0_D$ ($K_{2\pi D}$) decay has the same event signature as the production and prompt decay of the DP. The event selection comprises the identification of the π^+, e^-, e^+ and γ.

4.1.1 Vertex Selection

- It is required that at least one of the following trigger conditions is satisfied: the Control Trigger (also referred to as the Minimum Bias Trigger), the Multi-Track (MT) trigger, or the electron Multi-Track (eMT) trigger, described in Chapter 2.

- A single three-track vertex is required. The vertex must have a total momentum below 78 GeV/c, a total positive charge of $Q = 1$, a vertex fit $\chi^2 < 40$, and a position within the range 105 m $< Z_{\text{vtx}} <$ 180 m.

- The tracks within the vertex are checked if they are in acceptance of all four STRAW spectrometer chambers and the CHOD. The track momentum must be 5 GeV/$c < p <$ 60 GeV/c with $\chi^2 < 30$. The tracks must traverse the first STRAW chamber with separations of 20 mm from each other.

- A selected photon is required. The missing vertex momentum of the vertex is used to extrapolate a straight line from the vertex position to the Z-plane of the LKr calorimeter. The missing momentum is the difference between the kaon 3-momentum and the total vertex 3-momentum. Within a radius of 15 cm of the extrapolated position, a single Liquid Krypton Calorimeter (LKr) energy deposit with a minimum energy of 5 GeV is required and is considered as the photon candidate. The photon energy must be within 5 GeV of the missing vertex momentum.

4.1.2 Kinematic PID

The three-track vertex is required to consist of a positively charged pion (π^+), an electron and a positron ($e^\pm$). The pion is identified among the two positively charged tracks using the missing mass between the kaon 4-momentum and the track 4-momentum,

$$M^2_{miss} = (P_{K^+} - P_{\pi^+})^2. \tag{4.1}$$

If the missing mass is consistent with the π^0 mass hypothesis, the track is identified as a charged pion. The cut on M_{miss} is calculated using a $K_{2\pi D}$ MC sample and is shown in Figure 4.1. The width of the distribution is found to be

$$\sigma = (10.30 \pm 1.43)\,\mathrm{MeV}/c^2, \tag{4.2}$$

which results in the cut $|M_{miss} - M_{\pi^0}| < 5\,\sigma = 51.5\,\mathrm{MeV}/c^2$. If both positive tracks satisfy the condition, the event is vetoed. According to simulations, approximately 0.1 % of $K_{2\pi D}$ decays have both positively charged tracks satisfying the charged pion selection criteria. The positive track which does not pass the charged pion selection is identified as the positron. The electron is identified as the negative track.

An elliptical cut on the reconstructed masses $M_{ee\gamma}$ and $M_{\pi ee\gamma}$ is defined using a $K_{2\pi D}$ MC sample. An elliptical cut is required in order to account for the correlated uncertainties in the reconstructed masses $M_{\pi ee\gamma}$ and $M_{ee\gamma}$. This allows for efficient signal event selection while suppressing background contributions. The elliptical cut is defined as

$$\frac{((x - x_c)\cos\theta + (y - y_c)\sin\theta)^2}{a^2} + \frac{((y - y_c)\cos\theta - (x - x_c)\sin\theta)^2}{b^2} \leq 1 \tag{4.3}$$

where x_c and y_c are the coordinates of the ellipse centre. The θ is the angle of rotation of the ellipse, and a and b are the lengths of the semi-major and the semi-minor axis, respectively. For the candidate event $x = M_{\pi ee\gamma}$ and $y = M_{ee\gamma}$. The parameters are selected to produce a selection efficiency of 95 %. The parameters for the ellipse are defined below:

- $x_c = 493.677\,\mathrm{MeV}/c^2$: the x-coordinate of the ellipse centre (nominal K^+ mass).
- $y_c = 134.977\,\mathrm{MeV}/c^2$: the y-coordinate of the ellipse centre (nominal π^0 mass).

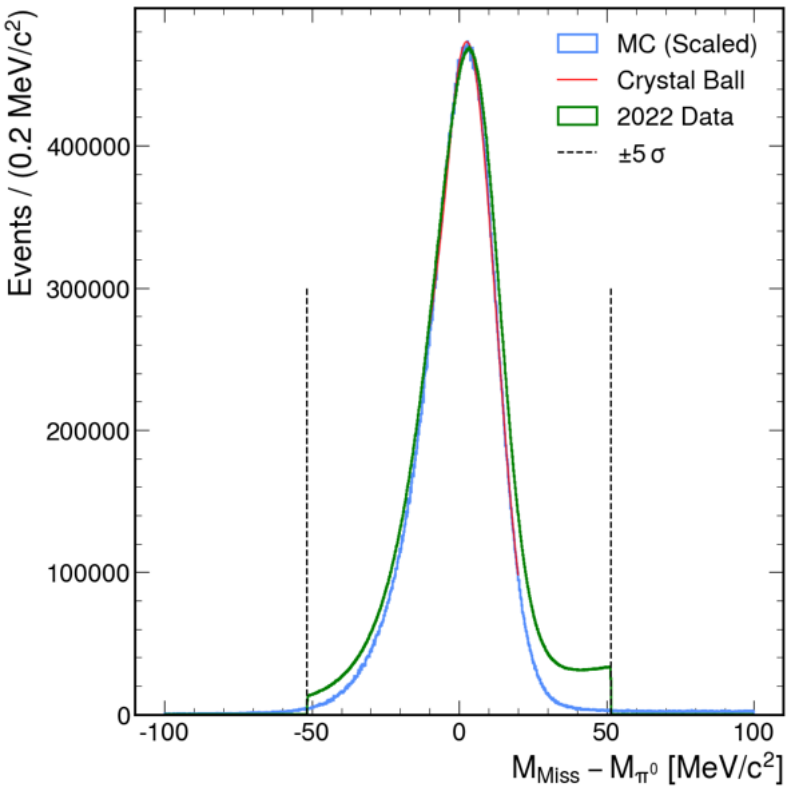

Figure 4.1: Reconstructed missing mass of kaon and charged pion compared to the known neutral pion mass. The blue distribution is the $K_{2\pi D}$ MC sample, fitted with a Crystal Ball function in red. This is compared against the 2022 data in green after the selection of the charged pion. The Crystal Ball function is a function that models a Gaussian peak with a power-law tail on one side. To ensure the correct particles are selected for the MC distribution the true MC information is used. The MC sample is scaled to match the number of events in the data. The data distribution is taken from the missing mass produced from selected pion track.

- $a = 40\,\mathrm{MeV}/c^2$: the semi-major axis of the ellipse.
- $b = 6\,\mathrm{MeV}/c^2$: the semi-minor axis of the ellipse.
- $\theta = 0.4887\,\mathrm{rad}$: the angle of rotation of the ellipse.

When utilised in Equation 4.3, the parameters described above produce an ellipse shown in Figure 4.2.

4.1.3 Selection Acceptance

The main trigger line for the analysis is the eMT. As described in Section 2.4 the eMT line contains the E20 L0 condition which requires at least 20 GeV to be deposited in the LKr. However, the selection uses kinematic Particle Identification (PID) to

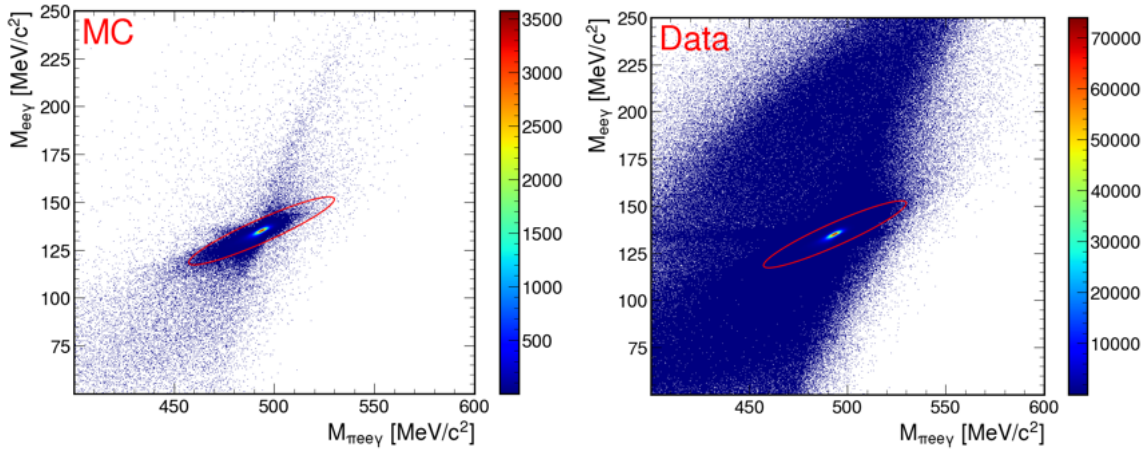

Figure 4.2: Reconstructed mass $M_{\pi ee\gamma}$ vs $M_{ee\gamma}$, from a $K_{2\pi D}$ MC sample on the left and 2022 data on the right, with the elliptical cut used in the selection.

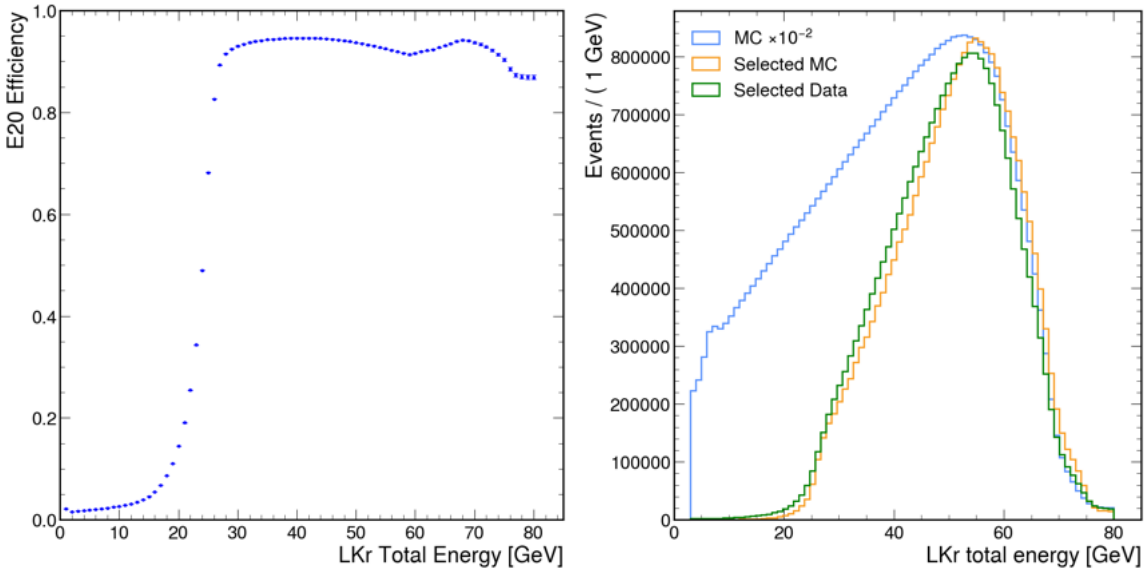

Figure 4.3: Left: The efficiency of the E20 trigger condition for the $K_{2\pi D}$ MC sample as a function of the total LKr energy before the selection. Right: Total LKr energy deposited for all (blue) $K_{2\pi D}$ MC events. Also shown is the selected $K_{2\pi D}$ events from MC (orange) and 2022 data (green). The E20 efficiency is calculated using the number of events passing the E20 trigger emulator divided by the total number of $K_{2\pi D}$ decays in the MC.

identify the charged pion, electron and positron. The efficiency of the E20 trigger condition for $K_{2\pi D}$ decay before the selection is measured with MC at 70.7 % and is shown as a function of total LKr energy in Figure 4.3. The total LKr energy deposited for the selected $K_{2\pi D}$ MC and 2022 data is also shown. The MC sample is scaled to match the number of events in the data.

The acceptance of the selection for the $K_{2\pi D}$ MC sample as a function of M_{ee} is

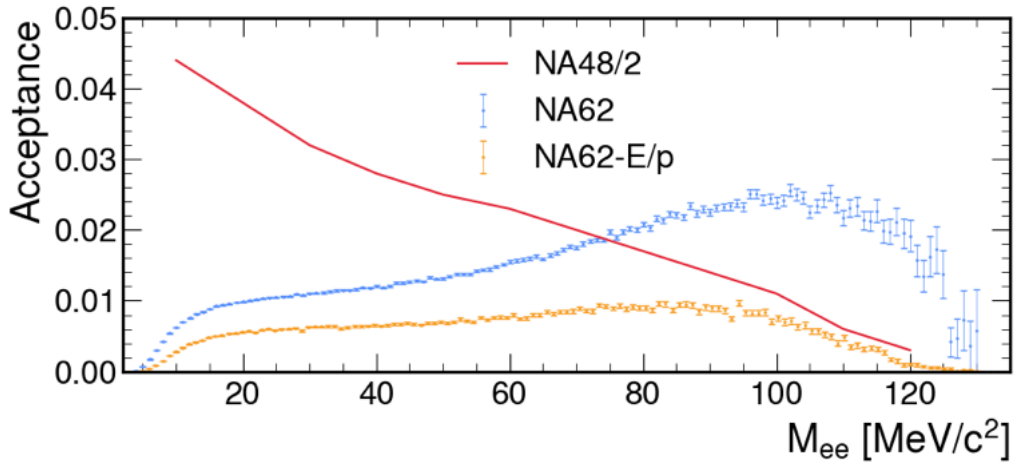

Figure 4.4: Acceptance for the $K_{2\pi D}$ decay with the NA62 selection with E/p PID and kinematic PID in M_{ee} bins, compared against the acceptance from the NA48/2 analysis [44].

compared against the acceptance of the NA48/2 analysis [44] in Figure 4.4. The acceptance is calculated from the number of events passing the selection divided by the number of events in the $K_{2\pi D}$ MC sample which decay within $105\,\text{m} < Z_{\text{vtx}} < 180\,\text{m}$. The difference between the selections used for the NA62 and the NA48/2 study is the PID. The study at NA48/2 uses calorimetric PID where the LKr is utilised to reconstruct the energies of the pion, electron and positron. The reconstructed energy to momentum ratio is used to distinguish between the pion and positron. In the NA62 study, PID uses the track momentum measurements to reconstruct the invariant masses, which are compared against the nominal PDG masses [12]. This approach is driven by the difference in experimental setup between NA48/2 and NA62. The NA62 setup is longer, as it requires enhanced PID satisfied by the Ring Imaging Cherenkov counter (RICH), and improved momentum measurements provided by the longer spectrometer. This results in the LKr placed further from the decay volume, reducing the acceptance of the $K_{2\pi D}$ decay at NA62 compared to NA48/2. The LKr is used in the analysis to reconstruct the photon energy only.

The impact of the different experimental setups is apparent at low M_{ee} where NA48/2 has an acceptance advantage. A study is conducted to test if the calorimetric PID could produce competitive results at NA62, with results shown in Figure 4.4. The calorimetric PID acceptance is worse compared to the kinematic PID method used for this study, across the M_{ee} spectrum.

The $K \to \pi^0_D \mu^+ \nu_\mu$ ($K_{\mu 3D}$) decay mode is essential to include as it passes the

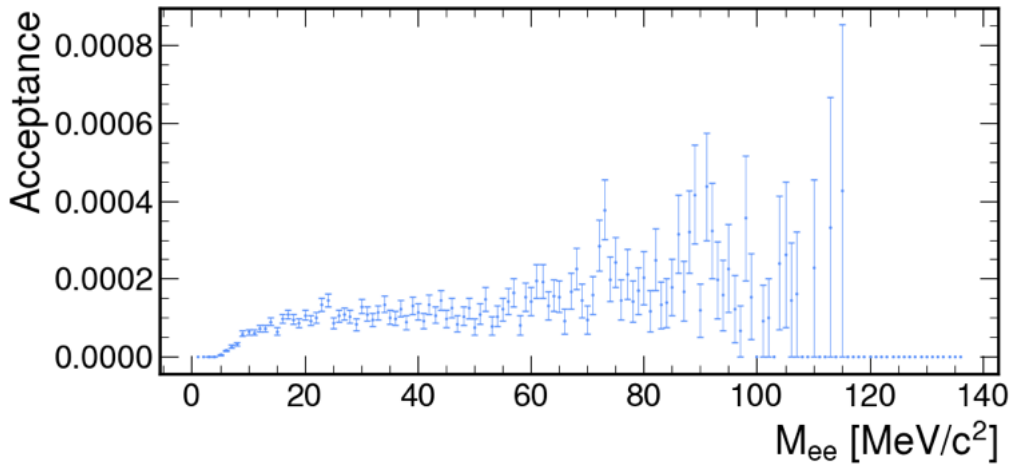

Figure 4.5: Acceptance for the $K_{\mu 3D}$ decay with the NA62 selection in M_{ee} bins.

MC Sample	Acceptance	Branching Ratio
$K_{2\pi D}$	$(0.59 \pm 0.01)\,\%$	$(0.243 \pm 0.007)\,\%$
$K_{\mu 3D}$	$(5.47 \pm 0.11) \times 10^{-5}$	$(3.94 \pm 0.12) \times 10^{-4}$

Table 4.1: Acceptances of $K_{2\pi D}$ and $K_{\mu 3D}$ samples for the $K_{2\pi D}$ selection. The branching ratios for both decays are shown [12]. The errors on the acceptances are statistical only.

$K_{2\pi D}$ selection when the μ is misidentified as a pion, contributing to the signal. The acceptance of the selection for the $K_{\mu 3D}$ decay is shown in Figure 4.5. The overall acceptances for the $K_{2\pi D}$ and $K_{\mu 3D}$ decays are shown in Table 4.1.

The MC samples employ trigger emulators provided by the NA62 framework. The inclusion of the trigger emulators results in the trigger efficiencies for both L0 and L1 being accounted for within the acceptances defined in Table 4.1.

4.2 Integrated Kaon Flux

The total number of data events passing the selection for the 2022–2024 dataset is $N_{selected} = 172,222,962$. The effective number of K^+ decays within the Fiducial Volume (FV) is computed as

$$N_K^{2022-24} = \frac{N_{selected}}{A_{2\pi D}\mathcal{B}_{2\pi D} + A_{\mu 3D}\mathcal{B}_{\mu 3D}} = (1.20 \pm 0.05) \times 10^{13}, \tag{4.4}$$

where $A_{2\pi D}$ and $A_{\mu 3D}$ are the acceptances of the $K_{2\pi D}$ and $K_{\mu 3D}$ decays for the $K_{2\pi D}$ selection, shown in Table 4.1 and $\mathcal{B}_{2\pi D}$ and $\mathcal{B}_{\mu 3D}$ are the branching fractions of the

Year	N_K
2022	$(1.67 \pm 0.07) \times 10^{12}$
2023	$(3.24 \pm 0.14) \times 10^{12}$
2024	$(7.02 \pm 0.30) \times 10^{12}$

Table 4.2: Effective numbers of kaon decays for each year of data taking.

$K_{2\pi D}$ and $K_{\mu 3D}$ decay chains [12]. The errors in N_K originate from the statistical uncertainty of the number of selected events, which are negligible, the errors on the acceptance and the external errors on the branching ratios which dominate.

The number of kaon decays in the FV for each year of data taking is shown in Table 4.2. The number of data events passing the selection increased in the 2023 and 2024 datasets compared to 2022 due to the change in downscaling for the eMT trigger from 3 to 1.

Each MC sample is scaled to match the data by a factor

$$f_{scale} = \frac{N_K \times \mathcal{B}_{Decay}}{N_{MC} \times A_{Decay}}, \tag{4.5}$$

where $\mathcal{B}_{Decay}$ is the branching ratio of the decay, N_{MC} is the number of events in the MC sample which decay between $105\,\text{m} < Z_{\text{vtx}} < 180\,\text{m}$ and A_{Decay} is the acceptance of the decay. The reconstructed mass spectra for data and scaled MC events passing the full $K_{2\pi D}$ selection are shown in Figure 4.6.

4.3 DP Search Method

This section describes the DP search method used by both the MC and data-driven background estimation methods. To conduct the DP search, the M_{ee} values must be converted to A' mass hypotheses. The mass resolution is considered when selecting the search window centres and the size of the windows. Each centre corresponds to a specific A' mass hypothesis with a window of a narrow mass range around that centre where a signal would be expected to appear. The mass resolution is calculated using $K_{2\pi D}$ MC, where the difference between the reconstructed and true M_{ee} values is calculated as shown in Figure 4.7. A Gaussian fit is conducted for the $M_{ee}^{Reco} - M_{ee}^{True}$ distribution in each M_{ee}^{True} bin. The width of the Gaussian function

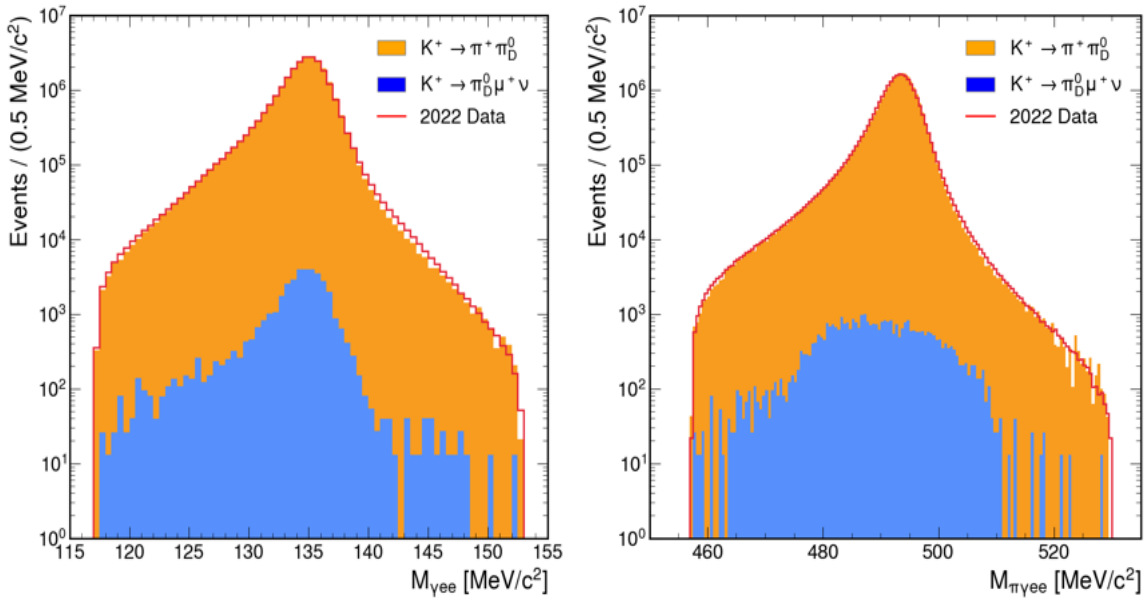

Figure 4.6: Reconstructed mass spectra for $K_{2\pi D}$ and $K_{\mu 3D}$ decays, for MC and data at the end of the selection.

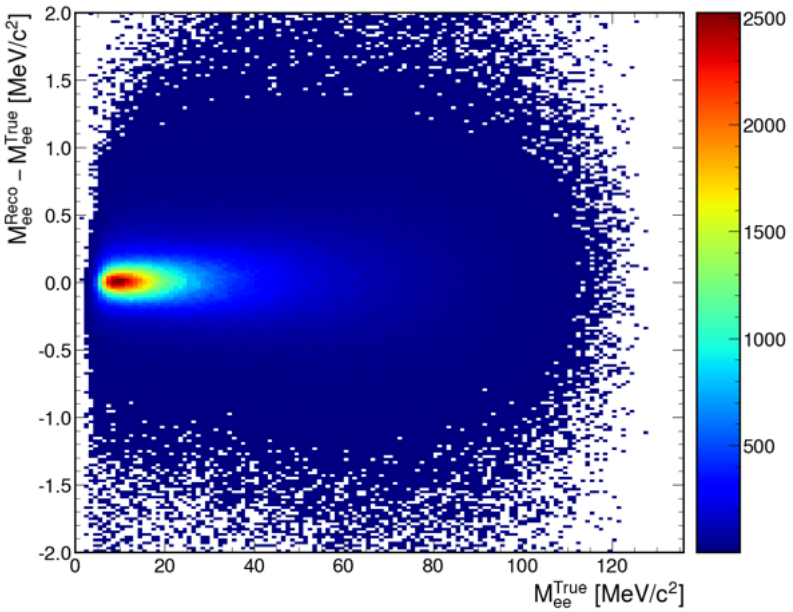

Figure 4.7: Reconstructed invariant mass minus true invariant mass M_{ee} vs true invariant mass.

at each M_{ee} value is used to produce Figure 4.8. A linear function is fitted, resulting in a parametrisation for the mass resolution:

$$\sigma_m(M_{ee}) = 3.76 \times 10^{-2}\,\mathrm{MeV}/c^2 + 5.54 \times 10^{-3} \times M_{ee}. \tag{4.6}$$

Due to the increased spectrometer length and increased B-field, there is a significant improvement in the NA62 resolution compared to NA48/2. The improvement in

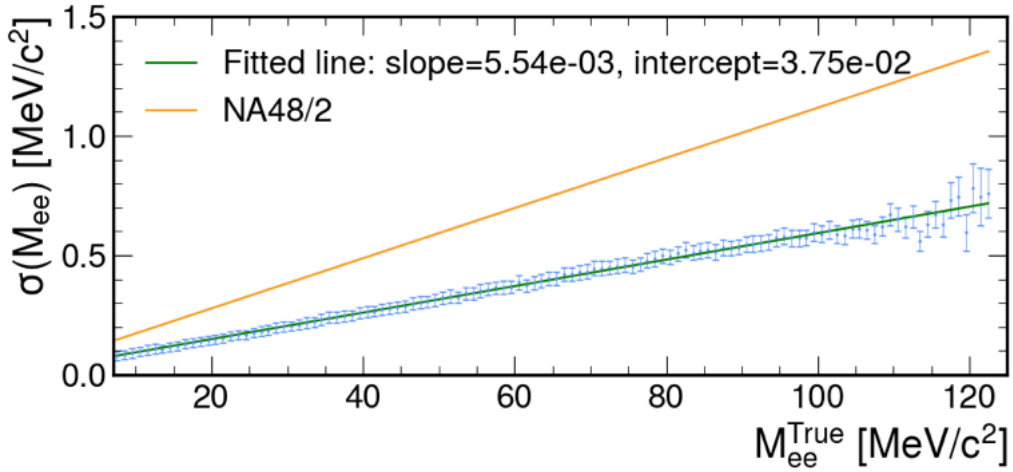

Figure 4.8: Resolution of the reconstructed M_{ee} against M_{ee}^{True}.

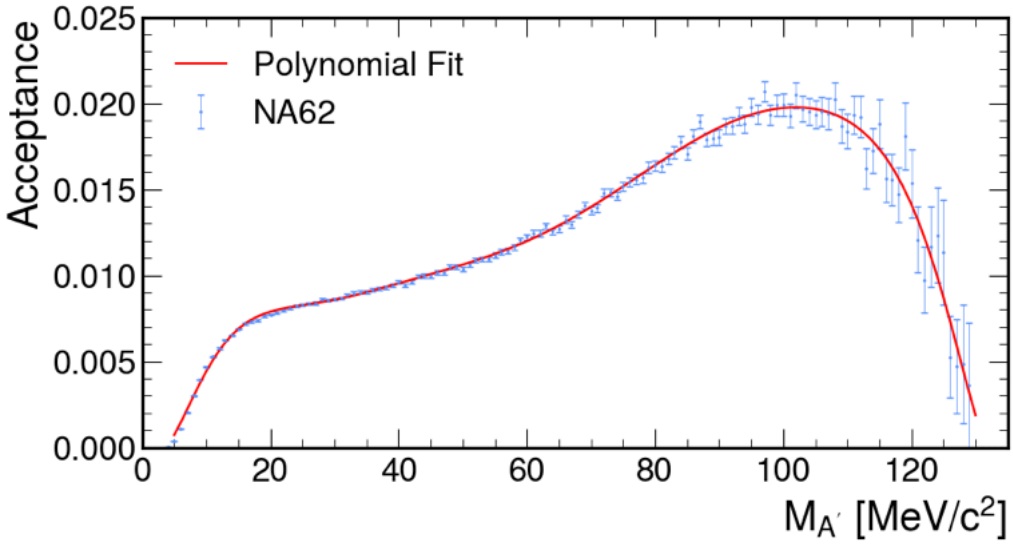

Figure 4.9: Acceptance for DP selection for NA62 across the $M_{A'}$ spectrum.

mass resolution allows for a narrower search mass window compared to the previous study at NA48/2. The window centres are separated by $1\sigma_m(M_{A'})$, with a window width of $\pm 1.5\sigma_m(M_{A'})$ rounded to the nearest $0.01\,\mathrm{MeV}/c^2$.

The DP selection acceptance is calculated using the $K_{2\pi D}$ MC sample in M_{ee} mass bins of $1\,\mathrm{MeV}/c^2$. Each event is checked if it fulfils

$$|M_{ee}^{Reco} - M_{ee}^{True}| < 1.5\sigma_m(M_{ee}^{True}) \tag{4.7}$$

and that it passes the $K_{2\pi D}$ selection. The acceptance is shown in Figure 4.9 as a function of $M_{A'}$. The acceptance is parametrised using a polynomial for later use in the analysis.

For each DP mass hypothesis, the number of data events (N_{obs}) is compared to

the number of expected background events (N_{exp}). The error on the number of observed events δN_{obs}, used for the significance calculation is defined as $\delta N_{obs} = \sqrt{N_{obs}}$. The error on the number of expected events (δN_{exp}) is dependent on the background estimation method. For each DP mass hypothesis, the local significance of the DP signal is calculated as

$$Z = \frac{N_{obs} - N_{exp}}{\sqrt{\delta N_{obs}^2 + \delta N_{exp}^2}}. \tag{4.8}$$

If the local significance is not greater than 3σ, no DP signal is observed. However, as there are a large number of DP mass hypotheses, it is necessary to account for the Look-Elseware Effect (LEE). The LEE is essential, as when searching across many mass hypotheses statistical fluctuations can produce locally significant results. To correct for this, toy MC simulations are generated under the background only hypothesis. For each toy dataset, the maximum local significance across all the tested mass hypotheses is calculated. This yields a distribution of expected fluctuations in the absence of any signal. The observed maximum local significance, calculated using Equation 4.8, is compared against the distribution of fluctuations and a global p-value is computed. The p-value quantifies the probability of observing the maximum local significance from the analysis. This p-value is then converted into a global significance by evaluating the inverse of the standard normal distribution. If the global significance does not exceed $3\,\sigma$, the maximum deviation is not statistically significant and no DP signal is observed.

The Upper Limit (UL) for the number of DP decays ($A' \to e^+e^-$) at a 90% Confidence Level (CL) for each DP mass value is calculated with N_{obs}, N_{exp} and δN_{exp} using the CLs method. This method is recommended by the Particle Data Group [68] and employs the process set out in [69, 70]. For setting an UL of the signal s from a counting experiment where N events are observed (N_{obs}), and there is a known expected background b, it is a hypothesis test between the two cases: signal+background and just background. According to the Neyman-Pearson lemma [71], the most powerful test statistic for the hypothesis is the likelihood ratio,

$$X = L_{s+b}/L_b = \frac{e^{-(s+b)}(s+b)^N}{N!} / \frac{e^{-b}b^N}{N!} = e^{-s}\left(1 + \frac{s}{b}\right)^N. \tag{4.9}$$

It is beneficial to denote the test statistic for the observed data as X_{obs}. A confidence level for the exclusion of the background hypothesis (CL_{s+b}) is the probability that

the test statistic defined in Equation 4.9 is less than or equal to the observed test statistic,

$$CL_{s+b} = P_{s+b}(X \leq X_{obs}). \tag{4.10}$$

To improve the computational efficiency, the test statistic defined in Equation 4.9 used for comparison is simplified to,

$$log(X) = Nlog\left(\frac{s+b}{b}\right). \tag{4.11}$$

The CL is calculated using a MC integration method where a large number of trials are used to calculate the probability defined in Equation 4.10. For each trial, the value N is sampled from a Poisson distribution with a mean of $s+b$. Where b is the background sampled from a normal distribution with a mean equal to the expected number of events (N_{exp}) and width equal to the error on the expected value (δN_{exp}). The test statistic is computed and compared with X_{obs}. The confidence level for the exclusion of the $s+b$ hypothesis (CL_b) is calculated, with N sampled from a Poisson distribution with a mean of b instead of $s+b$. After the trials the modified frequentist confidence level (CL_s) is calculated as,

$$CL_s = CL_{s+b}/CL_b. \tag{4.12}$$

A binary search is then completed using the above method to find the value of s, which satisfies the relation

$$CL_s(s) = 1 - \alpha, \tag{4.13}$$

which would be the UL of the signal for a confidence level of α.

4.4 MC Background Estimation Method

The MC background method is only used for the 2022 dataset, and only the statistical errors on the MC are considered. If the method was to produce competitive result with just the statistical errors, the systematic errors introduced from the MC estimation would be investigated. However, as this is not the case, only statistical errors are included.

As described above, the background for the search for DP comes from the $K_{2\pi D}$ and $K_{\mu 3D}$ decays. These decays are modelled and compared against the data to

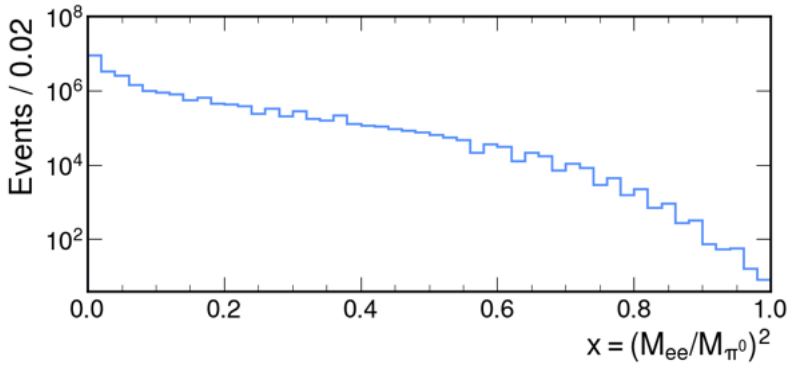

Figure 4.10: kinematic variable x distribution of the $K_{2\pi D}$ MC sample.

determine the sensitivity of the search. The MC samples are produced using the NA62 framework, which simulates the full detector response and the trigger system. The $K_{2\pi D}$ and $K_{\mu 3D}$ samples are produced with 2×10^8 and 5×10^6 events, respectively. The limited size of the MC samples impacts the final result. However, due to computing time, it is not feasible to significantly increase the statistics on the samples. Utilising a feature of the NA62 framework, the statistics across a portion of the reconstructed M_{ee} range are increased. The kinematic variable x is defined as

$$x = \frac{(Q_{e^-} + Q_{e^+})^2}{M_{\pi^0}^2} = \frac{M_{ee}^2}{M_{\pi^0}^2}, \tag{4.14}$$

where Q_{e^-} and Q_{e^+} are the four-momenta of the electron and positron, and M_{π^0} is the mass of the neutral pion. The x distribution is shown in Figure 4.10. The NA62 software framework allows for the simulation of the Dalitz decay only when the kinematic variable $x > 0.5$. From the true MC distribution in Figure 4.10 the fraction of events where $x > 0.5$ is 3.46×10^{-3}. Producing a simulation with the cut on the kinematic variable x with a fraction of the size of the larger sample decreases the statistical errors on the MC. For the rest of the study, the following MC samples are used:

- 200 M $K_{2\pi D}$ ($x < 0.5$) (main);
- 5 M $K_{2\pi D}$ ($x > 0.5$);
- 50 M $K_{\mu 3D}$.

Events with $x > 0.5$ are removed from the main $K_{2\pi D}$ sample at the selection stage.

After the full selection, the MC samples are combined into a single dataset to estimate the background. Using the method described in Section 4.2 for the 2022

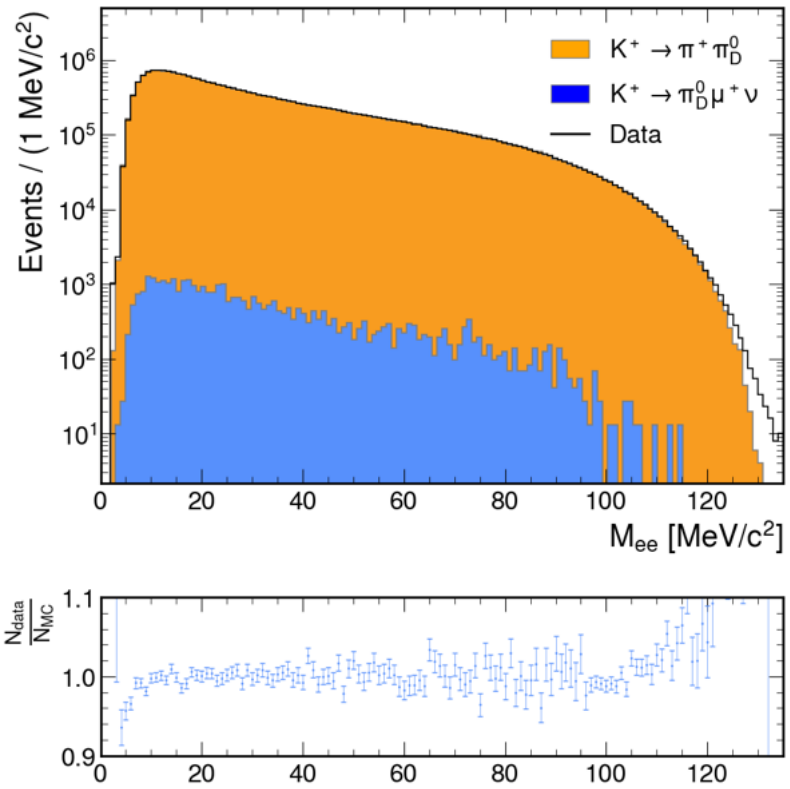

Figure 4.11: Reconstructed M_{ee} spectrum for the 2022 dataset and MC samples and the data/MC ratio. The error bars on the data/MC ratio are from the statistical errors from the MC and the data.

dataset the MC samples are scaled by the factor f_{scale} to match the number of events in the data. The background estimate in M_{ee} bins is shown in Figure 4.11. The numbers of events passing the selection across the M_{ee} spectrum for each MC sample are shown in Figure 4.12. Showing how the two $K_{2\pi D}$ samples have been combined to produce a continuous distribution and shows the contribution from the $K_{\mu 3D}$ decay. The statistical errors on the number of events in each bin are calculated for the MC samples and combined, shown in Figure 4.13. Using the biased $K_{2\pi D}$ $x > 0.5$ MC sample significantly reduces the statistical error of the combined sample compared to only using the main $K_{2\pi D}$ sample.

4.4.1 The π^0 Transition Form Factor

The simulation of the π^0_D decay uses the next-to-leading order (NLO) differential decay width [72]

$$\frac{d^2\Gamma}{dxdy} = \frac{d^2\Gamma^{LO}}{dxdy}(1 + \delta(x, y)), \tag{4.15}$$

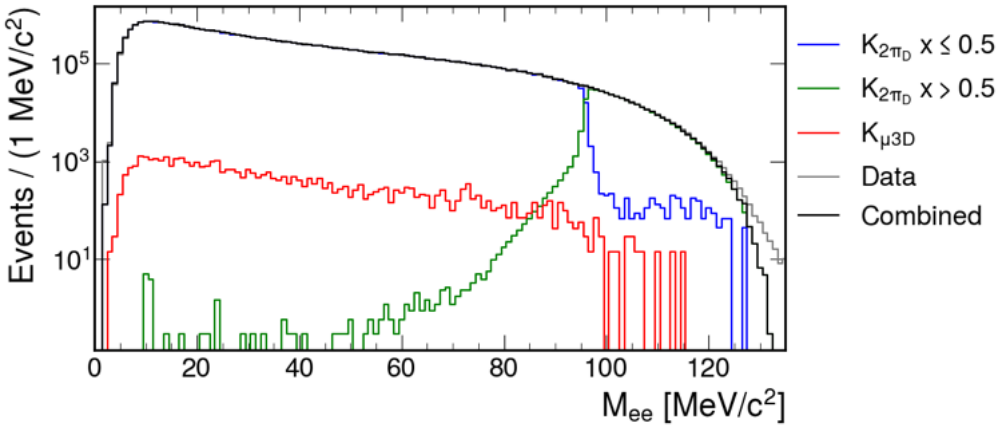

Figure 4.12: M_{ee} spectra for data, individual MC samples and the final combined MC.

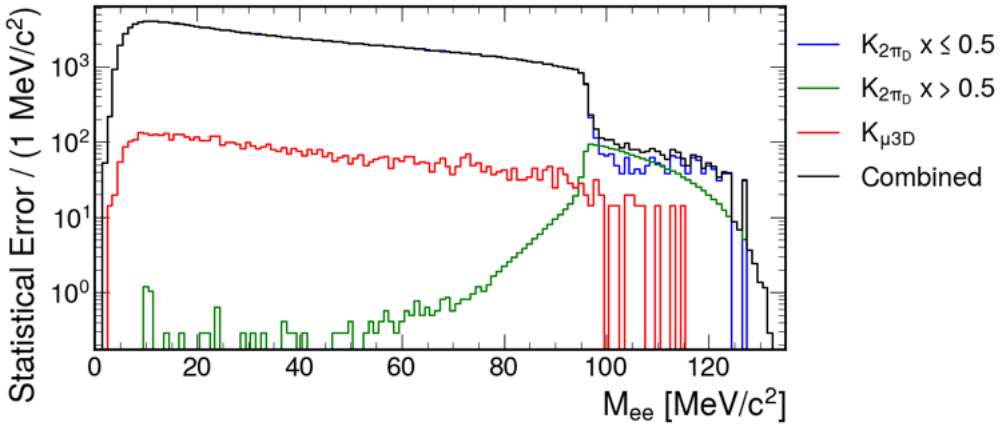

Figure 4.13: Statistical errors for the MC samples in M_{ee} bins.

with $\delta(x, y)$ being a function encoded from the NLO corrections [73, 74, 75]

$$\delta = \frac{d^2\Gamma^{NLO}}{dxdy} / \frac{d^2\Gamma^{LO}}{dxdy} = \delta^{virt} + \delta^{1\gamma IR} + \delta^{BR}, \tag{4.16}$$

where δ^{virt} is from virtual radiative corrections, $\delta^{1\gamma IR}$ one-photon irreducible contribution and δ^{BR} is the bremsstrahlung contribution. The leading-order differential decay width is defined as [74]

$$\frac{d^2\Gamma^{LO}}{dxdy} = \Gamma_0 \frac{\alpha}{\pi} |F(x)|^2 \frac{(1-x)^3}{4x} \left(1 + y^2 + \frac{r^2}{x}\right), \tag{4.17}$$

where Γ_0 is the $\pi^0 \to \gamma\gamma$ decay width, α is the fine-structure constant, $F(x)$ is the pion Transition Form Factor (TFF), x and y are dimensionless kinematic variables,

$$x = \frac{(Q_{e^-} + Q_{e^+})^2}{M_{\pi^0}^2} \quad \text{and} \quad y = \frac{2Q_{\pi^0}(Q_{e^-} - Q_{e^+})}{M_{\pi^0}^2(1-x)}. \tag{4.18}$$

The variables Q_{e^-}, Q_{e^+} and Q_{π^0} are the four-momenta of the electron, positron and pion. Within the kinematic region of $K_{2\pi D}$ decay, the TFF is approximated as

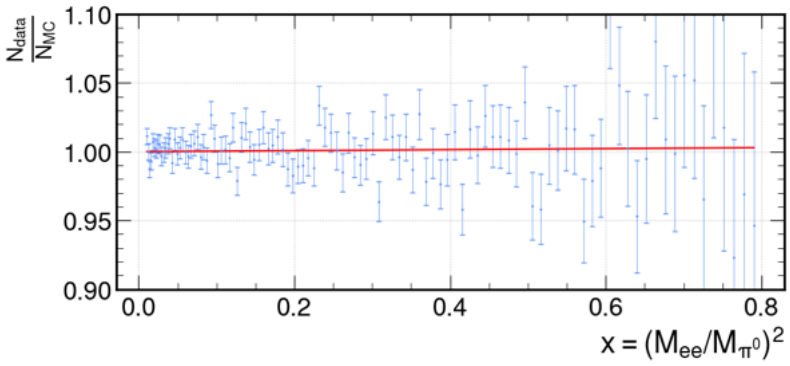

Figure 4.14: Data/MC in terms of the reconstructed kinematic variable x. The red line shows the fit of the Equation 4.19.

$F(x) = 1 + ax$. The parameter a is the slope factor, which has been set through theoretical predictions and a number of experiments. The Vector Meson Dominance (VMD) model expects that $a = M_{\pi^0}^2(M_\rho^{-2} + M_\omega^{-2})/2 = 0.03$ [76]. The Particle Data Group (PDG) average for all experiments is $a = 0.0335 \pm 0.0031$ [12]. In the NA62 framework, the slope is defined as $a_{Fw} = 0.032$ by default. It is not possible to rely on external values for the slope factor as this would assume that the MC perfectly models effects such as detector responses, resolutions and kinematic distributions. Relying on external slope factor can result in discrepancies between data and MC. To mitigate this and ensure an accurate background model an effective slope is defined using the data itself.

Figure 4.14 shows the ratio of data and MC from Figure 4.11 in bins of x. A correction is applied to modify the MC sample with an effective TFF slope. The effective TFF slope for this study is found by fitting the data/MC ratio to,

$$f(x) = \frac{(1 + ax)^2}{(1 + a_{Fw}x)^2}. \tag{4.19}$$

The line shown in Figure 4.14 is the result of the fit for Equation 4.19 using a least χ^2 method, producing a slope of

$$a = 0.034 \pm 0.003_{Stat}. \tag{4.20}$$

The MC samples are re-weighted with Equation 4.19 to correct for the TFF slope. After the applied weighting to all events the MC sample is re-scaled to match the data, as the total number of MC events has increased. The new effective slope results in an improved MC description of the data, shown in Figure 4.15 compared

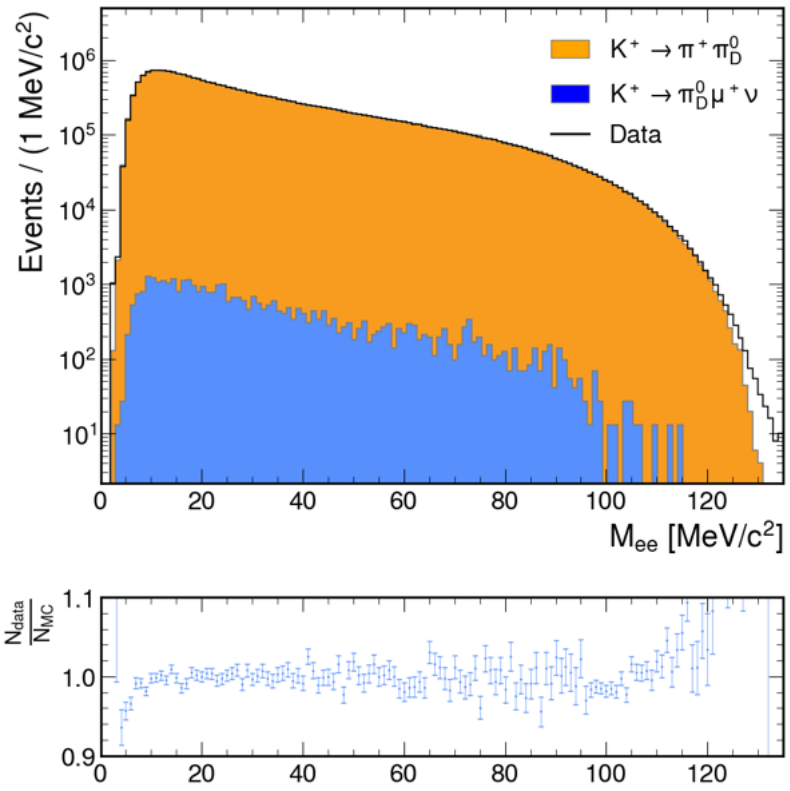

Figure 4.15: Reconstructed M_{ee} spectra for data and MC samples corrected for the effective TFF.

to Figure 4.11. The TFF correction is used throughout the study for the MC samples.

4.4.2 Upper Limit on the Mixing Parameter

The range of the DP search is defined as $7 \leq M_{A'} \leq 120\,\mathrm{MeV}/c^2$. The lower mass boundary is defined because of the falling geometric acceptance. The upper boundary is set due to the inability of the MC to model the non-Gaussian tails of the track reconstruction. Using the method described in Section 4.3, results in 379 DP mass values tested. The error on the number of expected background events is due to the statistical error of the expected events within the search window $\delta N_{exp} = \sqrt{N_{exp}}$. A correction is required due to the factor f_{scale} imposed on the MC to scale the sample to match the effective kaon flux. The N_{obs}, N_{exp} and their errors for the MC background estimation are shown in Figure 4.16. The local significance of the DP signal (Equation 4.8) is shown in Figure 4.17. The maximum local significance is $2.79\,\sigma$, which is below the $3\,\sigma$ threshold required for evidence of a signal. After accounting

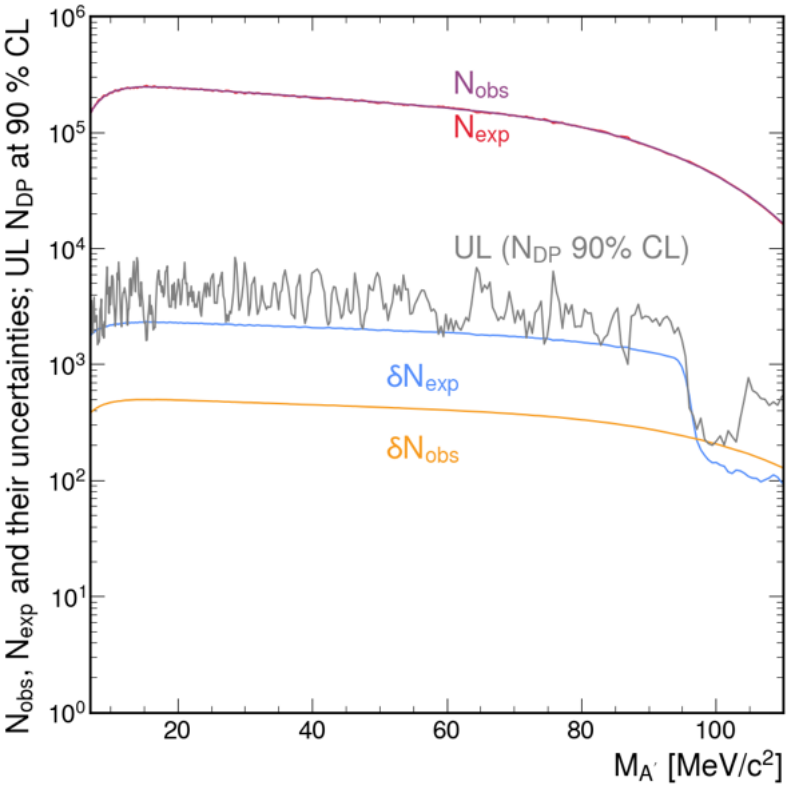

Figure 4.16: Number of observed data events (N_{obs}), expected number of events from MC (N_{exp}), the respective errors (δN_{obs} and δN_{exp}) and the resultant upper limit of the number of dark photon candidates to a 90% confidence level for the MC background estimation method. The error on the expected number of events is due to the statistical error of the MC samples.

for the LEE, the corresponding global p-value is estimated to be approximately 0.02, which translates to a global significance of 2.1 σ. This value is obtained using the toy MC method defined in Section 4.3. It indicates that under the background-only hypothesis, there is a 2 % probability that a statistical fluctuation anywhere in the scanned mass range would produce a local significance at least as large as the one observed. These results indicate that no DP signal is observed.

The UL of the number of DP candidates (N_{DP}) at a 90% CL is shown in Figure 4.16. The UL of the N_{DP} is used to calculate the UL at a 90 % CL of the branching fraction of the decay $\pi^0 \to \gamma A'$, with the assumption $\mathcal{B}(A' \to e^+e^-) = 1$:

$$\mathcal{B}(\pi^0 \to \gamma A') = \frac{N_{DP}}{N_K \mathcal{B}_{K_{2\pi}} A_{DP}}, \tag{4.21}$$

where N_K is the effective kaon flux defined in Section 4.2, $\mathcal{B}_{K_{2\pi}}$ is the branching fraction of the $K^+ \to \pi^+\pi^0$ decay [12] and A_{DP} is the acceptance of the DP signal, defined in Section 4.3. The UL of the branching fraction at a 90% CL across the

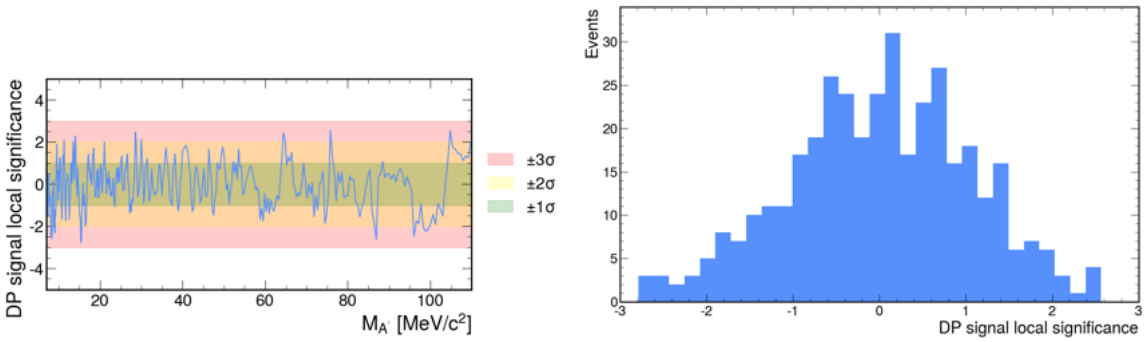

Figure 4.17: Local significance of the DP signal as a function of $M_{A'}$ for the MC background estimation. Left: the local significance plotted against $M_{A'}$. Right: the distribution of local significance values.

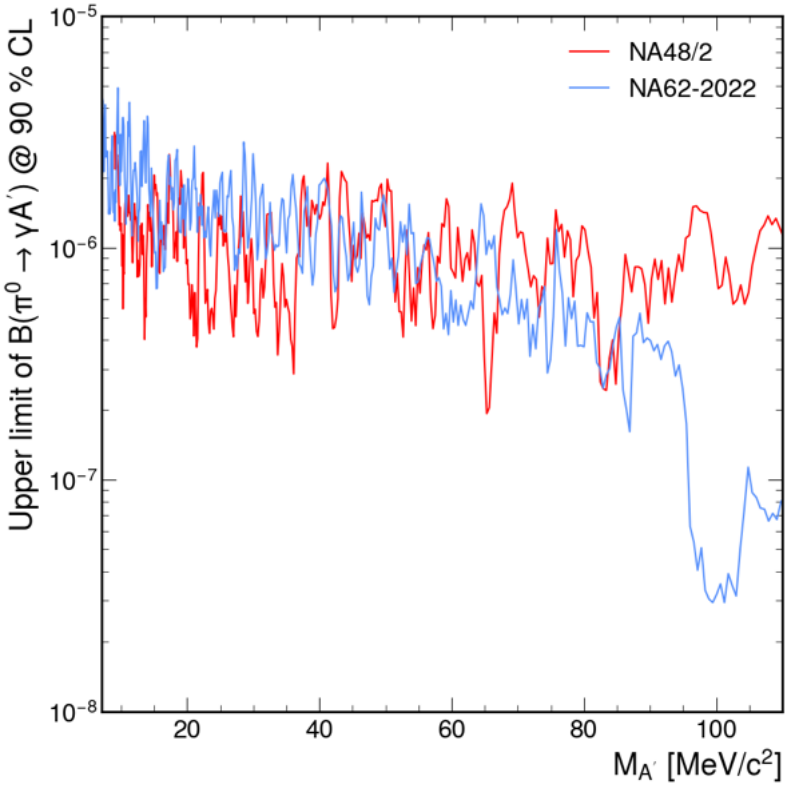

Figure 4.18: Upper limit of the branching fraction of $\pi^0 \to \gamma A'$ at a 90% CL for each dark photon mass value, using the MC background estimation. The result from NA48/2 is shown for comparison [44].

DP mass range is shown in Figure 4.18. The reduction of the UL above 90 MeV/c^2 is due to the improved statistical errors provided by using the biased $x > 0.5$ $K_{2\pi D}$ sample. The UL for NA62 is compared against the NA48/2 result [44]. The UL of the branching fraction is used to set the UL of the mixing parameter ϵ^2 for each DP

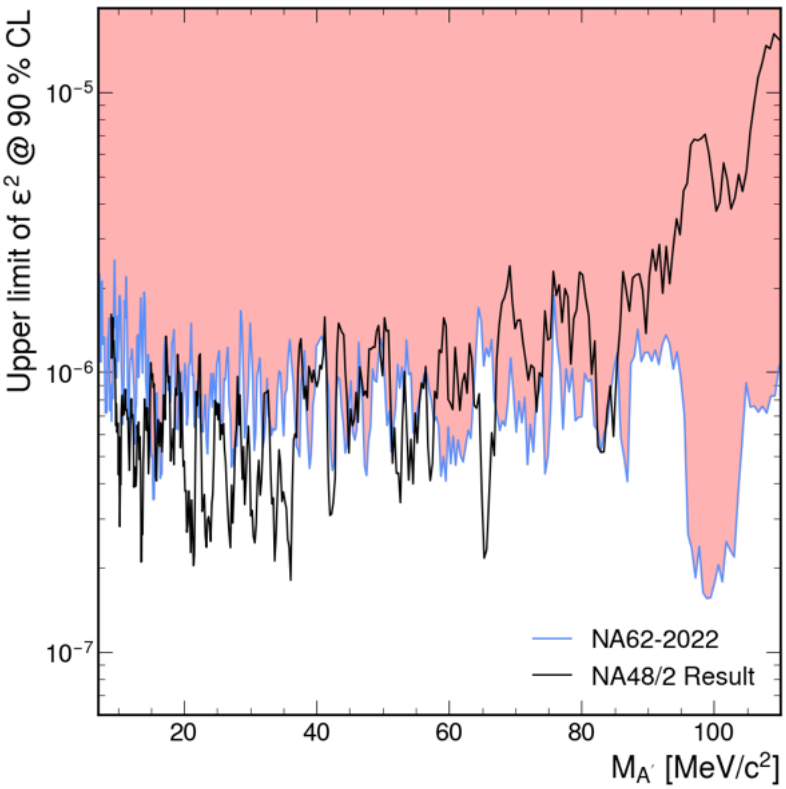

Figure 4.19: Upper limit of the mixing parameter ϵ^2 at a 90 % CL for each dark photon mass hypothesis, using the MC background estimation. The result from NA48/2 is shown for comparison [44].

mass value. The mixing parameter squared is calculated from Equation 1.34,

$$\epsilon^2 = \frac{\mathcal{B}(\pi^0 \to \gamma A')}{2\left(1 - \frac{M_{A'}^2}{M_{\pi^0}^2}\right)^3 \mathcal{B}(\pi^0 \to \gamma\gamma)}. \tag{4.22}$$

The UL of the mixing parameter ϵ^2 at a 90 % CL across the DP mass range is shown in Figure 4.19. If the main MC sample is produced at the same statistical level as the biased sample, the UL could be improved by at least an order of magnitude. This is as long as the systematic errors do not dominate if included in the study. Without increased MC statistics, the study is not competitive with the already published result from NA48/2 [44] except for $M_{A'} > 85\,\mathrm{MeV}/c^2$.

4.5 Background Estimation using Data

To improve the error in the background estimate, a data-driven method is employed that uses the data itself to estimate the background. In addition to the 2022 dataset used in the MC background study, the 2023 and 2024 datasets are included for this

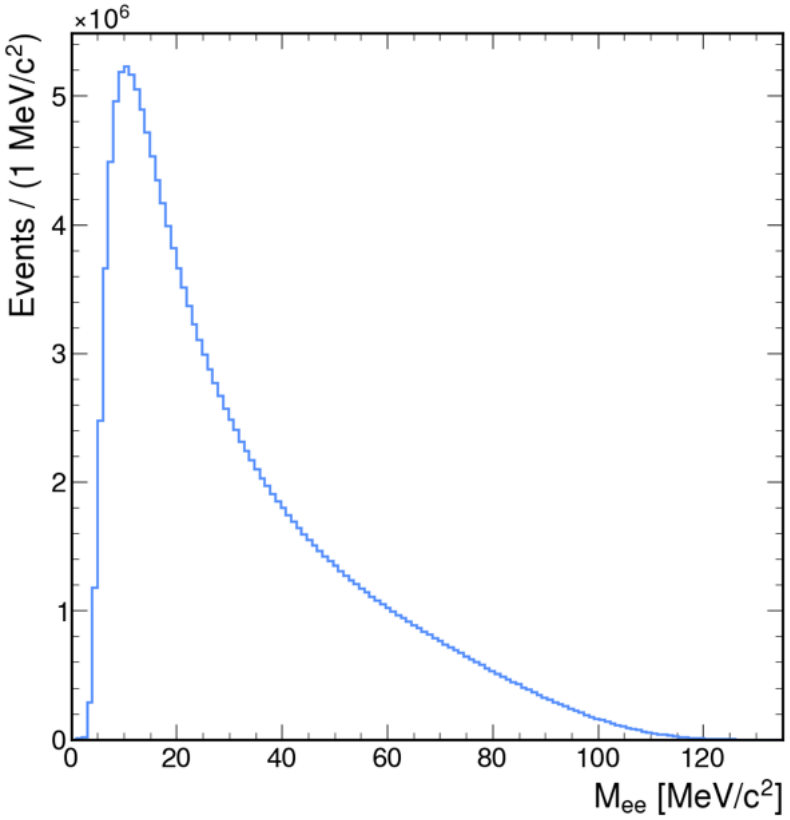

Figure 4.20: Reconstructed M_{ee} spectrum for events passing the selection from the 2022, 2023 and 2024 datasets.

study with the number of kaon decays in the FV defined in Section 4.2. The resultant reconstructed M_{ee} spectrum is shown in Figure 4.20.

4.5.1 Fitting the Data Distribution

The method described in Section 4.3 is used to convert bins of M_{ee} to DP candidate windows. The DP mass range is defined as $6 \leq M_{A'} \leq 121.6\,\text{MeV}/c^2$. The mass range is extended compared to the previous MC study. This is due to the large number of events in the mass bins at the edges of the distribution provided by using the data sample rather than the MC. Using the method defined in Section 4.3 results in 428 DP mass hypotheses tested. A 4th-order polynomial is fitted to the data distribution shown in Figure 4.20, using a least χ^2 method. The fitting region for each mass hypothesis is defined as $\pm 15\sigma_m(M_{A'})$ from the mass hypothesis, and the distribution is re-binned with a bin width of $\sigma_m(M_{A'})/5$. Data events in the mass bins above $125\,\text{MeV}/c^2$ are removed. This is because the small counts at the edge of the mass range cause instability with the fitting. Events in the mass bins

$\pm 1.5\sigma_m(M_{A'})$ from the mass hypothesis are excluded from the fit. This reduces the chance of a biased background estimate from potential signal contamination while preserving sensitivity across the scanned mass range.

The number of expected events N_{exp} is evaluated as the integral of the fitted function within the $\pm 1.5\sigma_m(M_{A'})$ mass window divided by the bin width. The error on the number of expected events δN_{exp} combines statistical and systematic uncertainties. The statistical component δN_{exp}^{stat} is computed from the propagation of the statistical errors of the polynomial parameters, provided in the form of a covariance matrix and calculated using an error propagation method available in the ROOT package (TF1::IntegralError()) [59] . The systematic error δN_{exp}^{sys} is estimated by fitting each distribution defined above with 3rd and 5th order polynomials. The resultant integrals are evaluated and compared to the integral calculated using the 4th order polynomial. The systematic error is calculated as the largest of the two differences from the 4th order polynomial.

Example fits for background estimation and systematic error estimation for the lowest DP mass hypothesis at $6\,\mathrm{MeV}/c^2$ are shown in Figure 4.21. The mass range of the plots is the entire $\pm 15\sigma_m(M_{A'})$ fitting range and shows the removed region within $\pm 1.5\sigma_m(M_{A'})$ from the mass hypothesis described above.

The polynomial fits for the final DP mass hypothesis at $121.6\,\mathrm{MeV}/c^2$ are shown in Figure 4.22, showing bins above $125\,\mathrm{MeV}/c^2$ removed from the fitting region. The upper boundary of the search region is set at the point where the polynomial fits become unstable due to the reduced number of data events.

The N_{obs}, N_{exp}, δN_{obs} and δN_{exp} values obtained for each $M_{A'}$ hypothesis are shown in Figure 4.23. The combined expected error δN_{obs} is reduced compared to the MC background presented in Figure 4.16. The statistical error is dominant over the systematic below $100\,\mathrm{MeV}/c^2$. Above $100\,\mathrm{MeV}/c^2$ the spikes in the systematic uncertainties are caused by the reduced fitting window due to the removed data events above $125\,\mathrm{MeV}/c^2$.

With N_{obs}, N_{exp}, δN_{obs} and δN_{exp} shown in Figure 4.23, the local significance of the DP signal is calculated with Equation 4.8 is shown in Figure 4.24. The maximum local significance for the data driven method is $2.88\,\sigma$, which does not exceed the $3\,\sigma$ threshold for evidence of a signal. Accounting for the LEE using

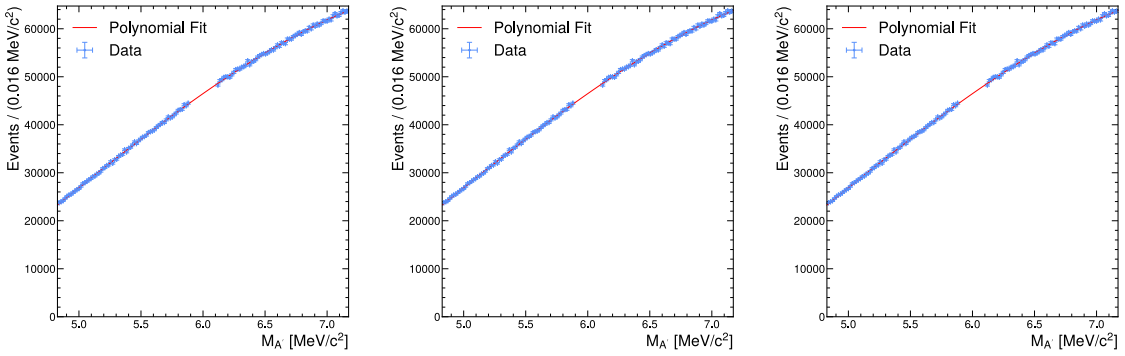

Figure 4.21: Fits to the data distributions with polynomial for the lowest DP mass hypothesis at $M_{A'} = 6\,\mathrm{MeV}/c^2$. Left: the data fitted with 3rd order used for the systematic uncertainty calculation, middle: 4th order polynomial for the background estimation, right: 5th order for the systematic uncertainty calculation.

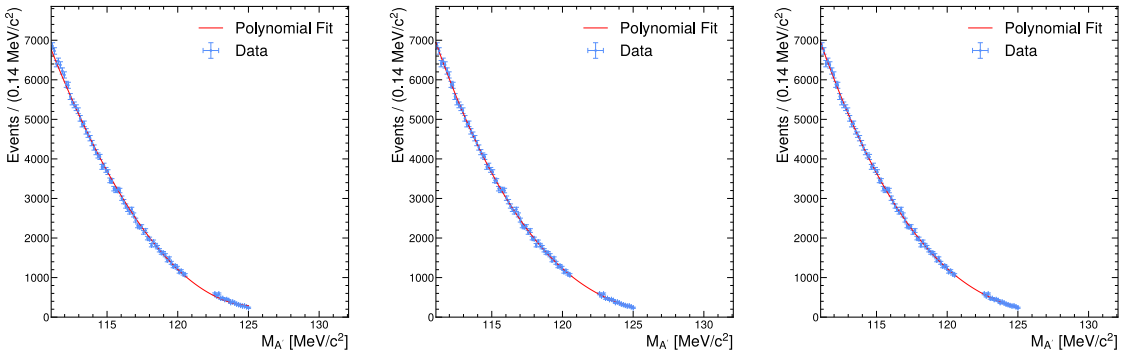

Figure 4.22: Fits to the data distributions with polynomial for the final DP mass hypothesis at $M_{A'} = 121.6\,\mathrm{MeV}/c^2$. Left: data fitted with 3rd order used for the systematic uncertainty calculation, middle: 4th order polynomial for the background estimation, right: 5th order for the systematic uncertainty calculation.

toy MC simulations across the 428 DP mass hypotheses results in a global p-value estimated at 0.60. This global p-value corresponds to a global significance of $0.25\,\sigma$. These results indicate that no DP signal is observed.

Using the same method as for the MC study and described in Section 4.3, N_{obs}, N_{exp} and δN_{exp} are used as inputs into the CLs method to calculate the UL of the number of DP candidates in each mass window shown in Figure 4.23. The error on the expected number of events is reduced compared to the MC study, which is shown in Figure 4.16. The reduction in δN_{exp} is from the new background estimation method. It is not possible to see the true reduction in uncertainties due to increase

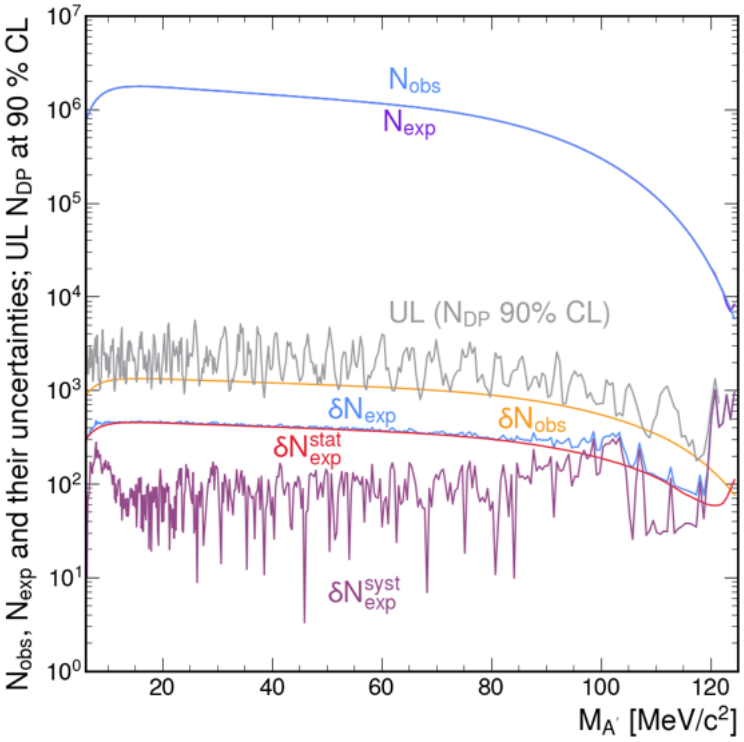

Figure 4.23: Numbers of observed data events (N_{obs}), expected numbers of background events (N_{exp}) calculated from 4th order polynomial fits to the data distribution, their respective errors (δN_{obs} and δN_{exp}) and the resultant UL of the number of dark photon candidates at a 90% CL for the data-driven background method. The error on the expected number of events is the combination of the statistical and systematic errors. δN^{stat}_{exp} is computed from the propagation of the statistical errors of the polynomial parameters. δN^{syst}_{exp} is estimated using 3rd and 5th order polynomial fits to the data distribution.

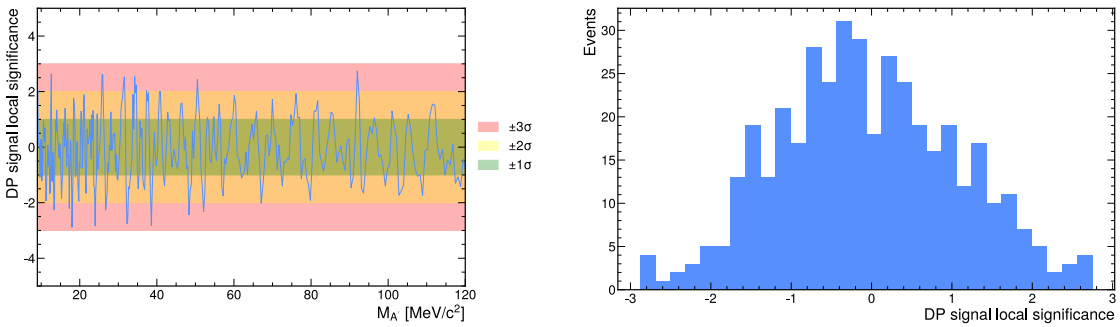

Figure 4.24: Local significance of the DP signal as a function of $M_{A'}$. Left: the local significance plotted against $M_{A'}$. Right: the distribution of local significance values.

in statistics when including the 2023 and 2024 datasets.

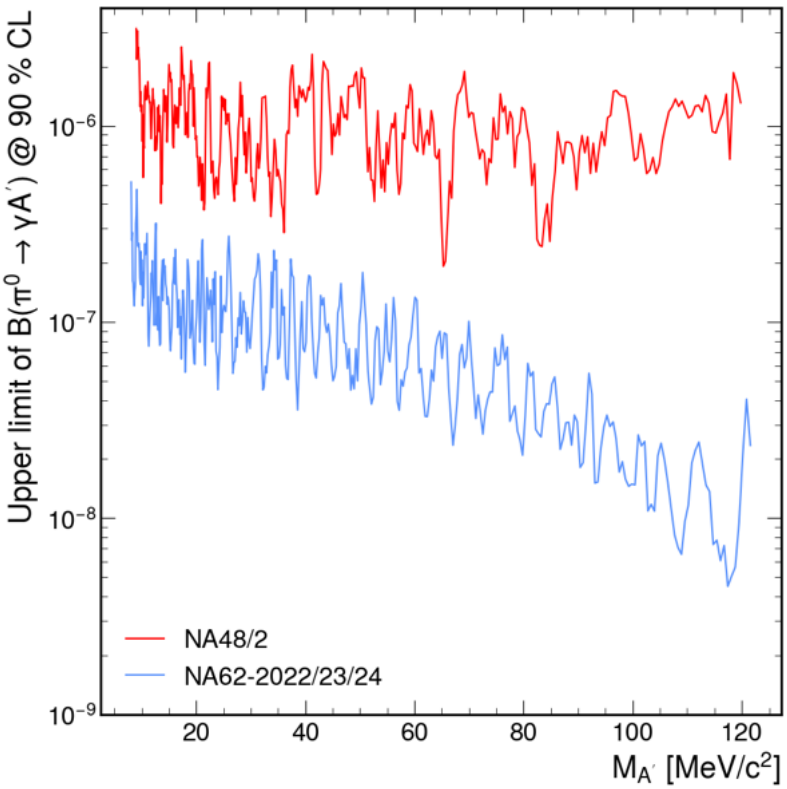

Figure 4.25: Upper limit of the $\mathrm{B}(\pi^0 \to \gamma A')$ at a 90 % CL for each dark photon mass hypothesis using the data-driven background estimation. The result from NA48/2 is shown for comparison [44].

4.5.2 Upper Limit on the Mixing Parameter

Using Equation 4.21 the UL of the number of DP, shown in Figure 4.23, is used to calculate the UL of the branching ratio to a 90 % CL, and is shown in Figure 4.25. The resultant UL of $\mathcal{B}(\pi^0 \to \gamma A')$ is a significant improvement compared to the result produced in the MC study shown in Figure 4.18.

The UL of the mixing parameter ϵ^2, calculated with Equation 4.22, is compared to the result from NA48/2 [44] in Figure 4.26. This study improves on the NA48/2 result by an order of magnitude. This is due to a 75-fold increase in kaon decays within the FV provided by NA62, an improved M_{ee} mass resolution, and a more refined method for using the data to estimate the background, which reduces the errors that previously limited the study.

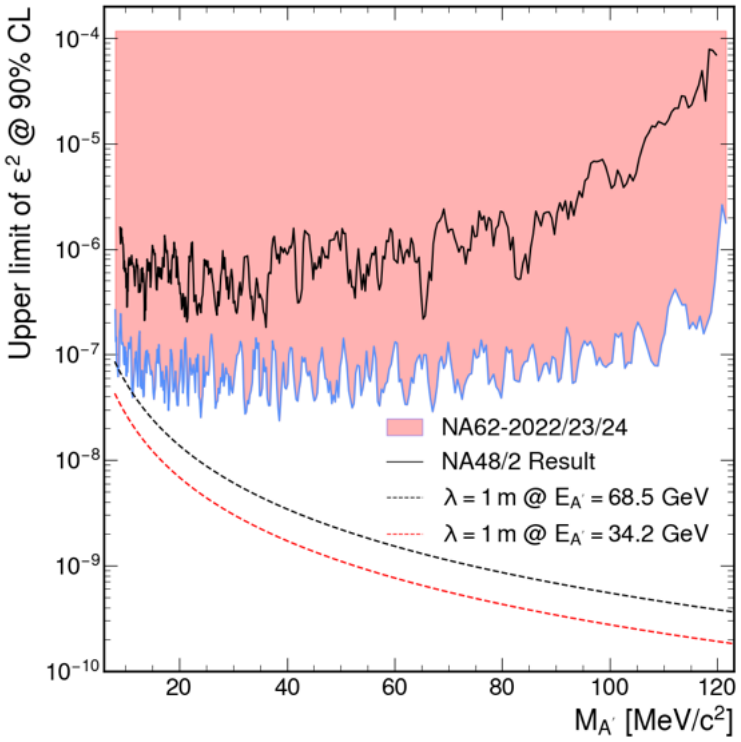

Figure 4.26: Upper limit mixing parameter ϵ^2 at a 90 % CL for each dark photon mass hypothesis for the data-driven background estimation method, with the result from NA48/2 for comparison [44]. Lines showing the $\lambda = 1\,\text{m}$ for the maximum and half of the maximum DP energy.

4.6 Validation of the Prompt Decay Assumption

Key to this analysis is the assumption of the prompt $A' \to e^+e^-$ decay, where $\text{B}(A' \to e^+e^-) = 1$. A check on the DP maximum mean path length is required to ensure that the above assumption holds and the calculated limits above are correct. The energy of the π^0 from the $K_{2\pi}$ decay in the kaon rest frame is

$$E_{\pi^0}^{rest} = \frac{M_K^2 + M_{\pi^0}^2 - M_{\pi^+}^2}{2M_K} = 0.246\,\text{GeV}, \tag{4.23}$$

where M_K, M_{π^0} and M_{π^+} are the kaon, neutral pion and charged pion masses, with the equation derived from basic two-body decay kinematics. The π^0 momentum in the kaon rest frame is computed as

$$p_{\pi^0}^{rest} = \sqrt{(E_{\pi^0}^{rest})^2 - M_{\pi^0}^2} = 0.205\,\text{GeV}/c. \tag{4.24}$$

With a nominal beam energy at NA62 of $E_K = 75\,\text{GeV}/c$, using Equations 4.23 and 4.24 the maximum energy of the π^0 in the laboratory reference frame via a Lorentz

boost is,

$$E_{\pi^0} = \gamma_K(E^{rest}_{\pi^0} + \beta_K p^{rest}_{\pi^0}) = 68.5\,\text{GeV}, \tag{4.25}$$

with $\gamma_K = E_K/M_K$ and $\beta_K^2 = 1 - 1/\gamma_K^2$. In the decay $\pi^0 \to \gamma A'$ the maximum energy of the DP occurs when the DP is emitted in the direction of the π^0 motion and the photon is emitted backwards in the π^0 rest frame, resulting in a maximum DP energy

$$E^{max}_{A'} = \gamma_{\pi^0}(E^{rest}_{A'} + \beta_{\pi^0} p^{rest}_{A'}) = 68.5\,\text{GeV}, \tag{4.26}$$

where $\gamma_{\pi^0} = E_{\pi^0}/M_{\pi^0}$ and $\beta_{\pi^0} = p_{\pi^0}/E_{\pi^0}$. The maximum DP energy and momentum in the π^0 rest frame is when the DP mass tends to zero, resulting in $E^{rest}_{A'} \approx M_{\pi^0}/2$ and $p^{rest}_{A'} \approx E^{rest}_{A'}$. The maximum DP mean free path is

$$\lambda^{max}_{A'} \approx \frac{E^{max}_{A'}}{M_{A'}c}\tau_{A'} = 0.55\,\text{mm} \times \frac{10^{-6}}{\epsilon^2} \times \left(\frac{100\,\text{MeV}/c^2}{M_{A'}}\right)^2, \tag{4.27}$$

where DP mean free path is inversely dependent on $\epsilon^2 M_{A'}^2$, and $\tau_{A'}$ is defined by Equation 1.36. The lowest UL of ϵ^2 from the analysis is found as $\epsilon^2 M_{A'}^2 = 4.59 \times 10^{-6}\,\text{MeV}^2/c^4$ corresponding to $\lambda^{max}_{A'} = 1.19\,\text{m}$. Due to the design of the three-track trigger and offline reconstruction, the resolution of a decay vertex position is about 1 m. As the distance between the production vertex and the A' decay point increases, the probability of reconstructing a single three-track vertex decreases. This results in the event being removed due to the requirement of a single three-track vertex during the selection, reducing the acceptance and reducing the sensitivity of the analysis. For a DP with the maximum energy, a dashed line corresponding to a decay length of $\lambda = 1\,\text{m}$ is shown in Figure 4.26. The fluctuations of the UL of the mixing parameter are just below the line for the maximum energy, suggesting that the prompt assumption is still valid except in the most extreme cases.

4.7 Global Results

This result for the UL of the mixing parameter is compared to other experiments in Figure 4.27. The figure is produced using the software package DarkCast [77, 78]. It shows the results from this study and a number of other searches: NA48/2 [44], BaBar [79], NA64 [80], KLOE [81], KLOE-2 [82], FASER [83] and others [84, 85]. The result from NA62 probes regions of phase space not explored by previous experiments.

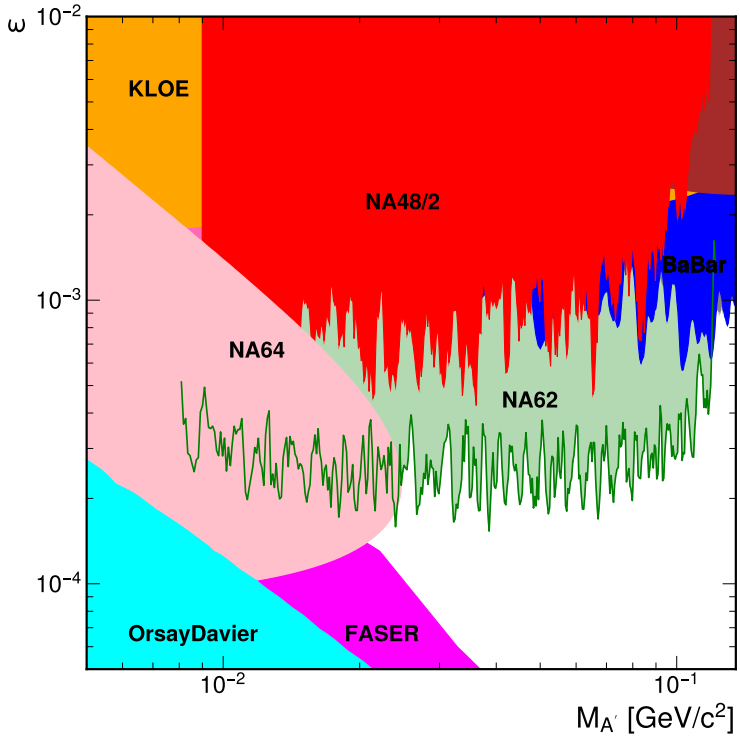

Figure 4.27: Upper limit at a 90% CL on the mixing parameter (green) compared to published exclusion limits [44, 79, 80, 81, 82, 83, 84, 85].

4.8 Conclusions

The search for DP at NA62 is expanded from the study conducted at NA48/2, utilising the 2022–2024 dataset. Two methods for the background estimation are presented: one using MC samples and the other using the data. The MC background estimation method produces uncompetitive results due to the limited size of MC samples produced and potential systematic errors in the background estimate. The data-driven background estimation produces improved limits compared to previously published results for the mixing parameter across the DP mass search range. The result sets limits in a region of phase space not yet covered by any other experiment.

Chapter 5

Future Kaon Experiments

Over the past 75 years the study of kaon physics has been integral to the development of the Standard Model (SM). Since 2016, the NA62 experiment has been the leading experiment in the field of kaon physics. However, with the NA62 experiment scheduled up to CERN Long Shutdown 3 (LS3), which is expected in autumn 2026, it is important to investigate future experiments. It is then required to investigate the future of kaon physics and the potential experiments that could succeed NA62. This chapter discusses the potential future of kaon physics, the experiments that could be used to further the field, and the work contributed to these experiments.

5.1 High Intensity Kaon Experiments (HIKE)

High-intensity Kaon Experiments (HIKE) is a proposed project to continue kaon physics at CERN in the ECN3 experimental hall and represents a phased program after LS3. HIKE is to benefit from a four to six-fold increase in beam intensity compared to NA62 and includes cutting-edge detector technologies as described in this section. The beam intensity requirements for HIKE are described in Table 5.1. To accommodate the higher intensities, upgrades are needed to the infrastructure that provide the beam to ECN3. A number of working groups such as the ECN3 beam delivery group within the Physics Beyond Colliders community at CERN [86], have already been conducting efforts to consolidate the work required to upgrade the infrastructure.

Three phases are foreseen within the HIKE program. The first being a contin-

uation of NA62 charged kaon physics with the high-intensity beam upgrades. This includes detector upgrades to accommodate for the rate increase and the goal of measuring the branching ratio of $K^+ \to \pi^+\nu\bar{\nu}$ to a 5 % precision in order to match the theoretical uncertainty in Equation 1.24. The second phase involves neutral kaon physics with charged secondary particle tracking with the goal to measure the branching ratio of $K_L \to \pi^0 l^+ l^-$ with $l = e, \mu$. The third phase is designed to observe the $K_L \to \pi^0\nu\bar{\nu}$ decay and measure its branching ratio to a 20 % precision.

HIKE Phase	**Protons on Target/Spill**	K **Decays/Year**
Phase 1 (K^+)	1.3×10^{13}	2×10^{13}
Phase 2 (K_L and tracking)	2×10^{13}	3.8×10^{13}
Phase 3 (K_L)	2×10^{13}	1.3×10^{13}

Table 5.1: Intensity requirements for three phases of HIKE. The number of kaon decays per year corresponds to those that decay within the HIKE fiducial volume.

5.1.1 Phase 1

The experimental design of NA62 has been proven as a successful setup for the precision measurement of the $K^+ \to \pi^+\nu\bar{\nu}$ decay, described in Section 2. The HIKE Phase 1 detector setup, shown in Figure 5.1, is similar to the NA62 setup described in Section 2 with new and upgraded detectors. The HIKE detectors are required to withstand a four times greater particle rate with respect to NA62 equating to 1.3×10^{13} protons per spill on the target. The expected HIKE Phase 1 beam has similar characteristics to the NA62 one, with a 75 GeV/c secondary hadron beam produced from a 400 GeV/c primary proton beam from the SPS accelerator onto a target at an angle of 0 rad. The detectors before the fiducial volume include an upgraded photon-detection system for the KTAG, described in Section 5.3, and a new GTK chip design. It is proposed to upgrade the existing NA62 Vetocounter with scintillating fibre (SciFi) technologies to improve the granularity and to accommodate the increased beam intensity.

Major upgrades are envisioned to the LAV and STRAW detectors within the fidu-

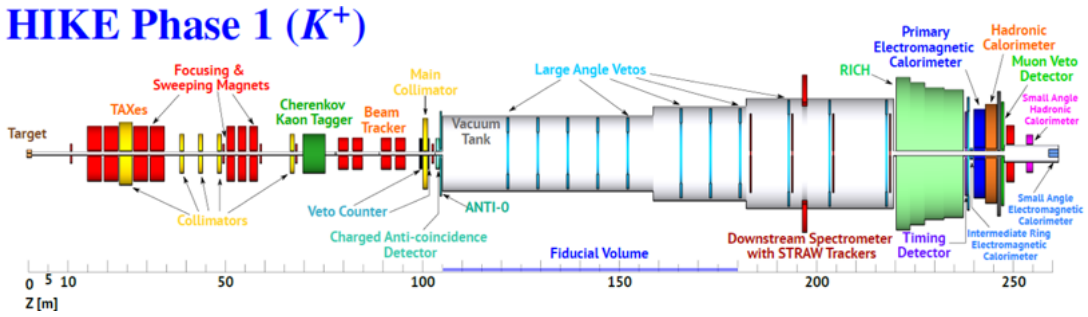

Figure 5.1: Diagram of HIKE Phase 1 detector setup [87].

cial volume. A number of LAV stations are to be upgraded to a new lead scintillator design, similar to the Vacuum Veto System (VVS) planned for the CKM experiment [88, 89]. The LAV detectors are crucial to the subsequent phases of HIKE, especially Phase 3, and are designed to fulfil the requirements of the $K_L \to \pi^0\nu\bar{\nu}$ measurement even when used in Phase 1. The STRAW spectrometer is to use an upgraded novel 5 mm straw design with a layout shown in Figure 5.2. The reduction in the straw diameter decreases the drift times while increasing granularity. This results in an expected improvement in the track angle and momentum resolution of 10–20 % compared to NA62.

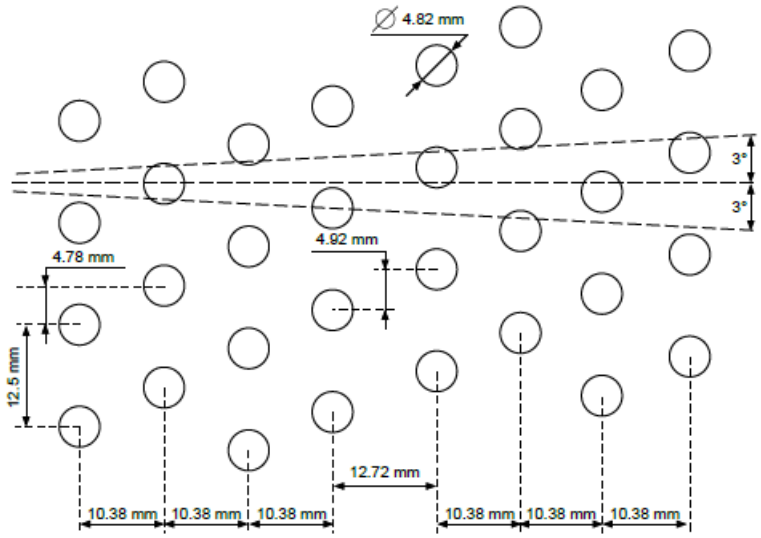

Figure 5.2: Diagram of the new STRAW spectrometer layout with 5 mm straw tubes [87].

Downstream of the fiducial volume, the PMT arrays of the RICH detector are upgraded, as described in Section 5.4. The HIKE timing detector profits from the current NA62-CHOD detector with upgraded Photomultiplier Tubes (PMTs), which

are to be chosen from the outcome of studies from other detectors such as KTAG, RICH and MUVs. For HIKE Phase 1, the LKr is proposed as the primary electromagnetic calorimeter given its excellent energy resolution. The required timing resolution is to be achieved by upgrading its electronic readout system. A number of other detectors are to be upgraded or replaced with higher granularity, such as the hadronic calorimeter, MUVs, IRC, and SAC.

About 2.5×10^{-6} kaon decays in the fiducial volume are expected per proton on target during HIKE phase 1. Given the expected protons per spill of 1.3×10^{13} (four times NA62) and a nominal year of 200 data-taking days with an average of 3000 spills per day, results in an expected 2×10^{13} kaon decays per year foreseen during HIKE phase 1. As a consequence the Phase 1 goals can be completed in 5 years of data taking.

5.1.2 Phase 2

HIKE Phase 2 is a multi-purpose neutral K_L decay experiment with the primary goal of measuring the branching ratios of the $K_L \to \pi^0 l^+ l^-$ decays. The detector setup, shown in Figure 5.3, would involve minimal modification to the experimental setup of Phase 1, with the removal of detectors that are only applicable to the charged kaon beam. The KTAG, GTK, RICH, and SAC detectors are to be removed, and the STRAW spectrometer is to be shortened. The STRAW chambers are to be reconfigured to have central beam holes to account for the neural beam. The MNP33 magnet requires a reduction in strength by 20 % to account for the shorter spectrometer, resulting in a momentum kick of 210 MeV/c. The fiducial volume is increased to 90 m compared to 75 m in Phase 1. The design proposed a production

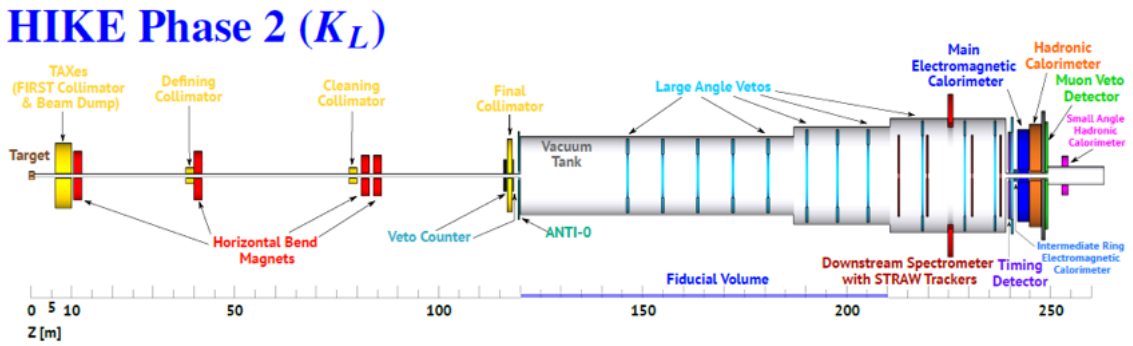

Figure 5.3: Diagram of HIKE Phase 2 detector setup [87].

angle of 2.4 mrad on the target producing an expected K_L yield of 5.4×10^{-5} per proton. Assuming an integrated proton flux of 1.2×10^{19} protons on target per year would result in 3.8×10^{13} K_L decays in the fiducial volume per year. The mean beam momentum at the entry of the fiducial volume is expected to be 79 GeV/c with a mean beam momentum for K_L which decay of 46 GeV/c.

HIKE Phase 2 is planned to follow after Phase 1. The expected protons per spill in Phase 2 is six times that of NA62 at 2×10^{13}. Assuming 200 days of data taking, 3000 spills per day (as in Phase 1) and 3.2×10^{-6} K_L decays in the Fiducial Volume (FV) per proton on target would result in 3.8×10^{13} decays per year. The expected time to Phase 2 goals is 6 years of data taking.

5.1.3 Phase 3 (KLEVER)

HIKE phase 3, previously known as KLEVER [90], is an experiment designed to measure the $K_L \to \pi^0 \nu \bar{\nu}$ decay. The experimental setup is shown in Figure 5.4 and differs from the design used at NA62 and HIKE Phase1/2. The setup consists of a large number of photon veto detectors located around a 160 m long vacuum volume to produce a complete coverage of photons produced from K_L decays. The detectors include coverage for photons emitted up to 100 mrad and allow for photons emitted with an angle up to 7.5 mrad to be detected by the main electromagnetic calorimeter (MEC). Due to the significantly different experimental setup, Phase 3 is separated

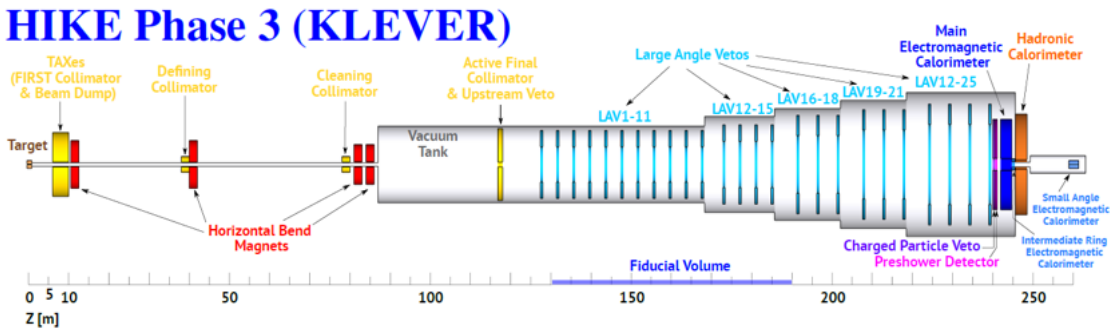

Figure 5.4: Diagram of HIKE phase 3 detector setup [87].

from the HIKE proposal submitted in 2023 [87]. However, some detectors would be shared between the two experiments as the granularity and efficiency requirements for Phase 3 have driven the detector requirements for the first two phases, reducing the overall costs. The LAVs, MEC, IRC, SAC and the hadronic calorimeters, which

are to be built for HIKE Phase 1/2, have all designs driven by their usage in Phase 3. The upstream veto, charged particle veto, and the pre-shower detectors are unique to Phase 3.

5.2 Flexible Simulation Software

As briefly described in Section 2.5, the software for NA62 is split into three main `C++` packages. NA62MC is a GEANT4 based Monte Carlo (MC) simulation package that simulates the NA62 experiment. The MC utilises functions within GEANT4 to construct the sub-detectors of NA62, including their materials, volumes and structures. It is possible to simulate a number of different kaon decays in order to create signals similar to what are produced in reality at the experiment. After the simulation is complete, the software outputs the signals in each detector in a ROOT file for use in reconstruction or analysis. NA62Reconstruction is then used to reconstruct either the MC output or collected data from the experiment. This reconstruction converts the signals into hits within the detectors and clusters them into candidates. NA62Analysis is used to analyse the data produced from the reconstruction to conduct all the physics studies that are performed at NA62.

The NA62 framework was designed for use only with the NA62 experimental setup, resulting in minimal configurability and flexibility. Within the simulation, the only option for users to modify was to enable/disable sub-detectors. An upgraded software package is required to allow for the development of new detectors for future kaon experiments. The software is required to be flexible and configurable to allow for the simultaneous use for NA62 data taking and physics analysis, as well as for the development of new experiments.

To implement a flexible framework, all detector classes are refactored to inherit from a common class, which contains the essential functions and variables for all detectors. This allowed for all classes of the detectors to be parsed using the same machinery. The input file for the configuration of the detectors is changed from a simple text file, listing enabled detectors, to a one that includes information for the correct placement and construction of the detectors. The configuration file contains arguments required for individual detectors which are defined in Table 5.2, including

detectors upgraded later on in this Chapter. The X, Y, and Z placement of the back face of the detectors, along with the rotation, are also defined in this file. An example entry in the configuration file for a STRAW station is shown in Figure 5.5, where a name is given for the station "STRAW0", along with a chamber ID, chamber type defining the size of the straws, and the chamber geometry which determines if the beam hole is symmetric or not.

```
    Name            Arguments       X Y    Z      θx θy θz
Spectrometer("STRAW0", 0, 0, 0) 0 0 183705.9 0  0  0
```

Figure 5.5: Example configuration for the STRAW0 in the geometry file for NA62MC.

Detector Name	**Arguments**
STRAW	Chamber Name: "STRAW0", "STRAW1", "STRAW2" or "STRAW3" Chamber ID: 0, 1, 2 or 3 Chamber Type: 0 (10mm) or 1 (5mm) Chamber Mode: 0 (default) or 1 (symmetric)
Spectrometer Magnet	Magnetic field intensity
Vessel	Length InnerRadius OuterRadius Type: "Bluetube", "BlueTubeNoRails" or "GreyTube"
GigaTracker	PixelType: 0 (NA62 sensor size), 1 (1/2 NA62 sensor size), 2 (1/3 NA62 sensor size)
RICH	Type: "NA62" or "HIKE" SiPMType: "3mm", "6mm" or "9mm"

Table 5.2: Arguments for detectors in the geometry file for use within NA62MC.

When constructed inside the simulation, each detector is contained in a separate outer volume called the "Responsibility Region" (RR). The creation of the RR is a simple task for most detectors except from the STRAW and LAV which are made up of multiple stations that are not continuous, resulting in multiple responsibility regions for each station.

5.2.1 Testing: Geometry and Magnetic Fields

After the simulation is upgraded, all the geometries of each detector are validated to ensure that they are still correct with respect to the previous version. This is due to

the complex nature of refactoring the detectors which results in a number of volume changes and the process in which the detectors are constructed. The validation is completed using a virtual particle within the GEANT4 framework called a Geantino. The Geantino is a particle that traverses the simulation in a straight line and passes through all volumes present in the simulation. The particle does not interact with any material and is not be affected by magnetic fields. A square distribution of these particles is sent through the simulation, and every time the particle passed across a boundary between two volumes, its position is saved. Using this information it is possible to reconstruct the entire geometry of each detector. This is in order to check the placement and geometry to ensure that the simulation is still accurate. An example of the Geantino hits on a single view of STRAW chamber 1 is shown in Figure 5.6. It is possible to see the features of the view, such as the missing straws within the centre used to produce the chamber beam hole. For the full validation, a larger sample of Geantinos is used to achieve the required precision. However, if there is a discrepancy between the new version and the previous, a smaller area is selected to create a more precise picture of what is incorrect. This information is used to modify the software to fix any geometry issues. This check is conducted for all sub-detectors within the simulation.

To reduce the chance of overlaps and to clean up the simulation, the size of the unused space in all sub-detectors surrounding the physical geometry are reduced. The RR for all sub-detectors is reduced to just slightly larger than the physical detector. It is possible to see this change in Figure 5.7, which depicts the direction of the magnetic fields. As the magnetic fields are only calculated in volumes, it is possible to see the reduction in RR size around the geometry. In Figure 5.7 (top) the field is calculated outside of the actual physical sub-detector due to the larger RR. Whereas in Figure 5.7 (bottom) the RR has been reduced to a few mm larger than the actual physical detector. As well as reducing the chance of overlaps, reducing the RR can speed up the simulation slightly due to the reduction in unnecessary calculations for the magnetic field outside of the detector geometry.

To improve the usability, a geometry check is completed every time before the simulation starts. Each outer detector volume is checked for any overlaps with other detectors, taking into account any rotations and the shape of the outer volumes. If

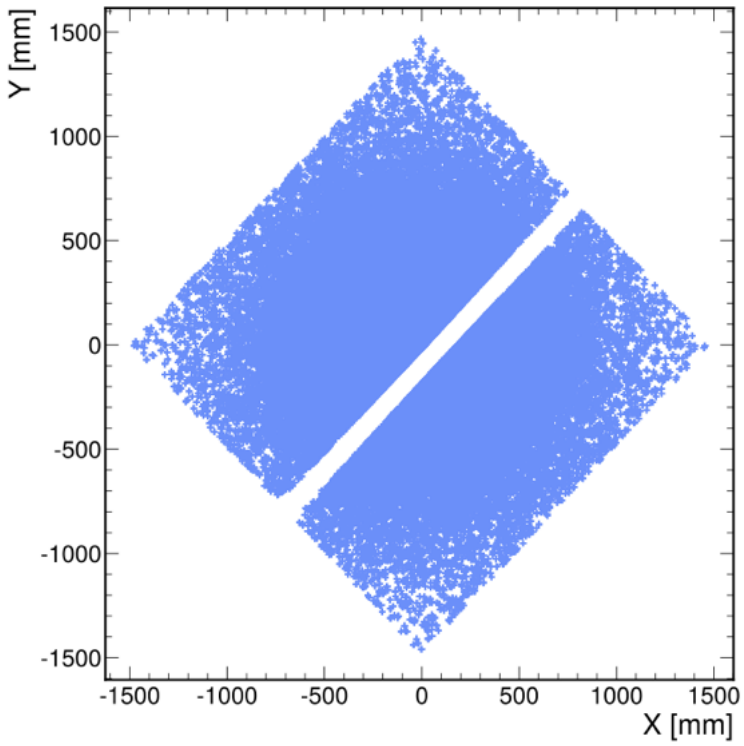

Figure 5.6: Geantino hits on a single view in STRAW chamber 1.

an overlap of two sub-detectors is found, the simulation does not start, and an error is produced describing where the overlap is and what sub-detectors are involved.

The magnetic field in the simulation is based on measurements of the magnetic field at NA62 from hall probes [91], saved in the form of data files used as inputs to calculate the magnetic field at various points in the simulation. In NA62MC the magnetic field is split into three distinct regions: the Bluetube field within the decay region, the fringe field located at the edges of the MNP33 magnetic field and the MNP33 field which is the main magnetic field from the MNP33 dipole magnet. In the previous version of the simulation, the position of the magnetic fields is written within the static code. However, with the flexible version, it is possible to move the MNP33 magnet to any position via the geometry input file. This requires the magnetic field to be calculated relative to the central position of the MNP33 dipole magnet. An example of this flexibility is shown in Figure 5.8 where the MNP33 magnet is moved from $Z = 198\,\mathrm{m}$ to $Z = 163\,\mathrm{m}$, which is in front of the STRAW chamber 1. The MNP33 and fringe magnetic fields is recalculated from the new position at 163 m to account for the placement of the MNP33 magnet.

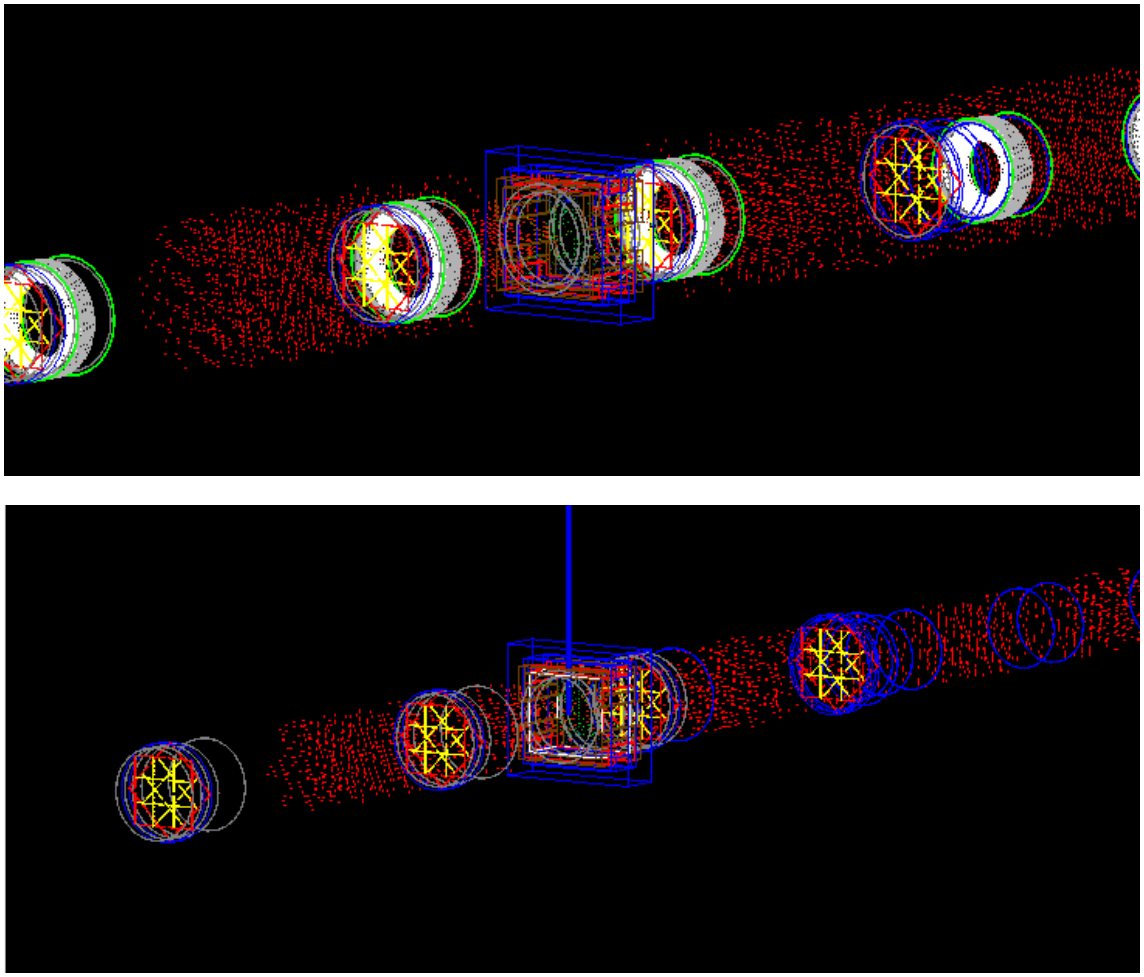

Figure 5.7: Visualisation of the magnetic fields in the spectrometer region from the simulation. Top, previous version with large outer volumes and bottom, new flexible version with reduced outer volumes. The red arrows represent the direction of the magnetic field in the volumes.

Similar to the changes in the sub-detector construction, the modification of the magnetic fields required validation. The validation is done using similar machinery to the geometry test completed previously but with a different GEANT particle, the charged Geantino. This is similar to a normal Geantino, where the particle traverses all volumes within its path but interacts with magnetic fields. As the charged Geantino enters a magnetic field, it is deflected as if it is a positively charged particle. This test ensured that the same tracks of the charged Geantinos between the previous version and the new flexible version are being produced within the magnetic fields. An example of the tracks taken by the charged Geantinos within the simulation is shown in Figure 5.9, where it is possible to see the displacement of the particles within the magnetic field regions. The exact XY positions when

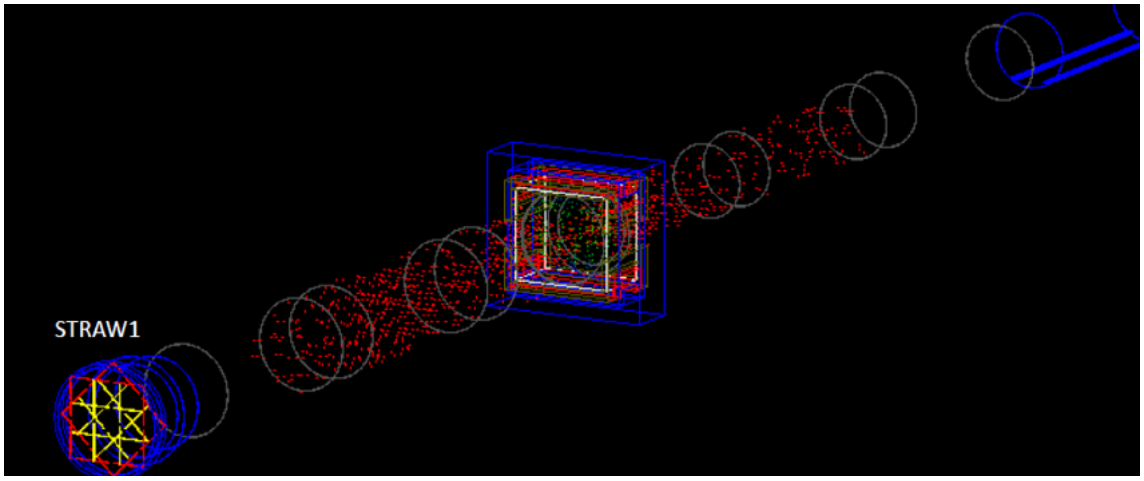

Figure 5.8: Visualisation of the MNP33 magnet placed in front of the STRAW chamber 1 at Z=163 m from the target in the simulation. Originally, the magnet is placed at Z=198 m, which is after the STRAW chamber 2. The red arrows represent the direction of the magnetic field in the volumes.

the particles traverses a detector volume would then be validated against a sample of charged Geantinos with the exact same characteristics and starting parameters produced with the previous version of the software. With minimal modification it is also possible to add the functionality to add multiple magnets within the simulation. After the geometry and magnetic field tests are completed, full test

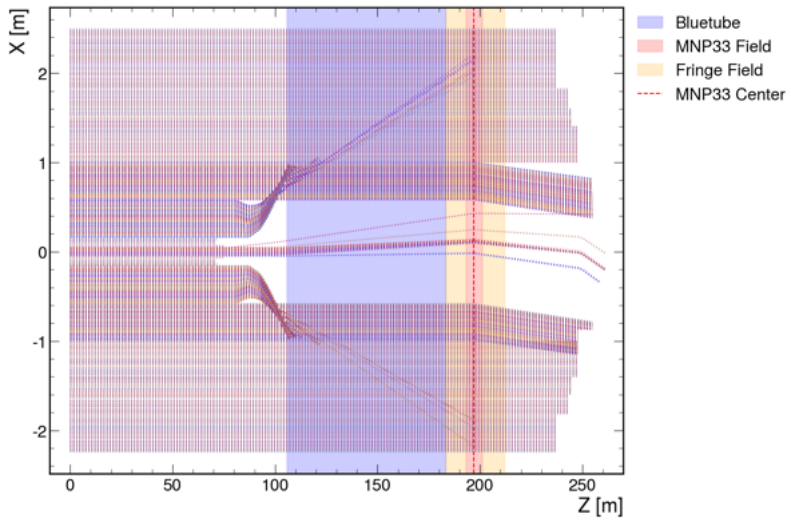

Figure 5.9: Tracks for charged Geantinos with a 75 GeV/c momentum through the NA62 detector. The extent of the magnetic fields from the MNP33 dipole magnet and the Bluetube field regions are shown.

productions of $K^+ \to \pi^+\pi^0$, $K^+ \to \pi^+\pi^-\pi^+$ and $K^+ \to \mu^+\nu$, are produced to test the validity of the existing NA62 setup along with the entire software chain (MC→Reconstruction→Analysis).

After testing, the software is ready to be used to develop new detectors and produce physics studies for HIKE.

5.3 The KTAG Upgrades for HIKE

The contents of this section contains work completed by the Birmingham group on the upgrades to the KTAG detector for HIKE Phase 1 and its implementation into the NA62 software framework.

To sustain the increased kaon rate, the KTAG requires upgrades to the photon-detection and data acquisition systems, allowing to reach the required time resolution of 15–20 ps and kaon identification efficiency of greater than 95 %. The expected kaon rate in HIKE Phase 1 is 200 MHz, which corresponds to a maximum rate of 10 MHz/cm^2 for the detected photons at the PMT array. This rate takes into account the production of Cherenkov photons in CEDAR-H and the resultant acceptance of the photons on the PMT plane. It is proposed that the NA62 PMT arrays are replaced with arrays of Micro-Channel Plate Photomultipliers (MCP-PMTs). The MCP-PMTs would provide a single photon time resolution of 50–70 ps depending on the model, a low dark rate of 1 kHz/cm^2 and the ability to sustain the required photon rate. A downside of the MCP-PMTs is their limited lifetime from the ageing of the photocathode caused by feedback ions from the residual gas resulting in a rapid reduction in the Quantum Efficiency (QE) [92]. This is measured as degradation of PMT QE as a function of the increasing Integrated Anode Charge (IAC). MCP-PMTs are similar to normal PMTs except that the dynode section is replaced by a micro-channel plate. An example diagram is shown in Figure 5.10, where a photon hits the photocathode window, producing a single electron, which is then accelerated towards the MCP by an electric field provided by a voltage difference across the gap. The electron then collides with the walls of the MCP, producing secondary electrons, which results in a cascade collected by the anodes below. The dual layer design, or chevron, provides additional benefits compared to a single layer design.

Such as improved gains due to the increased surface for secondary electrons to be produced. Major breakthroughs to improve the lifetime of the MCP-PMT have

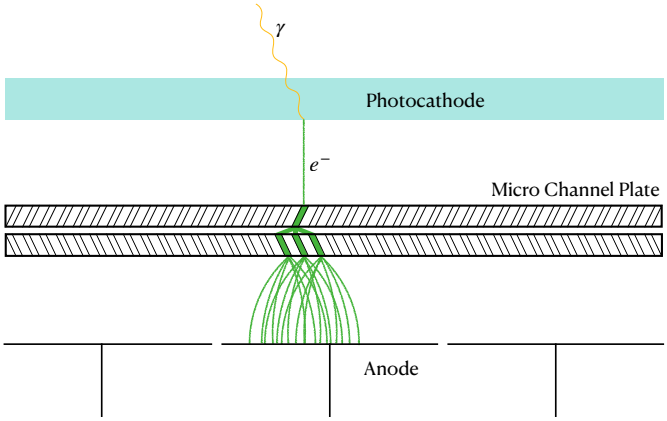

Figure 5.10: Diagram describing the inner workings of a MCP-PMT.

come with the method of Atomic Layer Deposition (ALD) [93], where the channels of the MCP are coated with a ultra-thin layer of Al_2O_3 or MgO. The layer prevents the out-gassing from the MCP glass substrate and drastically reduces the heavy ions reaching the photocathode resulting in significant increases in lifetime of the MCP-PMTs [94]. Utilising the method of ALD, MCP-PMTs from Photonis have been demonstrated to withstand an IAC greater than $20\,\mathrm{C/cm^2}$ [95], corresponding to a lifetime improvement of a factor of 100 compared to standard MCP-PMTs, shown in Figure 5.11.

An example of MCP-PMT model proposed for the KTAG is shown in Figure 5.12. The module consists of an 8×8 array of pixels which can individually be read out. Simulations of the KTAG with the upgraded photon-detection system for use in HIKE Phase 1 show that each of the eight KTAG sectors would use four of these MCP-PMT, shown in Figure 5.13. The four MCP-PMTs per sector are required for full coverage of the light spot produced when the light exiting the CEDAR is reflected by the spherical mirror. The schematic in Figure 5.12 shows there is some unused space around the active area of each MCP-PMT, which would result in reduced efficiency, especially in the centre, where the maximum amount of light is expected. To mitigate this, reflective surfaces are attached to each side of the individual MCP-PMTs shown in Figure 5.13 to reflect the light onto the active surface. The resultant light spot for one of the sectors is shown in Figure 5.14, where the inactive areas

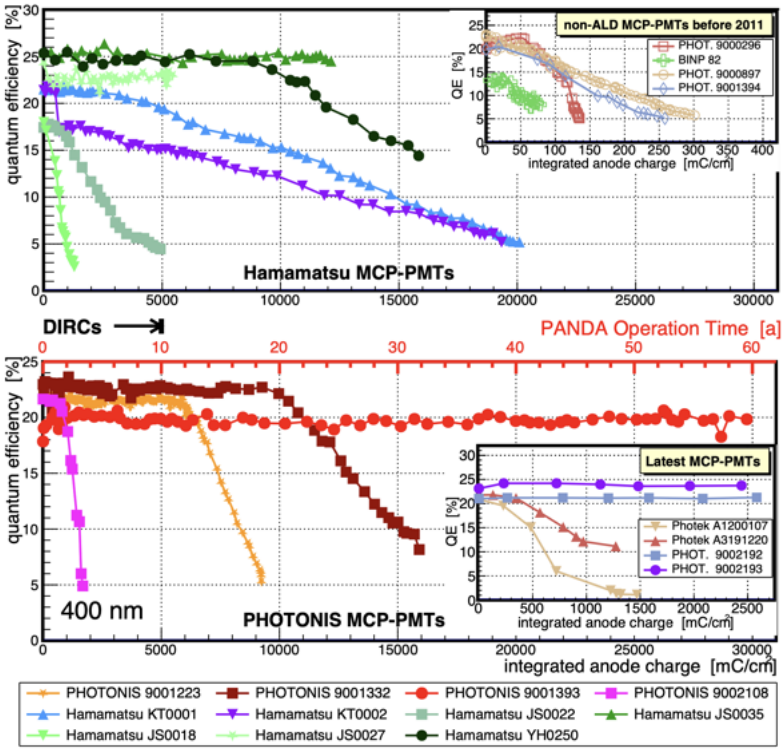

Figure 5.11: Lifetimes of available MCP-PMTs with the photocathode QE vs IAC for photons at 400 nm wavelength. Top, old ALD coated MCP-PMTs from Hamamatsu with non coated versions shown in the insert plot. Bottom, more recent ALD coated MCP-PMTs from PHOTONIS and Photek in the inserted plot [96].

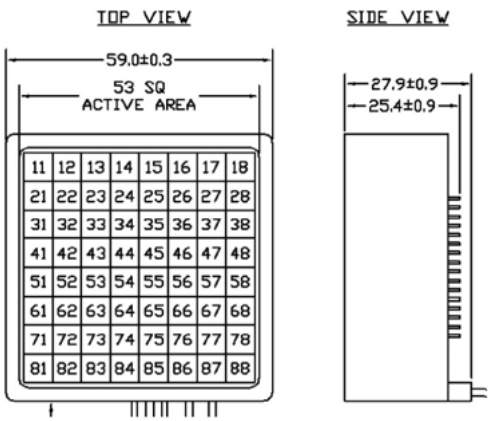

Figure 5.12: Schematic of Photonis MCP-PMT [97].

between the individual MCP-PMT and the increased amount of light at the edges produced from the reflective surfaces are shown. The position of the MCP-PMT in the KTAG sector is optimised to produce the maximum number of photo-electrons per kaon candidate. HIKE Phase 1 requires the MCP-PMTs to be installed within

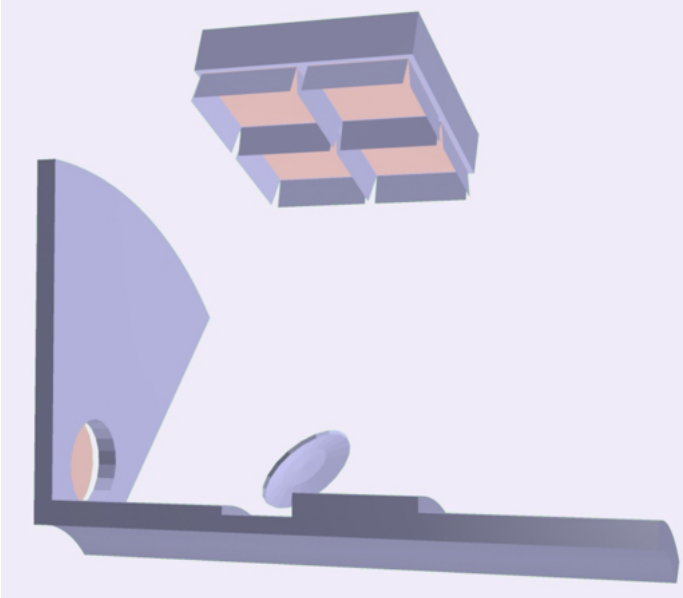

Figure 5.13: Visualisation of the MCP-PMT array placed inside of the KTAG.

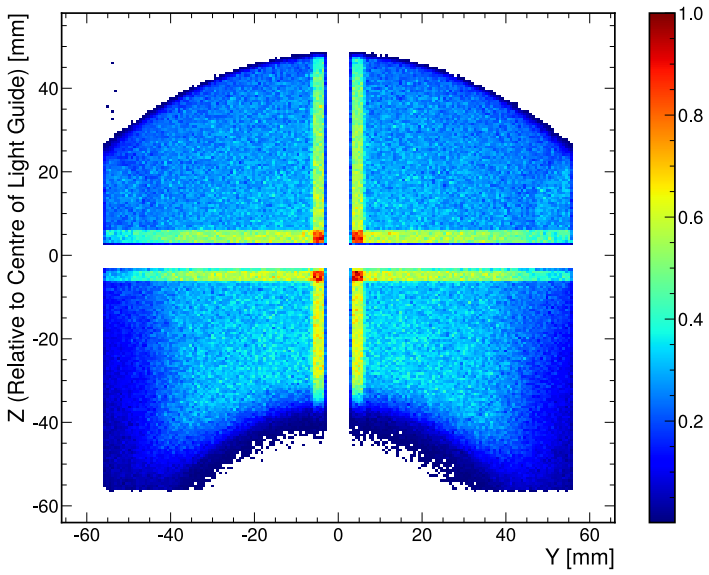

Figure 5.14: Collected light distribution for the MCP-PMT installed in the KTAG.

the KTAG photon-detection system to have a demonstrated lifetime of $50\,\mathrm{C/cm^2}$. Other requirements set by HIKE for the MCP-PMT is a single photon detection rate of $10\,\mathrm{MHz/cm^2}$ without degradation of the signal due to charge saturation effects. The single photon detection requires a high amplification factor (gain) of $\mathcal{O}(10^6)$. The MCP-PMTs manufactured by Photonis with two ALD layers, provide the best lifetime, with no degradation in QE after $30\,\mathrm{C/cm^2}$, shown in Figure 5.11. A candidate model for the MCP-PMT for HIKE is the Photonis XP85012-S-R2D2

of the PLANACON line. However, the Photonis MCP-PMT does not match with the HIKE Phase 1 rate requirements, with a reduced gain above 1 MHz/cm^2, shown in Figure 5.15. It is possible to reach 10 MHz/cm^2 with smaller sensor size but this would result in a quadrupling of the cost to cover the light spot. Future research looking at reducing the resistance, capacitance and gain for single photon detection could possibly allow the XP85012-S-R2D2 to accommodate up to 10 MHz/cm^2.

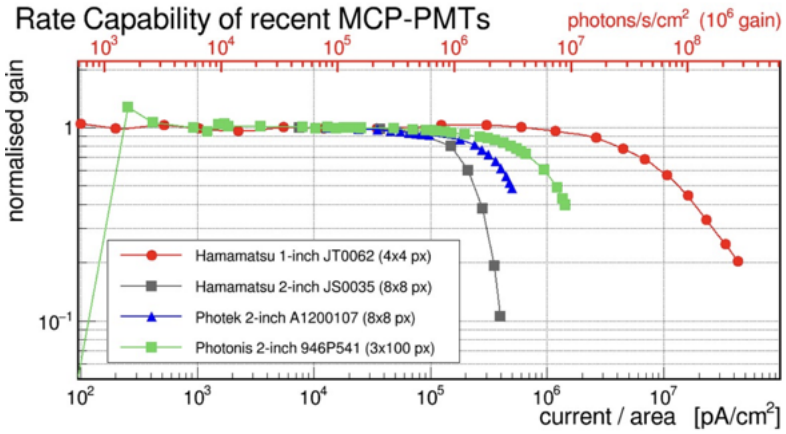

Figure 5.15: Rate capability of state of the art MCP-PMTs [98].

The Photonis MCP-PMT has a Collection Efficiency (CE) of above 60 %, which is the probability of the photo-electron passing through the micro channels of the MCP-PMT and producing a signal. With current technologies it is possible for MCP-PMTs to reach CE of over to 90 % [99], however the Photonis MCP-PMT is selected as it better fits the HIKE Phase 1 timing requirements as the higher CE models utilise late photo-electrons resulting in higher time resolutions. The XP85012-S-R2D2 MCP-PMT has a transit time spread of 50 ps with a timing precision RMS of 120 ps [100] and results in a time response shown in Figure 5.16 which is implemented for the HIKE simulations. The QE for the MCP-PMT from Photonis is shown in Figure 5.17. There are two options for the photocathode of the MCP-PMT available: a standard Bialkali (Sb-Rb-Cs, Sb-K-Cs) or a Hi-QE Blue. The HI-QE are more recent models, however there is no lifetime data available so the standard Bialkali is chosen for use in the simulation.

Further studies at the University of Birmingham are planned to characterise the Photonis XP85012-S-R2D2 MCP-PMT by measuring the lifetime, QE, CE, and other characteristics in order to decide which type would be used for high-intensity

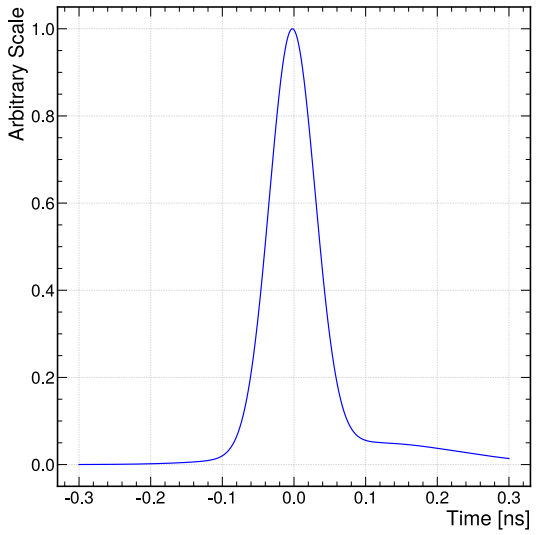

Figure 5.16: Time response of the Photonis XP85012-S-R2D2 MCP-PMT. The distribution is normalized such that the maximum bin has a value of 1.

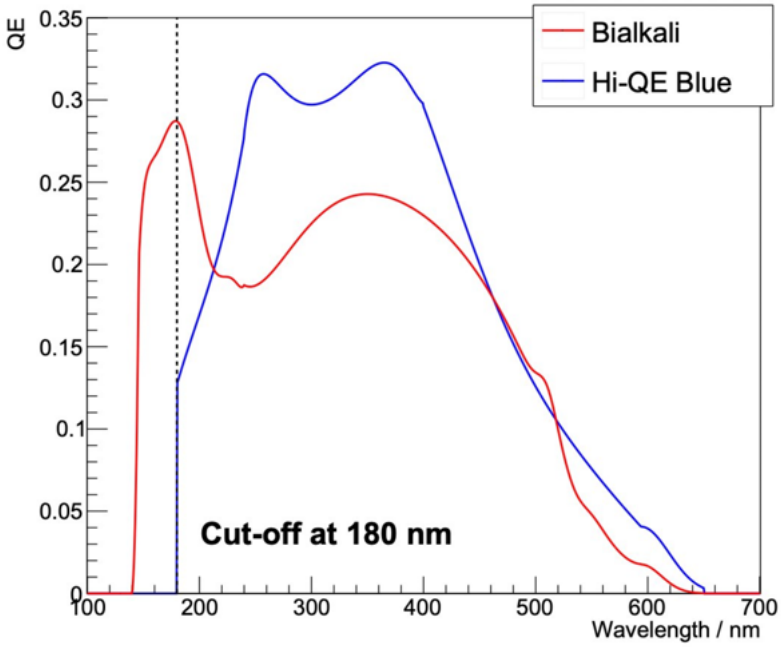

Figure 5.17: Quantum Efficiency of Photonis MCP-PMT as a function of wavelength.

kaon physics at HIKE.

From the MC simulation, the implemented MCP-PMTs results are shown in Figure 5.18. The MCP-PMT produced 24.3 photo-electrons per kaon candidate with a time resolution of 18 ps, taken from the Gaussian sigma of the distribution

in Figure 5.18 (Right). The results surpassed the requirements for the KTAG in HIKE and the upgrades are ready to be used in the HIKE simulations providing the lifetime and rate capability are acceptable.

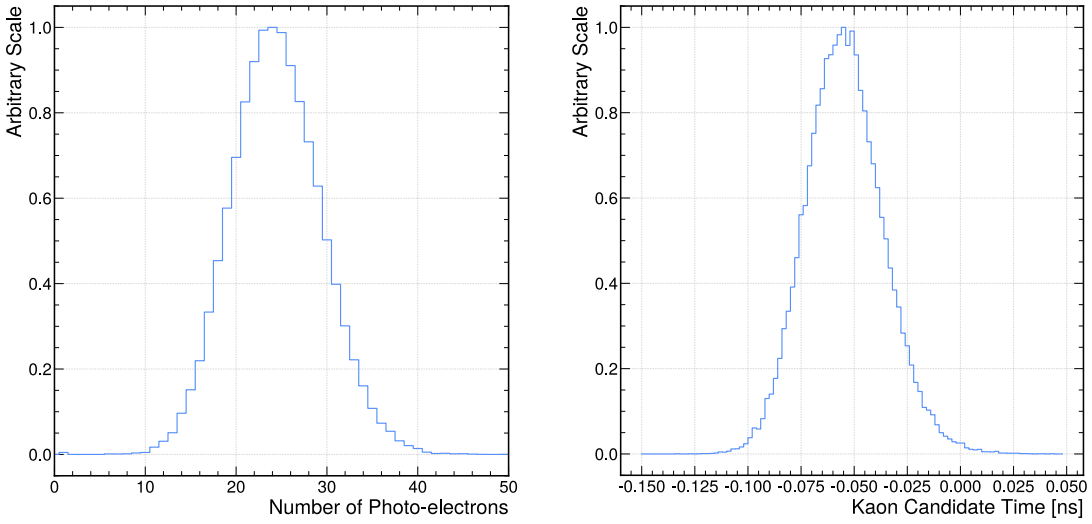

Figure 5.18: Results from the Monte Carlo simulation of CEDAR-H and MCP-PMT. Left, the number of photo-electrons per kaon candidate and right, the Kaon Candidate time. The distribution is normalized such that the maximum bin has a value of 1.

5.4 RICH Upgrade

The overall design of the NA62 RICH described in Section 2.3.5 is well suited for re-use within HIKE, but with an upgrade to the photon-detection system. The NA62 RICH photon detection system comprises two arrays on either side of the beam pipe, equipped with Hamamatsu R7400-U03 PMTs placed in a pattern shown in Figure 5.19. The PMTs have a single hit time resolution of 240 ps and a maximum quantum efficiency of 20 %. Due to the placement of the PMTs, the distance between the centre of each PMT is 18 mm, which is constrained by the sensor size and the geometry of the PMT itself. This distance between sensors is the main contributor to the single hit position resolution of 4.7 mm, resulting in an overall ring radius resolution of 1.5 mm. The number of hits per ring candidate and the single hit time resolution results in a ring time resolution of 80 ps. Due to the increased

beam intensity, the main requirement of the RICH for HIKE is a time resolution of 20–30 ps.

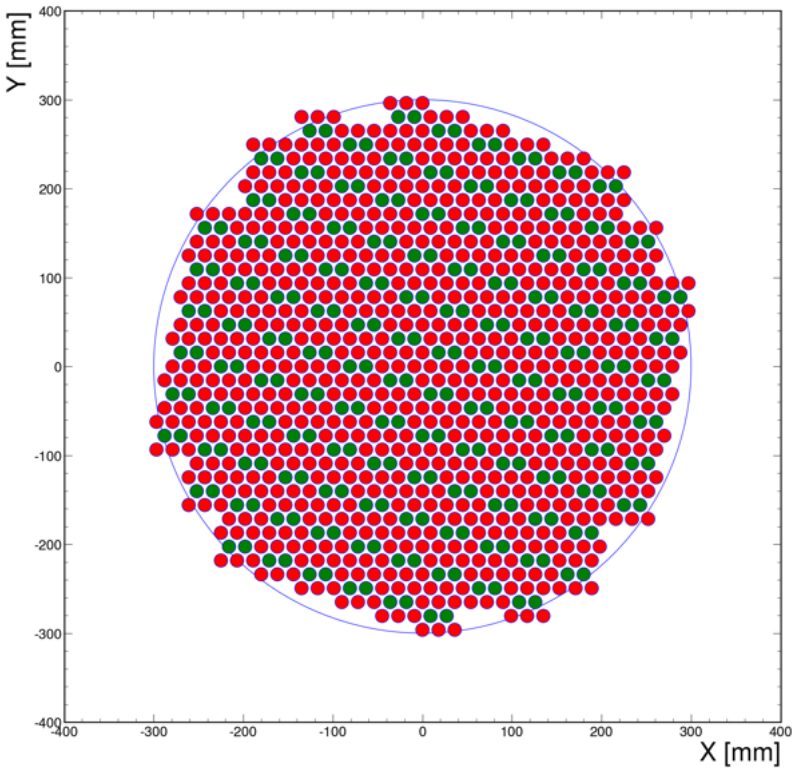

Figure 5.19: Diagram of the NA62 RICH PMT array. The blue circle depicts the extent of the Cherenkov light spot at the PMT array. The two colours are to aid viewing and do not represent physical differences between the PMTs.

The proposed RICH photon detection system upgrade is to replace the NA62 PMTs with a smaller sensor size, allowing for a reduced distances between sensor centres and reducing the hit position resolution. An excellent candidate for a sensor replacement are Silicon Photomultiplier (SiPM). SiPMs with small sensor sizes, a maximum quantum efficiency of 40 % and a single hit time resolution of at least 100 ps are available from major manufacturers. Three sensor sizes are selected for further investigation, $9 \times 9\,\mathrm{mm}^2$, $6 \times 6\,\mathrm{mm}^2$, and $3 \times 3\,\mathrm{mm}^2$. Each SiPM sensor size has apparent benefits and downsides, and a balance between performance and complexity/price has to be taken into account. The smaller sensors would produce a better hit position resolution but at an increased cost and complexity. A study is conducted to determine the optimal sensor size for the SiPMs, balancing overall detector performance with cost and complexity.

Using the upgraded NA62 software package described in Section 5.2, the new

SiPMs are implemented into the RICH Monte Carlo simulation, with the arrays shown in Figure 5.20. Compared to the PMT arrays currently used in NA62, the SiPM are aligned on the vertical axis to simplify the placement, allowed by their square geometry. The area of the expected light spot, shown in Figure 5.20, as a grey circle, is completely covered by the SiPMs with no gaps between the sensors which is an improvement compared to the NA62 setup shown in Figure 5.19. The

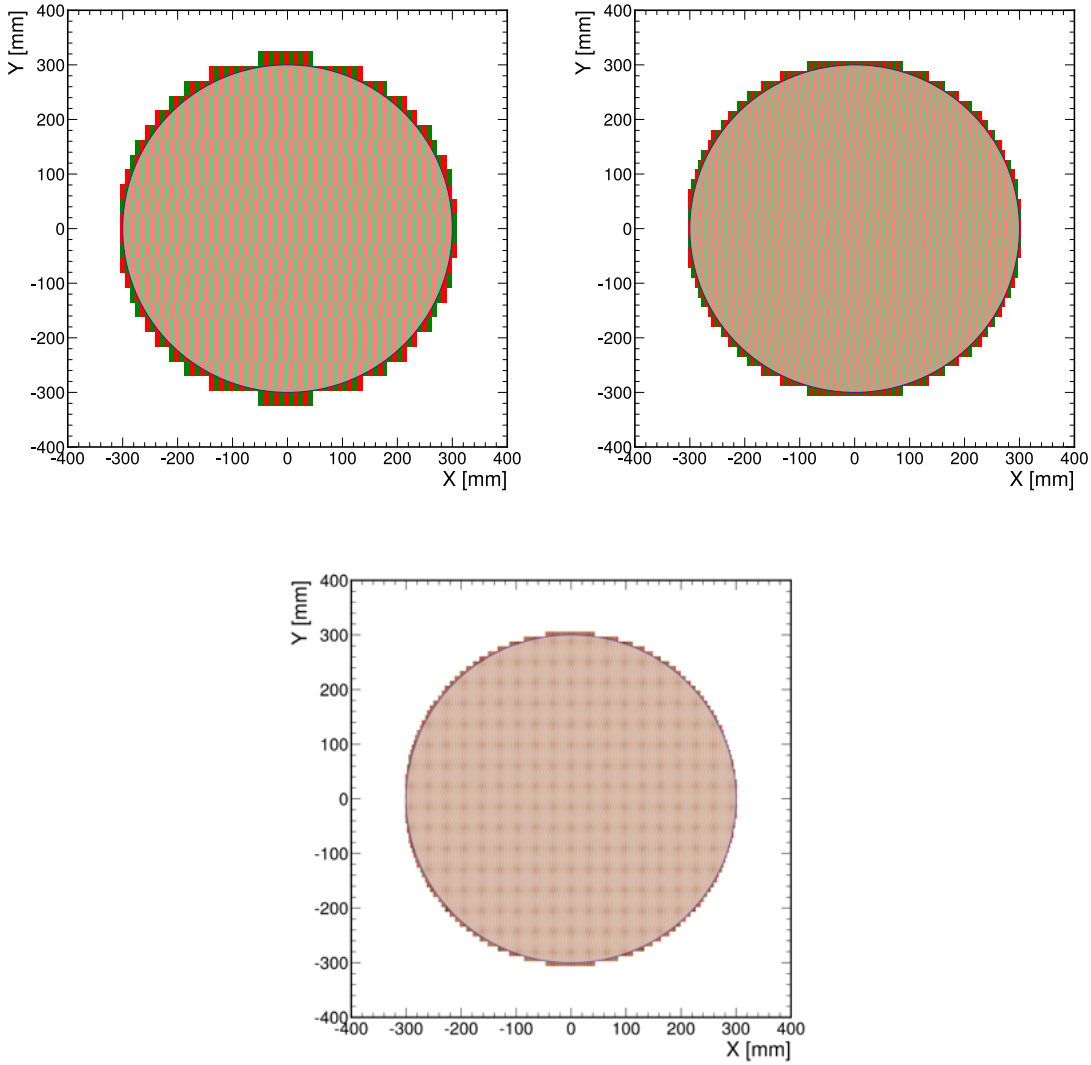

Figure 5.20: Diagram of proposed placement of the RICH SiPM arrays for use in HIKE using different sensor sizes. Left, 9x9 mm, center 6x6 mm and right 3x3 mm SiPMs. The grey circle shows the expected light spot at the PMT array.

performance for HIKE requires a SiPM with a maximum QE of 40 % [87]. The Hamamatsu S13360-**50CS series is selected as the preliminary candidate for the

RICH PMT upgrade to achieve this requirement. Hamamatsu offers a number of SiPMs in the S13360 series, with the **50CS selected for its improved Ultra Violet (UV) sensitivity and high maximum QE of 40 % at 460 nm, shown in Figure 5.21. Along with the QE efficiency, a single hit time resolution of 100 ps is required [87].

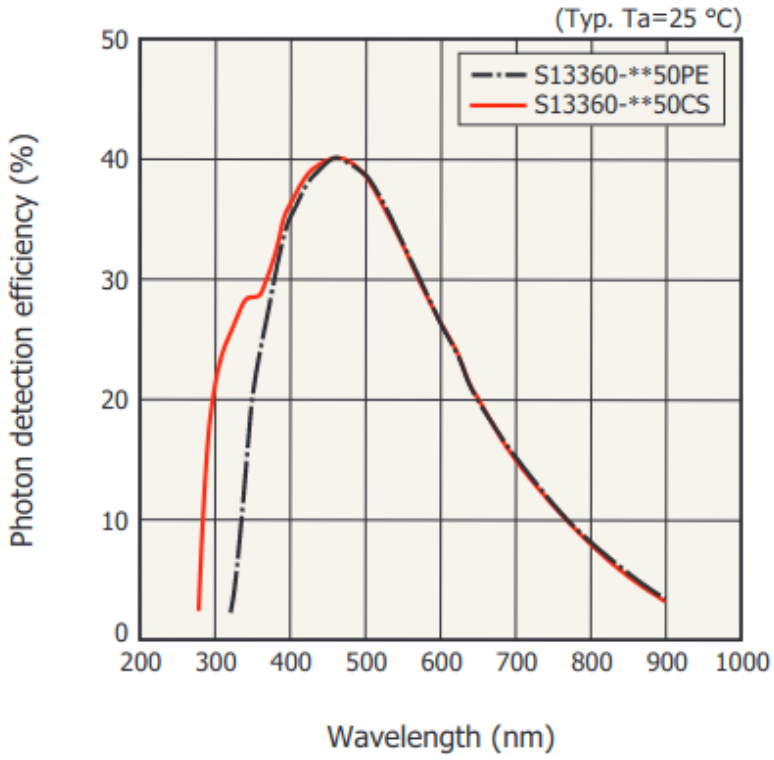

Figure 5.21: SiPM quantum efficiency taken from Hamamatsu S13360 data-sheet [101].

The manufacturer states the Hamamatsu S13360-**50CS series has excellent time resolution, but no definite value is given. The time resolution also depends on the final design of the RICH readout electronics and is to be measured in a test setup. The SiPMs from Hamamatsu have previously been tested and have reached a single hit time resolution below 100 ps [102]. For use in the simulation a conservative simple Gaussian time response curve with a width of 100 ps is used, to be updated in the future for a specific model when selected.

The expected performance of the RICH detector with SiPMs is compared to the current NA62 RICH detector in Table 5.3. With the increased QE, the expected number hits per π^+ is expected to increase by a factor of two. This, along with the improved time resolution of the new SiPMs resulted in an expected π^+ time resolution of 27 ps at 15 GeV/c and 20 ps at 45 GeV/c.

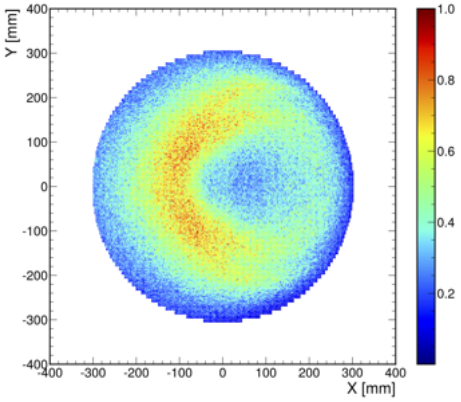

(a) 3 mm SiPMs Saleve.

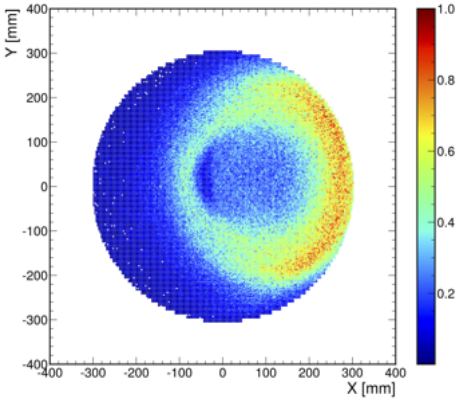

(b) 3 mm SiPMs Jura.

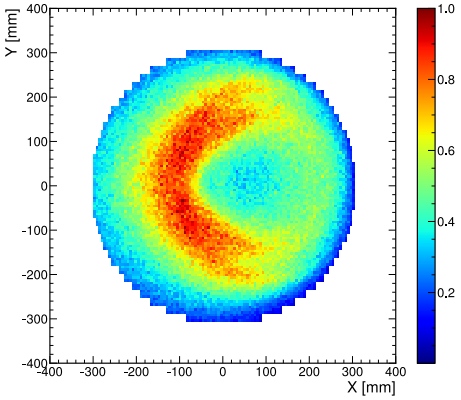

(c) 6 mm SiPMs Saleve.

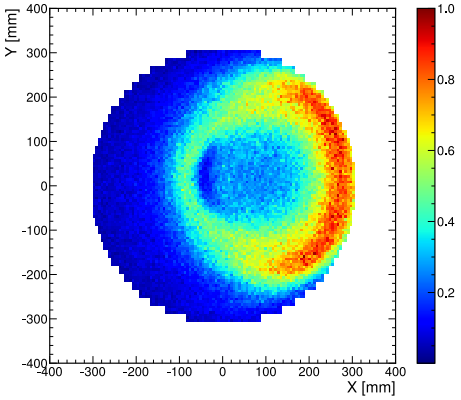

(d) 6 mm SiPMs Jura.

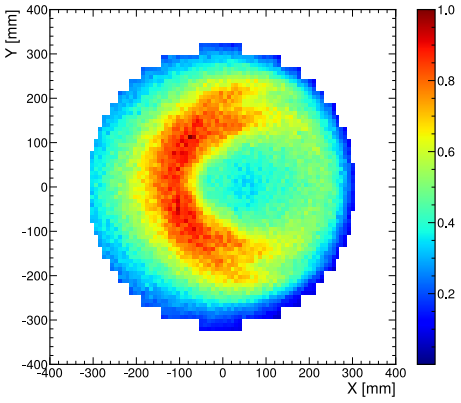

(e) 9 mm SiPMs Saleve.

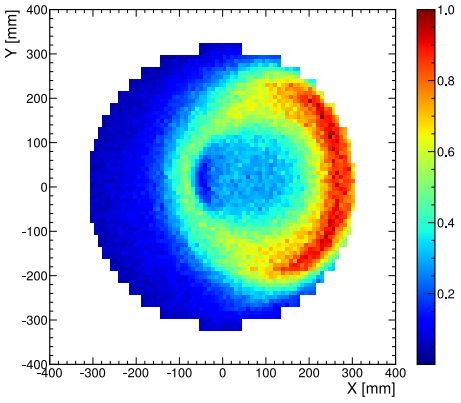

(f) 9 mm SiPMs Jura.

Figure 5.22: Cherenkov light illumination of RICH SiPM arrays for the three different sensor sizes produced from a MC sample of $K^+ \to \pi^0 e^+ \nu$ (K_{e3}). The left column shows illumination on the Saleve side of the RICH detector, which is the South-East side, facing Geneva. The right column shows the Jura side, which is the North-West side of the detector.

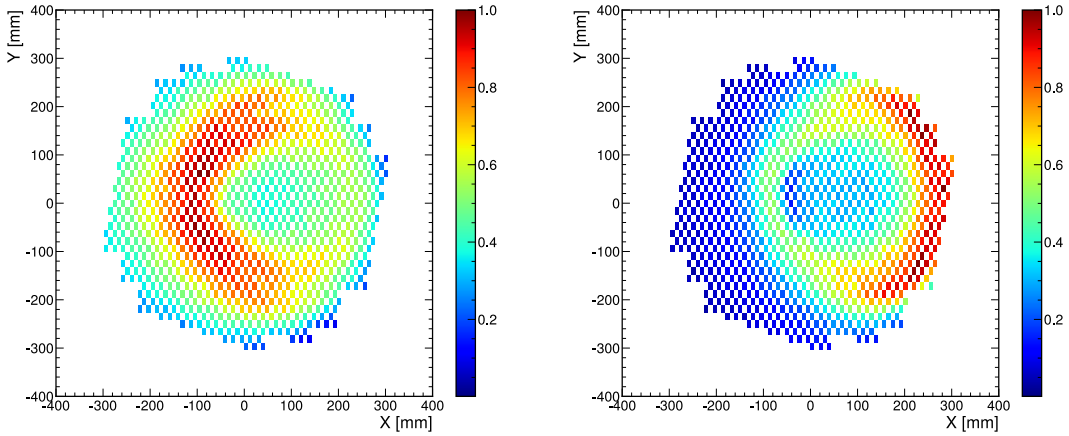

Figure 5.23: Cherenkov light illumination of the NA62 RICH PMT arrays produced from a MC sample of K_{e3}. The left plot shows illumination on the Saleve side of the RICH detector, which is the South-East side of the detector, facing Geneva. The right plot shows the Jura side, which is the North-West side of the detector.

	NA62 RICH	**HIKE RICH**
Sensor time resolution	240ps	100ps
Sensor maximum quantum efficiency	20%	40%
Number of photo-electrons for π^+ at 15 GeV/c	7	14
Number of photo-electrons for π^+ at 45 GeV/c	12	24
Time resolution for π^+ at 15 GeV/c	90ps	27ps
Time resolution for π^+ at 45 GeV/c	70ps	20ps

Table 5.3: Comparisons of the expected performance of the NA62 and HIKE RICH detectors [87].

Using the upgrades to the RICH detectors, the above expectations are confirmed by a Monte Carlo sample of K_{e3}.

For the three sensor sizes, a test production of 1M K_{e3} is used to determine the preliminary performance of the detector and compare to the NA62 setup. The plots in Figure 5.22 show the light distribution on the arrays for the three sensor sizes: 3 mm (a,b), 6 mm (c,d), and 9 mm (e,f) compared to the illumination on the current NA62 arrays in Figure 5.23. Due to the better placement of the square sensors, there is improved coverage of the light ring, especially in the Jura side which is the side in the positive x direction. The negative x is defined as the Saleve side. It is

clear to see that either sensor size would be an improvement on the current NA62 setup.

The reconstruction for the RICH was modified to accept the new configurations of the SiPMs and made flexible to allow for new designs in the future. In the reconstruction, the photo-electrons are clustered into ring candidates. The distribution of the number of reconstructed photo-electrons is shown in Figure 5.24, with the SiPM sensors resulting in a two-times increase in the number of hits per ring candidate. The improved number of reconstructed photo-electrons is due to the enhanced quantum efficiency of the SiPMs. There are minimal differences between the three sensor sizes shown in Figure 5.24(b-d), with the 3 mm sensors having a higher number of hits per ring candidate when compared to the 9 mm sensors.

The distribution of reconstructed ring candidate radius is shown in Figure 5.25, with the NA62 PMT array producing a resolution of 1.68 mm compared to 0.72 mm for the HIKE array with 9 mm SiPMs. With the smallest sensor size at 3 mm improving further to 0.41 mm. However, with the small sensor sizes the ring radius resolution is no longer dominated by the sensor size, but due to errors produced by small misalignments in the mirror and the chromatic dispersion in the radiator gas. The expected resolution of the ring radius for 3 mm sensor is calculated from the single hit position resolution

$$\sigma_{hit} = \frac{3}{\sqrt{12}} = 0.87\,\text{mm}, \tag{5.1}$$

where 3 mm is the distance between the centre of the sensors and $\sqrt{12}$ is the standard deviation of the uniform distribution. The single hit position resolution is then used with the number of photo-electrons per ring candidate to estimate the ring radius resolution of the ring candidate

$$\sigma_{ring}^{3\,\text{mm}} = \frac{\sigma_{hit}}{\sqrt{N_{hits}}} = \frac{0.87}{\sqrt{28.86}} = 0.16\,\text{mm}, \tag{5.2}$$

where N_{hits} is the average number of hits per ring candidate. The ring radius resolutions are produced in ideal circumstances in the MC where the placement of the mirrors is perfect. In reality the ring resolutions are expected to be worse. The expected resolution is calculated for the 6 mm $\sigma_{ring}^{6\,\text{mm}} = 0.33\,\text{mm}$ and the 9 mm $\sigma_{ring}^{9\,\text{mm}} = 0.51\,\text{mm}$ sensor sizes. As all the sensor sizes are dominated by the mirror misalignment and the chromatic dispersion, the ideal candidate would be the 9 mm

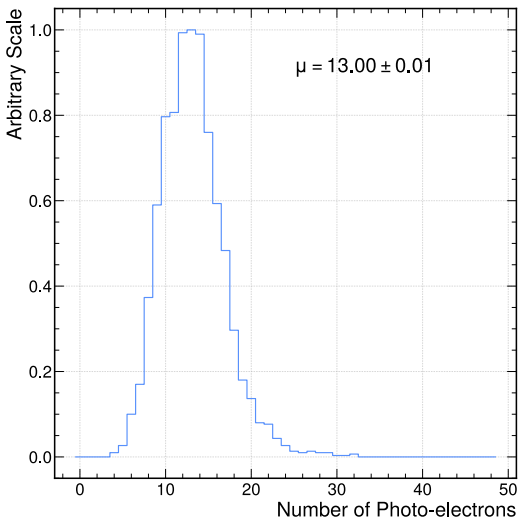

(a) NA62 PMT arrays.

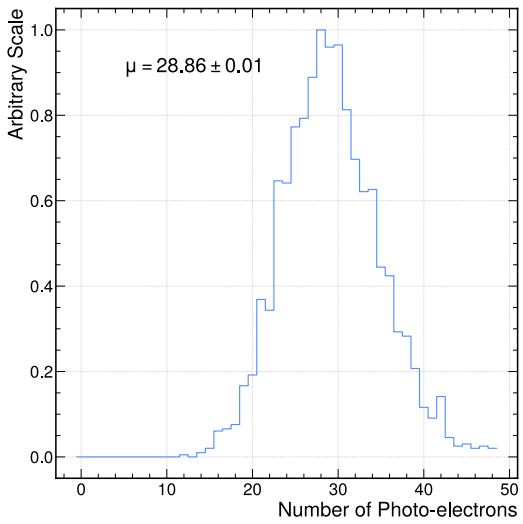

(b) 3 mm SiPMs.

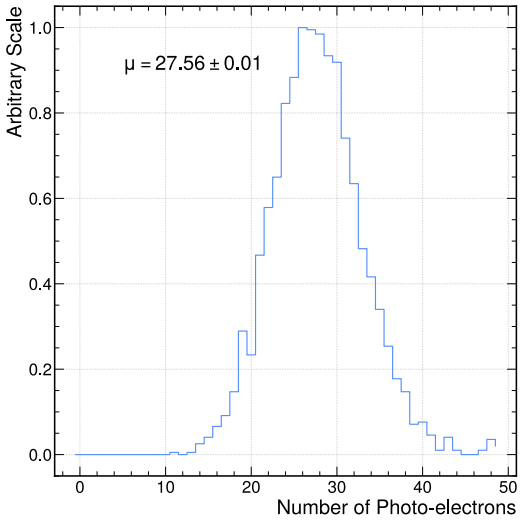

(c) 6 mm SiPMs.

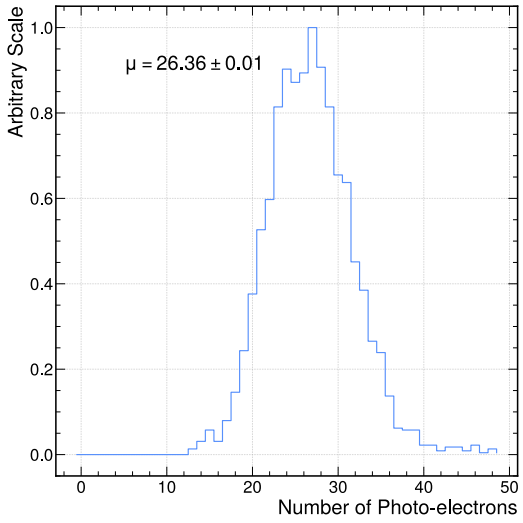

(d) 9 mm SiPMs.

Figure 5.24: Number of photo-electrons per ring candidate for NA62 PMTs and the three possible HIKE SiPMs produced from a MC sample of K_{e3}. The distribution is normalized such that the maximum bin has a value of 1.

sensor size due to its reduced cost and complexity. The 3 mm sensor size would be the best choice if the mirror misalignment and chromatic dispersion could be reduced, however this is not possible with the current design of the RICH detector.

The time resolution of the RICH detector is calculated using the K_{e3} sample by equally splitting the photo-electrons of the ring candidates into two sets and

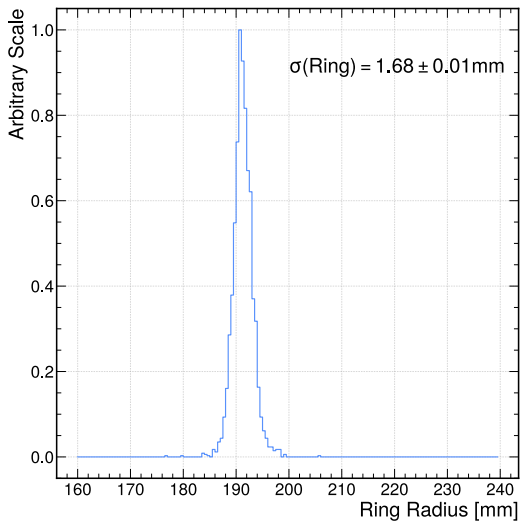

(a) NA62 PMT arrays.

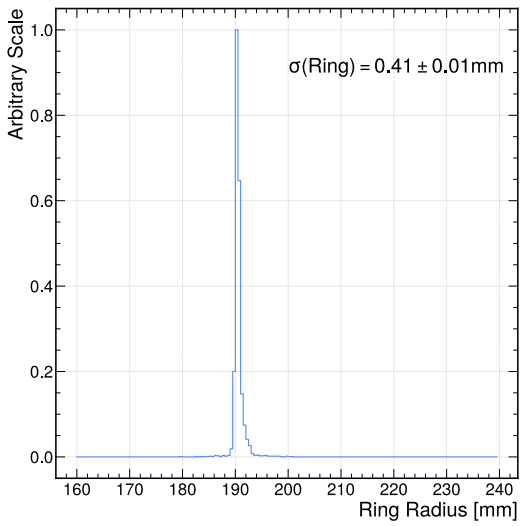

(b) 3 mm SiPMs.

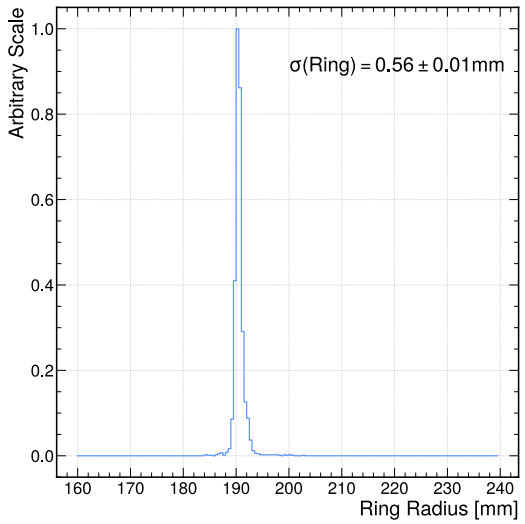

(c) 6 mm SiPMs.

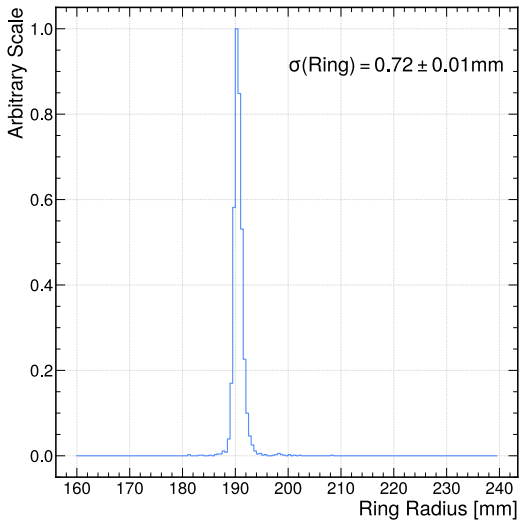

(d) 9 mm SiPMs.

Figure 5.25: Reconstructed ring radius for electron candidates for NA62 PMTs and the three possible HIKE SiPMs produced from a MC sample of $K^+ \to \pi^0 e^+ \nu$ (Ke3). The distribution is normalized such that the maximum bin has a value of 1.

calculating the mean time difference between them, with the results are shown in Figure 5.26. This method is used to remove any dependence on the reference time with respect to the single hit times. The 3×3 mm sensors produced the best time resolution of 20.04 ps compared to the 9x9 mm sensors with a time resolution of 21.22 ps. However, each sensor size produces a time resolution of less than 30 ps,

fulfilling the requirements of HIKE. The improvement is clear with using the SiPMs when compared with the NA62 PMTs in Figure 5.26, with a time resolution of 61.35 ps.

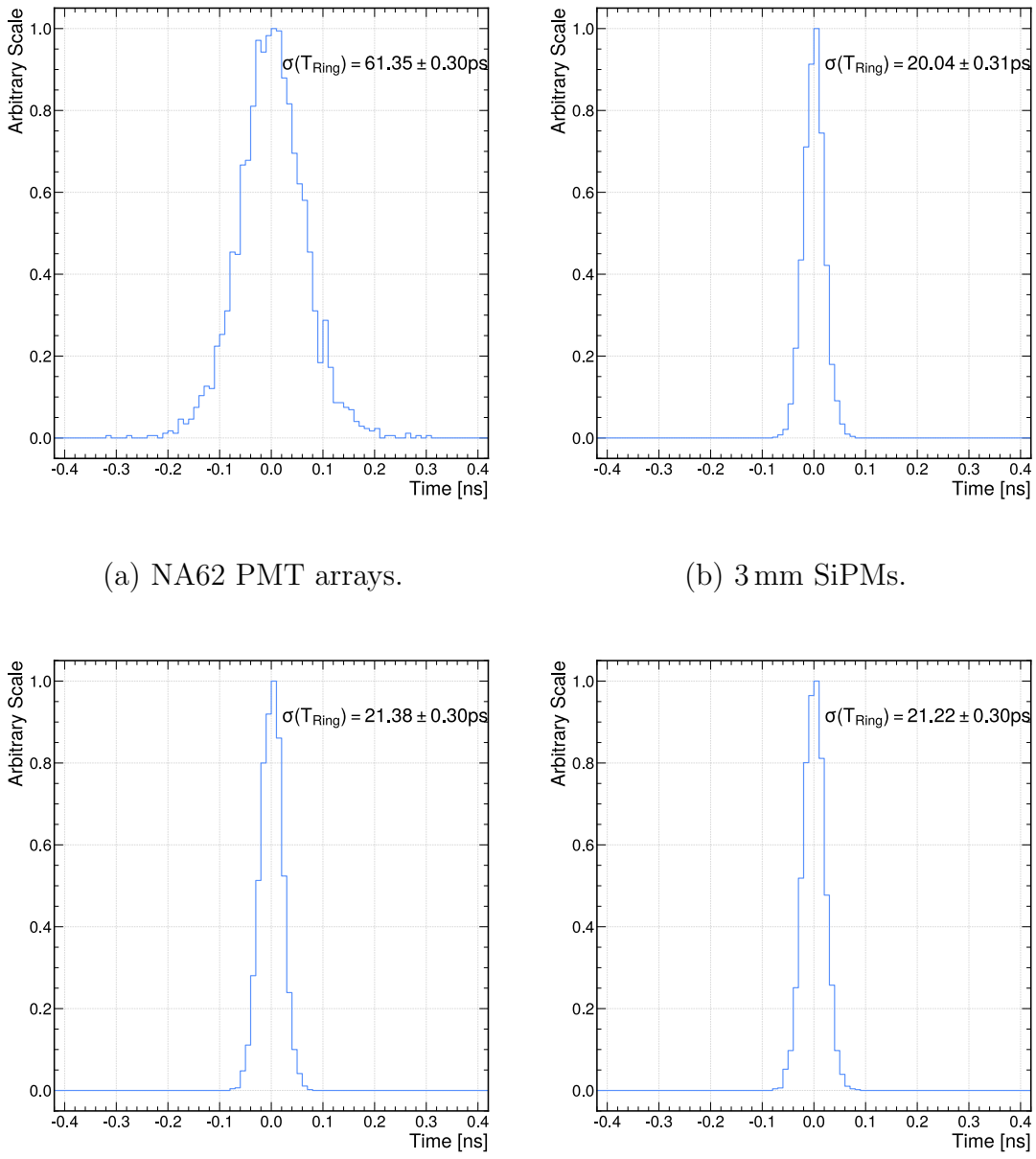

(a) NA62 PMT arrays.

(b) 3 mm SiPMs.

(c) 6 mm SiPMs.

(d) 9 mm SiPMs.

Figure 5.26: Time resolution for NA62 PMTs and the three possible HIKE SiPMs, calculated from the time difference between two equally populated subsets of hits within the ring candidate. A detailed description of the procedure is provided here [103]. The distribution is normalized such that the maximum bin has a value of 1.

All three SiPM sensor sizes produce results which exceed the requirements for

HIKE with a time resolution of around 20 ps and improvements on the reconstructed ring radius resolution. From the results of the HIKE simulation, the 9×9 mm SiPMs are to be used as they provide excellent performance at a reduced cost and complexity compared to implementing the smaller sensor sizes in the detector. A clear benefit is reducing the number of channels from 72,780 for the $3 \times 3\,\mathrm{mm}^2$ SiPMs to 8,588 for the $9 \times 9\,\mathrm{mm}^2$ SiPMs.

5.5 Detector Particle Rates for HIKE Phase 2

It is necessary to determine the expected particle rate in the upgraded and yet to be upgraded detectors. The upgraded STRAW detector utilising 5 mm diameter straws is also included in the HIKE simulations. The expected rate for Phase 1 is calculated by scaling the known NA62 rates by the expected increase in beam intensity by a factor of 4 compared to NA62. The rates for Phase 2 are calculated using the new simulation software described in the previous sections.

An array of input files are produced in BDSIM [104] from the simulation of the target and the expected beam components by the CERN beam group. Each file contains the simulated HIKE beam components at a Z position of 120 m from the target, which is the start of the FV. The files are used as an input to the NA62MC software as the primary beam. Each file contains 10,000 events, corresponding to 10,000 protons on target. As there are 18,000 files produced in total, this is equivalent to 1.8×10^8 protons on target. However, the statistics are not enough to obtain a reasonable estimate of the rates, so each file is used 11 times as an input to the simulation with random seeds to increase the sample size. The simulation is run allowing for four main K_L decays: $K_L \to \pi^{\pm} e^{\mp} \nu_e$ (K^0_{e3}), $K_L \to \pi^{\pm} \mu^{\mp} \nu_\mu$ ($K^0_{\mu 3}$), $K_L \to \pi^0 \pi^0 \pi^0$ and $K_L \to \pi^+ \pi^- \pi^0$. After the simulation, the output is reconstructed using the NA62 reconstruction software. The rates are calculated by scaling the numbers in the output by the expected HIKE Phase 2 beam conditions, i.e, a spill time of 4.8 seconds and a beam intensity of 2×10^{13} protons per spill.

From the simulation the K_L rate at the entrance of the fiducial volume is calculated as 304.1 MHz. The rate of the four main K_L decays inside the FV is shown in Table 5.4.

KL decay	**Rate [MHz]**
$K_L \to \pi^{\pm} e^{\mp} \nu_e$ (K^0_{e3})	13.89
$K_L \to \pi^{\pm} \mu^{\mp} \nu_\mu$ ($K^0_{\mu 3}$)	9.63
$K_L \to \pi^0 \pi^0 \pi^0$	6.60
$K_L \to \pi^+ \pi^- \pi^0$	4.45

Table 5.4: Rates of the four main K_L decays in the HIKE Phase 2 fiducial volume, calculated from simulations.

The total particle rates in the detectors from K_L decays in the FV are shown in Table 5.5. The rate is calculated using the hits in each detector channel and then converted to the expected rate. There is an discrepancy with the large particle rate in the spectrometer for the $K_L \to \pi^0\pi^0\pi^0$ decay. A much lower rate is expected due to the lack of charged daughter particles from the decay. Even with a lower branching ratio, it is expected that the $K_L \to \pi^+\pi^-\pi^0$ decay should have a higher rate in the spectrometer due to the charged pions in the final state. It is due to the large number of particles produced from secondary interactions which needs to be investigated.

Detector	$\boldsymbol{K_L}$ **Decay [MHz]**			
	$\boldsymbol{K_L \to \pi^{\pm} e^{\mp} \nu_e}$ **BR = (40.55 ± 0.11)%**	$\boldsymbol{K_L \to \pi^{\pm} \mu^{\mp} \nu_\mu}$ **BR = (27.04 ± 0.07)%**	$\boldsymbol{K_L \to \pi^0 \pi^0 \pi^0}$ **BR = (19.52 ± 0.12)%**	$\boldsymbol{K_L \to \pi^+ \pi^- \pi^0}$ **BR = (12.54 ± 0.05)%**
STRAW-1	126.8	79.9	50.5	49.2
STRAW-2	162.8	85.1	80.7	58.0
STRAW-3	165.7	89.3	67.7	56.1
STRAW-4	189.2	93.6	87.5	64.4
NCHOD	10.3	5.2	4.9	3.7
CHOD	90.5	33.4	61.3	33.8
IRC	3.8	1.2	4.2	2.0
LKr	609.5	266.0	440.7	298.3
MUV1	129.9	102.4	0.6	64.1
MUV2	10.3	17.9	0.1	4.7
MUV3	0.9	5.2	0.2	0.6
HAC	10.0	11.5	0.3	6.1

Table 5.5: Total rates in the detectors for the four main K_L decays: $K_L \to \pi^{\pm} e^{\mp} \nu_e$ (K^0_{e3}), $K_L \to \pi^{\pm} \mu^{\mp} \nu_\mu$ ($K^0_{\mu 3}$), $K_L \to \pi^0\pi^0\pi^0$ and $K_L \to \pi^+\pi^-\pi^0$, along with their Branching Ratios (BR).

By using information from the MC, the origin of the particles that produce the hits in the spectrometer are found. The production Z and radius of particles which produce a hit in the spectrometer is shown in Figure 5.27. For the $K_L \to \pi^0\pi^0\pi^0$ decay, the majority (80 %) of the particles are produced after Z=210 m in the walls of the vacuum decay tube and the spectrometer chambers themselves. With only 20 % of particles produced before Z=210 m, from the primary decay process. Figure 5.28

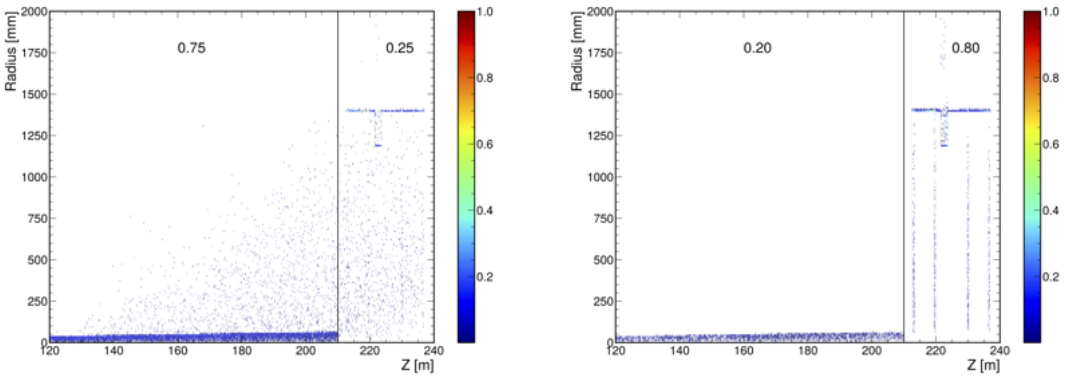

Figure 5.27: Production Z and radius of particles producing a hit in the Spectrometer with the fraction of particles produced before and after Z=210 m. Left, for the $K_L \to \pi^+\pi^-\pi^0$ decay and right, for the $K_L \to \pi^0\pi^0\pi^0$ decay.

illustrates this further, where the MC particle identification code of the particles producing hits in the spectrometer is shown. For the $K_L \to \pi^0\pi^0\pi^0$ the majority of the particles are electron/positron pairs, produced in interactions of photons in the walls of the vacuum decay vessel and the spectrometer chambers. This is compared to the $K_L \to \pi^+\pi^-\pi^0$ decay where the majority of the particles are pions produced in the decay within the FV.

The rate in the detectors produced by only the daughter particles of the K_L decays is used to remove the contribution from the secondary particles. The daughter particles are selected with using MC information where the GEANT4 production process is "Decay", which should include any subsequent decays of the daughter particles, e.g. $\pi^0 \to \gamma\gamma$. This excludes all hits from particles produced by "gamma conversion", which produce electron-positron pairs and impact the rate, as described above.

The rates for each detector are shown in Table 5.6. The rates from the decay daughter particles are lower when compared to the total rates in Table 5.5. The

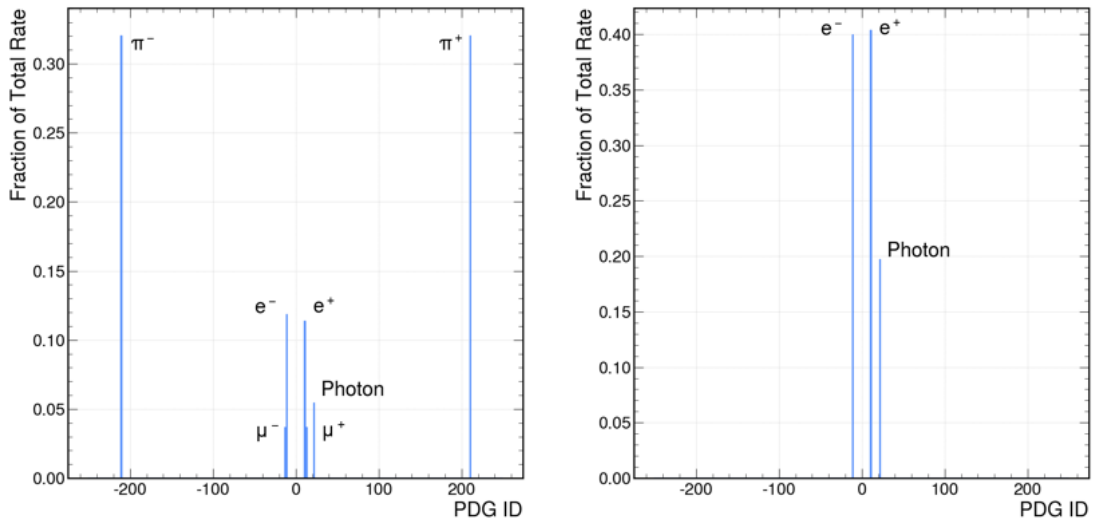

Figure 5.28: The fraction of the the total rate for particles producing a hit in the Spectrometer. Left, for the $K_L \to \pi^+\pi^-\pi^0$ decay and right, for the $K_L \to \pi^0\pi^0\pi^0$ decay. The particles are selected using the PDG particle identification code [12].

rates in the spectrometer for the $K_L \to \pi^0\pi^0\pi^0$ decay are much lower, which is expected. Overall, the rates are acceptable for the detectors. It is assumed that most of the hits not produced from the decay of the K_L or other subsequent decays would be removed by the trigger system as they would be outside the time window of the K_L decay.

It is essential to understand the rates of the detectors in order to determine the overall detector design, especially for the electronics that would need to be designed to meet the high rates for HIKE. The calculated rates will inform the development of the overall data acquisition and trigger systems. It is vital to know the maximum channel rates in the detectors to design the electronics to handle the highest expected rate. The maximum channel rates for each detector is calculated and is shown in Table 5.7.

The detectors that have finalised designs are implemented in the simulation, which allows for correct rate calculation. This includes the STRAW and RICH detectors. Other detectors that need to be upgraded to increase their granularity, were not yet finalised and therefore are not implemented in the simulation. This results in an incorrect calculation for the channel rates as it is determined by the detector design and the layout of the channels in NA62. However, the rates are still

Detector	K_L Decay Particle Rates [MHz]			
	$K_L \to \pi^{\pm} e^{\mp} \nu_e$ $(40.55 \pm 0.11)\%$	$K_L \to \pi^{\pm} \mu^{\mp} \nu_\mu$ $(27.04 \pm 0.07)\%$	$K_L \to \pi^0 \pi^0 \pi^0$ $(19.52 \pm 0.12)\%$	$K_L \to \pi^+ \pi^- \pi^0$ $(12.54 \pm 0.05)\%$
STRAW-1	14.7	11.2	1.3	5.6
STRAW-2	15.4	11.7	2.1	6.2
STRAW-3	16.1	12.1	2.5	6.6
STRAW-4	16.5	12.2	3.4	6.9
NCHOD	19.9	10.8	9.4	7.0
CHOD	16.1	11.3	8.1	7.8
IRC	1.9	0.8	1.8	1.0
LKr	15.4	11.6	19.9	10.5
MUV1	7.6	9.8	0.3	4.7
MUV2	2.7	7.2	0.1	1.5
MUV3	1.1	6.7	0.3	0.9
HAC	0.6	1.0	0.1	0.3

Table 5.6: Detector rates for the four main K_L decays: $K_L \to \pi^{\pm} e^{\mp} \nu_e$ (K^0_{e3}), $K_L \to \pi^{\pm} \mu^{\mp} \nu_\mu$ ($K^0_{\mu 3}$), $K_L \to \pi^0 \pi^0 \pi^0$ and $K_L \to \pi^+ \pi^- \pi^0$, produced directly from the daughter particles of the K_L decays.

used to inform the detector design.

The rates for the cross-sections of the detectors are calculated by collecting particles passing through the Z plane of the detector. This uses information from the MC for particles at specific points along the HIKE detector setup, called checkpoints. The rates for charged particles produced from the four K_L decays at each checkpoint are shown in Table 5.8. This allows for the correct determination of the rates for the detectors not yet finalised. The particle rates are collected from the cross-section of the outer volume for each sub-detector found in the MC simulation. For the Straw-1&3 the values of the cross-section used are, a circle of radius of 141.5 mm, NCHOD a square of length 330 mm, CHOD a square of length 244 mm, IRC a square of length 122 mm, MEC a circle of radius 182.5 mm, MUV-1&2 a square of length 320 mm, MUV-3 a square of length 281 mm and HAC a square of length 281 mm.

However, the rates are collected from the cross-section at the expected detector position, without accounting for the beam hole to accommodate beam particles passing through the detector. This results in higher maximum rates. An example

Detector	K_L Decay Daughter Max Channel Rates [kHz]			
	$K_L \to \pi^{\pm} e^{\mp} \nu_e$ $(40.55 \pm 0.11)\%$	$K_L \to \pi^{\pm} \mu^{\mp} \nu_\mu$ $(27.04 \pm 0.07)\%$	$K_L \to \pi^0 \pi^0 \pi^0$ $(19.52 \pm 0.12)\%$	$K_L \to \pi^+ \pi^- \pi^0$ $(12.54 \pm 0.05)\%$
STRAW-1	325	254	51	186
STRAW-2	377	254	27	154
STRAW-3	329	265	19	138
STRAW-4	365	258	39	138
NCHOD	484	329	186	206
CHOD	1290	635	786	559
IRC	1020	345	1063	516
LKr	575	321	385	293
MUV1	1830	1496	19	1032
MUV2	329	583	15	190
MUV3	79	234	39	43
HAC	206	210	27	138

Table 5.7: Maximum channel rates for the four main K_L decays: $K_L \to \pi^{\pm} e^{\mp} \nu_e$ (K^0_{e3}), $K_L \to \pi^{\pm} \mu^{\mp} \nu_\mu$ ($K^0_{\mu 3}$), $K_L \to \pi^0 \pi^0 \pi^0$ and $K_L \to \pi^+ \pi^- \pi^0$, produced directly from the daughter particles of the K_L decays.

Checkpoints (Z Position)	K_L Decay Particle Rates [kHz/cm^2]							
	$K_L \to \pi^{\pm} e^{\mp} \nu_e$ $(40.55 \pm 0.11)\%$		$K_L \to \pi^{\pm} \mu^{\mp} \nu_\mu$ $(27.04 \pm 0.07)\%$		$K_L \to \pi^0 \pi^0 \pi^0$ $(19.52 \pm 0.12)\%$		$K_L \to \pi^+ \pi^- \pi^0$ $(12.54 \pm 0.05)\%$	
	Max	Average	Max	Average	Max	Average	Max	Average
STRAW-1 Entry (213.5 m)	19.28	0.34	16.64	0.25	0.05	10^{-3}	10.55	0.13
STRAW-3 Entry (230.5 m)	6.93	0.29	6.23	0.23	0.14	0.02	4.04	0.12
NCHOD Entry (237.6 m)	4.93	0.16	4.43	0.13	0.17	0.01	2.66	0.06
CHOD Entry (238.9 m)	4.60	0.27	4.07	0.21	0.14	0.02	2.55	0.11
IRC Entry (239.5 m)	4.77	0.26	3.89	0.21	0.13	0.02	2.43	0.11
LKr Entry (240.4 m)	4.60	0.15	3.72	0.13	0.10	0.01	2.34	0.06
MUV1 Entry (243.2 m)	3.92	0.02	3.38	0.08	0.03	10^{-4}	1.96	0.02
MUV2 Entry (244.4 m)	3.70	0.01	3.25	0.08	0.03	10^{-4}	1.82	0.01
MUV3 Entry (245.3 m)	0.15	0.08	1.05	0.08	0.01	10^{-7}	0.09	0.01
HAC Entry (253.3 m)	3.40	0.09	2.88	0.09	0.02	10^{-5}	1.44	0.01

Table 5.8: Particle rates at specified checkpoints along the HIKE detector setup. Including the average rate across the cross-section and the maximum rate per cm^2 for the four main K_L decays: $K_L \to \pi^{\pm} e^{\mp} \nu_e$ (K^0_{e3}), $K_L \to \pi^{\pm} \mu^{\mp} \nu_\mu$ ($K^0_{\mu 3}$), $K_L \to \pi^0 \pi^0 \pi^0$ and $K_L \to \pi^+ \pi^- \pi^0$, produced directly from the daughter particles of the K_L decays.

cross-section at the entry of the first STRAW chamber is shown in Figure 5.29, where it is clear that the highest rate is found at the centre. As the detectors are not yet designed and the beam hole size is unknown, the size of the beam hole is estimated by calculating the beam divergence at the detector Z position. The beam divergence is calculated using the formula

$$\delta_{beam} = 0.4\,\text{mrad} \times \text{Z}. \tag{5.3}$$

Using Equation 5.3, a mask simulating the beam hole is applied to remove any

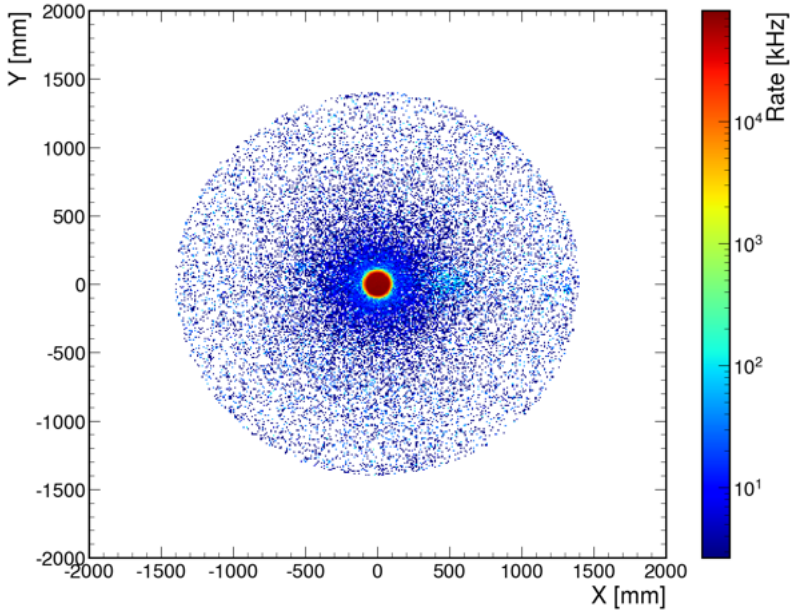

Figure 5.29: Rate of particles across the cross section at the first STRAW chamber entrance at Z=213.5 m.

particles that would pass through beam pipe. The particle rates with the beam hole mask applied are shown in Table 5.9. As expected, this reduced the maximum rate for most detectors without impacting the average rate across the detector plane.

For the design of each detector, it is also important to calculate the total rates produced by different particles, which is shown in Table 5.10. These rates include all particles, including those from secondary interactions. The majority of the particle rates at the detector planes are from photons, especially in the spectrometer. The rate from charged particles suggests that the detectors could be designed and built with current technologies.

All particle rate information from the simulation, shown in this section, will drive the design of the detectors that are not already upgraded. Table 5.10 is used

		K_L Decay Particle Rates [kHz/cm^2]							
		$K_L \to \pi^\pm e^\mp \nu_e$ $(40.55 \pm 0.11)\%$		$K_L \to \pi^\pm \mu^\mp \nu_\mu$ $(27.04 \pm 0.07)\%$		$K_L \to \pi^0\pi^0\pi^0$ $(19.52 \pm 0.12)\%$		$K_L \to \pi^+\pi^-\pi^0$ $(12.54 \pm 0.05)\%$	
Checkpoints (Z Position)	**Beam radius [mm]**	**Max**	**Average**	**Max**	**Average**	**Max**	**Average**	**Max**	**Average**
STRAW-1 Entry (213.5 m)	85.4	11.59	0.305	9.504	0.226	0.047	0.001	5.863	0.109
STRAW-3 Entry (230.5 m)	92.2	5.515	0.280	4.900	0.219	0.139	0.017	3.087	0.113
NCHOD Entry (237.6 m)	95.0	3.959	0.152	3.143	0.124	0.166	0.012	2.032	0.063
CHOD Entry (238.9 m)	95.6	3.418	0.256	3.017	0.202	0.139	0.017	1.849	0.104
IRC Entry (239.5 m)	95.8	3.418	0.249	2.921	0.198	0.133	0.016	1.733	0.100
LKr Entry (240.4 m)	96.2	2.501	0.145	2.053	0.122	0.100	0.010	1.314	0.059
MUV1 Entry (243.2 m)	97.3	0.279	0.016	1.311	0.074	0.033	10^{-4}	0.227	0.012
MUV2 Entry (244.4 m)	97.8	0.167	0.008	1.215	0.069	0.027	10^{-4}	0.116	0.007
MUV3 Entry (245.3 m)	98.1	0.153	0.008	1.051	0.079	0.007	10^{-7}	0.089	0.007
HAC Entry (253.3 m)	101.3	0.167	0.008	1.147	0.078	0.013	10^{-6}	0.138	0.007

Table 5.9: Particle rates per cm^2 at specified checkpoints along the HIKE detector setup excluding particles passing within the expected beam radius for the four main K_L decays: $K_L \to \pi^\pm e^\mp \nu_e$ (K^0_{e3}), $K_L \to \pi^\pm \mu^\mp \nu_\mu$ ($K^0_{\mu 3}$), $K_L \to \pi^0\pi^0\pi^0$ and $K_L \to \pi^+\pi^-\pi^0$, produced directly from the daughter particles of the K_L decays.

Checkpoints	**Total Particle Rates kHz/cm^2**									
	$e^{+/-}$		$\mu^{+/-}$		$\pi^{+/-}$		γ		**Charged Particles**	
	Max	**Average**	**Max**	**Average**	**Max**	**Average**	**Max**	**Average**	**Max**	**Average**
STRAW-1 Entry (213.5 m)	264	0.26	224	1.58	117	0.41	13426	13.87	360	2.56
STRAW-3 Entry (230.5 m)	246	0.59	179	1.34	120	0.40	11076	14.02	291	2.62
NCHOD Entry (237.6 m)	216	0.45	174	1.13	115	0.24	11770	8.50	238	1.98
CHOD Entry (238.9 m)	318	2.96	176	1.18	112	0.41	11687	15.57	376	5.79
IRC Entry (239.5 m)	251	3.85	176	1.17	85	0.40	11481	15.58	291	5.64
MEC Entry (240.4 m)	85	1.76	174	1.12	109	0.24	166	0.30	238	3.25
MUV1 Entry (243.2 m)	5	0.01	190	1.04	32	0.03	29	0.01	190	1.07
MUV2 Entry (244.4 m)	8	10^{-3}	162	1.00	5	10^{-3}	5	10^{-3}	163	0.98
MUV3 Entry (245.3 m)	5	10^{-4}	115	0.89	3	10^{-4}	3	10^{-3}	115	0.88
HAC Entry (253.3 m)	11	0.02	120	0.89	5	10^{-3}	3	10^{-3}	120	0.89

Table 5.10: Average and maximum particle rates per cm^2 for specified checkpoints along the length of the HIKE detector.

in the HIKE proposal to demonstrate the requirement for upgrading the detectors to handle the increased rates.

5.6 Conclusions

Unfortunately, in 2024, the CERN management did not approve HIKE for operation in ECN3. However, the development of the detectors, software and the subsequent

physics studies is currently being utilised for studies within the KOTO II proposal [105].

Chapter 6

Conclusions

The CEDAR-KTAG system delivers kaon identification for the NA62 experiment. A new differential Cherenkov counter with achromatic ring focus (CEDAR) with hydrogen gas (H_2) as a radiator gas was designed by NA62 group at the University of Birmingham and built at CERN where it was characterised and tested at a test-beam in 2022. CEDAR-Hydrogen (CEDAR-H) was installed and commissioned in the NA62 beam-line for the 2023 run. A number of pressure scans and other tests were completed to ensure that the detector was ready for data taking. The detector produced excellent results with 13 % greater light yield compared with CEDAR-West (CEDAR-W) with nitrogen gas (N_2). CEDAR-H has been in operation since 2023 and has performed flawlessly. The KTAG with CEDAR-H resulted in a kaon identification efficiency of 99.7 % and a kaon time resolution of 66 ps.

The search for the dark photon in π^0 decays at NA62 was conducted with two studies with different background estimation methods: simulation (MC) and data-driven. The MC study did not produce competitive results in the search region when compared to previous experiments. Utilising the data-driven method the Upper Limit (UL) of the mixing parameter provides improved coverage across the phase space not covered by any other experiments. It is planned that this search will continue by analysing data collected in 2025 at NA62 to further improve the result.

The NA62 software package was upgraded to allow for more flexibility. The upgrade was rigorously tested to ensure stability and compatibility with earlier software versions. This allowed for the implementation and testing of new detectors for future experiments such as HIKE. The upgrades planned for the KTAG and RICH

and their performances within HIKE Phase 1 are shown. The particle rates for the detectors for HIKE Phase 2 were obtained. These results aided the conceptual design of the HIKE detectors. The results from the simulations were used in the HIKE proposal submitted in 2023 to the CERN SPS committee. Unfortunately the HIKE experiment was not approved. However, the upgraded software and detector studies have been used to produce the KOTO-II proposal submitted to the J-PARC committee in 2024.

References

[1] Glashow S L 1961 *Nuclear Physics* **22** 579–588 ISSN 0029-5582 URL https://www.sciencedirect.com/science/article/pii/0029558261904692

[2] Higgs P W 1964 *Phys. Rev. Lett.* **13** 508–509

[3] Cabibbo N 1963 *Phys. Rev. Lett.* **10**(12) 531–533 URL https://link.aps.org/doi/10.1103/PhysRevLett.10.531

[4] Kobayashi M and Maskawa T 1973 *Progress of Theoretical Physics* **49** 652–657 ISSN 0033-068X (*Preprint* https://academic.oup.com/ptp/article-pdf/49/2/652/5257692/49-2-652.pdf) URL https://doi.org/10.1143/PTP.49.652

[5] Chau L L and Keung W Y 1984 *Phys. Rev. Lett.* **53**(19) 1802–1805 URL https://link.aps.org/doi/10.1103/PhysRevLett.53.1802

[6] Wolfenstein L 1983 *Phys. Rev. Lett.* **51**(21) 1945–1947 URL https://link.aps.org/doi/10.1103/PhysRevLett.51.1945

[7] Buras A J, Lautenbacher M E and Ostermaier G 1994 *Phys. Rev. D* **50**(5) 3433–3446 URL https://link.aps.org/doi/10.1103/PhysRevD.50.3433

[8] Charles J and others (CKMfitter Group) 2005 *Eur. Phys. J. C* **41** 1–131 URL http://ckmfitter.in2p3.fr

[9] 2009 *The Experimental Foundations of Particle Physics* 2nd ed (Cambridge University Press)

[10] Degrange B, Fontaine G and Fleury P 2013 *Physics Today* **66** 8–8 ISSN 0031-9228 (*Preprint* https://pubs.aip.org/physicstoday/article-pdf/66/6/8/10097679/8_1_online.pdf) URL https://doi.org/10.1063/PT.3.1989

[11] Lattes C M G, Occhialini G P S and Powell C F 1947 *Nature* **160** 453–456

[12] Navas S *et al.* (Particle Data Group) 2024 *Phys. Rev. D* **110** 030001 URL http://pdg.lbl.gov

[13] Rochester G D and Butler C C 1947 *Nature* **160** 855–857

[14] Seriff A J, Leighton R B, Hsiao C, Cowan E W and Anderson C D 1950 *Phys. Rev.* **78** 290

[15] Brown R, Camerini U, Fowler P *et al.* 1949 *Nature* **163** 82–87

[16] Lee T D and Yang C N 1956 *Phys. Rev.* **104**(1) 254–258 URL https://link.aps.org/doi/10.1103/PhysRev.104.254

[17] Pais A 1952 *Phys. Rev.* **86**(5) 663–672 URL https://link.aps.org/doi/10.1103/PhysRev.86.663

[18] Gell-Mann M 1953 *Phys. Rev.* **92**(3) 833–834 URL https://link.aps.org/doi/10.1103/PhysRev.92.833

[19] Gell-Mann M 1956 *Nuovo Cim.* **4** 848–866

[20] Bardon M, Lande K, Lederman L and Chinowsky W 1958 *Annals of Physics* **5** 156–181 ISSN 0003-4916 URL https://www.sciencedirect.com/science/article/pii/0003491658900484

[21] Christenson J H, Cronin J W, Fitch V L and Turlay R 1964 *Phys. Rev. Lett.* **13**(4) 138–140 URL https://link.aps.org/doi/10.1103/PhysRevLett.13.138

[22] Barr G, *et al.* 1993 *Physics Letters B* **317** 233–242 ISSN 0370-2693 URL https://www.sciencedirect.com/science/article/pii/037026939391599I

[23] Fanti V *et al.* 1999 *Physics Letters B* **465** 335–348 ISSN 0370-2693 URL https://www.sciencedirect.com/science/article/pii/S0370269399010308

[24] Alavi-Harati A *et al.* (KTeV Collaboration) 1999 *Phys. Rev. Lett.* **83**(1) 22–27 URL https://link.aps.org/doi/10.1103/PhysRevLett.83.22

[25] Glashow S L, Iliopoulos J and Maiani L 1970 *Phys. Rev. D* **2**(7) 1285–1292 URL https://link.aps.org/doi/10.1103/PhysRevD.2.1285

[26] Buras A J, Buttazzo D, Girrbach-Noe J and Knegjens R 2015 *JHEP* **11** 033 (*Preprint* 1503.02693)

[27] Brod J, Gorbahn M and Stamou E 2011 *Phys. Rev. D* **83**(3) 034030 URL https://link.aps.org/doi/10.1103/PhysRevD.83.034030

[28] Buras A J, Buttazzo D, Girrbach-Noe J and Knegjens R 2015 *Journal of High Energy Physics* **2015** ISSN 1029-8479 URL http://dx.doi.org/10.1007/JHEP11(2015)033

[29] Buchalla G, Buras A J and Lautenbacher M E 1996 *Rev. Mod. Phys.* **68** 1125–1144 (*Preprint* hep-ph/9512380)

[30] Littenberg L S 1989 *Phys. Rev. D* **39**(11) 3322–3324 URL https://link.aps.org/doi/10.1103/PhysRevD.39.3322

[31] Buras A J and Venturini E 2022 *The European Physical Journal C* **82** URL https://doi.org/10.1140/epjc/s10052-022-10583-8

[32] Ahn J K *et al.* (KOTO Collaboration) 2025 *Phys. Rev. Lett.* **134**(8) 081802 URL https://link.aps.org/doi/10.1103/PhysRevLett.134.081802

[33] Buchalla G, D'Ambrosio G and Isidori G 2003 *Nucl. Phys. B* **672** 387–408 (*Preprint* hep-ph/0308008)

[34] Isidori G, Smith C and Unterdorfer R 2004 *The European Physical Journal C* **36** 57–66 URL https://doi.org/10.1140/epjc/s2004-01879-0

[35] Batley J R *et al.* (NA48/1) 2003 *Phys. Lett. B* **576** 43–54 (*Preprint* hep-ex/0309075)

[36] Batley J R *et al.* (NA48/1) 2004 *Phys. Lett. B* **599** 197–211 (*Preprint* hep-ex/0409011)

[37] Mescia F, Smith C and Trine S 2006 *JHEP* **08** 088 (*Preprint* hep-ph/0606081)

[38] Alavi-Harati A *et al.* 2004 *Phys. Rev. Lett.* **93**(2) 021805 URL https://link.aps.org/doi/10.1103/PhysRevLett.93.021805

[39] Alavi-Harati A *et al.* 2000 *Phys. Rev. Lett.* **84**(23) 5279–5282 URL https://link.aps.org/doi/10.1103/PhysRevLett.84.5279

[40] Aguillard D P *et al.* (Muon g-2) 2023 *Phys. Rev. Lett.* **131** 161802 (*Preprint* 2308.06230)

[41] Fabbrichesi M, Gabrielli E and Lanfranchi G 2020 (*Preprint* 2005.01515)

[42] Beacham J *et al.* 2019 *Journal of Physics G: Nuclear and Particle Physics* **47** 010501 URL https://dx.doi.org/10.1088/1361-6471/ab4cd2

[43] Batell B, Pospelov M and Ritz A 2009 *Phys. Rev. D* **80**(9) 095024 URL https://link.aps.org/doi/10.1103/PhysRevD.80.095024

[44] Batley J *et al.* 2015 *Physics Letters B* **746** 178–185 ISSN 0370-2693 URL https://www.sciencedirect.com/science/article/pii/S0370269315003342

[45] Cortina Gil E *et al.* (NA62) 2024 (*Preprint* 2412.12015)

[46] NA62Collaboration 2017 *Journal of Instrumentation* **12** P05025–P05025 URL https://doi.org/10.1088%2F1748-0221%2F12%2F05%2Fp05025

[47] Bovet C, Maleyran R, Piemontese L, Placci A and Placidi M 1982 *The CEDAR counters for particle identification in the SPS secondary beams* CERN Yellow Reports: Monographs (Geneva: CERN) URL https://cds.cern.ch/record/142935

[48] Goudzovski E *et al.* 2015 *Nuclear Instruments and Methods in Physics Research Section A: Accelerators, Spectrometers, Detectors and Associated Equipment* **801** 86–94 ISSN 0168-9002 URL https://www.sciencedirect.com/science/article/pii/S0168900215009493

[49] Aglieri Rinella G *et al.* 2019 *JINST* **14** P07010 (*Preprint* 1904.12837)

[50] Sergi A 2012 *Physics Procedia* **37** 530–534 ISSN 1875-3892 proceedings of the 2nd International Conference on Technology and Instrumentation in Particle Physics (TIPP 2011) URL https://www.sciencedirect.com/science/article/pii/S1875389212017348

[51] Bizzeti A 2018 *Springer Proc. Phys.* **212** 279–282 (*Preprint* 1706.08496)

[52] OPAL Collaboration 1991 *Nucl. Instrum. Meth. Phys. Res. A* **305** 275

[53] Cortina Gil E *et al.* (NA62) 2021 *JHEP* **02** 201 (*Preprint* 2010.07644)

[54] Fanti V and et al [NA48 Collaboration] 2007 *Nucl. Instrum. Meth. A* **574** 433

[55] Kholodenko S 2017 *Journal of Instrumentation* **12** C06042 URL https://dx.doi.org/10.1088/1748-0221/12/06/C06042

[56] Danielsson H, Gavrishchuk O, Giudici P A, Goudzovski E, Kholodenko S, Kholodenko M, Mannelli I, Obraztsov V, Sugonyaev V and Wanke R 2020 *Journal of Instrumentation* **15** C07007 URL https://dx.doi.org/10.1088/1748-0221/15/07/C07007

[57] Cortina Gil E *et al.* 2023 *Journal of High Energy Physics* **2023**

[58] Agostinelli S *et al.* 2003 *Nuclear Instruments and Methods in Physics Research Section A* **506** 250–303

[59] Brun R and Rademakers F 1997 *Nuclear Instruments and Methods in Physics Research Section A* **389** 81–86 proceedings AIHENP'96 Workshop, Lausanne, Sep. 1996

[60] Bethani A *et al.* (NA62) 2024 *JINST* **19** P05005 (*Preprint* 2312.17188)

[61] Frank I M and Tamm I E 1937 *Compt. Rend. Acad. Sci. URSS* **14** 109–114

[62] Riedl M J 1974 *Appl. Opt.* **13** 1690–1694 URL https://opg.optica.org/ao/abstract.cfm?URI=ao-13-7-1690

[63] Bache T 2022 Branching ratio measurement of the π^0 Dalitz decay at NA62 presented 03 Nov 2022 URL https://cds.cern.ch/record/2845388

[64] Henshaw J C 2023 Beam intensity effects on the $K^+ \to \pi^+ \nu\bar{\nu}$ measurement at NA62 presented 01 Dec 2023 URL https://cds.cern.ch/record/2915320

[65] Winlight System: 35, rue Benjamin Franklin, ZA Saint Martin, 84120 Pertuis, FRANCE

[66] CERN Engineers 2022 personal communication

[67] Enrico Bravin (CERN) 2023 personal communication

[68] Tanabashi M *et al.* (Particle Data Group) 2018 *Phys. Rev. D* **98**(3) 030001 URL https://link.aps.org/doi/10.1103/PhysRevD.98.030001

[69] Junk T 1999 *Nucl. Instrum. Meth. A* **434** 435–443 (*Preprint* hep-ex/9902006)

[70] Read A L 2000 Modified frequentist analysis of search results (The CLs method) *Workshop on Confidence Limits* (*CERN Yellow Reports: Monographs* vol CERN-2000-005) ed James F, Lyons L and Perrin Y pp 81–101 URL https://cds.cern.ch/record/411537/files/CERN-2000-005.pdf

[71] Neyman J and Pearson E S 1933 *Philosophical Transactions of the Royal Society of London. Series A, Containing Papers of a Mathematical or Physical Character* **231** 289–337

[72] Lurkin N 2017 Neutral Pion Transition Form Factor Measurement and Run Control at the NA62 experiment presented 2017 URL https://cds.cern.ch/record/2280295

[73] Lautrup B E and Smith J 1971 *Phys. Rev. D* **3**(5) 1122–1135 URL https://link.aps.org/doi/10.1103/PhysRevD.3.1122

[74] Mikaelian K O and Smith J 1972 *Phys. Rev. D* **5**(7) 1763–1773 URL https://link.aps.org/doi/10.1103/PhysRevD.5.1763

[75] Husek T, Kampf K and Novotný J 2015 *Phys. Rev. D* **92**(5) 054027 URL https://link.aps.org/doi/10.1103/PhysRevD.92.054027

[76] Lichard P 2011 *Phys. Rev. D* **83**(3) 037503 URL https://link.aps.org/doi/10.1103/PhysRevD.83.037503

[77] Ilten P, Soreq Y, Williams M *et al.* 2018 *Journal of High Energy Physics* **2018** URL https://doi.org/10.1007/JHEP06(2018)004

[78] Baruch C, Ilten P, Soreq Y *et al.* 2022 *Journal of High Energy Physics* **2022** URL https://doi.org/10.1007/JHEP11(2022)124

[79] Lees J P *et al.* (BaBar Collaboration) 2014 *Phys. Rev. Lett.* **113**(20) 201801 URL https://link.aps.org/doi/10.1103/PhysRevLett.113.201801

[80] Banerjee D *et al.* (The NA64 Collaboration) 2020 *Phys. Rev. D* **101**(7) 071101 URL https://link.aps.org/doi/10.1103/PhysRevD.101.071101

[81] Anastasi A *et al.* 2015 *Physics Letters B* **750** 633–637 ISSN 0370-2693 URL https://www.sciencedirect.com/science/article/pii/S0370269315007546

[82] Babusci D *et al.* 2013 *Physics Letters B* **720** 111–115 ISSN 0370-2693 URL https://www.sciencedirect.com/science/article/pii/S037026931300124X

[83] Petersen B (FASER) 2023 First Physics Results from the FASER Experiment *57th Rencontres de Moriond on Electroweak Interactions and Unified Theories* (*Preprint* 2305.08665)

[84] Davier M and Nguyen Ngoc H 1989 *Phys. Lett.* **B229** 150–155

[85] Bodas A, Coy R and King S J D 2021 *The European Physical Journal C* **81** ISSN 1434-6052 URL http://dx.doi.org/10.1140/epjc/s10052-021-09850-x

[86] Gatignon L *et al.* 2022 Report from the Conventional Beams Working Group to the Physics Beyond Collider Study and to the European Strategy for Particle Physics Tech. rep. CERN Geneva URL https://cds.cern.ch/record/2650989

[87] Ashraf M *et al.* (HIKE) 2023 High Intensity Kaon Experiments (HIKE) at the CERN SPS: Proposal for Phases 1 and 2 Tech. rep. CERN Geneva (*Preprint* 2311.08231) URL https://cds.cern.ch/record/2878543

[88] Frank J *et al.* 2001 Charged Kaons at the Main Injector (CKM): A Proposal for a Precision Measurement of the Decay $K^+ \to \pi^+\nu\bar{\nu}$ and Other Rare K^+ Processes at Fermilab Using the Main Injector Tech. rep. URL https://lss.fnal.gov/archive/test-proposal/0000/fermilab-proposal-0921.pdf

[89] Ramberg E, Cooper P and Tschirhart R 2003 A photon veto detector for the CKM experiment *2003 IEEE Nuclear Science Symposium. Conference Record (IEEE Cat. No.03CH37515)* pp 210–214 Vol.1

[90] Ambrosino F *et al.* (KLEVERProject) 2019 KLEVER: An experiment to measure BR($K_L \to \pi^0\nu\bar{\nu}$) at the CERN SPS Tech. rep. (*Preprint* 1901.03099) URL https://cds.cern.ch/record/2654942

[91] Fry J R, Ruggiero G and Bergsma F 2016 *Journal of Physics G: Nuclear and Particle Physics* **43** 125004 URL https://doi.org/10.1088/0954-3899/43/12/125004

[92] Kishimoto N, Nagamine M, Inami K, Enari Y and Ohshima T 2006 *Nuclear Instruments and Methods in Physics Research Section A: Accelerators, Spectrometers, Detectors and Associated Equipment* **564** 204–211 ISSN 0168-9002 URL https://www.sciencedirect.com/science/article/pii/S0168900206006991

[93] Beaulieu D, Gorelikov D, de Rouffignac P, Saadatmand K, Stenton K, Sullivan N and Tremsin A 2009 *Nuclear Instruments and Methods in Physics Research Section A: Accelerators, Spectrometers, Detectors and Associated Equipment* **607** 81–84 ISSN 0168-9002 radiation Imaging Detectors 2008 URL https://www.sciencedirect.com/science/article/pii/S0168900209006093

[94] Lehmann A *et al.* 2018 *Journal of Instrumentation* **13** C02010 URL https://dx.doi.org/10.1088/1748-0221/13/02/C02010

[95] Lehmann A *et al.* 2020 *Nuclear Instruments and Methods in Physics Research Section A: Accelerators, Spectrometers, Detectors and Associated Equipment* **952** 161821 ISSN 0168-9002 10th International Workshop on Ring Imaging Cherenkov Detectors (RICH 2018) URL https://www.sciencedirect.com/science/article/pii/S0168900219300865

[96] Lehmann A *et al.* 2022 *Journal of Physics: Conference Series* **2374** 012128 URL https://dx.doi.org/10.1088/1742-6596/2374/1/012128

[97] Ronzhin A, Los S, Ramberg E, Apresyan A, Xie S, Spiropulu M and Kim H 2015 *Nuclear Instruments and Methods in Physics Research Section A: Accelerators, Spectrometers, Detectors and Associated Equipment* **795** 52–57 ISSN 0168-9002 URL https://www.sciencedirect.com/science/article/pii/S0168900215006610

[98] Lehmann A 2022 Status and Perspectives of Vacuum-based Photon Detectors https://indico.cern.ch/event/1094055/contributions/4974129/attachments/2508971/4311863/Lehmann_Talk_RICH2022_final.pdf presented at RICH 2022, Edinburgh, Scotland, September 15, 2022

[99] Orlov D, Ruardij T, Pinto S D, Glazenborg R and Kernen E 2018 *Journal of Instrumentation* **13** C01047 URL https://dx.doi.org/10.1088/1748-0221/13/01/C01047

[100] Photonis Specification MCP-PMT TYPE XP85112-S-BA PLANACON Technical Specification, Document No. 184-7774A1 Available from Photonis or related sources

[101] MPPC (Multi-Pixel Photon Counter) S13360 Series Hamamatsu Photonics URL https://www.hamamatsu.com/content/dam/hamamatsu-photonics/sites/documents/99_SALES_LIBRARY/ssd/s13360_series_kapd1052e.pdf

[102] Carnesecchi F *et al.* 2020 *Nuclear Instruments and Methods in Physics Research Section A: Accelerators, Spectrometers, Detectors and Associated Equipment* **982** 164484 ISSN 0168-9002 URL https://www.sciencedirect.com/science/article/pii/S0168900220308810

[103] Anzivino G *et al.* 2020 *Journal of Instrumentation* **15** P10025 URL https://dx.doi.org/10.1088/1748-0221/15/10/P10025

[104] Nevay L J *et al.* 2020 *Computer Physics Communications* **252** 107200

[105] Ahn J K *et al.* 2025 Proposal of the KOTO II experiment (*Preprint* 2501.14827) URL https://arxiv.org/abs/2501.14827